Synthesis and Characterization of Platinum-free Catalysts for Proton Exchange Membrane Fuel Cell

Hongxin Ge

PSL UNIVERSITÉ PARIS

THÈSE DE DOCTORAT
DE L'UNIVERSITÉ PSL

Préparée à Mines Paris-PSL

Synthèse et caractérisation de catalyseurs sans platine pour pile à combustible PEM

Synthesis and Characterization of Platinum-free Catalysts for Proton Exchange Membrane Fuel Cell

Soutenue par

Hongxin GE

Le 17/03/2023

Ecole doctorale n° 621

Ingénierie des systèmes, matériaux, mécanique, énergétique

Spécialité

Energétique et génie des procédés

Composition du jury :

Nathalie, JOB Professeure, Université de Liège	*Rapportrice, Présidente*
Deborah, JONES Directrice de recherche, ICGM Université de Montpellier	*Rapportrice*
Marian, CHATENET Professeur, LEPMI Université Grenoble Alpes	*Examinateur*
Cuong, PHAM-HUU Directeur de recherche, ICPEES, Université de Strasbourg	*Examinateur*
Katia, GUÉRIN Maître de conférences HC, ICCF Université Clermont	*Examinatrice*
Sandrine, BERTHON-FABRY Ingénieure de recherche, Mines Paris - PSL	*Directrice de thèse*

MINES PARIS | PSL

Content

Acknowledgements

Firstly, I would like to give my deepest thanks to Dr. Sandrine Berthon-Fabry for taking me into the lab as a fresh graduate from ESPCI, and providing me with the opportunities to complete my thesis in the center PERSEE of MINES Paris. You developed my skills as a researcher and opened my mind on designing experiments and analyzing results. I passed impressive 3 years here with aerogel and it is an honor to work with you.

I would like to thank all members in the lab, Pierre Ilbizian and Julien Jaxel for supercritical drying and assistance of experiments, Suzanne Jacomet for SEM, Frédéric Georgi for XPS, and Gabriel Monge for XRD characterization. These synthesis and characterization methods construct the skeleton of my thesis. I cannot achieve my goals without your supports.

I would like to thank all partners of ANR project for the characterizations and fruitful discussions, Frédéric Maillard, Kavita Kumar, Keyla Teixeira Santos, and Laetitia Dubau from LEPMI; Frédéric Jaouen, Nicolas Bibent, and Moulay Sougrati from ICGM. I am particularly grateful for the experiences provided at ICGM. The training on MEA provided by Nicolas is very useful and help me better understand the MEA structure. The discussion with Frédéric Jaouen dispelled my confusion on Mössbauer spectrum and inspired me on the mechanism of active site formation.

I would like to thank my defense committee, Nathalie Job, Deborah Jones, Marian Chatenet, Cuong Pham-Huu, and Katia Guérin, for their kind and meaningful comments on my thesis. We have had an in-depth discussion on the electrochemistry and polycondensation mechanism of aerogel. Although 3 years have been focused on Fe-N-C materials, I can still get deeper understanding through the discussion.

I would like to give special thanks to the team T&P of PERSEE, Vandad-Julien Rohani, Frédéric Fabry, Maxime Spinnato, Sylvain Pagnon, and Yannick Malhot. We worked together for several months aiming to develop a new ammonia treatment method by low temperature plasma. Although the treatment conditions are hard to be determined, we successfully built a magnificent device and realized wonderful plasma.

I would like to thank my colleagues in PERSEE and MINES Paris, especially for Kevin Bellinguer. We passed 3 years together in the same office and you give me unwavering support. You help me celebrate the best of times and to pick me up during the worst of times. I also give my thanks to Miaomiao Wen and Julia Wagner for their helps in the lab. We cooperated with each other to organize the equipment in the lab and exchange our minds on the research.

Finally, my most sincere gratitude to my parents, Fengsen GE and Shuli Zhao, and my girlfriend, Kaili Mi. You have always been supportive of my decisions throughout life and have always displayed such pride in my achievements. I will be your pride in the future.

Introduction

Modern society proposed higher requirements on energy to protect the environment. In the past decades, the exponential growth of fossil fuel consumption significantly increased greenhouse gas (GHG) emissions, leading to global concern about climate change. To substantially reduce global GHG emissions, renewable energies, such as wind, solar, and tide should play a crucial role. However, due to the intrinsically unstable power generation of these renewable energies, it is necessary to convert them with an intermediate carrier that can generate power stably and sustainably. Hydrogen (H_2) is a promising candidate as an energy carrier for wide applications in the near future, especially when produced from renewable electricity by water electrolyzers, stored for long periods, and reconverted on demand to electric power in fuel cells without any GHG emission.

H_2/air proton exchange membrane fuel cell (PEMFC) is one of the most promising fuel cell types, especially for transport and portable power applications. However, due to the sluggish oxygen reduction reaction (ORR) on the cathode and the acidic environment of PEMFC, large quantities of platinum (Pt)-based electrocatalysts are necessary to reach the acceptable power performance of PEMFCs, which impedes their broader commercialization and threatens their sustainability. While advances have been made in reducing Pt usage in PEMFCs, such as using Pt-alloys to increase the intrinsic activity of Pt, the cost of automotive fuel cell system is still prohibitively high. Therefore, developing platinum-group metal-free catalysts for ORR in acidic media to ultimately replace Pt-based catalysts is highly desirable. Nowadays, the leading platinum-group metal-free catalysts for ORR in PEMFCs are single transition metal atoms (M=Fe, Mn, or Co) embedded in a nitrogen-doped carbon matrix (M-N-C). Nevertheless, this subclass of catalysts is insufficient for automotive PEMFCs. It is necessary to further improve the performance by increasing the turnover frequency and/or density of active sites in M-N-C materials. Both require rationalizing synthesis methods. Besides the intrinsic activity, the mass transport properties are also important to improve the fuel cell performance of M-N-C catalysts in PEMFC, because a thicker layer on the cathode is required with M-N-C compared to Pt-based catalysts, to compensate for their lower mass activity. In this case, the design of micro-meso or micro-meso-macroporous textures is important to improve the mass transport properties of M-N-C cathodes, facilitating O_2 diffusion to the active sites. In this thesis, aerogel-based Fe-N-C catalysts were successfully synthesized by pyrolyzing Fe-doped Resorcinol-Formaldehyde-Melamine (RMF) aerogel. The synthesis conditions were carefully investigated to elucidate the variation of their electrochemical performance with the porosity of catalysts.

Chapter 1 gives the context of this study, provides a global view of the PEMFC, and focuses on the development of Fe-N-C catalysts and the key factors affecting their performance in PEMFC.

Chapter 2 describes the synthesis method of Fe-doped RMF aerogel and post-treatment conditions. The investigations on parameters of ball-milling and ammonia treatment are presented and the best condition is employed for the synthesis of all catalysts. The electrochemical test conditions in the RDE setup and single cell of PEMFC are detailed as well.

Chapter 3 discusses the impact of Fe precursors on the catalytic performance and the porosity of Fe-N-C catalyst. Since Fe is the center of Fe-N_4 active sites, the nature of Fe in the precursor solution plays a crucial role during the formation of Fe-N_4 structure, thus deeply affecting the activity of catalysts. The factors impacting the dispersion of ferrous and ferric ions in the precursor solution should be considered, including oxide states of Fe, the counter ion of Fe salts, and the ligands attached. Catalysts were synthesized from different iron precursors and

nitrogenous ligand additives to explore the relationship between Fe precursor and ORR performance of catalysts. In addition, the impacts of different pH values in precursor solution and quantity of Fe precursor were discussed as well with catalysts synthesized from Fe phthalocyanine.

Chapter 4 investigates the impacts of melamine content in the RMF aerogel on the catalytic performance and porosity of Fe-N-C catalysts. Different from the post-introduction of N and Fe sources onto a pre-existing carbon substrate, the presence of well-dispersed N and Fe sources in the aerogel precursor can promote the formation of Fe-N_4 active sites and reduces the yield of Fe-rich nanoparticles during pyrolysis. However, excessive M content can decrease the porosity of the aerogel and even impede the gelation process. A series of Fe-N-C catalysts were synthesized by modulating the M content in order to define the limits of the gelation parameters and to identify the relationships between the gelation parameters, materials' structure, porosity, activity, and mass-transport properties.

Chapter 5 discusses the impacts of ammonia treatment on the catalytic performance of Fe-N-C catalysts compared to N_2 treatment. The main clue is the variation of different N species distinguished from their X-ray photoelectron spectra. In the document, we discuss the three possible functions of NH_3 treatment: (i) creating micropores to host Fe-N_4 active sites; (ii) forming new Fe-N_4 active sites; (iii) introducing basic N groups in the carbon layer to promote the turnover frequency of Fe-N_4 sites.

Because the durability of catalysts is also a major concern, chapter 6 makes a first attempt to enhance the durability of Fe-N-C aerogel catalyst by doping with CeO_2 as a scavenger of peroxide. Two different Ce precursors and Ce content are investigated. The Ce precursors were introduced into the system with Fe precursor, or directly as CeO_2 nanoparticles. the impact on the gelation of the system and their durability are observed.

Chapter 1 State-of-the-art on Platinum-group metal-free catalyst for Oxygen Reduction Reaction in Proton Exchange Membrane Fuel Cell

Résumé Français

L'énergie est la pierre angulaire de la civilisation moderne et la produire de façon durable est une condition préalable nécessaire. L'augmentation des émissions de gaz à effet de serre causée par la consommation de combustibles fossiles suscite des préoccupations mondiales concernant le changement climatique. Développer une économie de l'hydrogène vert basée sur les énergies renouvelables est largement considérée comme une solution prometteuse pour l'avenir de l'énergie. La pile à combustible à membrane échangeuse de protons (PEMFC) est un dispositif propre et performant permettant l'utilisation de l'hydrogène dans le domaine des transports et du portable. Cependant, en raison de la lenteur de la réaction de réduction de l'oxygène (ORR) à la cathode et de l'environnement acide des PEMFC, de grandes quantités d'électrocatalyseurs à base de platine (Pt) sont nécessaires pour atteindre les performances de puissance acceptables, ce qui entrave leur commercialisation plus large échelle. Bien que des progrès aient été réalisés pour réduire les quantités de Pt utilisées dans les PEMFC, comme l'utilisation d'alliages de Pt pour augmenter l'activité intrinsèque du Pt, le coût du système de pile à combustible reste prohibitif. Par conséquent, le développement de catalyseurs à base de métaux non nobles pour l'ORR en milieu acide pour remplacer à terme les catalyseurs à base de Pt est hautement souhaitable. De nos jours, ces principaux catalyseurs pour l'ORR dans les PEMFC sont à base de métaux de transition (M = Fe, Mn ou Co) intégrés dans une matrice de carbone dopée à l'azote (M-N-C). Néanmoins, l'activité de ce catalyseur est insuffisante pour alimenter les PEMFC dans le secteur automobile. Il est nécessaire d'améliorer encore les performances en augmentant la fréquence de rotation (TOF) et/ou la densité des sites actifs (SD) dans les catalyseurs M-N-C.

Ce chapitre passe en revue les progrès réalisés sur les électrocatalyseurs Fe-N-C. Il commence par présenter le mécanisme ORR et de la structure du site actif dans les catalyseurs Fe-N-C. Différent du catalyseur à base de Pt, l'étape qui définit la cinétique du catalyseur Fe-N-C implique un transfert d'électrons couplé aux protons dans la région contrôlée par le transport de masse, conduisant ainsi à une activité intrinsèque inférieure à une surtension élevée. Au contraire, ce n'est pas le facteur limitant dans la région contrôlée par la cinétique. Par conséquent, grâce à une optimisation minutieuse de leur structure, les catalyseurs Fe-N-C pourraient concurrencer avec succès les catalyseurs à base de Pt. Le site actif du catalyseur Fe-N-C est généralement considéré comme une structure de coordination $Fe\text{-}N_4$. Sur la base des analyses faites par ^{57}Fe Mössbauer et par spectroscopie d'absorption des rayons X, trois configurations $Fe\text{-}N_4$ différentes ont été distinguées, le spin bas ($Fe(II)\text{-}N_4/C$, D1), le spin intermédiaire ($Fe(II)\text{-}N_{2+2}/C$, D2) et le spin haut ($N\text{-}Fe\text{-}N_{2+2}/C$, D3). Parmi eux, les sites D1 et D3 ont une orbitale $3d_{z^2}$ inoccupée ou occupée par un seul spin, ils se lient donc directement à l'extrémité de l'oxygène accompagnant l'oxydation de Fe (II) en Fe (III). D'autre part, puisque le site D2 a entièrement occupé l'orbite $3d_z^2$, cela suggère qu'il n'est pas accessible à O_2 ou qu'il se lie faiblement à O_2.

Les facteurs affectant l'activité du catalyseur Fe-N-C sont ensuite discutés. Les différents centres métalliques présentent une activité intrinsèque différente. Fe est le plus actif parmi les différents centres de métaux de transition et certains catalyseurs bimétalliques peuvent améliorer la durabilité du catalyseur. Les propriétés de transport de masse sont également importantes pour améliorer les performances des catalyseurs Fe-N-C dans les PEMFC, car une couche plus épaisse à la cathode est nécessaire pour compenser une activité massique inférieure du catalyseur sans Pt. Dans ce cas, un support carboné hautement poreux est important pour améliorer les propriétés de transport de masse des cathodes Fe-N-C, facilitant la diffusion de l'O_2 vers les sites actifs et l'évacuation de H_2O produite. De nos jours, les catalyseurs Fe-N-C les plus performants sont des catalyseurs à base de mésopores, soit préparés à partir d'une

méthode de « hard templating », soit d'un catalyseur à base de structure organométallique (MOF). Les deux types de catalyseurs contiennent un volume de micropores élevé pour héberger des sites actifs et un volume de méso/macropores pour améliorer les propriétés de transport de matière. Récemment, certains catalyseurs Fe-N-C à base d'aérogel ont été synthétisés avec succès en pyrolysant un aérogel de résorcinol-formaldéhyde-mélamine (RMF) dopé au Fe. Les aérogels sont des candidats idéaux comme support de carbone mésoporeux en raison de leur surface spécifique élevée et de leurs larges volumes de pores. De plus, la porosité et la surface spécifique des aérogels de carbone sont ajustables en modifiant les conditions de synthèse et de procédés. Le protocole de synthèse de l'aérogel RMF évite l'utilisation de « hard templating » avec de l'acide fluorhydrique, et est donc plus respectueux de l'environnement et adapté à une production à grande échelle.

La durabilité du catalyseur Fe-N-C est un autre facteur important qui doit être pris en compte avant qu'il ne soit largement utilisé dans les PEMFC. La perte d'activité des catalyseurs Fe-N-C est principalement attribuée à l'oxydation/attaque du site actif par H_2O_2 en milieu acide. L'augmentation du degré de graphitisation pourrait être une méthode prometteuse pour réduire la corrosion du carbone au cours du processus ORR, préservant ainsi davantage de sites actifs. En outre, différentes configurations de sites actifs présentent également une stabilité différente. Le site D1 n'est pas durable durant le fonctionnement de la PEMFC, se transformant rapidement en oxydes, car il est exposé en surface et se lie directement à l'oxygène. En revanche, le site D2 est plus durable en raison de l'absence de changement d'état d'oxydation pendant le processus ORR. Par conséquent, la durabilité des catalyseurs Fe-N-C pourrait être améliorée en augmentant la densité des sites D2 et en intégrant les sites D1 dans un support de carbone plus graphitique.

1.1 General context

Energy is the cornerstone of modern civilization and the prerequisite for sustainable development. Over the past few decades, global primary energy consumption increased enormously with the step of population growth and industrialization of developing countries. Since fossil fuels are the primary energy source for almost all countries, greenhouse gas (GHG) emission, which mainly indicates carbon dioxide and methane, significantly increased and resulted in environmental pollution and the global warming effect cannot be ignored[1]. According to the statistic of the International Energy Agency (IEA), the average annual growth of GHG emission is 2.6% per year between 1950 and 2009, as seen in **Figure 1.1**. In recent years, many countries have experienced an unprecedented number of climate events, with extreme weather leading to flooding, drought, and wildfires, and causing food shortages, health problems, and major damage to ecosystems and human habitats. How best to combat climate change and global warming while satisfying the world's energy consumption without impairing the global economy is an urgent problem for every country.

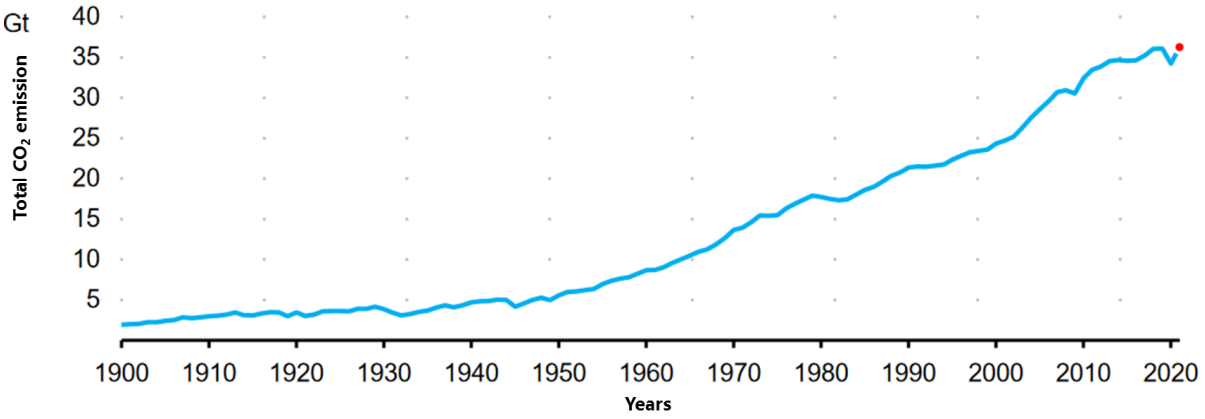

Figure 1.1 Total CO_2 emissions from energy combustion and industrial processes from 1900-2021[2].

Fortunately, since the 21st United Nations Climate Change Conference (COP 21) in Paris, Parties to the United Nations Framework Convention on Climate Change (UNFCCC) reached a landmark agreement to combat climate change and to accelerate and intensify the actions and investments needed for a sustainable low carbon future. In 2018 the Intergovernmental Panel on Climate Change (IPCC) found that global net anthropogenic CO_2 emission would need to reach net zero around 2050 in a pathway consistent with limited global temperature increases to 1.5 ℃[3]. The European Union (EU) is considering zero emissions as an objective for 2050, and others are likely to do the same. As a result, the average annual growth of GHG emission rate in the past decade (2010-2019) has been slowed to 1.1% per year, and the total CO_2 emission reached a high of 36.1 gigatonnes (Gt) in 2019. Reasons for this decadal slowdown include a global reduction in new coal capacity additions, the steady substitution of coal for gas in the power sectors of developed countries, and the increasing pace of renewable energy deployments worldwide[2]. However, global GHG emissions are still far from reaching a plateau, not to mention a reversal of this trend. Although the total GHG emission was reduced by 5.1% in 2020 due to the impacts of the Covid-19 pandemic, this value quickly rebounded to reach its highest-ever annual level, accompanied by the recovery of energy demand from the Covid-19 pandemic in 2021. A 6% increase from 2020 pushed emissions to 36.3 Gt.

The EU's energy policy aims to ensure a competitive, sustainable, and secure energy supply[4]. To achieve this energy policy triangle, a serious impetus exists to diversify our energy sources, reducing our reliance on fossil fuels by turning to renewable energy such as solar, wind, and hydroelectric power[5,6]. However, due to the uncontrollable change of weather conditions, the stability of their output poses a challenge when their share of the future primary energy mix rises. To get over this hurdle, a hydrogen (H_2) economy based on renewable energy, including H_2 production, storage, and conversion, is widely considered a promising solution for the future of energy. H_2 is an excellent energy carrier to alternate fossil fuels that gear to the requirements of renewable, zero emission, and high quantity. Its potential role has similarities with that of electricity, but the crucial difference is that H_2 is a chemical energy carrier composed of molecules and not only electrons. This distinction underpins all the reasons H_2 might outcompete electricity in some situations[3,7]. As a low-carbon chemical energy carrier, hydrogen is a leading option for reducing those hard-to-abate emissions, such as transport, heating, and industrial raw materials, because it can be stored, combusted, and combined in chemical reactions similar to natural gas, oil, and coal. H_2 can be obtained from several resources, such as water electrolytic splitting or hydrocarbon reforming. Since the latter method still has a high CO_2 intensity upstream, the water-splitting method has a better prospect. Nowadays, the electricity cost for water splitting is one of the significant barriers to a sustainable energy system and economy. However, there are opportunities to produce low-carbon H_2 on a large scale if renewable power generation becomes sufficiently cheap and widespread. This offers a means of escaping the constraint of burning carbon-based fossil fuels[7].

In the hydrogen economy, fuel cells are regarded as the energy conversion devices of the future due to their excellent compatibility with H_2 energy carrier. They enable secure and suitable energy conversion in an environmental and relatively cost-effective way[8,9]. A fuel cell is an electrochemical device that converts the chemical energy of a fuel directly into electrical energy, accompanied by some thermal energy and H_2O as byproducts. While in the case of heat engines, producing electricity is a multi-step process that involves combustion to produce thermal energy from the internal chemical energy of the fuel. Then this thermal energy is converted into mechanical energy, and finally, this mechanical energy is converted into electrical energy using a generator. Generally, as the number of energy conversion processes increases in a certain device, the overall system efficiency of the device decreases. The one-step nature of fuel cell provides an efficient and clean mechanism for energy conversion compared with the traditional combustion-based processes[8]. On the other hand, heat engines are limited by the Carnot efficiency between their low and high working temperatures. Additionally, the conception without moving parts of fuel cells also means quiet operation without the noise of vibration. At the same time, their inherent modularity allows for simple construction and a diverse range of applications in portable, stationary, and transportation power generation. The following introductory section provides a brief overview of the electrochemical technologies targeting fuel cells, especially proton exchange membrane fuel cells.

1.2 Proton Exchange Membrane Fuel Cell

1.2.1 Fundamentals of fuel cell

A fuel cell stack consists of a stack of membrane electrode assemblies (MEA) and bipolar plates. As the core of a single cell, the MEA consists of a membrane, two dispersed catalyst

layers, and two gas diffusion layers (GDL)[10]. The electrodes consist of a porous material covered with a layer of catalyst. In a fuel cell stack, each bipolar plate supports two adjacent cells. The bipolar plates typically have four functions: (1) to distribute the fuel and oxidant within the cell, (2) to facilitate water management within the cell, (3) to separate the individual cells in the stack, and (4) to carry current away from the cell. Additionally, in the absence of cooling plates, they also facilitate heat management.

Figure 1.2 illustrates the elemental composition of a single cell of proton exchange membrane fuel cell (PEMFC). H_2 fuel is delivered from a gas-flow stream to the anode and then oxidized to protons by the half-cell reaction (1-1), called hydrogen oxidation reaction (HOR). The protons migrate through the proton exchange membrane (PEM) to the cathode, while the electrons are forced through an external circuit to the cathode. At the cathode, the electrons and protons react with the oxygen (O_2) supplied from an external gas-flow stream to form water, as the half-cell reaction (1-2), which is called oxygen reduction reaction (ORR). Thus the overall reaction in the fuel cell can be written as (1-3), with every stack unit offering a maximum potential of 1.229 V without consideration of any dissipation.

Anode: $2H_2 \rightarrow 4H^+ + 4e^-$ $E^0 = 0.000$ V *vs.* SHE (1-1)

Cathode: $O_2 + 4H^+ + 4e^- \rightarrow 2H_2O$ $E^0 = 1.229$ V *vs.* SHE (1-2)

Total: $H_2 + ½\ O_2 \rightarrow H_2O + W_{electrical} + Q_{heat}$ $E^0 = 1.229$ V (1-3)

The efficiency can then be calculated from the ratio between the electrical power output and the fuel input, as showed in equation (1-4)[11]:

$$\eta_{FC} = \frac{\text{electrical power output } (P_{FC})}{\text{fuel input } (F_{in})}. \quad (1\text{-}4)$$

P_{FC} is simply a product of potential (V) and current (I):

$$P_{FC} = V \cdot I \quad (1\text{-}5)$$

F_{in} is a product of fuel consumption rate and its energy content, usually given as enthalpy (ΔH). Hydrogen's heating value is 142 kJ g^{-1}. According to the Faraday's Law and reaction (1-1), the quantity of hydrogen consumption (q_{H_2}) can be expressed as equation (1-6):

$$q_{H_2} = \frac{mI}{nF} \quad (1\text{-}6)$$

where m is hydrogen molecular weight (2.016), n is number of electrons transferred for every hydrogen molecule (2), and F is Faraday constant (96,485 C mol^{-1}). The F_{in} is therefore:

$$F_{in} = q_{H_2} \cdot \Delta H = \frac{m\Delta H}{nF} I \quad (1\text{-}7)$$

For the electrochemical reaction (1-1), the expression $m\Delta H/nF$ has a value of 1.482 V. This is also called the thermoneutral or reversible potential, which corresponds to the maximum possible energy (both electrical and thermal) resulting from the chemical reaction. The η_{FC} can then be simplified by elimination current and expressed as the ratio of operating voltage and 1.482V:

$$\eta_{FC} = \frac{\mathrm{V}}{1.482} \quad (1\text{-}8)$$

Therefore, the maximum theoretical hydrogen fuel cell efficiency at 25 ℃ is 1.229/1.482 = 0.83.

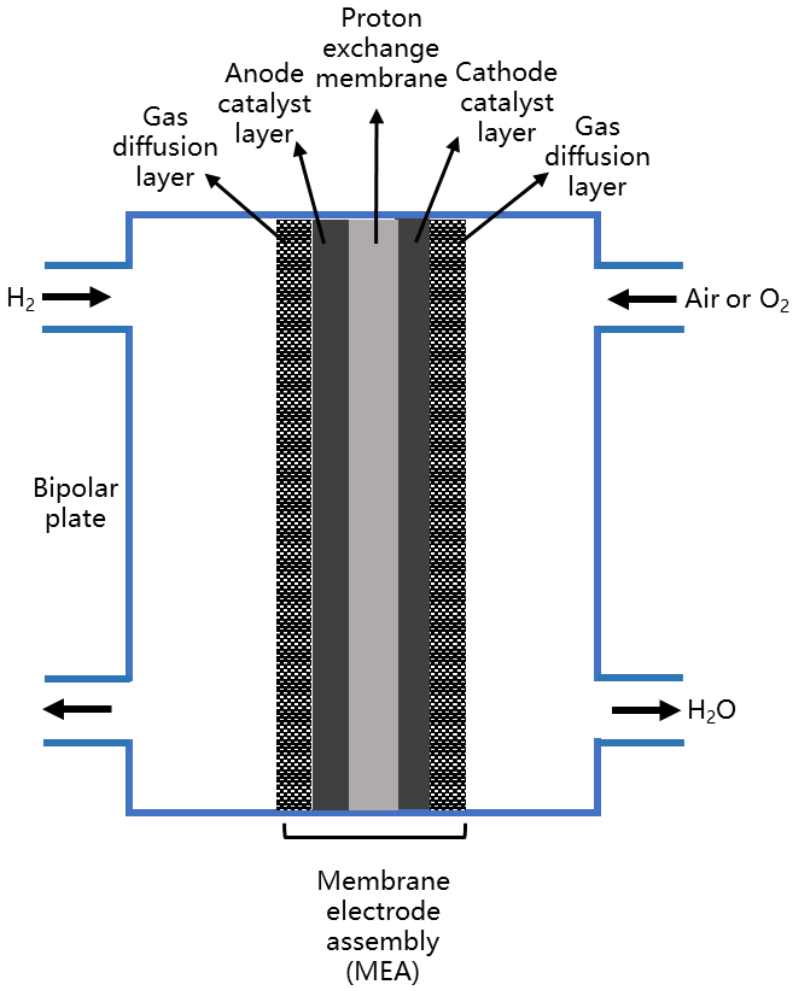

Figure 1.2 Schematic of a single cell of PEMFC.

The actual cell potential in operation is lower than the thermodynamic potential due to various losses, such as:

(a) activation losses:

$$V_{\mathrm{act}} = \frac{RT}{\alpha n \mathrm{F}} \ln\left(\frac{j}{j_0}\right) \tag{1-9}$$

(b) mass transport losses:

$$V_{\mathrm{mt}} = \frac{RT}{n\mathrm{F}} \ln\left(1 - \frac{j}{j_L}\right) \tag{1-10}$$

(c) and ohmic losses:

$$V_{\mathrm{ohm}} = jR_j \tag{1-11}$$

where, α is the transfer coefficient; j is current density (A cm^{-2}); j_0 is exchange current density (A cm^{-2}); j_L is limiting current density (A cm^{-2}); and R_j is cell resistance (Ω cm^2).

Activation and mass transport losses can exist at both the cathode and anode, while the ohmic losses are mainly due to resistance in electrolyte. The cell potential can be then present as:

$$V_{\text{cell}} = V_0 - V_{\text{act,a}} - V_{\text{act,c}} - V_{\text{mt,a}} - V_{\text{mt,c}} - V_{\text{ohm}} \quad (1\text{-}12)$$

When no load is connected to the fuel cell, *i.e.*, at open circuit, the potential of PEMFC is typically around 1 V. When the load is connected to the fuel cell, the cell potential decreases further as more current is generated, leading to lower efficiency. Since the power density of fuel cells increases with decreasing cell voltage, the efficiency at the maximum power density of fuel cells is much lower than that at partial loads, which makes the fuel cells very attractive and efficient for applications with highly variable loads where most of the time fuel cells are operated at low load and high efficiency. Therefore, the fuel cell nominal efficiency is an arbitrary value, ranging anywhere between 0.3 and 0.6, depending on the operation potential. This result implies the efficiency of a fuel cell may be increased by adding more cells to achieve the expected output power density. However, due to the economic factors limit, the individual cells should be controlled at an adapted number. Reducing the potential loss in the single cell is crucial in increasing the efficiency of fuel cell. The ohmic losses are generally minimal among overall potential losses if an appropriate coating method is employed[12]. Therefore, the efforts should be focused on reducing the activation and mass transport losses.

The activation losses are determined by the property of the electrode, which contributes the most to the total loss of voltage[13]. If the electrode is metallic, it has strongly overlapping orbitals and energy levels as a continuum. Therefore, the energy of the electrons can be increased by increasing the applied voltage, which can affect the Fermi-Level of the metal. Suppose the electrode is in contact with a solution containing reducible species, the Fermi-Level of the electrode may be increased enough to help the electron overcome the barrier of reaction and reduce them, such as ORR[14]. The electron is transferred from the metal to the lowest unoccupied molecular orbital (LUMO) of the solution species. The reverse may also occur: Fermi-Level can be reduced to oxidize solution species by accepting the electron from their highest occupied molecular orbital (HOMO) in the metal (such as HOR). The difference between the energy levels of the metal and the solution species determines whether the electron transfer is thermodynamically favorable but not its kinetics. Electrode kinetics describes how the rate of electron transfer at an electrode surface is affected by the applied voltage.

The reduction reaction can be written as the reaction:

$$O + e^- \leftrightarrow R \quad (1\text{-}13)$$

where O represents the oxidized form of the solution species and R represents the reduced form. The rates of the forward, reduction R_{red}, and backward, oxidation R_{ox}, reactions can be expressed as

$$R_{red} = k_{red}[O] \qquad R_{ox} = k_{ox}[R] \quad (1\text{-}14)$$

where k_{red} and k_{ox} are the rate constants of reduction and oxidation and $[O]$ and $[R]$ are the concentrations of the species O and R respectively. As well as the expression of concentration, the reaction rate can also be expressed by the electrical current at the electrode surface, i, as this

is the rate of electron transfer. The reductive current (i_{red}) and oxidative current (i_{ox}) are then written as

$$i_{red} = nFAk_{red}[O]_s \qquad i_{ox} = nFAk_{ox}[R]_s \tag{1-15}$$

where n, F, and A are the number of electrons transferred during the reaction, Faraday's constant, and the electrode area, respectively. $[O]_s$ and $[R]_s$ are the concentration of species O and R at the electrode surface, where the corner mark indicates they are different from the concentration in bulk solution. The net rate of reaction (R_{net}) is the difference between forward and backward reaction rates. Therefore, the net current (i_{net}) can be expressed as

$$i_{net} = i_{red} - i_{ox} = nFAk_{red}[O]_s - nFAk_{red}[R]_s \tag{1-16}$$

Rate constants vary with temperature according to the Arrhenius rate equation:

$$k = A\, exp(-E_a/RT) \tag{1-17}$$

where E_a is the activation energy of the reaction, R is the gas constant, T is the temperature in Kelvin, and A is the pre exponential factor. Because the rate constants k_{red} and k_{ox} are also affected by the applied potential at the electrode surface, the kinetic equation must describe the effect of potential (E) upon rate, as the Arrhenius equation does with temperature. To achieve this, the Butler-Volmer equation of electrochemical kinetics has been proposed, which can be written as (1-18) for the single electron transfer reaction[15]:

$$i_{net} = i_0 \left(e^{\frac{\alpha F\left(E-E_{eq}\right)}{RT}} - e^{-\frac{(1-\alpha)F\left(E-E_{eq}\right)}{RT}}\right) \tag{1-18}$$

where E_{eq} is the equilibrium potential for the reaction and E is the potential applied to the electrode surface. i_0 is the exchange current, representing the current flowing both ways at E_{eq} (i_{red} or i_{ox}, where there is zero net current). i_0 has equation:

$$i_0 = FAk^0[R]^{\alpha}[O]^{1-\alpha} \tag{1-19}$$

where k^0 is the rate constant for the reaction at E_{eq}. α is called the symmetry factor. The physical meaning of the terms α and 1-α in equation (1-18) and (1-19) are to do with the position of the activation energy peak for the reaction along the reaction coordinate. α here is the position of the activation energy peak along the reaction coordinate of the oxidation reaction. Therefore 1-α represents the peak position along the reaction coordinate of the reverse reaction (reduction reaction). A value for α of 0.5 (1-α = 0.5) signifies that the peak for the activation energy barrier of both the reduction and oxidation reaction is halfway along the reaction coordinate. Thus, half of the energy from the potential drop at the electrode-electrolyte interface is used to push the reaction, as the reaction coordinate is downhill after that. Values of α different from 0.5 imply an asymmetry in the reaction coordinate, which means the peak of the activation energy barrier lying closer to reactants or products. In these cases, the proportion of the energy from the potential drop is different for the oxidation and reduction reactions.

As E-E_{eq} above is the difference between the applied and equilibrium potential, it is commonly replaced with the symbol η, which is known as the overpotential. Thus, the equation (1-18) can also be written as the most common form:

$$j_{net} = j_0 \left(e^{\frac{\alpha F\eta}{RT}} - e^{-\frac{(1-\alpha)F\eta}{RT}}\right) \quad (1\text{-}20)$$

where j_0 is the exchange current density and j_{net} is the net current density. The effect of exchange current density on the current-potential response is shown in **Figure 1.3**[14]. High values of j_0 are observed for fast, well-catalyzed reactions such as the HOR in PEMFCs. The complimentary ORR has a j_0 several orders of magnitude lower than this due to its slow kinetics. This is in line with the equation(1-10) that a higher j_0 close to the E_{eq} leads to a lower activation loss. To overcome this low j_0, excess overpotential has to be paid for the ORR, which reduces the voltage of every unit cell. In order to increase the efficiency of PEMFCs, a high quantity of catalysts on the cathode is necessary, thus significantly increasing the cost. In this case, j_0 is crucial in electrocatalysis as it describes the ability of the catalyst to promote the reaction.

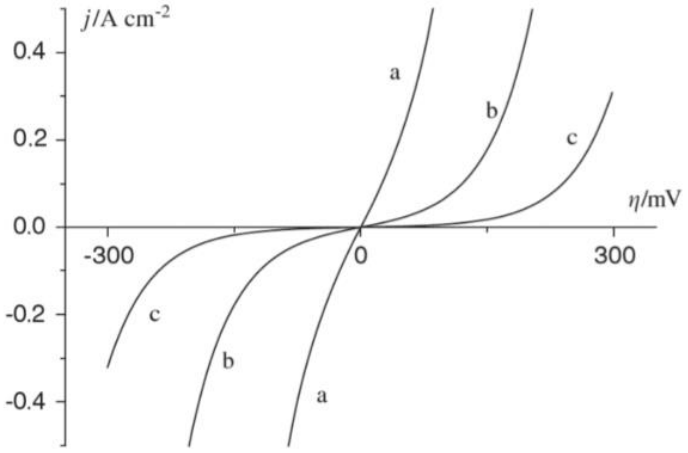

Figure 1.3 Influence of the exchange current density, j_0, on the j-η response when n=1 and α=0.5. (a) j_0 = 0.1, (b) j_0 = 0.01, and (c) j_0 = 0.001 A cm^{-2} [14].

Mass transport losses are essential factors that should be considered as well. In order to maintain the continuous isothermal operation of fuel cells, the heat and water byproducts must be continuously removed from the cells. Otherwise, the accumulated water in the MEA would mute the O_2 to access the catalyst. **Figure 1.4** exhibits a structure of MEA in the single cell[16]. The thickness of catalyst layer on the cathode (~90 μm) is much higher than that on the anode (< 10 μm) due to huge quantity of catalysts was employed to promote the sluggish ORR, leading to higher mass transport resistance. In general, mass transport losses in the platinum-group metal-free catalyst MEA are much higher than that in the platinum-contained cell due to their significantly thicker catalyst layer (more than 50-70 μm for platinum-group metal-free catalyst compared to 4-8 μm for Pt-based catalyst). As a result, a highly porous structure is usually necessary for platinum-group metal-free catalysts to reduce the mass transport resistance[12,17,18]. In PEMFC, the proton exchange membrane also contributes partial mass transport losses. The membrane separates two half-reactions and allows the protons to pass through to balance the proton concentration of two sides. An ideal membrane for high-power PEMFCs should possess high proton conductivity under low humidity conditions and good electrochemical and mechanical stability[8]. Nowadays, perfluorosulfonic acid (PESA) is the most commonly used membrane material for PEMFCs[19], which benefits from the stability of the backbone and high ionic conductivities[20]. PESA consists of three regions: (1) a polytetrafluoroethylene acts as the backbone, (2) side chains of -O-CF_2-CF_2-O-CF_2-CF_2- which connect the molecular backbone to the third region, and (3) ion clusters consisting of sulfonic acid ions[21]. When the membrane

becomes hydrated, the protons in the third region become mobile and moving between sulfonic acid sites with the help of hydrogen bond[20,21]. The most commonly used PFSA membrane is Dupont's Nafion®, a copolymer of tetrafluoroethylene backbone and sulfonic acid-terminated perfluoro vinyl ether pendant, which offers a proton conductivity of 0.13 S cm^{-1} (75 ℃ and 100% relative humidity (RH)) and durability above 60,000 h[22]. To improve the power density of PEMFCs, the primary strategy is to reduce the thickness of the membrane. However, thin membranes also face challenges of mechanical damage or electrochemical degradation[19]. Besides, the operation temperature of PESA membranes is below 100 ℃ because the water-filled channels determine the proton conductivity. Unfortunately, heat is necessary for an excellent kinetic reaction, but too much heat will cause the membrane to dry up and increase the mass transport resistance. Therefore, some new membranes used in high-temperature PEMFC, such as sulfonated hydrocarbon polymers, have been considered promising alternatives owing to their high proton conductivity and thermal stability at high temperatures and humidities[19].

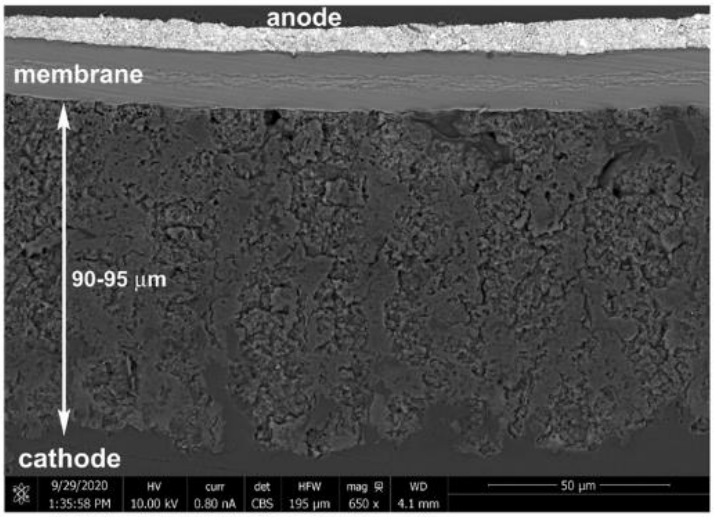

Figure 1.4 Schematic of the MEA in a single cell of PEMFC[16]. Anode: Pt/C catalyst, Cathode: Fe-Mn-N-C catalyst.

1.2.2 Different types of fuel cell

There are several major types of fuel cells, as showed in **Table 1.1**[23,24], which are mainly classified by different electrolytes, charge carriers, and operating temperatures. Phosphoric Acid Fuel Cells (PAFCs), High/Low Temperature Proton Exchange Membrane Fuel Cells (HT/LT-PEMFCs), Alkaline Fuel Cells (AFCs), and Alkaline anion exchange membrane fuel cells (AAEMFCs) work at relatively low temperatures, which essentially require pure hydrogen to be supplied to the anode. Accordingly, using hydrocarbon or alcohol fuels requires an external fuel processor that converts the fossil fuel into hydrogen to be incorporated into the system. In contrast, the Solid Oxide Fuel Cells (SOFCs) and Molten-Carbonate Fuel Cells (MCFC) operating at higher temperatures have the advantage that both CO and H_2 can be electroactive at the anode, thus more suitable for hydrocarbon fuel. Air can be employed directly as the reactant at the cathode of almost all of these types of fuel cell except AFC because the electrolyte risks the degradation by the CO_2 in air. Among these different fuel cells, PEMFCs have many advantages such as low operating temperature, sustained operation at a

high current density, low weight, compactness, the potential for low cost and volume, long stack life, fast start-ups, and suitability for discontinuous operation[21]. These features make PEMFCs the most promising candidate for wide applications ranging from portable power and transportation to large-scale stationary power systems for buildings and distributed generation.

Table 1.1 Summary of different types of fuel cell.

Types	Electrolyte	Charge carriers	Operating temperature	Application
SOFC	Metallic oxide solid ceramic	O^{2-}	500-1000 ℃	Stationary power generation system[24]
MCFC	Molten carbonate salt mixture	CO_3^{2-}	500-1000 ℃	Electric utility for natural gas and coal-based power plants, industrial, and military applications[24]
PAFC	Phosphoric acid	H^+	150-220 ℃	High capacity power station[24]
AFC	Potassium hydroxide	OH^-	60-90 ℃	Electric power in submarines, boats, forklift trucks and niche transportation applications[24]
AAEMFC	Alkaline anion exchange membrane	OH^-	60-100 ℃	Energy storage device for grid applications[25]
PEMFC HT	Proton conductor polymer membrane for high temperature	H^+	120-180 ℃	Portable and stationary power system, especially in transportation[24,26]
PEMFC LT	Proton exchange membrane	H^+	60-100 ℃	

Fuel cell vehicle (FCV) is one of the major applications of PEMFC. Compared with battery electric vehicles (BEVs), H_2 has inherent advantages over lithium-ion batteries, including higher energy density and shorter refueling time for FCVs[27]. The FCV also outperforms the BEV under sub-zero temperature conditions because the BEV often exhibits considerably reduced discharge capacity[19]. The cost of FCVs is currently higher than that of BEVs for short-range vehicles (below 322 km); however, the sequence is inversed with high annual production rates, particularly for long-range vehicles (above 483 km)[27]. As a significant milestone in PEMFC commercialization, Toyota introduced their first FCV, Mirai, in 2017. The fuel cell system adopts advanced design and materials to achieve a Pt-loading of 0.365 mg cm^{-2}, 2.0 kW kg^{-1}, and 3.1 kW L^{-1} for 114 kW generations[22]. At the end of 2020, the stack power density of the second generation reached 4.4 kW L^{-1}, an increase of 42% compared with the previous generation. The European Union Fuel Cells and Hydrogen 2 Joint Undertaking (EU-FCH2JU) recently demonstrated a PEMFC stack with a power density of 5.38 kW L^{-1} at a current density of 2.67 A cm^{-2} and a single-cell voltage of 0.6 V, and the goal is 9.3 kW L^{-1} by 2024[19].

Currently, there are two major barriers to the wide application of PEMFC: cost and durability. The total cost of a PEMFC system includes all the major components: the stack and the balance of plant (BOP), the latter including the air loop, humidifier and water recovery loop, high- and low-temperature coolant loops, the fuel loop, and the fuel cell system controller. Each of the two parts accounts for about 50% of the total system cost. The most significant contributions to the stack cost are the MEAs and bipolar plates, and the air loop is by far the costliest subsystem within the BOP[10]. The current state is 40 \$ kW^{-1} for 500,000 per year product volume, reduced by 60% in the past decades. The ultimate DOE target is 30 \$ kW^{-1} for fuel

cells in FCVs and 600,000 $ per bus for FC bus[22]. Among all the crucial technologies, catalysts are the fundament of fuel cells that decide the cost and conversion efficiency of the devices. However, even if the manufacturing cost has been reduced as much as possible by mass manufacture, the cost of catalysts is less dependent on manufacturing volume. As seen in **Figure 1.5**, among the components, the catalysts contribute 41% of the total cost of PEMFC at high-volume production, primarily due to the use of noble metal catalysts to promote the sluggish ORR on the cathode[10]. It is thus obvious that the use of Pt affects significantly the PEMFC cost and consequently its competitiveness on the market. Furthermore, Pt is considered as a critical raw material by European Union due to its irreplaceable character in several highly important industrial applications, lack of interior resources and general scarcity[28]. On the other hand, the old catalysts cannot be directly reused in a new MEA owing to the chemical and structural modifications of the MEA components during the operation of PEMFC. Therefore, the application of Pt-based catalysts requires a mature recycling system to manage the Pt in a closed loop[28]. The well-established methods are based on a pyrometallurgical process, which is not economically and environmentally viable due to a huge emission of toxic hydrofluoric acid (HF) [29,30]. For example, Xu *et al.*[29] recovered Pt by dipping waste MEA in hot sulfuric acid, where the polymeric membrane and carbon support were oxidized and dissolved. The Pt catalyst was collected as metallic particles with an average diameter of 35 nm. The novel recovery processes focus on selective dissolution of Pt to reduce the HF release. Duclos *et al.*[31] leached the Pt from MEA by a mixture an oxidant (H_2O_2 or HNO_3) and hydrochloric acid. Since no incineration is carried-out within this pure hydrometallurgical process, no HF is released. Recently, Sharma *et al.*[32] recovered Pt in MEA by electrochemical dissolution in a dilute acidic bath. The Pt was then precipitated in form of $(NH_4)_2PtCl_6$, a precursor for preparing Pt/C electrocatalyst. This method shows high overall recovery efficiency of >90% and is suitable for industrial upscaling, which is possible to be the last piece for closing the loop of Pt.

To date, the DOE 2025 target for Pt-based catalysts has been fulfilled (activity of 1.08 A mg_{Pt}^{-1} at 0.9 V with 0.1 mg_{Pt} cm^{-2})[33], the long-term, large-scale deployment of PEMFCs in the field of automotive production still requires the use of elements that are far less expensive and more abundant than Pt. Therefore, developing highly efficient platinum-group metal-free catalysts is crucial to make the PEMFC more economical.

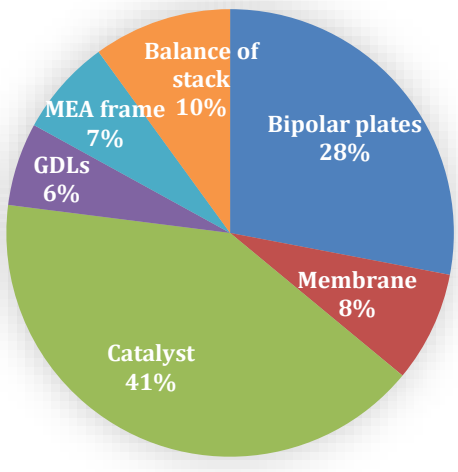

Figure 1.5 Diagram of the cost of different part in proton exchange membrane fuel cell[10].

The lifespan is another critical issue that restricts the large-scale commercialization of PEMFC. Currently, the lifetime of PEMFCs is only 2500-3000 h when it is used as a power plant for passenger vehicles, which is far from the near-term durability target of DoE (5000 h). Compared with the lifetime of vehicle PEMFCs, their life as a fixed power source can reach 30,000 h. The main reason for this huge disparity is that the operating conditions of the vehicle fuel cell are very complex, requiring frequent switches between start-stop, idling, high power, and load changing[34]. Studies have shown that gas starvation during load change is the leading cause of fuel cell decay, which causes severe consequences of interaction: corrosion of the carbon support, cell reversal, and uneven current distribution. These consequences will further lead to catalyst agglomeration, loss, detachment, increased diameter of catalyst particles, reduced active surface area, and decreased catalyst layer thickness. Therefore, to ensure the fuel cell system can perform sufficiently long to serve the whole vehicle lifetime (5000 h or 150,000 miles on average), efforts to enhance the durability of catalysts are emergency.

1.3 Electrocatalysts of Oxygen Reduction Reaction (ORR)

In the PEMFC system, the ORR pathway always requires more energy input than the HOR pathway, which results in a more significant part of polarization resistance due to its sluggish kinetics at a low temperature (80-100 ℃)[35]. As presented in **Table 1.2**, ORR is a multi-step reaction processing via either a four-electron ($4e^-$) path to directly produce H_2O as final products or a two-step two-electron ($2e^-$) path with H_2O_2 as the intermediate species, depending on the inherently electrocatalytic properties of catalysts. A higher selectivity of $4e^-$ reduction indicates better electrocatalytic ORR efficiency of a given catalyst. In conventional fuel cell technology, precious Pt supported on a conductive carbon composite (Pt/C) is the most commonly used $4e^-$ ORR catalyst due to the excellent activity of Pt[36,37]. The kinetic barriers require a higher Pt loading (~0.4 mg cm^{-2}) at the cathode to achieve a desirable fuel cell performance[38], which dedicates to the high cost of FCVs. Therefore, reducing its loading by nano-structuring and alloying, or even completely replacing it with low-cost platinum-group metal-free catalysts of ORR, is necessary for PEMFC. In order to well design the high-performance catalysts for ORR, the mechanism of the reaction on the electrode should be investigated and presented below.

Table 1.2 The possible reaction pathways during ORR in acidic media and their standard potentials.

	Reaction	E^0/V *vs* SHE
Direct $4e^-$ pathway	$O_2 + 4H^+ + 4e^- \rightarrow 2H_2O$	1.23
Peroxide ($2e^-$) pathway	$O_2 + 2H^+ + 2e^- \rightarrow H_2O_2$	0.67
	$2H_2O_2 + 2H^+ + 2e^- \rightarrow 2H_2O$	1.77

1.3.1 Noble metal electrocatalysts

The detailed mechanism of ORR in acidic media can be divided into three pathways, as shown in **Figure 1.6**[39]. The O_2 molecule is first adsorbed and activated on the surface of the catalyst to form O_2* (I), where * represents the active site of the catalyst. The O-O bond is then cleaved in the following three different ways: (i) Dissociative pathway: the O-O bond is cleaved directly into two O* intermediates (II), which are then successively reduced to OH* (III and IV) and H_2O* and eventually end up with desorption of H_2O*(V); (ii) Associative-dissociative pathway: OOH* is first generated from O_2* (VI), and then the O-O bond is cleaved into O* and OH* (VII), followed by their successive reductions to form H_2O (IV and V); (iii) Associative

pathway: the O_2* is sequentially reduced to OOH* (VI) and HOOH* (VIII), then 2 OH* can be generated and finally reduced to H_2O* (IX)[39]. For Pt-based and Fe-N-C catalysts, the associative-dissociative pathway is considered dominant[40,41], containing three different intermediates OOH*, O*, and OH*. However, their binding energies are strongly correlated and change monotonically for different catalysts because all the adsorbates bind to the surface through an O atom, *i.e.*, $\Delta G_{OH^*} = 1/2\ \Delta G_{O^*}$ and $\Delta G_{OH^*} = \Delta G_{OOH^*} - 3.2$ eV. In this case, the catalyst surface reactivity can be quantified as the function of the binding energy of OH*. An ideal ORR electrocatalyst should bind intermediates neither too strongly nor too weakly[39]. This results in a volcano-plot-like correlation between the activity and the binding energy of the intermediates. Among all investigated elements, Pt exhibits the closest-to-optimum OH* binding energy, being only 0.1-0.2 eV too strong[41]. The ORR selectivity ($2e^-$ or $4e^-$ pathway) mainly depends on the dissociation energy barrier of absorbed O_2 molecules on the surface of active sites. The O_2 dissociation energy barrier on the surface of Pt is very low, thus greatly favoring the $4e^-$ pathway[36,42,43].

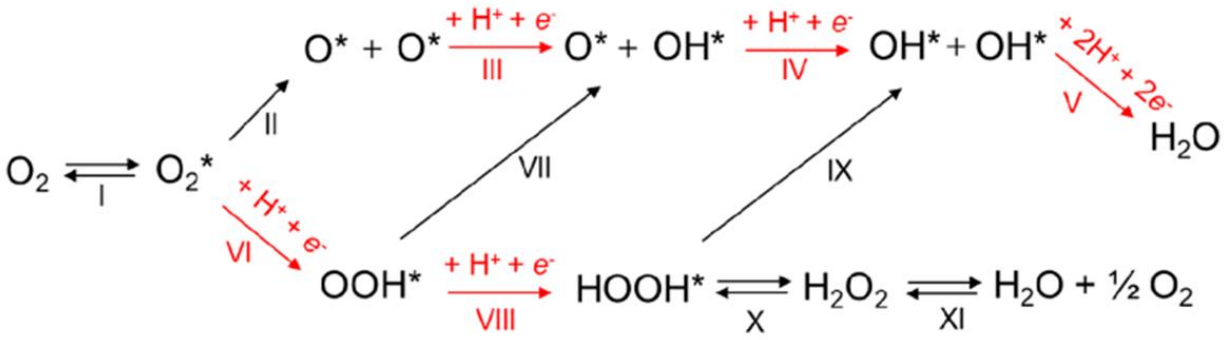

Figure 1.6 Reaction schemes of ORR process in acidic media[39].

The ORR behaviors of low-index Pt surfaces follow the order of Pt(100) < Pt(111) < Pt(110) in the weakly adsorbed electrolyte, such as $HClO_4$ solution[39,42,44]. As a result, octahedral Pt nanoparticles bound by (111) facets were found to be more active in ORR than cubic ones bound by (100) facets, consistent with the bulk single crystal regular[45]. The particle size effect on ORR has also been a long-standing problem that has yet to be solved. Smaller particle sizes can reach a larger specific surface, which suggests an enhancement of mass activity. The optimized mass activity for Pt nanoparticles is observed in the size of 2-3 nm[46,47]. Further downsizing of the Pt nanoparticles results in inferior intrinsic specific activity due to dominating low coordinated steps and kinks leading to too strong oxygen binding[47].

Because of the limitation of monometallic Pt, alloy catalysts with a lower content of expensive Pt become a better choice to reduce the cost. In past years, many Pt-based alloy systems with a wide range of compositions, such as PtPd, PtAu, PtAg, PtCu, PtFe, PtNi, PtCo, and PtW, have been studied and accordingly, improved ORR activities of these alloy systems have been reported[48]. Several hypotheses have been proposed to draw correlations between the enhanced activity of Pt alloys over Pt and their properties, such as structural factors and electronic factors. According to the mechanism of ORR on Pt surface discussed before, the shortening of Pt-Pt interatomic distance, which is favorable for the dissociative adsorption of O_2, the increasing catalytic activity of Pt alloys shows a strong correlation with the decrease in interatomic distance between Pt atoms. It is found the base-metal elements smaller than Pt, when alloyed with Pt, enter the crystal structure through substitution and cause a lattice

contraction resulting in more favorable sites that enhance the dissociative adsorption of oxygen. From the view of the surface electronic structure of Pt, the electron density in the 5*d* orbitals of Pt can be modified by base-metal elements[41]. Some DFT calculations have shown that modified chemisorption properties for adsorbed oxygen species on a Pt alloy surface are largely caused by short-range electronic charge-transfer effects and long-range geometric lattice strain. These electronic and geometric effects result in a shift of the energetic center of Pt-projected d-states affecting surface adsorbate bond strengths and thus leading to altered chemisorption of reactants, intermediates, and products[42,44].

Stamenkovic *et al.* investigated the polycrystalline alloy films of Pt_3M catalysts (M = Ni, Co, Fe, V, and Ti) to understand the role of 3d metals in the catalytic activity of Pt alloys[49]. They found that the catalytic activity for the ORR on such alloys was dependent on the nature of the 3*d* metal. The relationship exhibited a 'volcano-type' behavior, as shown in **Figure 1.7**[50]. The maximum catalytic activity was controlled by a balance between adsorption energies of reactive intermediates and surface coverage by spectator species. In this aspect, Ni, Co, and Fe were found to be the most effective alloying elements. The nanoparticles of Pt_3M (M = Fe, Ni, and Co) were synthesized and supported on high specific area carbon to investigate their ORR performance. The alloys showed more than 2-fold specific activity versus Pt at 0.9 V. Among them, Pt_3Co/C had the highest activity, reaching 3.2 mA cm^{-2}. Chong *et al.* further composed Pt_3Co alloy with a platinum group metal-free catalyst (Co-N-C) to overcome the shortages of ultralow Pt catalysts through a synergistic interaction, reaching both high mass activity of 1.08 A mg_{Pt}^{-1} at 0.9 V in PEMFC and good durability[33].

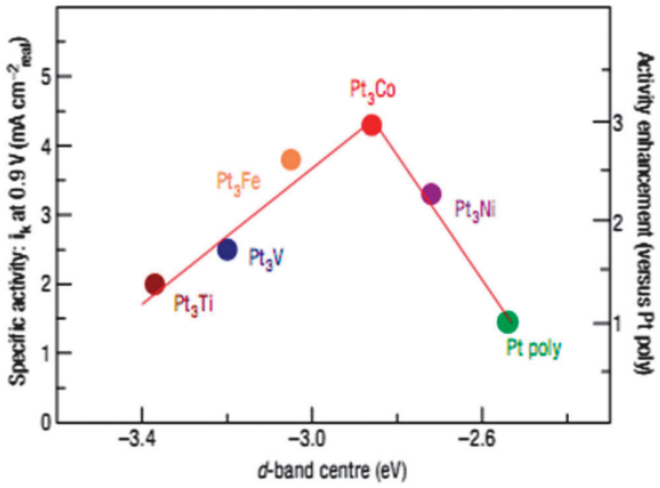

Figure 1.7 Relationships between experimentally measured specific activity for the ORR on Pt_3M surfaces in 0.1 M $HClO_4$ versus the d-band center position[50].

1.3.2 M-N-C electrocatalysts

Non-noble metal electrocatalysts are the most promising candidates for the large-scale applied catalysts of ORR. In the past decades, numerous materials have been widely investigated for ORR in acid and/or alkaline media, such as metal oxides,[51–53] metal chalcogenides,[54–56] metal-free nanostructured carbon materials,[57,58] and especially metal-nitrogen-carbon (M-N-C) catalysts[59–64]. These catalysts have shown promising activity towards ORR, but their performances are still relatively low compared with Pt-based catalysts. Therefore, intensive research has been carried out in order to improve their reactions. The low cost of platinum-group metal-free catalysts allows a higher catalyst load on the cathode to offset

their lower catalytic performance compared with Pt-based catalysts. However, the mass transport problems become more considerable due to a thicker catalyst layer[65].

Among various non-precious metal ORR catalysts, metal-nitrogen-carbon (M-N-C) materials (M = Co, Fe, Ni, Mn) are the most promising platinum-group metal-free catalysts for ORR, which have gained increasing attention due to their promising catalytic activity displayed towards ORR and the utilization of inexpensive precursor materials. Research into M-N-C complexes for ORR started in 1964 when Jasinski discovered that cobalt phthalocyanine showed ORR activity[66]. Later, Yeager reported the first M-N-C composites for ORR by the pyrolysis of non-N_4-macrocycles precursors[67]. After that, numerous efficient ORR catalysts based on different M-N-C sources have been developed. Some recently reported Fe-N-C catalysts present an initial ORR activity approaching that of platinum-based catalysts in rotating disk electrode (RDE) setup and in PEMFC[13,68–71]. To prepare a M-N-C catalyst, the synthesis usually starts from a metal precursor, a nitrogen precursor, and a carbon support (which can also be replaced by a carbon precursor). A high-temperature pyrolysis of the mix of precursors is necessary to obtain the catalytic sites for ORR in the acid medium of PEMFC. As a result, various preparation conditions can affect the performance of the final catalysts, mainly including the metal precursor and ligand, metal loading, carbon support/precursor, and heat treatment conditions. However, the ORR mechanism on M-N-C catalysts and the properties of active sites should be clarified first to enhance the trial and error efficiency.

According to previous research, the associative-dissociative pathway is considered dominant in both Pt-based and M-N-C catalysts[40,41]. The slowest step of this pathway is the first charge transfer, *i.e.*, the rate-determining step (RDS). A similar volcano plot is also established for several M-N-C catalysts by Sun *et al.*, that Fe-N_4 active site presents a closest-to-optimum OH* binding energy (ΔG_{OH}*), similar to the Pt[72]. However, the Fe-N-C catalysts are far less active than Pt-based catalysts. Tse *et al.* proposed the low activity of Fe-N-C catalysts might be due to a different mechanism in acidic media[73]. Unlike the Pt-based catalyst, which does not involve a proton transfer step (*i.e.*, $Pt + O_2 + e^- \rightarrow Pt\text{-}OO^{*-}$), the RDS of Fe-N-C involves a proton-coupled electron transfer (PCET), *i.e.*, $N_x\text{-}Fe + O_2 + H^+ + e^- \rightarrow N_x\text{-}Fe\text{-}OOH^*$)[73]. They investigated the change of kinetic rate of Pt-based and Fe-N-C catalysts by replacing proton with deuteron (*i.e.*, kinetic isotope effect KIE). The Pt-based catalyst shows a KIE of 1, indicating its RDS is a proton-independent electron transfer process. However, for the Fe-N-C catalyst, a higher KIE of 2 was observed, demonstrating the involvement of protons in the ORR mechanism at or before the RDS[73]. This would suggest that the ORR performance of the Fe-N-C catalyst in acidic media is intrinsically inferior to that of the Pt-based catalyst due to the increased complexity of the PCET on the Fe-N-C catalyst. Chen *et al.* further elucidated that the PCET arises from the $2e^-$ pathway with the generation of H_2O_2[74]. They investigated the KIE of a Fe-N-C catalyst for ORR extrapolated from the mass-transport-controlled region (at 0.425 V *vs.* reversible hydrogen electrode RHE) and the kinetic-controlled region (0.7-0.9 V *vs.* RHE). In the mass-transport-controlled region, the protons are involved in the RDS due to the change of mechanism, leading to a higher peroxide yield. On the other hand, the RDS at low overpotential is proton-independent in the kinetic-controlled region. Therefore, the proton dependency is not the limiting factor for the ORR performances of Fe-N-C catalysts[74]. These materials could successfully compete with Pt-based catalysts, through careful optimization of their structure.

Similar to Pt-based catalysts, the Fe-N-C catalysts derived from separated iron and carbon/nitrogen precursors present a wide diversity of active sites. Hitherto, three different types of active sites have been explored to display ORR activity in acid electrolyte: (i) atomically dispersed iron moiety (Fe-N_xC_y)[75–80], (ii) N-doped carbon moiety (C-N)[35,81,82], and (iii) iron-based nanoparticles encapsulated by N-doped carbon[83–87]. Generally, Fe-N_xC_y

moieties are considered to be the most effective ORR active sites of Fe-N-C catalysts, in which Fe plays a major role as the core of the active site,[78,79,88] and the turnover frequency of Fe-N_xC_y moieties is controlled by the structure of macrocycle (*x*, *y* values)[64,89]. The precise identification of *x* and *y* values is complicated due to the multiple chemical environments of Fe in catalysts, which will be further discussed later. On the contrary, some researchers also reported that N-doped carbons with 'metal-free' active sites (C-N) catalyze the ORR[35]. They claimed that metals only help to develop more active sites and promote the formation of a high degree of sp^2-hybridized carbon required for high electrical conductivity[81,82]. The Fe-rich nanoparticles can be observed in highly loaded Fe-N-C catalysts, but assessing their reactivity towards ORR remains challenging because of the simultaneous presence of Fe-N_xC_y moieties[39]. Specifically, a synergetic effect between Fe-rich nanoparticles and Fe-N_xC_y moieties has been widely proposed[90–93]. Jiang *et al.* proposed that Fe/Fe_3C nanoparticles could dramatically improve the activity of the adjacent Fe-N_x by modifying its electronic structure, favoring the O_2 adsorption in alkaline media. In acidic media, the Fe-rich nanoparticles encapsulated into a thin graphitic N-doped carbon layer (Fe@N-C) usually present excellent ORR activity and durability[94–97]. In this case, the encapsulated Fe-rich nanoparticles are not involved in the ORR process, but they exert a positive electronic effect on the outer surface of the graphitic carbon layer that favors the stabilization of the peroxide intermediates, leading to $4e^-$ pathway[94].

The precise structure of Fe-N_xC_y moieties is conventionally extrapolated from Mössbauer and X-ray adsorption spectroscopy[88,98]. The possible Fe-N_x coordination number in the first shell ranges from 1-4, and the different coordination structures of the Fe-N_x configuration will result in different catalytic performances[77,99,100]. The iron atom with two pyridinic N atoms on the edge of the carbon layer (Fe-N_2/C) was initially proposed as an active species[79]. The in-plane Fe-N_3 and Fe*-N_xC_{4-x} (C is located at the first coordination shell) moieties are also observed[101,102]. In the research of Li *et al.*, three Fe-N_xC_{4-x} (x=1, 3, 4) were prepared by pyrolysis of N-doped carbon with Fe salts at increasing temperature and observed that the ORR activity decreased in the order of Fe-N_4 > Fe-N_3C > Fe-N_1C_3[100]. Consequently, Fe-N_4 sites were considered the best moieties for ORR, including Fe-N_4 and Fe-N_{2+2}[103], and the investigation of the second coordination shell is established on this coordination number. Recent works also proposed higher coordination numbers, including a nitrogen atom below the plane, leading to a N-FeN_4 structure[104,105]. However, these higher coordination numbers can still be regarded as a deviation from Fe-N_4 sites. On the basis of Mössbauer Spectroscopy, Kramm *et al.* originally distinguished different Fe-N_4 moieties in the catalysts prepared using Fe acetate, Fe porphyrin, and NH_3 as the precursor[88]. Fe-containing moieties consisted of low spin (Fe(II)-N_4/C moiety, D1), intermediate spin (Fe(II)-N_{2+2}/C, D2), and high spin (N-Fe-N_{2+2}/C, D3), as shown in **Figure 1.8**. D1 is structurally similar to the Fe-N_4 center in FePc. These species are generally obtained after iron porphyrin complexes pyrolysis and are moderately active in acid medium[106]. The Fe in both D2 and D3 sites are coordinated with four pyridinic N atoms, which are attached to the edges of opposite graphene planes and restricted to the micropores in the carbon structure. Different from D2 site, D3 has an extra fifth graphitic nitrogen atom in the plane underneath the Fe atom. Among them, only D1 and D3 sites are active for ORR because of the electronic population of the 3d orbitals in the Fe(II) ion, among which the $3d_z^2$ orbital is reputed to bind oxygen end-on. This energy level is unoccupied for D1 (S = 0) or singly occupied for D3 (S = 2), while it is fully occupied for D2 (S=1). Therefore, D2 is unable to accept one electron from oxygen to form an adduct to the Fe-N_{2+2}/C site. D3 is proposed to be the most active site for ORR due to the presence of N_{prot} in the vicinity of D3[88,107].

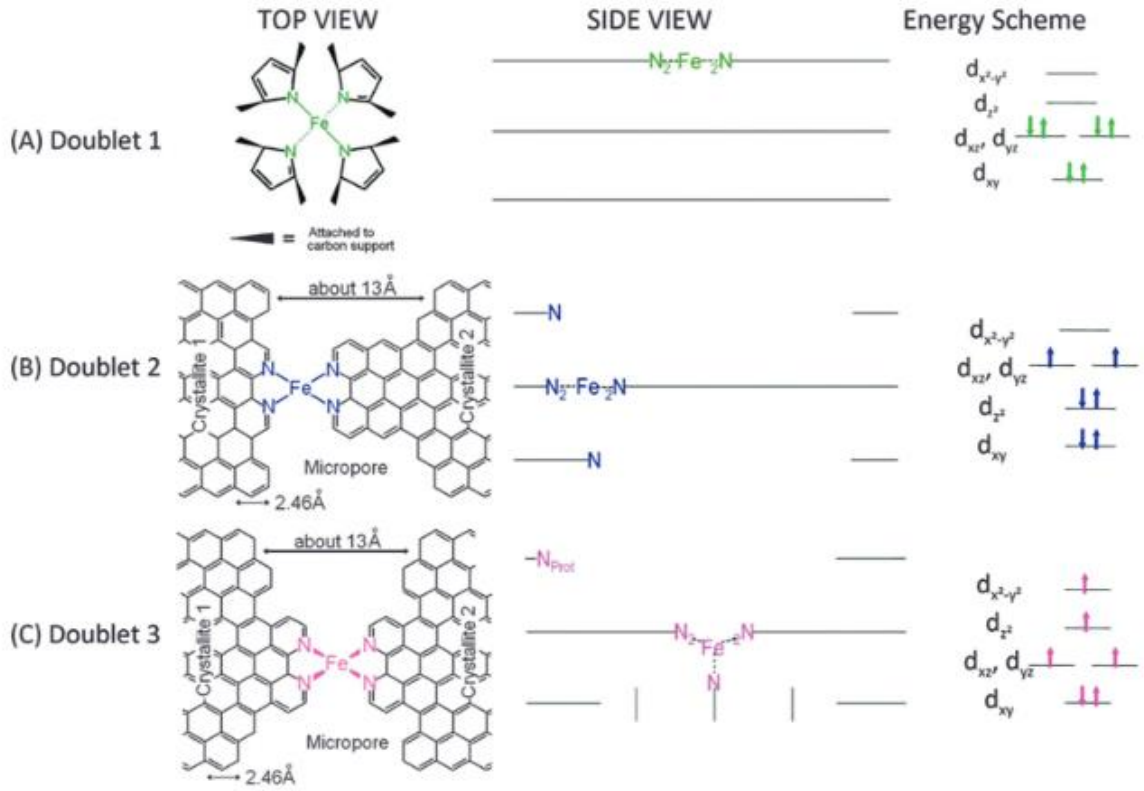

Figure 1.8 Side views and top views of the proposed structures of Fe-N_x species: (Doublet 1): the Fe-N_4/C catalytic site in heat-treated, macrocycle-based catalysts. (Doublet 2): the Fe-N_{2+2} like micropore-hosted site found in the catalyst prepared with Fe acetate and heat-treated in ammonia[88].

In later research, Mukerjee's group provided further insights on the D1 moiety and its variations as a function of potential[108–110]. The active sites undergo the Fe^{2+}/Fe^{3+} redox transition, forming high spin "in-plane" OH-Fe(III)-N_4 sites at high potential and "out-of-plane" Fe(II)-N_4 sites at low potential as the D1 site described in **Figure 1.9**[109]. The latter is considered the active site, while the site-blocking effect resulting from water activation was viewed as detrimental[111]. On the basis of in-situ Mössbauer spectra, Li *et al.* further confirmed this reversible switch from Fe(III)N_4C_{12} to Fe(II)N_4C_{12} with the decrease of potential from 0.8 V to 0.2 V, also triggering the removal of an axial OH adsorbate[105]. The site-blocking effect plays a prominent role in limiting ORR, describing the phenomenon of active sites being blocked by reaction intermediates. Since the metal-oxygen binding energy (ΔG_{OH}*) for the Fe-N_4 center is slightly stronger than the optimum value and the active sites for ORR are generated from the reversible redox reaction (1-21), increasing the redox potential can significantly enhance the intrinsic activity due to an increased turnover frequency[111]. This result is in line with the conclusion that the D2 site is less active. In the research of Li *et al.*[111], the D2 site with pyridinic N coordinated Fe exhibits a Fe^{2+}/Fe^{3+} redox peak around 0.64 V. In contrast, the Fe-MOF derived catalyst exhibits a redox peak at 0.78 V, which is coupled to the D1 moiety with pyrrolic N coordinated Fe. The higher redox potential of D1 as compared to D2 is related to the longer Fe-N-C bond length that enriches the charge of the Fe center by suppressing the Fe-to-ligand back-donation[109].

$$Fe^{3+}\text{-}OH^* + H^+ + e^- \leftrightarrow Fe^{2+} + H_2O \qquad (1\text{-}21)$$

$$Fe^{2+} + O_2 + H^+ + e^- \rightarrow Fe^{3+}\text{-}OOH^* \quad (1\text{-}22)$$

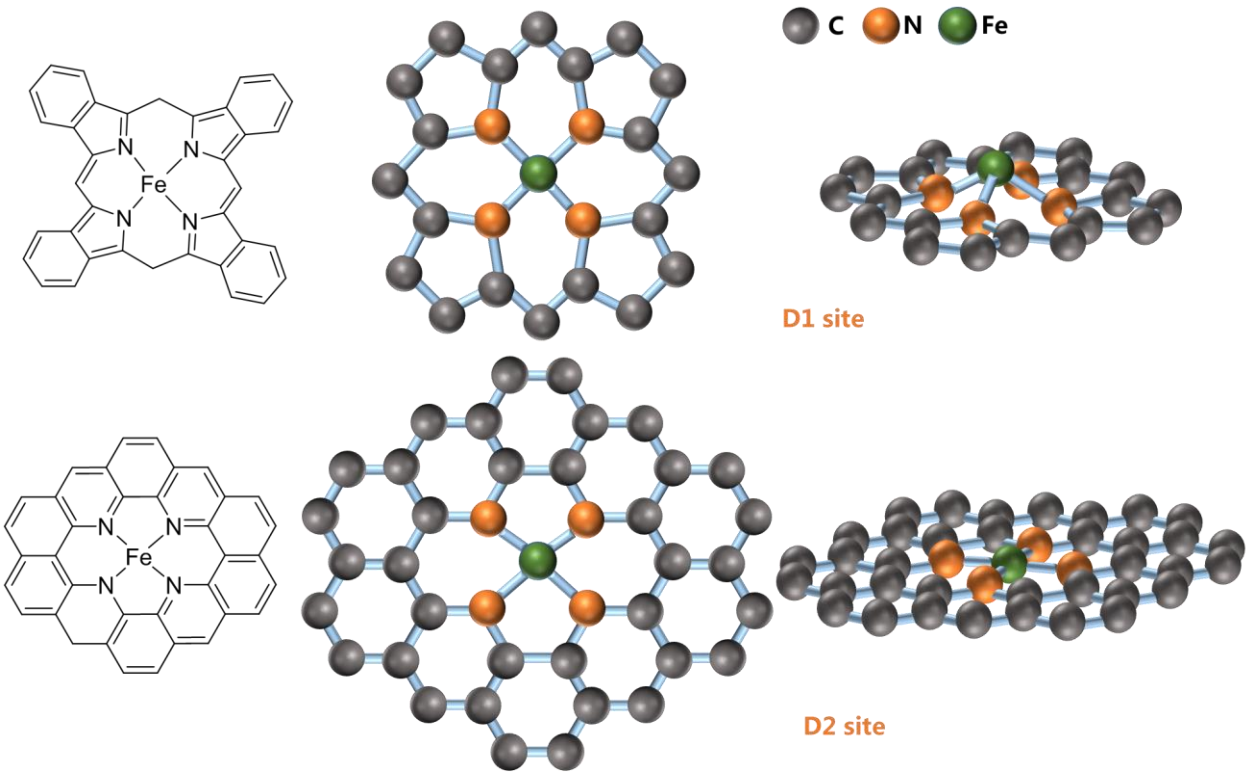

Figure 1.9 Schematic of "out-of-plane" Fe(II)N_4C_{12} D1 site and "in-plane" Fe(II)N_4C_{10} D2 site .

Zitolo *et al.* investigated the detailed structures of the Fe-N_xC_y sites using X-ray absorption near-edge spectroscopy (XANES)[98]. XANES is more sensitive to the arrangement of atoms around the photo-absorber, which helps investigate the chemical environment of the nitrogen atoms[112]. The simulation results show that the Fe-N_4C_{12} structure (**Figure 1.10**c) fits best with the experimental data up to 90 eV above the absorption edge, but a discrepancy is still present at higher energies. When the analysis is refined by including a second oxygen molecule along the axial direction, two curves are perfectly coincident as shown in **Figure 1.10**e. This result further demonstrated the ability of O_2 to bind on the D1 site along with a reversible switch of Fe(II)/(III)[113]. On the contrary, the oxide state of Fe in the D2 site is independent of the change of potential, which indicates that it is either not accessible to O_2 or binds O_2 weakly[105].

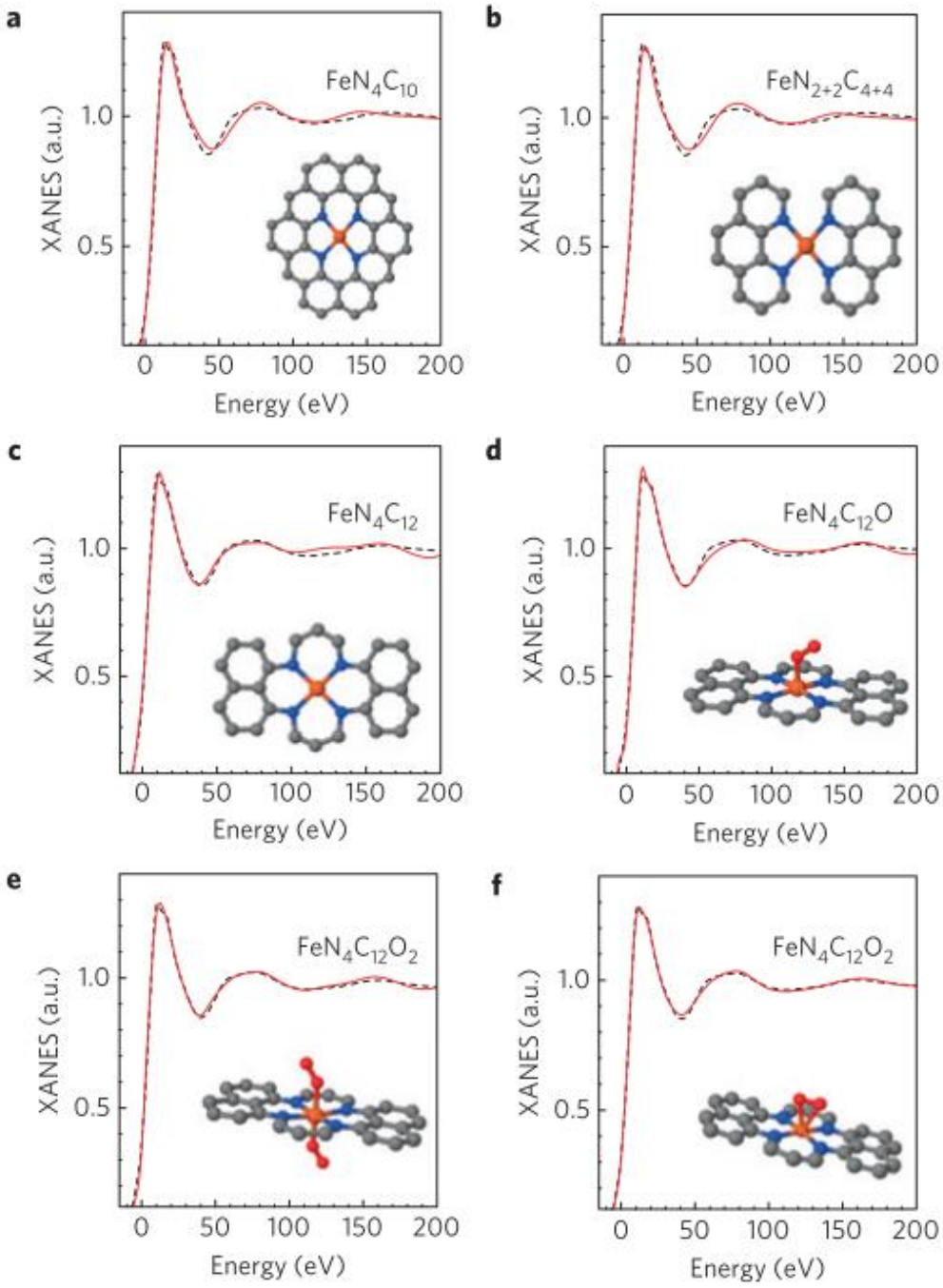

Figure 1.10 Comparison between the K-edge XANES experimental spectrum of Fe (black dashed lines) and the theoretical spectrum calculated with the depicted structures (solid red lines). **(a)** FeN_4C_{10} moiety; **(b)** $FeN_{2+2}C_{4+4}$ moiety; **(c)** FeN_4C_{12} moiety; **(d)** FeN_4C_{12} moiety with one O_2 molecule adsorbed in end-on mode; (**e)** FeN_4C_{12} moiety with two O_2 molecules adsorbed in end-on mode; **(f)** FeN_4C_{10} moiety with one O_2 molecule adsorbed in side-on mode. The brown, blue, grey and red spheres represent iron, nitrogen, carbon and oxygen atoms respectively[98].

Newly emerging evidence suggests that the Fe-N_4 might not be exactly the active site: the chemical environment around this center could also significantly impact the ORR activity. It was demonstrated that the porosity in the pristine carbon black during the pyrolysis is important for achieving high catalytic activity[114]. This implies that the active site forms at/near the micropores of the nitrogenized graphite. Besides, they also found that a supply of nitrogen

atoms is necessary to activate the Fe-N_x complexes during the pyrolysis, which accords with the theory of Doublet 3 structure.

1.3.3 Parameters that impact performance of catalysts

According to the mechanism of ORR on the M-N-C catalysts discussed before, the M-N_4 center is the active site of the catalyst. Therefore, all experimental conditions that affect the state of the M-N_4 center can simultaneously affect the catalytic performance. The metal precursor and ligand structure decide the properties of the M-N_4 center. The different metal centers exhibit different activity towards ORR and different oxidation states of metal can also impact the formation of M-N_4 center[115]. The ligand added during the impregnation procedure assists the formation of active sites and becomes a part of the nitrogen source in the following heat treatment step[116]. Metal loading also plays an important role in achieving high catalytic activity because it decides the concentration of active site in the catalyst. However, the optimum loading cannot be discussed independently. The nature of the precursors used, surface properties of carbon support, and the heat-treatment conditions can significantly affect the state and distribution of the M-N_4 center, thus impacting the best metal loading[117]. The porosity of carbon support can deeply affect the mass transfer property during the oxygen reduction reaction and may also contain some nitrogen atoms. Generally, a larger specific surface and higher nitrogen content can lead to higher ORR activity[118]. Heat treatment is the most complicated procedure during the preparation because a series of reactions happen during pyrolysis. Both the temperature and atmosphere can significantly affect the formation of M-N_4 moieties, thus having different ORR activity[119]. The influence of these conditions has been widely investigated, and some of the results are summarized in **Table 1.3**.

Table 1.3 Preparation precursors, support and pyrolysis condition of the Fe (or Co)/N/C catalysts.

Metal precursor	Support	Heat treatment (℃; time in h; atmosphere)
FeTPP-Cl[120]	Vulcan XC-72R	700 ; 2 ; Ar
FeTPP[121]	rho-ZIF	950 ; 3 ; N_2
FeTPP[122]	Vulcan XC-72R	1000 ; 2 ; Ar
FePc[123]	Vulcan XC-72R	300-600 ; 2 ; N_2
Ferrocene[122]	Vulcan XC-72R	1000 ; 2 ; Ar
Fe(Co)Ac [124]	PTCDA	600-1000 ; 1 ; Ar/H_2/NH_3
$FeSO_4$-PAN[125,115]	P33	850 ; 5 ; Ar
$Fe(NO_3)_3$-PAN[126]	-	800 ; 2 ; Ar
FeAc-phenanthroline(phen)[127]	Black Pearls 2000	1050 ; 1 ; Ar 950 ; 0.8 ; NH_3
FeAc-phen/PANI[128]	KL 600 carbon black	
$Fe(Phen)_3$[116]	adenine	900 ; 1 ; Ar
$FeCl_3$-Phen[118]	Mesoporous carbon	800 ; 1 ; N_2
$FeCl_3$- 2-ABI[129]	KL 600 carbon black	950 ; 3 ; Ar
$Fe(NO_3)_3$-PEI[130]	-	700-900 ; 1-3 ; N_2
$Co(NO_3)_2$-PEI[131]	Graphene oxide	850 ; 0.5 ; NH_3

1.3.3.1 Metal precursor and ligands

Table 1.4.1 shows the details of the preparation of typical Fe(Co)/N/C electrocatalysts. The metal precursors are either organometallic (ferrocene), metal chelates (iron phenanthroline FePhen, iron phthalocyanine FePc), or simple Fe salts such as acetate or chloride. The nature of the metallic center in the precursor plays a crucial role in activity improvement after heat

treatment. All research clearly show that iron and cobalt exhibit the highest activity towards ORR among all metal centers. Ohms *et al.* studied the influence of different transition metal ions on oxygen reduction[115]. They prepared catalysts with different metal centers by a heat-treatment process using MSO_4 (M=Mn, Fe, Co, Ni, Cu) and $ZnCl_2$ as metal precursors and polyacrylonitrile (PAN) as the nitrogen source. **Figure 1.11** shows the polarization curves of synthetic catalysts as the function of the metal precursor in acidic media (**Figure 1.11 a**) and alkaline media (**Figure 1.11 b**)[115]. The results indicate that the presence of metal ions is essential to obtain materials of high electrocatalytic activity towards ORR. The different metal ions influence the electrocatalytic behavior of the materials formed to a different extent. Fe is considered to be the best at E=0.8 V, followed by Co and Mn. As indicated by the authors, a Fe-containing catalyst can catalyze the ORR through a quasi-4e$^-$ reduction. However, in an alkaline electrolyte, different metal centers show similar performance due to the activity of carbon base in an alkaline solution.

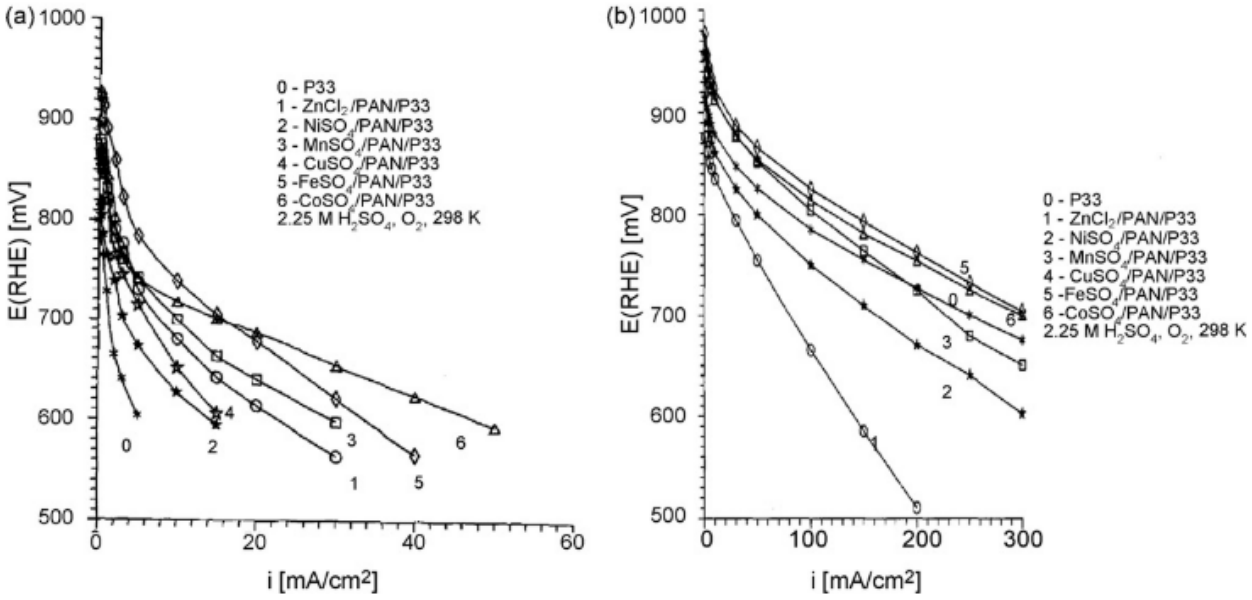

Figure 1.11 Polarization curves of oxygen electrodes made from different catalysts in **(a)** 2.25 M H_2SO_4; **(b)** 7 M KOH at 25 ℃.[115]

Chu and Jiang found that high ORR activity can also be achieved from binary transition metal macrocycles.[132] They synthesized Fe and Co tetraphenylporphyrin (FeTPP/CoTPP) catalyst, which shows the optimum catalytic activity towards ORR compared with the single metalloporphyrin (FeTPP or CoTPP), as seen in **Figure 1.12**. Generally, CoTPP catalyzes 2e$^-$ reduction of oxygen to hydrogen peroxide at more positive potentials, and FeTPP catalyzes 4e$^-$ reduction of oxygen to water at less positive potentials. However, iron porphyrin can also catalyze hydrogen peroxide reduction to water. Adding iron porphyrin to cobalt porphyrin makes it possible to obtain a more positive onset potential and achieve 4e$^-$ reduction of oxygen to water by removing the intermediate product of peroxide. On the other hand, Co species can facilitate the formation of graphitized carbon during pyrolysis, potentially benefiting ORR catalysts by enhancing the stability of the catalysts[133]. Therefore, it is an efficient approach to generating excellent catalysts with the combination of Fe and Co. Most recently, Tatyana *et al.* developed a set of bi-metallic Fe-Mn-N-C electrocatalysts by hard templating method[16]. Adding Mn decreases the amount of hydrogen peroxide formation, which should improve the durability of the catalyst.

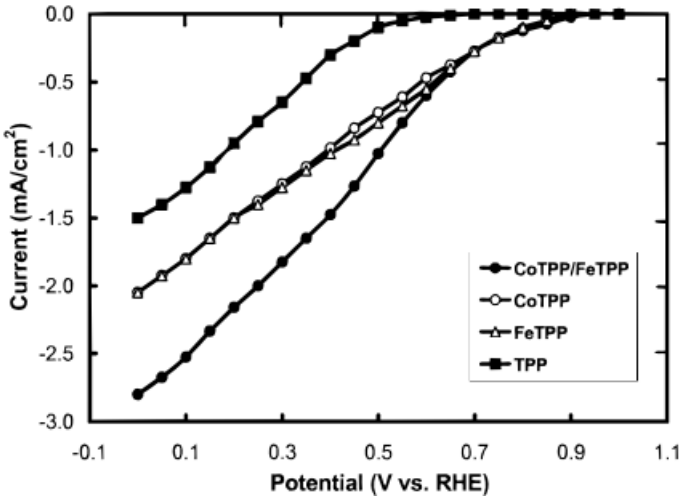

Figure 1.12 Effect of metal atoms on the polarization behavior for ORR at various heat-treated metalloporphyrins coated RDE in oxygen saturated 0.5 M H_2SO_4 solution[132].

According to the mechanism established by Dodelet *et al.*[134] and now widely confirmed by experiments, nitrogen is a necessary component of the catalyst in order to form active sites. The various resources of nitrogen precursors can affect the morphology of catalysts and the structure of active sites. Therefore, the catalytic performance can be improved by selecting different nitrogen precursors. At present, the typical nitrogen precursors are tetraphenylporphyrin (TPP)[120–122], polyaniline (PANI)[128], polyacrylonitrile (PAN)[115,125,128], phthalocyanine (Pc)[123], phenanthroline (Phen)[116,118,127,128], 2-aminobenzimidazole (2-ABI)[129], and polyethyleneimine (PEI)[130] *et al.*, as listed in **Table 1.3**. Alexey *et al.* synthesized a series of Fe-PEI-based catalysts using the sacrificial support method to investigate the impact of the iron-to-PEI ratio and molecular weight of PET[130]. The Fe-N-C materials obtained at 800 ℃ and the sacrificial support method ensure the surface area for all materials is over 1000 m^2 g^{-1} as well as the quantity of mesoporous. In this case, the catalytic activity of ORR was not significantly affected by the variation of molecular weight but highly depended on the mass ratio of Fe to PEI. The iron-free material possesses extremely low activity, and the maximum catalytic activity is found for samples with the mass ratio of Fe-PEI of 1:3. The higher PEI content decreases the catalytic activity due to the dilution of the active sites when excess PEI is used. Another research conducted by Fu *et al.* investigated the effect of dual nitrogen sources, PANI and Phen, which becomes an efficient strategy to produce Fe-N-C catalyst with higher ORR activity[128]. As seen in **Figure 1.13**d, the dual-N source product exhibits the best ORR performance compared with the other catalysts prepared by using only one single N source, and its yield of H_2O_2 is also controlled under a poor level. The excellent ORR performance could be attributed to the unique structure of the catalyst. Its high electrochemical surface area can host a large number of active sites and control meso/macropores sizes and their distribution to promote the mass transfer property on the surface and within bulk of the catalyst. Here, Phen acts as a pore-forming agent that can expand the external PANI shell during the decomposition. Simultaneously, the PANI shell converted to graphene-like structures through graphitization in the presence of iron species during pyrolysis processes[135]. Therefore, the obtained graphene-like morphology can serve as a high surface area carbon matrix hosting active sites to catalyze the ORR. Meantime, the generated abundant mesopores inside the graphene framework can facilitate mass transfers. The membrane electrode assembly using this catalyst at the cathode delivered exceptional P_{max} values of 1.06 and 0.38 W cm^{-2} in the H_2-O_2 and H_2-air fuel cell, respectively. This progress

indicates that the N precursor directly affects the structure of the final catalyst, including its morphology and concentration of active sites, thus impacting the ORR activity of the catalyst.

Besides different precursors of Fe and N used, Li *et al.* reveal that the preexisting Fe-N coordination structure can also help form Fe-N_4 active sites in the nitrogen-doped carbon with a high degree of graphitization[136]. They synthesized Fe-N-C materials from iron precursors with preexisting Fe-N coordination (FePc or $FePhen_3$) and compared their performance with the catalyst synthesized from individual iron and nitrogen precursors (FeAc and Phen). The ionothermal carbonization method (ICM) was used as an efficient strategy to synthesize N-doped carbons with tailored porous structures and high specific surface areas. The addition of eutectic $ZnCl_2$/NaCl to organic carbon and nitrogen precursors can modulate the porous structure. $ZnCl_2$ with a low melting point acted as a porogen due to its early evaporation during pyrolysis. On the other hand, NaCl salt with a high melting point remained in the carbon matrix during the entire pyrolysis process, being removed only after pyrolysis via acid washing, generating a specific porous structure through a templating effect. The RDE results of the different catalysts showed that using individual iron and nitrogen precursors leads to poor ORR activity due to the low density of FeN_x moieties. A significant fraction of Fe was present in the form of iron carbide and nanoparticles of oxides. Their research suggests that compared with the highly disordered N-C matrix (e.g., ZIF-8 derived Fe-N-C catalysts), it is more challenging to integrate a high density of FeN_x moieties in a highly graphitic carbon matrix.

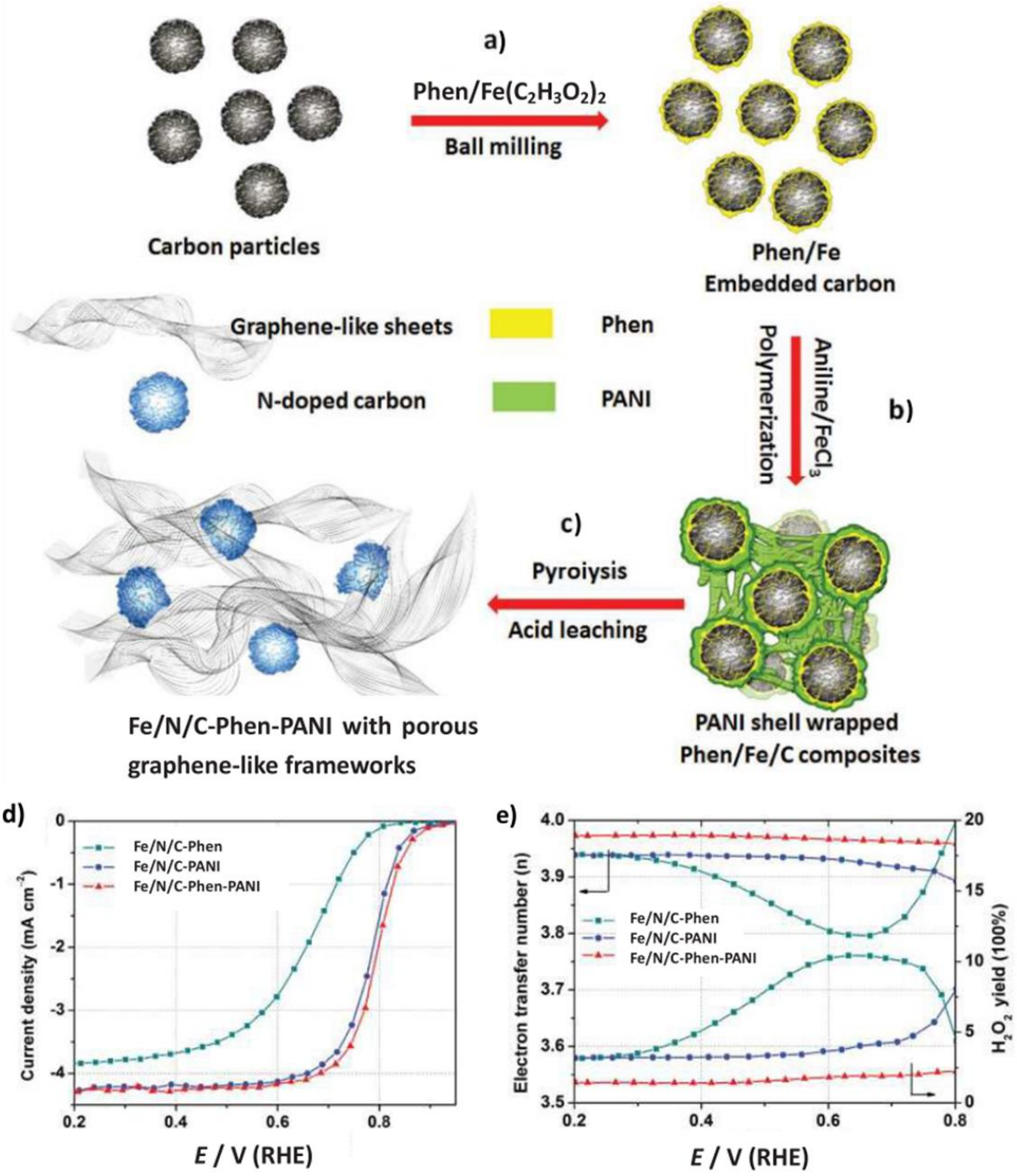

Figure 1.13 **(a-c)** Schematic illustration of the synthesis of Fe-N-C catalysts using PANI and Phen as nitrogen sources; **(d)** ORR polarization plots of different Fe-N-C catalysts (0.5 M H_2SO_4; electrode rotation speed: 900 rpm; loading: 0.6 mg cm^{-2}; scan rate: 10 mV s^{-1}); **(e)** electron transfer number and H_2O_2 yield of prepared catalysts.[128]

1.3.3.2 Metal loading in the catalysts

Besides the nature of the iron and nitrogen precursors used, metal loading also plays an important role in achieving high catalytic activity. The optimum metal loading is determined by the nature of the precursors used (both metal and nitrogen), the carbon support, and the heat-treatment conditions[117,137–140]. In general, when metal loading is far less than the optimum concentration, the activity of the catalysts increases linearly with metal content. When the metal loading far exceeds the optimum concentration, the clusters of metal begin to appear and lead to degradation of activity.

Dodelet *et al.* investigated the catalytic activity of Fe-N-C materials prepared with various Fe contents[138], as seen in **Figure 1.14**a. Two curves show different tendencies of two catalysts prepared with different Fe precursors, FeAc or Fe tetramethoxyphenyl porphyrin (FeTMPP). The activity of these catalysts improves drastically as soon as the Fe content is increased to a few tens of ppm and saturates at the same potential for both Fe precursors. However, the activity of catalysts prepared with FeTMPP precursor saturates at higher Fe contents than FeAc due to a better dispersion of the FeTMPP on carbon base. The macrocyclic structure of FeTMPP guarantees the isolation of the atomic Fe moieties during the pyrolysis process, preventing the formation of Fe-containing particles[121]. The higher saturated content of FeTMPP also corresponds to better performance than FeAc in the fuel cell, as shown in **Figure 1.14**b. Their TEM results confirm the appearance of Fe clusters when Fe loading is more than saturation, which interprets the degradation of catalytic activity for high Fe content.

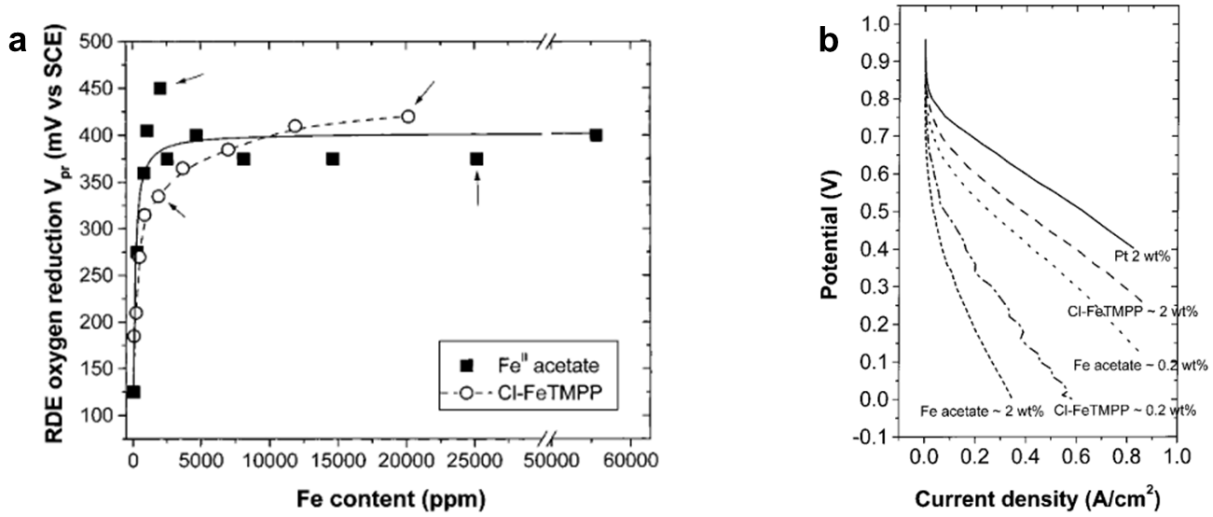

Figure 1.14 **(a)** Changes in RDE of the catalytic activity for ORR, expressed as V_{pr} (Voltage at peak reduction for 0 rpm) with the Fe content for materials prepared with FeAc or FeTMPP as precursors; **(b)** polarization curves obtained at 80 ℃ in H_2-O_2 fuel cell using the catalysts prepared with FeAc and FeTMPP as precursors[138].

Different metal centers also have different optimum concentrations. Jaouen and Dodelet synthesized a series of Fe-N-C and Co-N-C catalysts with metal loading spanned from 0.005 to 5 wt.% on the same carbon support to investigate the impact of metal content[117]. The metal saturation of the catalysts was determined by the kinetic current, which relates to the average turn-over frequency of the active sites directly. As seen in **Figure 1.15**a, at low metal content (≤0.2 wt.% for Fe and ≤1 wt.% for Co), the activity increases with increasing metal content because only the metal content limits the activity. Whereas at the threshold metal content, the activity levels off and, upon larger metal contents (>1 wt.% for Fe and Co), even decreases dramatically by one to two decades. The explanation for this is the drop in the micropore area, as seen in **Figure 1.15**b, which suggests reducing active sites concentration. A more interesting result is the different behaviors of the catalysts with different metal centers. The linear increase in activity of Fe catalysts in the region 0-0.2 wt.% can be explained by all Fe atoms forming active sites during the heat treatment, which is in accordance with previous research[113]. However, for the Co catalysts, the ORR activity increases about as the square root of the metal content (region 0-1 wt.%). One possible explanation is Co can form several species, among which only one catalyzes the ORR. If the fraction of the Co species active for the ORR to the total Co species decreases with increasing Co content, then this could increase the ORR activity with Co content being less than proportional. Some inactive Co species can also agglomerate

onto the active Co species, which leads to higher threshold metal content than Fe ones (1 wt.% against 0.2). This hypothesis is reinforced by the results of time-of-flight secondary-ion mass spectroscopy, in which none of the four families of ions ($CoNC_y^+$, $CoN_2C_y^+$, $CoN_3C_y^+$, $CoN_4C_y^+$) gives a particularly strong signal compared with others[141].

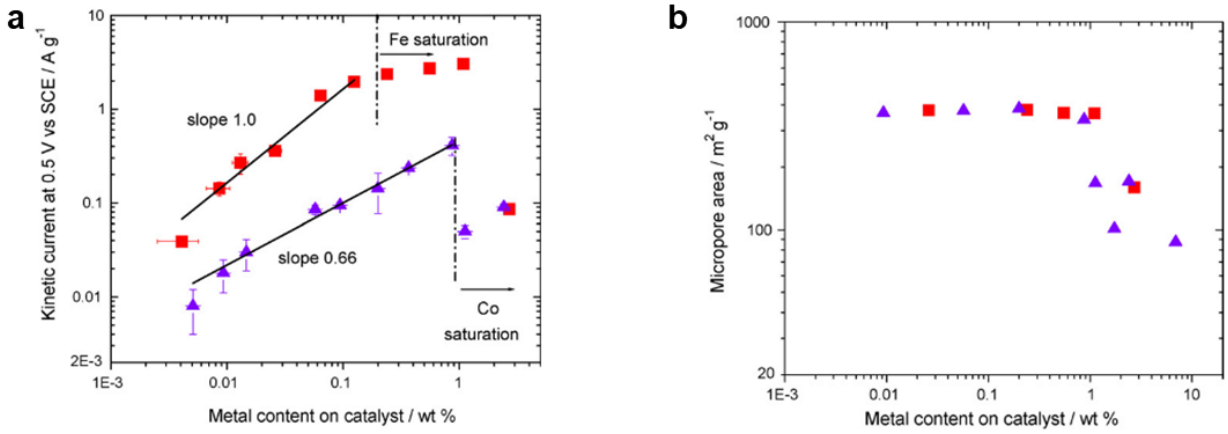

Figure 1.15 **(a)** Activity for ORR at room temperature and **(b)** micropore specific area against metal content for Fe (■) and Co (▲)-based catalysts[117].

The properties of carbon support also affect optimum metal loading. Wang *et al.* proposed the nitrogen content limited the formation of active centers[137]. In the case of low nitrogen content, the best activity reaches a lower mass loading than the carbon support with high nitrogen content. The texture and specific surface of carbon support are the main factors that impact the optimum metal loading. Large specific surface area and tailored porous structure carbon can generally contain more active sites compared with amorphous carbon support. For example, using *rho*-ZIF, which possesses interior cavities to host metal precursor, Wei *et al.*[121] found that 3.8 wt.% of Fe is the optimum value for the highest activity. Wang *et al.* use a carbon black KJ-600, which possesses a high BET surface area (~1400 m^2 g^{-1}), reach to 10 wt.% as the optimum mass loading[139]. However, as for the catalysts using carbonized polymer, such as PANI, which possesses neither a porous structure nor a high specific surface, their optimum values are usually lower than 1 wt.% [108,140].

1.3.3.3 Carbon supports

Carbon supports are one of the components of M-N-C materials to endow the catalysts with a high density of exposed active sites and excellent mass transfer properties owing to their high specific surface area and porous structure. In addition, the nature of the carbon surface can also influence the structure of the active sites in the final catalyst[133,142–145]. In the early research of M-N-C materials, carbon blacks were almost exclusively used as catalyst support. New carbon materials have been tested to improve the electrochemical activity and stability of the catalysts, such as carbon nanotubes[146], mesoporous carbons[118], and MOF materials[116,142]. With respect to carbon blacks, these new carbon materials are different both in their structural conformation and porous structure.

As seen in **Table 1.3**, the most popular carbon supports are Vulcan XC 72 and Black Pearls. Jaouen *et al.* measured the ORR activity of several Fe-N-C catalysts prepared with different carbon black supports[145] to investigate the influence of specific surface area, porous structure,

and surface property on catalytic activity. In their synthetic procedure, iron (II) acetate was firstly adsorbed on the carbon black, followed by pyrolysis of the mixture at 900 ℃ in $NH_3/H_2/Ar$ to introduce N into the catalysts, thus the N content in the catalysts is limited. They found that the activity of the catalysts varies significantly from one carbon support to another, but neither the specific surface area of the catalysts nor the distribution of their macro/mesopores is a determining factor for the catalytic activity. The most crucial factor is the N content of the materials; the higher it is, the higher the density of the catalytic sites on their surface and the better the electrocatalyst, as seen in **Figure 1.16**a. This result is because the low N content limits the concentration of active sites. As the pyridinic nitrogen is the most crucial component of the active sites, if the proportion of the pyridinic nitrogen keeps constant for all catalysts, the variation in total nitrogen content accounts for the ORR activity. The vertical line at very little nitrogen content in **Figure 1.16**a demonstrates the catalytic effect caused by other factors. As seen in **Figure 1.16**b, the oxygen concentration accounts for the variation because iron oxide sites can also present catalytic activity even if they are much weaker than the $Fe\text{-}N_4$ center. The larger specific surface area is supposed to lead to a higher concentration of the catalytic sites, resulting in better catalytic activity. However, their research shows little relation between the activity and total specific surface area, as seen in **Figure 1.16**c. On the other hand, it seems to be a weak correlation between the catalytic activity and the micropore area, as shown in **Figure 1.16**d. This relationship corresponds to the active sites hosted in micropores of catalysts[119]. Some chemical treatments can activate the carbon blacks to increase the catalytic activity. Popov *et al.* prepared a Fe-N-C catalyst using the HNO_3-treated carbon black as the carbon support. The catalyst presented higher ORR performance on RDE than one prepared with as-received carbon thanks to more hydrophilic oxygen groups introduced by HNO_3 treatment[143].

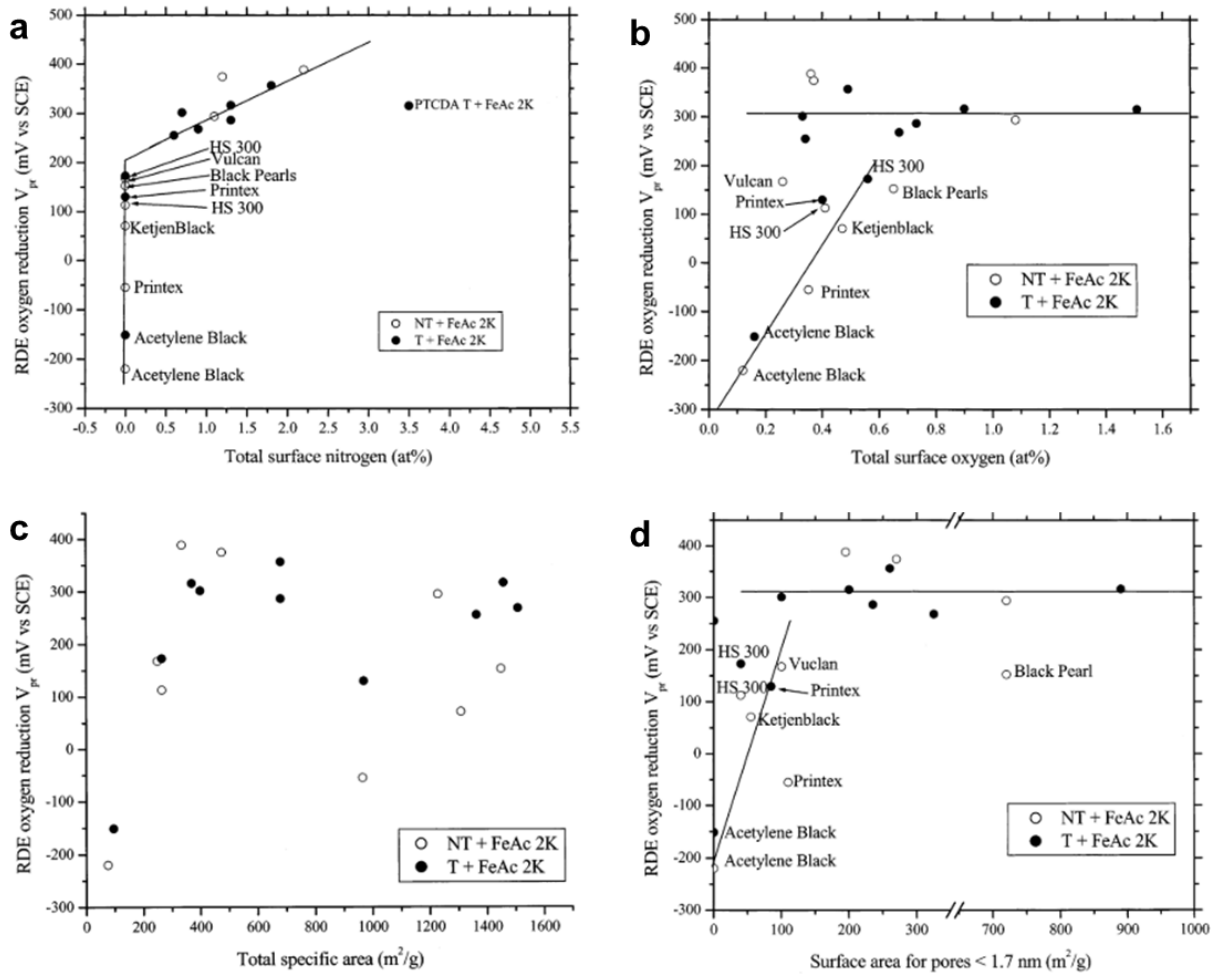

Figure 1.16 Change in catalytic activity (from Vpr) with **(a)** total N surface concentration of the catalysts from XPS results; **(b)** total O surface concentration of the catalysts from XPS results; **(c)** total specific surface area of the catalysts from BET; **(d)** micropore surface area of the catalysts from BET[145].

Generally, carbon blacks with a high specific surface area are mainly contributed by micropores less than 1 nm. This feature can host a large quantity of active sites but disadvantages the carbon when used as catalyst support. When the average diameter of the pores is less than 2 nm, the fuel supply may not occur fluently, and the activity of the catalyst may be limited[133]. Compared with carbon blacks, mesoporous carbons present a higher specific surface area and mesopore volume, thus possessing better mass transfer properties. The ordered mesoporous carbons have recently received great attention due to their controllable pore sizes, high specific surface areas, and large pore volumes. Nanoporous carbons with a 3D-ordered pore structure have shown abilities to improve the mass transport of reactants and products during fuel cell operation[118]. Osmieri *et al.* synthesized mesoporous carbon supported Fe-N-C catalyst (Fe-N/MPC)[130]. The carbon support was synthesized via the hard-templating method. The carbon source was impregnated into commercial silica mesoporous nanoparticles, followed by a heat treatment at 830 ℃ under a nitrogen atmosphere to complete the carbonization. Finally, the silica template was removed by washing it with HF solution.

As seen in **Figure 1.17**a[133], among all the catalysts prepared with different carbon support, the most active is Fe-N/MPC, which has 100 mV higher E_{on} (onset potential is defined as the potential required to generate a current density of 0.1 mA cm^{-2}) in comparison with the less

active catalyst, acetylene black supported catalyst (Fe-N/AB). The reason of better performance with mesoporous carbon is revealed in **Figure 1.17**b. The pore size distribution analysis shows the majority of the pores in the mesoporous carbon supported catalysts (Fe-N/MPC1 and Fe-N/MPC2) catalysts are between 2 and 4 nm, whereas for the AB and multi-walled carbon nanotubes (MWCNT) supported catalysts mainly contain macropores and mesopores with diameter >20 nm. Using carbon support with a high specific surface area and an ordered porous structure seems helpful to allow the formation of more active ensembles and favor their accessibility to the reactants. Another interesting phenomenon is MWCNT support shows a higher diffusion-limited current density. MWCNTs tend to form agglomerates which are very difficult to disperse in the ink solution and consequently have a bad dispersion onto the glassy carbon.

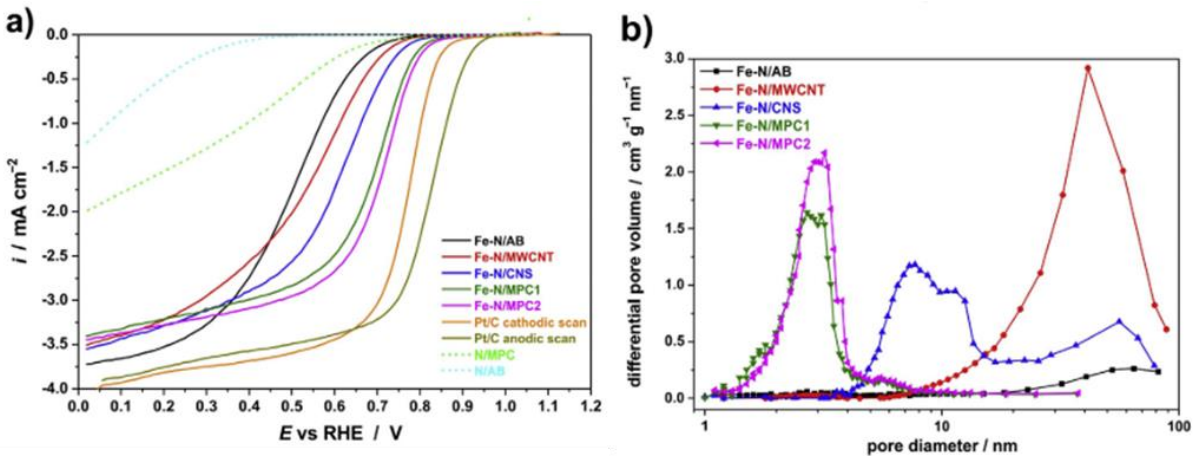

Figure 1.17 **(a)** Polarization curves for the five Fe-N-C catalysts, the two I/C catalysts, and a commercial 20 wt.% Pt/C catalyst recorded in RDE at 900 rpm in O_2-saturated 0.5 M H_2SO_4; **(b)** BJH desorption pore-size distribution of the Fe-N-C catalysts[133].

Besides ordered mesoporous carbons prepared by hard templates, carbon gels have recently attracted attention as a new form of mesoporous carbon. Their surface area, pore volume, and pore-size distribution are tunable surface properties related to the synthesis and processing conditions, which can produce a wide spectrum of materials with unique properties[147]. In addition, no need to remove the silica template during synthesis makes them more environmentally friendly than ordered mesoporous carbons prepared by the hard template method. Generally, carbon gels are obtained from the sol-gel polycondensation of specific organic monomers, typically resorcinol (R) and formaldehyde (F). Two monomers are dissolved in solution with catalyst to conduct polycondensation, followed by drying and pyrolysis in an inert atmosphere. According to the drying method, there are three types of carbon gels: carbon xerogels, carbon aerogels, and carbon cryogels[133]. The xerogels are produced by conventional drying methods such as evaporation under heating conditions. The evaporation of the solvent by heating the wet gel leads to a collapse of the pore structure due to changes in the surface tension of the solvent upon the formation of the vapor-liquid interface. This collapse results in a significant gel shrinkage, giving a dense polymer. Job *et al.* found the shrinkage of porous structure in xerogel was in evitable, even though the evaporation condition was carefully controlled[148]. To maintain the entire porous structure of the wet gels, they must be dried in supercritical conditions of the solvent. In this case, the solvent can be removed in the absence of a vapor-liquid interface, and the surface tension can be eliminated[149]. The resulting materials are called aerogels. According to the solvent, the pressure and/or the temperature can be elevated. By exchanging the solvent contained within the voids of a wet gel

(for example, water) with an alternative solvent (for example, acetone) miscible in supercritical CO_2, conditions can be softened. Ideally, this supercritical drying process leaves the gel structure unchanged without shrinkage of the internal voids or pores, thus having higher specific surface area and pore volumes than the corresponding xerogels. Zanto *et al.* synthesized a series of carbon aerogels and xerogels with different parameters to compare their surface properties[150]. On average, the carbon aerogels exhibited higher specific surface areas and pore volumes than the carbon xerogels. The highest specific surface area and pore volume for carbon aerogels were 929 m^2 g^{-1} and 1.42 cm^3 g^{-1}, respectively. The corresponding values for the carbon xerogels were 591 m^2 g^{-1} and 0.44 cm^3 g^{-1}. However, the supercritical drying process also makes carbon aerogels quite expensive. Hence, the freeze-drying method is proposed as a less expensive and safer procedure for obtaining mesoporous carbons called cryogels. Suzuki *et al.*[151] compared the porous properties of the RF cryogels with aerogels. They prepared organic RF hydrogels with different ratios of resorcinol to catalyst (R/Cat) and different ratios of resorcinol to water (R/W). Meantime, the pH of the solution and R/F ratio were kept constant. They found for the same organic gel, the total pore volume of cryogels only reached 60% of aerogel because the shrinkage during freeze drying is more significant than during supercritical drying. Fe-N-C aerogel catalysts for ORR were synthesized recently from RF aerogel[152,153] and will be further discussed in section 1.4.

Metal-organic frameworks (MOFs) are crystalline porous hybrid materials comprising coupling units coordinated by electron-donating organic ligands[154]. MOFs have the highest specific surface areas reported for porous materials (up to 6200 m^2 g^{-1})[155] and large internal pore volumes with tailored pore sizes and apertures. These features make them become ideal candidates for carbon support of Fe-N-C catalysts. MOFs can be obtained using inexpensive and high-yield synthesis methods at low temperatures (~250 ℃). Synthesis under hydrothermal conditions is the most frequent method. To date most commonly used MOFs are zeolitic imidazolate frameworks (ZIFs) which possess the topology of zeolites but are composed of synthetically versatile imidazolate groups coordinating either Zn(II) or Co(II). ZIFs own large interior cages and relatively small windows, which make them extremely attractive as host matrice for encapsulating and immobilizing large guest molecules[121]. Based on the features of ZIFs, ball milling is a fast, energy-efficient method for promoting reactions between iron precursors and ZIFs in the solid state. A typical synthesis procedure is shown in **Figure 1.18**. Wei *et al.* synthesized *rho*-ZIF-supported Fe-N-C catalysts. Iron precursor (Fe-TPP) acted as a pore filler that filled into the large interior cages of *rho*-ZIF by ball milling to form the host-guest Fe-TPP ⊂ *rho*-ZIF complexes. The complexes were then conducted pyrolysis to get the final Fe-N-C catalysts. In their research, the onset potential (current density reaches 0.1 mA cm^{-2}) of the best catalysts is 1.04 V in 0.1 M KOH solution at a rotation rate of 1600 rpm, which is very close to that of commercial Pt/C (1.02V).

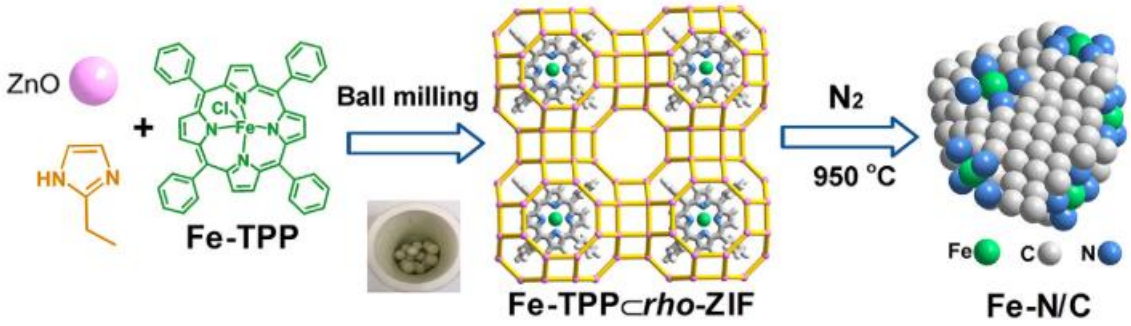

Figure 1.18 The schematic illustration for the non-solution fabrication process of Fe-N-C catalyst[121].

Jaouen *et al.* compared the electrocatalytic activity of ZIF-supported Fe-N-C catalysts with carbon black[127]. The ball milling method was used to prepare the mixtures of iron precursor and carbon support. Black Pearls 2000 was selected due to its large specific surface area (1379 m^2 g^{-1}), close to that of ZIF used (1700 m^2 g^{-1}). Therefore, the only difference between the two supports was the porous structure. According to their results, the catalysts prepared with ZIF support exhibit better electrochemical performance both in RDE and in PEMFC, where the current density can reach 4.4 A g^{-1} in RDE and 4.33 A g^{-1} in PEMFC at 0.9 V *vs*. RHE. However, the corresponding values of the Black Pearl 2000 supported catalyst can only reach 0.41 A g^{-1} in RDE and 2.07 A g^{-1} in PEMFC. Currently, the most state-of-the-art Fe-N-C catalyst was prepared by a ZIF-based precursor, which was reported by Jiao *et al.*[70]. A Zn-N-C material was first prepared from ZIF-8 precursor, followed by a chemical vapor deposition of $FeCl_3$ vapor on the Zn-N-C bed. The Zn in Zn-N_4 can be atomically replaced by $FeCl_3$ vapor to form highly accessible Fe-N_4 active sites at a relatively low temperature (750 ℃ in this method), thus retaining higher N content necessary for high site density. The performance of the final catalyst in H_2/O_2 PEMFC reached a current density of 44 mA cm^{-2} at 0.89 V, only 0.01 V lower than the DOE 2025 target[156].

In summary, ideal carbon support should simultaneously feature a large surface area, appropriately porous structure, and high conductivity, facilitating reactant diffusion and electron transfer during the electrocatalytic reactions.

1.3.3.4 Heat-treatment conditions

A high-temperature treatment condition also significantly affects the active-site formation for the Fe-N-C catalysts and properties of carbon supports, thus impacts on both ORR activity and stability of the catalysts[119,130,157]. As we mentioned before, although the pyrolysis temperature of Fe-N-C materials can range from 500 to 2500 ℃, the catalysts with the best electrochemical performance are obtained under 1000 ℃ generally, as seen in **Table 1.3**. The ultrahigh temperature (>2000 ℃) is only used for some phenolic-based carbons because they are not very graphitizable[157]. The pyrolysis can be carried in inert environments (Ar or N_2) or a reactive environment (H_2 or NH_3). In inert environments, the temperature decides the concentration of active sites formed and the properties of the carbon support. Serov *et al.* investigated the impacts of pyrolysis temperature (from 700 to 900 ℃) in an inert atmosphere on the activity of Fe-N-C catalysts[130]. For all the catalysts prepared with different carbon supports, the products pyrolyzed at 800 ℃ always have the best electrochemical performance. According to the analysis of XPS, the products at 800 ℃ have the largest amounts of pyridinic N and N associated with Fe, which are the moieties that have been suggested to be one of the possible active sites. At higher temperatures of pyrolysis increase in quaternary, graphitic, and pyrrolic N is observed, which reduces the quantity of active site, thus leading to the decrease of electrocatalytic activity. The impacts of pyrolysis temperature on the surface properties of RF carbon aerogels were investigated by Pekala *et al.*[157]. The specific surface area decreases as the pyrolysis temperature increases, reaching a limiting value of 900 ℃. However, the situation in the NH_3 atmosphere is different. The ammonia treatment can activate carbon support to increase the electrochemical activity at high pyrolysis temperatures (typically 950 ℃). Jaouen *et al.* proposed three consecutive steps to illustrate the effect of NH_3 on carbon support [119]. The first step is the incorporation of nitrogen atoms in the carbon. During the ammonia treatment, ammonia might react with carbon matrix or surface groups by the reaction 3.6.1[158]. This reaction increases the surface area with the formation of micropores and basic N functionalities are integrated into the carbon matrix. The final step is completing active sites in the micropores by reacting iron with ammonia. According to their research, the micropores created during

ammonia treatment are crucial for catalytic activity, which means the active sites are hosted in the micropores. However, a different opinion was proposed by Kramm *et al.* that the improved ORR activity by NH_3-induced iron nitride formation cannot be clarified[158]. They found the hydrogen peroxide formation is increased for the NH_3-treated catalysts, as seen in **Figure 1.19**, which indicates a variation of the reduction mechanism from $4e^-$ to $2e^-$. However, the Fe-N_4 active sites prefer a $4e^-$ mechanism. On the basis of these results, the increased turnover frequency may be due to the iron nitride or other ORR active surface groups on the carbon base formed during the NH_3 treatment.

$$C_{solid} + NH_3 \rightarrow HCN \uparrow + H_2 \uparrow$$

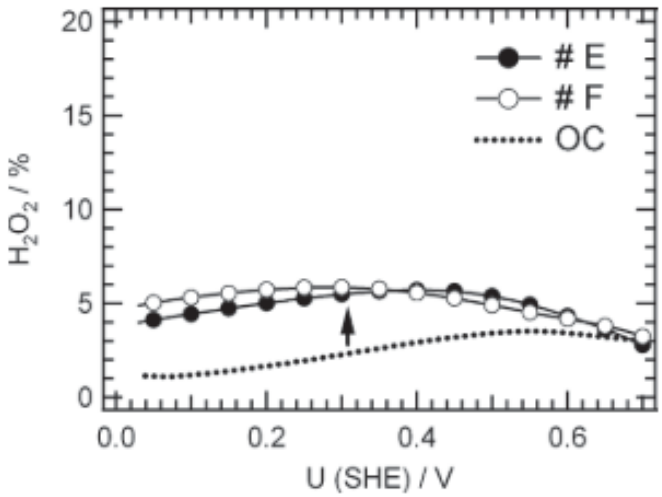

Figure 1.19 Relative hydrogen peroxide formation in dependence of the potential for the original catalyst (OC) and samples #E (NH_3-treated catalyst) and #F (acid-leached product of #E)[158].

According to the pyrolysis conditions mentioned before, high temperature pyrolysis in inert atmosphere will lose the active nitrogen (pyrrolic and pyridinic N) on the surface, whereas NH_3 can introduce new nitrogen groups and active sites. Therefore, recent reports proposed a second pyrolysis procedure on synthesized M-N-C catalysts. Koslowski *et al.* prepared Fe-N-C catalysts by a secondary heat-treatment method[159]. The mixture of Fe precursor and carbon support was first pyrolyzed at 800 ℃ in N_2. The obtained catalyst was then conducted ammonia treatment at 800 ℃ in NH_3 or N_2 as a contrast. The results of XPS measurements show that the treatment in NH_3 leads to incorporation of nitrogen. Meantime, the increasing percentage of pyrrolic N suggests an increased concentration of catalytic centers (Fe-N_4), which can explain the remarkable improvement of catalytic activity after the NH_3 treatment.

Besides the effect on catalytic activity, the pyrolysis temperature also deeply impacts the stability of the catalysts. Improved stability has been observed for catalysts synthesized at high pyrolysis temperatures in N_2 or Ar because high pyrolysis temperature can lead to generating more quaternary nitrogen functionalities, which have less prone to degradation by the protonation reaction. At the same time, the graphitized carbon would be easily formed at high temperatures, which can enhance the corrosion resistance of the catalysts to an acidic medium[130]. However, these catalysts displayed an initial ORR activity inferior to that resulting from lower temperature heat treatment procedures due to low active site concentration[160].

In summary, the ORR performance of the Fe-N-C catalysts highly depends on the pyrolysis condition, both the temperature and atmosphere. The target of pyrolysis is to obtain the maximum concentration of active sites and retain the porous structure of the carbon base. In general, the first pyrolysis of organic gels prefers the temperature of 800 ℃ in N_2 or Ar to maximize the density of active sites. It is also an efficient method to create active sites by second pyrolysis in NH_3 at higher temperatures, typically 950 ℃. The higher temperature also plays a positive role in helping the graphitization of the carbon support to improve the catalytic stability.

1.4 Carbon aerogels

Carbon aerogels are ideal candidates for mesoporous carbon support due to their high specific surface and pore volumes. In addition, the porosity and specific surface of carbon aerogels are tunable according to synthesis and processing conditions. Ritter *et al.* summarized the influence of synthesis conditions on the final properties of the RF organic and carbon aerogels[161]. Overall, RF organic gels undergo two main stages during synthesis. The first stage is associated with the preparation of the sol mixture and the subsequent gelation and curing of the gel. The second stage is associated with the drying of the wet gel, which has been discussed before. The most important factors that affect the properties of the organic gel during the first stage are the catalyst concentration, the initial gel pH, and the concentration of the solids in the sol. Na_2CO_3 is the most commonly used alkaline catalyst for the polymerization reaction. This catalyst activates a small portion of R to act as the site for the growth of the monomer particles. Typically, the molar R/Cat ratio ranges between 50 and 300. Low R/Cat ratios result in small polymer particles (3-5 nm) that are interconnected with large necks; this produces higher-density gels[162]. In contrast, high R/C ratios result in large polymer particles that are connected by narrow necks in a “string-of-pearls” fashion[161]. The initial gel pH depends on the ratio of catalyst to water (Cat/W). The impact of pH is schematically shown in **Figure 1.20**. If the concentration of the catalyst is high (Cat/W) is large), the starting points of the growth of the particles exist densely. Therefore, a small amount of the reactant is consumed per particle, and consequently, the size of the particles becomes small. On the other hand, if the concentration of the catalyst is low (Cat/W is small), the starting points exist sparsely. Hence, a large amount of the reactant is consumed per particle, and consequently, the particles can grow large. Accordingly, the pore size becomes relatively small if Cat/W is large, and vice versa[163]. As for the solid content (R/W), low R/W gives a large pore volume in carbon aerogel because the pores are the gel voids formed by the interconnected particles, and the voids depend on the amount of water used as a diluent in the synthesis of the gels[151].

The corresponding carbon aerogels are produced by the carbonization of the dried gel and sometimes the activation of the carbonized derivative. The detailed conditions will be further discussed in the section. Here, some phenomena are summarized. The carbonization procedure is carried out by heating the sample in flowing N_2 or Ar at a temperature ranging from 500 to 2500 ℃. During carbonization, the aerogel loses oxygen and hydrogen functionalities and there is an enrichment in carbon, giving a highly pure carbon structure. At low carbonization temperatures, the macropore volume decreases, and the mesopore volume increases due to the shrinkage of the material, whereas the micropore volume and surface area are enlarged due to the evolution of gases during carbonization. At higher temperatures, all these parameters tend to decrease due to the graphitization of the carbon aerogel[164].

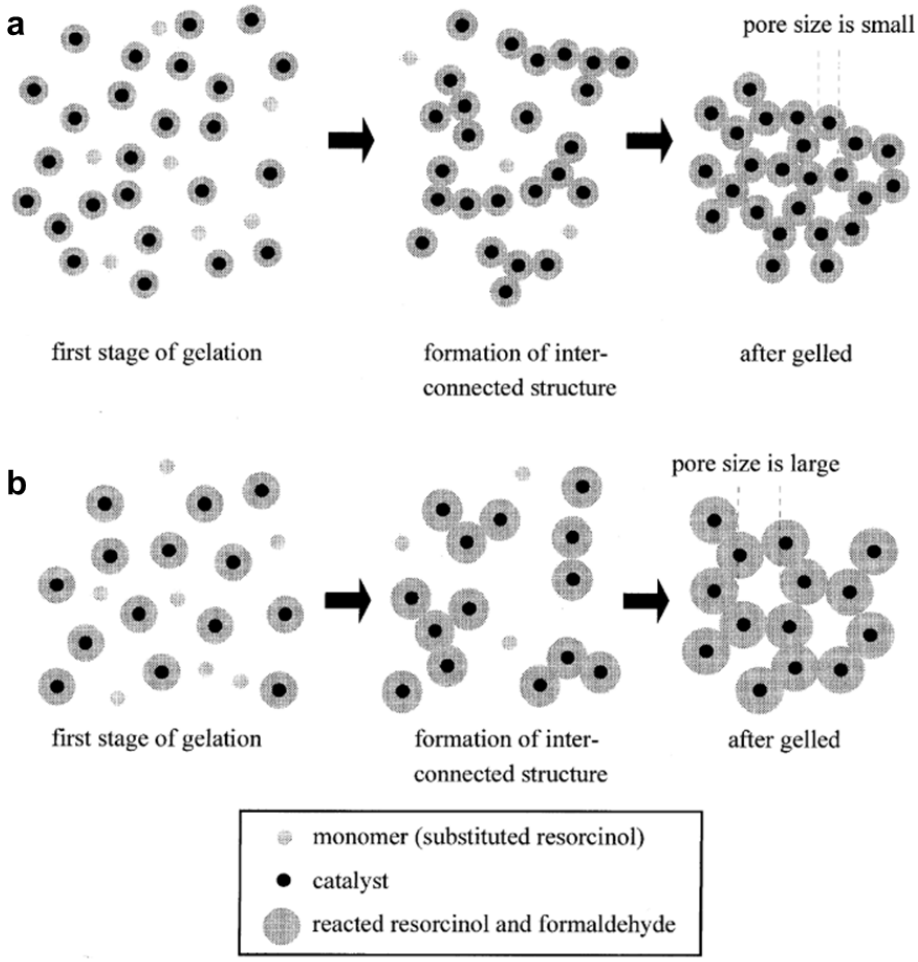

Figure 1.20 Images of gelation **(a)** C/W is large; **(b)** C/W is small[163].

Besides the specific surface area and porosity of the carbon aerogel, nitrogen functionalities on the surface of the porous carbons also play an important role either in catalytic reactions themselves or in increasing the dispersion of active components and, thus, the activity. N-containing can be introduced into carbon aerogels in several ways. The most common method is adding nitrogen-containing compounds, such as melamine (M) [165–173], urea[167], and aminophenol[166], into the initial polycondensation mixture of RF. Another approach is the use of ammonia-assisted pyrolysis of dry organic gel[174]. Besides, the physical methods are also useful to yield carbons with high nitrogen content, such as N_2 or NH_3 plasma treatment[175,176]. However, the porous structure of carbon aerogels can hardly retain under the conditions of plasma. Among all the nitrogen-containing compounds, M is the most widely used monomer in RF gels. Therefore, the melamine-containing RF gels is also noted as RMF gels. Although M has outstandingly high nitrogen content, the polymerization reaction between M and F leads to polymers with only limited specific surface area. The area can be improved by adding R to the reaction mixture. As shown in **Figure 1.21**, a condensation reaction occurs among the hydroxymethyl groups between MF and RF to form methylene and methylene ether bridged polymers, which can co-condense to form small clusters consisting of branched polymeric species. The small clusters act as nucleation sites with plenty of unreacted particles capable of reaction, which can continuously grow to form a 3D polymer, and thus may result in a homogeneous RMF network[165]. According to this mechanism of polymerization, the final surface properties and porosity of aerogels are sensitive to the ratio of M to R (M/R)[177,178]. Nagy

et al. prepared a series of mesoporous RMF carbon aerogels with 0-4 wt.% nitrogen content by tuning the M/R ratio during the polymerization process[179]. The M/R ratio ranges from 0.07 to 1. At low melamine content, where M/R <0.4, the samples display the familiar structure of quasi-uniform spherical units, which become more compact with increasing initial melamine content. Although they have similar specific surface area and total pore volume (~700 $m^2 g^{-1}$), their pore size distribution reveals that increasing the M/R ratio shifts the peak position to lower values and, at the same time, reduces the area, i.e., both the size and the volume of the mesopores decrease. Whereas the sample with high melamine content (M/R=1) has a different morphology, which contains irregular interconnected open cells of size around 500 nm, thus leading to a low specific surface area (80 $m^2 g^{-1}$).

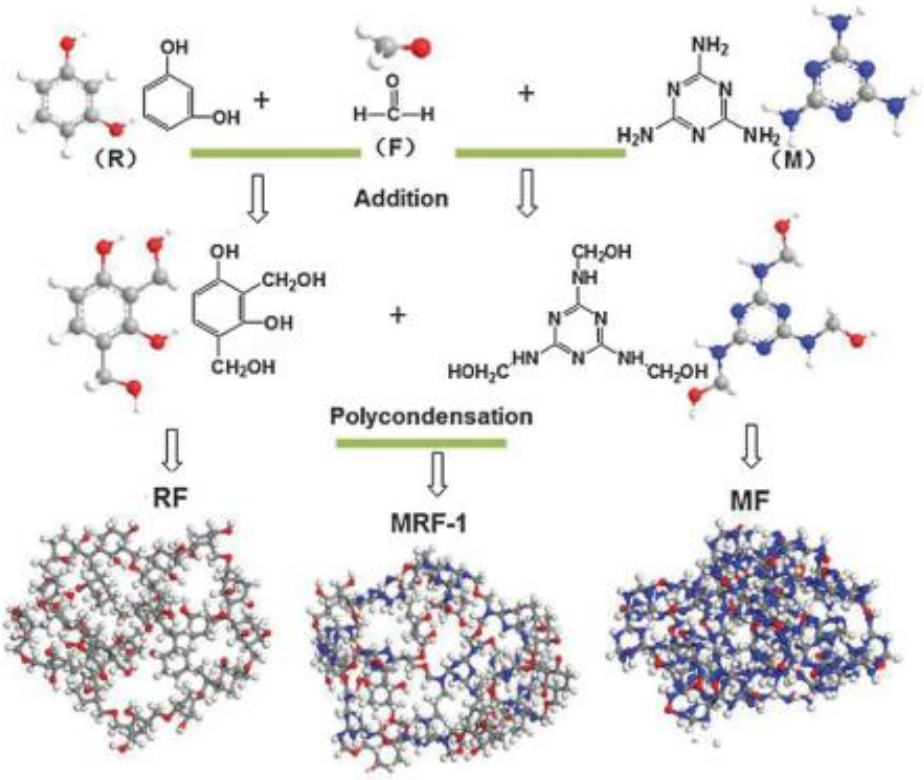

Figure 1.21 Schematic representation of the preparation of RMF frameworks and their optimized network fragments[165].

Although the advantages possessed by carbon aerogel and the wide application as the support of metal nanoparticles[133], little research has been reported using carbon aerogel as the support of Fe-N-C catalysts. Wang *et al.* prepared a Fe-N-C catalyst with carbon aerogel as the support[180]. The ferrocene and melamine were used as the precursors of iron and nitrogen, respectively. The carbon aerogel was firstly activated by the KOH solution, and then the iron and nitrogen precursors were impregnated into the support. The final products were obtained by pyrolysis under 700 (Fe-N-CA-700), 800 (Fe-N-CA-800), and 900 ℃ (Fe-N-CA-900). As seen in **Figure 1.22** a, trace Fe plays a crucial role in ORR activity. The uniform Fe-N_4 active sites account for excellent ORR activity of Fe-N-CA catalysts. The most active catalyst (Fe-N-CA-800) has a positive E_{onset} of 0.92 V, which is only slightly lower than that of Pt/C. The excellent mass transfer property of carbon aerogel support suggests a promising application in Fe-N-C catalysts.

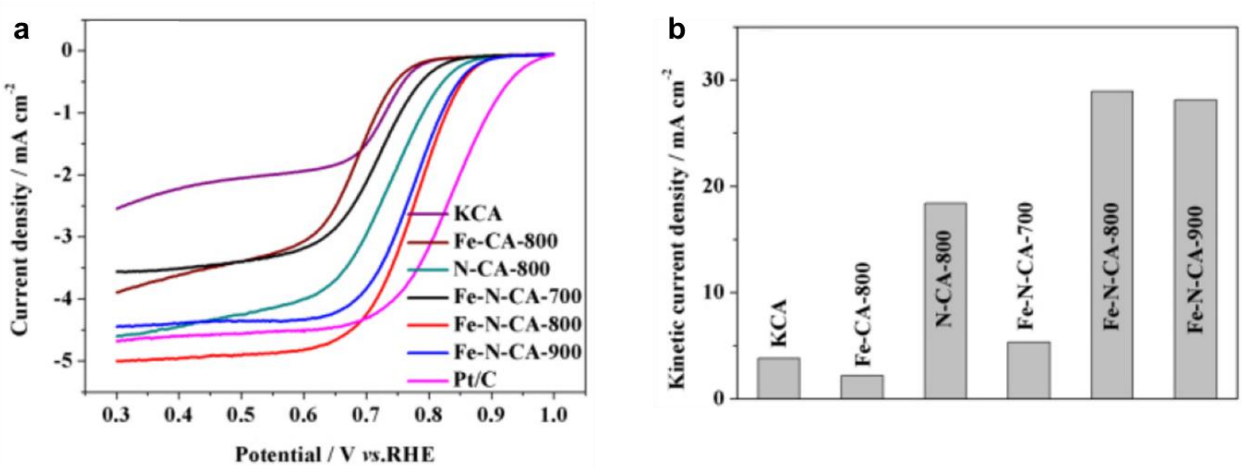

Figure 1.22 **(a)** Polarization curves of different samples at 1600 rpm in O_2-saturated 0.1 M KOH solution; **(b)** kinetic current at 0.7 V of different samples[180].

1.5 Stability of M-N-C catalysts in acidic media and PEMFC

Even if a lot of research on M-N-C catalysts has focused on increasing the initial activity and power performance in PEMFC, the stability of the catalysts is another important factor that should be considered in the development of new catalysts. If the catalyst particles cannot maintain their structure over the lifetime of the fuel cell, changes in the morphology of the catalyst layer from the initial state will result in a loss of electrochemical activity. The near-term durability target of DoE is 5000 h (equivalent to 150,000 miles on the road) for fuel cell vehicles and 50,000 h for stationary devices[181,182].

Some works have reported that detrimental H_2O_2 byproducts may result in the degradation of active site structures. Lefevre and Dodelet treated pyrolyzed Fe-N-C catalysts with a 5% H_2O_2 in H_2SO_4[183]. They attributed the activity loss to the oxidation/attack of the active site structures by H_2O_2 itself or radical species formed by the simultaneous presence of H_2O_2 and Fe ions. Jaouen *et al.* investigated the degradation of a highly active Fe-N-C catalyst in an acidic medium by identical-location electron microscopy and Mössbauer spectroscopy to give an in-suit view of the degradation process[184]. They found the degradation effect of H_2O_2 mainly aims at carbon corrosion, whereas the Fe-N_4 is more resistant to H_2O_2. The high environmental temperature and work potential can accelerate this degradation. The carbon corrosion obviously destroys the porous structure of the carbon support, thus leading to the decay of mass transfer property and reducing the electrocatalytic activity of the catalysts. Meantime, the carbon corrosion also slightly increases the charge-transport resistance of the cycled cathode, which is another factor that leads to high Tafel slopes of the polarization curves. On the other hand, the corrosion of carbon destroys the active sites indirectly. As seen in **Figure 1.23**, the Fe-N-C catalyst initially contains two types of FeN_x sites assigned to micropore-hosted and graphene-defect sites. Since the carbon oxidation rate is faster on zigzag and armchair edges than on the basal plane, micropore-hosted FeN_x sites, the main active sites for ORR, are eliminated faster than graphene-defect FeN_x sites. Loss of the ligand environment of the Fe ions leads to their solvation and removal from the cathode with PEMFC exhaust water.

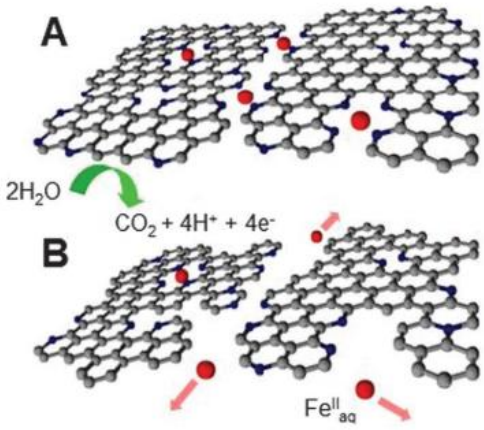

Figure 1.23 Schematic illustration of carbon corrosion and the ensuring loss of micropore-hosted and graphene-defect Fe-N_x sites. N: blue, Fe: red[184].

In summary, pyrolyzed M-N-C materials are promising platinum-group metal-free catalysts for the ORR in fuel cell applications. The metal center, metal content, nitrogen source content, carbon support, and heat treatment conditions show significantly impacts on the catalytic performance of M-N-C materials. Among them, Fe is generally considered as the most active metal center in M-N-C materials, whereas the impacts of other factors should be further determined based on different synthesis methods. Therefore, this thesis concentrated on Fe-N-C materials and selected carbon aerogel with high specific surface area and pore volume as the carbon support. The impacts of Fe precursor, melamine (nitrogen source) content, and heat treatment conditions on the catalytic performance will be discussed.

On the other hand, it is well-accepted that a high degree of graphitization is important for catalyst durability, as we mentioned in sections 1.3.3.3 and 1.3.3.4. Although pyrolysis at a high temperature can efficiently increase the degree of graphitization, thus enhancing the durability, the adverse impacts on the active sites and porosity of carbon support should also be taken into account.

In the end, it seems to have a trade-off between activity and stability in Fe-N-C catalysts, and the heat treatment conditions, specifically the pyrolysis temperature employed, will result in performance variations, with the optimal conditions being material dependent and determined by the systematic investigation.

Chapter 2 Preliminary Investigation to Establish the Synthesis Protocol and Characterization Methods

Résumé Français

Ce chapitre présente la méthode de synthèse générale des catalyseurs d'aérogel Fe-N-C basés sur l'aérogel RMF et décrit les techniques principales de caractérisation des échantillons. La synthèse a commencé à partir de la préparation de l'hydrogel RMF en mélangeant les précurseurs qui sont le résorcinol (R), le formaldéhyde (F), la mélamine (M) et le précurseur de Fe, dans de l'eau. Une solution de Na_2CO_3 a été utilisée comme catalyseur de polycondensation. L'hydrogel obtenu a été vieilli à 70 °C pendant 120 h, puis soumis à une procédure d'échange eau-acétone avant le séchage supercritique au CO_2. Ensuite, le gel séché a été pyrolysé à 800 °C dans un flux de N_2 pendant 1 h pour obtenir l'aérogel de carbone. Les aérogels ont été broyés, suivis par un lavage à l'acide pour éliminer les nanoparticules de Fe non souhaitées. Enfin, un deuxième traitement thermique dans un flux de NH_3/N_2 (10/90) à 950 °C a été effectué pour activer la poudre de catalyseur.

Les conditions de broyage par ball milling et le second traitement thermique ont d'abord été étudiées. Afin de préparer une couche de catalyseur de haute qualité, le broyage à billes est une procédure importante pour obtenir des particules de catalyseurs de taille appropriée et uniforme. Les impacts de la taille des billes et du temps de broyage ont été considérés comme les principaux facteurs. Nous avons comparé la distribution granulométrique de la poudre après différents temps de broyage à l'aide d'une analyse de diffusion dynamique de la lumière. La condition finale choisie est un pré-broyage de l'aérogel carbonisé avec une combinaison de billes de ZrO_2 de 6×10 mm+3×20 mm à 400 rpm/min pendant 15 min pour obtenir une poudre de carbone grossière, puis broyé avec des billes de ZrO_2 de 5 mm à 400 rpm/min pendant 60 min. Le traitement à l'ammoniac crée des micropores hébergeant des sites Fe-N_4 et affecte la nature de l'azote dans le carbone. Ces caractéristiques en ont fait une méthode efficace pour augmenter l'activité catalytique des catalyseurs Fe-N-C. Nous avons étudié l'impact de ce traitement en regardant l'effet de la dilution du NH_3 sur la modification du catalyseur. Une atmosphère diluée de NH_3 dans du N_2 permet d'uniformiser le traitement dans notre four tubulaire par rapport à un traitement sous NH_3 pur. Les tests électrochimiques montrent que tous les échantillons à différentes positions dans le four présentent des performances ORR similaires avec du NH_3 dilué, alors qu'elles sont significativement différentes pour le catalyseur traité dans l'atmosphère de NH_3 pur.

Les caractérisations physico-chimiques utilisées dans ce manuscrit ont été brièvement introduites et les conditions de tests électrochimiques en configuration d'électrode tournante (RDE) et en monocellule de PEMFC ont été discutées en détail. Un rapport ionomère/catalyseur (I/C) approprié est crucial pour la mesure correcte de l'activité catalytique. Il est important de maintenir une couche d'encre composée de ionomère (I, classiquement du Nafion) et de catalyseur (C) sur la surface du carbone vitreux de l'électrode tournante, mais trop d'ionomère augmente également la résistance du transfert d'électrons à l'interface entre le catalyseur et l'oxygène. Le rapport I/C=0.44 a été utilisé pour notre test RDE. L'augmentation supplémentaire de la teneur en ionomère augmente la résistance de la couche catalytique et est défavorable. La situation est différente dans les tests en PEMFC car seuls les sites actifs couverts de Nafion peuvent présenter une activité ORR. Par conséquent, une valeur I/C plus élevée est nécessaire pour maximiser l'activité massique des catalyseurs. La valeur I/C optimale est de 2.0 pour nos catalyseurs à base d'aérogel de carbone en raison de leur surface BET et de leur volume de micro-mésopores très élevés.

This chapter presents the general synthesis method of the Fe-N-C aerogel catalysts and describes the crucial techniques that were utilized in the characterization of samples.

2.1 Synthesis Fe-N-C aerogel catalysts

2.1.1 Fe-N-C aerogel catalysts

The carbon aerogels have a high specific surface area and a porous structure. These features allow them both to host a large number of active sites on the surface and to facilitate water evacuation and oxygen diffusion in MEA. Therefore, they are ideal candidates to prepare Fe-N-C catalysts with high activity and good mass transport properties[185]. Herein, The Fe-N-C aerogel catalysts were synthesized based on a one-pot sol-gel method, which was developed by our group[186,187]. Overall, the synthesis undergoes three main stages, as the protocol shown in **Figure 2.1**.

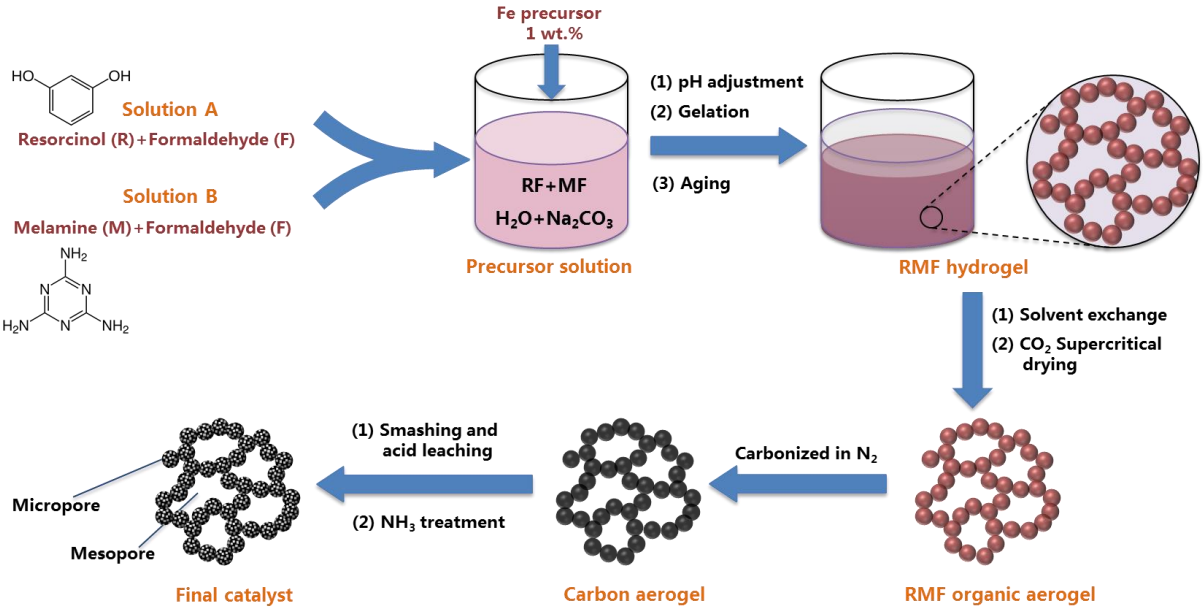

Figure 2.1 Schematic illustration of synthesis procedure of Fe-N-C aerogel catalysts.

The first stage is the preparation of the hydrogel containing carbon, nitrogen, and iron precursors (sol, gelation, aging). Then drying is conducted, leading to an organic aerogel (exchange of solvent, supercritical drying). The final step is the thermal treatments, obtaining the Fe-N doped carbon aerogel (pyrolysis in inert flow, grinding, acid washing, and ammonia treatment). A detailed protocol is described below.

All chemicals were utilized as received. The resorcinol (99%) and NaOH (98%) were purchased from Alfa Aesar. Melamine (99%) and formaldehyde (37 wt% sol. in water, stabilized with 5-15% methanol) were obtained from Acros Organics. Na_2CO_3 (99.99%) was produced by Honeywell Fluka. All the iron precursors were obtained from Sigma Aldrich.

The first is the preparation of the hydrogel, including the gelation and aging step. In this stage, the hydrogels were prepared based on polycondensation of resorcinol (R), formaldehyde (F),

and melamine (M), where R and M are the carbon and nitrogen source, respectively, and F is the cross-linker which helps form the network. R-F and M-F pre-polymers were prepared separately. When they were mixed, the co-condensation reaction occurred among the hydroxymethyl groups between M-F and R-F pre-polymers to form methylene and methylene ether bridged polymers, which build up the skeleton of the hydrogel. In this stage, the iron precursor is added, and the pH adjusted. Therefore, the recipe of hydrogel is crucial to control the texture of the gel, including the mesopore volume in the final catalyst. The second stage involves water-acetone solvent exchange and drying of the wet gel. Supercritical drying is employed to maintain the texture of the hydrogel in the dried gel (aerogel). The last step is the pyrolysis of the iron-organic aerogel into carbonaceous aerogel under the inert flow (carbonization), which is the crucial step for the formation of active sites[188].

Here is a typical recipe for Fe-N-C catalysts. The absolute quantity of reagents can be varied according to the expected quantity of the final product.

First, solution A (R-F pre-polymer) contained 3.6 g of R, 5 mL of F solution, and 22 ml of water. 0.75 ml of 0.38 M aqueous Na_2CO_3 (Cat) solution was then added as the catalyst of polycondensation and was stirred for 45 min at 40 ^{o}C in a water bath, with R:F: Cat = 1:2:0.008. The solid content in solution A is 22%, estimated according to the formula (2-1):

$$Solid\ content = \frac{total\ mass\ of\ solid}{mass\ of\ solvent} \tag{2-1}$$

Separately, solution B (M-F pre-polymer) was prepared from 2.0 g of M, 3.5 mL of F, 0.7 mL of Cat solution, and 12 mL water with the mole ratio of M:F:Cat = 1:3:0.016. The mixture was stirred for 30 min at 70 ℃. The solid content of solution B was also kept at 22%.

Subsequently, solution A and B were mixed and stirred for 5 min at room temperature. The mole ratio of R to M in the mixture solution is 2/1 in this recipe. Afterward, Fe precursor was added and stirred for 5 min, followed by the pH adjustment to 8 (or 6 according to the nature of the Fe precursor) by adding NaOH solution. The quantity of Fe precursor ($m_{Fe\ precursor}$) in this step can only be roughly estimated because we can neither predict the exact mass loss of organic aerogel after two heat treatments process nor know the loss of Fe during acid leaching. According to our previous experiments, the total mass loss of organic aerogel is around 70%. Assuming Fe won't be removed during acid leaching, $m_{Fe\ precursor}$ can be estimated by formula (2-2):

$$m_{Fe\ precursor} = total\ mass\ of\ solid \times w \times 30\% \times \frac{M_{Fe\ precursor}}{M_{Fe}} \tag{2-2}$$

where $M_{Fe\ precursor}$ and M_{Fe} are the molecular weight of Fe precursor and Fe, respectively, and *w* is the expected weight percentage of Fe in the final catalyst. For example, when the Fe precursor is $FeCl_3$ (M_w 162.20 g mol^{-1}), and the expected Fe content is 1 wt.%, 0.08 g of $FeCl_3$ is required. It must be noted that this value cannot ensure the expected Fe content due to the constraints we mentioned before. The real value must be determined by other characterization methods, such as inductively coupled plasma mass spectrometry (ICP-MS).

The phenomenon worth taking care of in this step is that red rust precipitation occurred once the iron precursor was added, which is caused by the coagulation of low-weight RF and MF pre-polymers in the mixture solution. This phenomenon was significant when Fe salts were used because free Fe ions could act as the coagulation center. In general, around 3 mL NaOH solution was consumed to dissolve the precipitation and adjust pH to 8. The increased pH made

these pre-polymers negatively charged, thus being separated. In order to obtain a homogenous texture, the sol was kept stirring at 70 ℃ until gelation occurred. 10 mL of distilled water was covered on the surface of the gel to avoid unexpected evaporation of solvent during the aging process, which probably crashed the porous structure of hydrogel. The hydrogel was then conserved in a water bath at 70 ℃ for 120 h to complete polymerization.

The aged hydrogel was immersed in 300 mL of acetone for a water-acetone solvent exchange procedure. The solvent was refreshed 3 times a day for 3 days to remove traces of water. This procedure is necessary because acetone is miscible in supercritical CO_2. Therefore, the conditions of supercritical drying will be softened compared to water ones. After all these exchanges, the hydrogel was subjected to the supercritical drying to get the RMF aerogel.

The carbon aerogel was obtained by pyrolyzing RMF aerogels at 800 ℃ in N_2 flow for 1 hour. Before heating, the atmosphere in the tube furnace was purged by N_2 flow. The heating program was set as follows: 2 ℃ min^{-1} from room temperature to 350 ℃ and dwelling for 30 min. Most of the decomposition reactions started at this stage with the loss of volatile species. The temperature was then increased to 800 ℃ with a ramp of 4 ℃ min^{-1} and stabilized for 1 h to complete the carbonization.

To obtain the powders that satisfy the application on the membrane electrode assembly, the aerogel blocks were then ball milled to fine powders. The conditions will be detailed in section 2.1.2. The obtained powder was then subjected to acid leaching with 0.5 M H_2SO_4 at 80 ℃ for 7 h in a refluxing device to remove the iron nanoparticles that were possibly generated during the pyrolysis[187]. The suspension was separated by centrifugation to get the powder and washed several times with distilled water until the pH of the solution was close to neutral. Finally, the sample was dried in an oven at 100 ℃ overnight.

In order to create more active sites, a second pyrolysis was conducted on the sample at 950 ℃ in NH_3 flow. According to our previous research, when pure NH_3 was used, the degree of treatment was uneven for different positions of the tube due to the dilution of NH_3, which led to different catalytic activity for the same batch of samples. Therefore, diluted NH_3 was used to improve the uniformity of treatment regardless of the position in the oven. The investigation will be discussed in section 2.1.3.

Since the recipe of hydrogel plays a decisive role in the texture and the catalytic activity of the final catalyst, most of my research has focused on the first stage by modifying the synthesis parameters to obtain a panel of catalysts with various characteristics in order to select the best conditions leading to the performing catalyst, eventually. The investigation of this stage can be divided into two aspects:

1. Impact of Fe precursor: different Fe precursors, Fe contents, and states of Fe in the precursor lead to different Fe states in the organic aerogel, such as hydroxide or coordinated Fe, which will further impact the active sites in the final catalysts.
2. Composition of RMF hydrogel: since the M is the main nitrogen source in this stage, the increasing M content could introduce more active N, which can coordinate with Fe.

2.1.2 Ball milling conditions

The cathode catalyst layer consists of a mixture of catalyst particles, ionomer membrane, and void space[189]. For Pt-based catalysts, a typical thickness of this layer is 5-10 μm due to their ultrahigh activity to ORR that only a small quantity (0.1-0.4 mg cm^{-2}) is enough to get

appropriate power density[16,190]. On the contrary, the loading of Fe-N-C catalysts (1-5 mg cm^{-2}) is *ca.* 10 times of Pt-based catalysts to compensate for their lower intrinsic activity, which leads to a thicker catalyst layer (~4 mg cm^{-2}, resulting in 70-100 μm thick layer)[16,65,191,192]. In order to prepare high-quality catalyst layer, ball milling is an important procedure to get catalyst particles with suitable and uniform sizes. Besides, previous research of Ratso *et al.* also demonstrated that the Fe-N-C catalyst prepared with modified ball milling conditions could increase the diffusion-limited current density values because the decreased particle size leads to an increase in the active surface on the electrode[193]. The impacts of ball size and the time of grinding were considered the main factors. In general, longer grinding time can lead to smaller particles size before reaching the limit of ball milling. Our target was to find the minimum time to reach the limit. We also investigated the impacts of pre-grinding before or after the first pyrolysis. The pre-grinding of large dried gel blocks is also important to make sure the initial particle size satisfies the machine specifications. Organic aerogel is more fragile than carbon aerogel, which is easier to be smashed. On the other hand, the melt of MF gel during pyrolysis will lead to agglomeration of pre-ground powder, which is possible to increase the grinding time.

The ZrO_2 pot and balls are shown in Figure 2.2, where 3 sizes of the ball (20 mm, 10 mm, and 5 mm diameter) were prepared. In the pre-grind step, a mixed size of 20 mm and 10 mm balls were used to ensure the large blocks were completely smashed to a coarse powder. The 5 mm balls were used in the following grinding step to get fine powder.

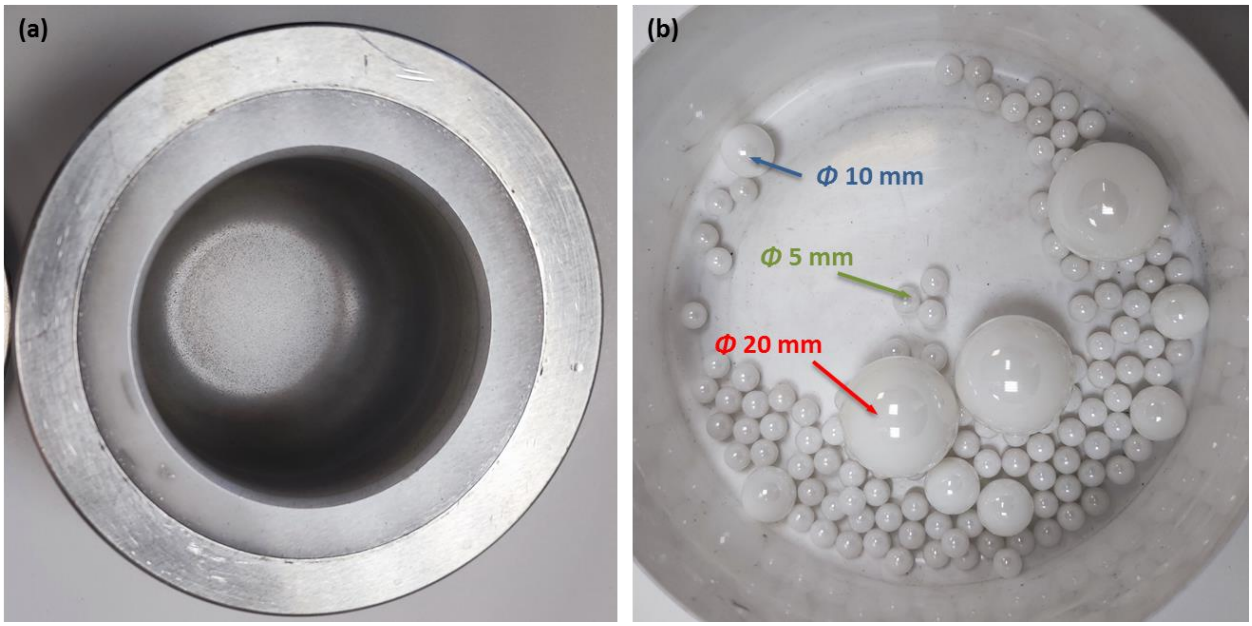

Figure 2.2 **(a)** ZrO_2 pot and **(b)** balls for planetary ball milling method.

The organic aerogel sample pre-ground before pyrolysis was named AN1-1. In contrast, the sample pre-ground after pyrolysis was named AN1-2. The flow diagram of the two methods is shown in **Figure 2.3**. For the AN1-1, 3 g of dried gel was poured into a 50 ml ZrO_2 pot with 90 g ZrO_2 balls combination of 6×10 mm + 3×20 mm. The ball-to-powder mass ratio was kept at 30:1 for all grinds. The pot was then sealed under air and ball-milled for 15 min at 400 rpm milling speed to smash the large gel blocks. The powder of organic aerogel was then pyrolyzed in N_2 at 800 ℃. 1.5 g of the obtained carbon aerogel was ground with 45 g zirconium-oxide balls of 5 mm diameter at 400 rpm for 1 h. The samples were collected every 15 min in order

to investigate the impact of the grind time. As for the AN1-2, the organic aerogel block was first pyrolyzed in N_2 at 800 ℃ to get carbon aerogel. 3.0 g of material were smashed with 10 mm + 20 mm ZrO_2 balls (pre-grind step) and ground with 5 mm ZrO_2 balls.

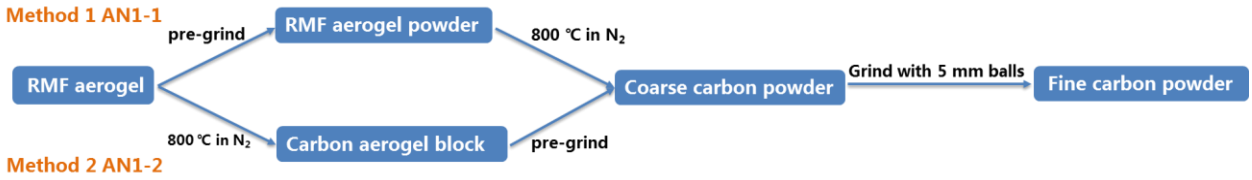

Figure 2.3 Flow diagram of two grinding methods.

The distribution of the particle sizes was measured in ethanol using a dynamic light scattering (DLS) analyzer (HPPS, Malvern instruments Inc, Worcestershire, UK) at ICGM/CNRS (seen in annex A.2.1). The results were shown in **Figure 2.4**. For both methods, the particle sizes are smaller than 5 µm, which satisfies the minimum powder size in the catalyst layer. Initially, DLS curves present two peaks at small (around 200 nm) and large (>1 µm) particle sizes. As time went on, the peak area at large size gradually reduced. For the AN1-1, which is pre-ground before pyrolysis, large particles at *ca.* 500 nm were found after the first 15 min of grind. This result conformed to the agglomeration of powder during pyrolysis. As a result, the peak at large particle size didn't disappear even after 1 h grind. In contrast, the particle sizes of AN1-2 were reduced to less than 1 µm after grinding for 60 min and got the uniform distribution of the particle size. The carbonized blocks can be well smashed in the pre-grind stage, thus more efficient.

In conclusion, we choose method 2 as the ball milling condition: First, carbonization at 800 ℃, then pre-grind with ZrO_2 balls combination of 6×10 mm + 3×20 mm at 400 rpm for 15 min to get the coarse carbon powder, and finally, the product was ground with 5 mm ZrO_2 balls at 400 rpm for 60 min.

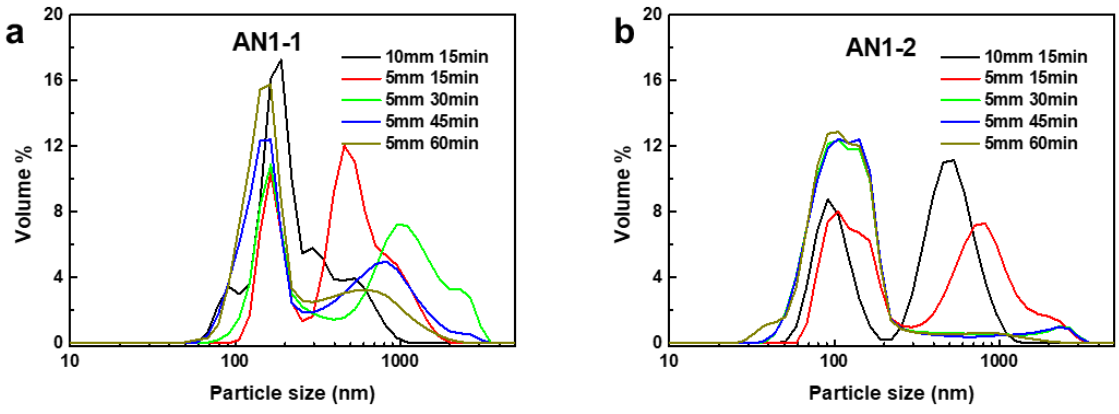

Figure 2.4 The distribution of the ball milled particles sizes for **(a)** AN1-1 and **(b)** AN 1-2.

2.1.3 Conditions of NH_3 treatment

The ammonia treatment creates micropores hosting Fe-N_4 sites and affects the nature of nitrogen in the carbon[194]. These features made it an effective method to increase the catalytic

activity of Fe-N-C catalysts. However, in our tubular furnace, the first trail shows that pure NH_3 leads to an uneven treatment degree due to the decreasing concentration gradient from inlet to outlet. Here, a diluted NH_3 (10% NH_3 + 90% N_2) was employed to improve the diffusion of the active component, thus increasing the homogeneity of treatment. To investigate the impact of different positions in the furnace, 4 ceramic boats containing 300 mg of carbon aerogel powder spread in the center of the boat, were placed one by one, as seen in **Figure 2.5**a. The heating program was set up as follows: increase the temperature from room temperature to 950 ℃ with a ramp 4 ℃ min^{-1} and stabilize for 15 min under 0.5 L min^{-1} N_2 flow, then switch the gas to 0.6 L min^{-1} NH_3/N_2 mixture flow dwelling for 30 min. Finally, the system is cooled down under N_2 flow to room temperature.

Table 2.1 Mass loss and catalytic activity of products in the different position of tube furnace treated with pure or 10% NH_3.

NH_3 concentration	Position	Mass loss	Current density at 0.8 V (A/g)
100%	1	64%	3.15
	2	72%	2.56
	3	80%	1.78
	4	97%	1.70
10%	1	45%	2.09
	2	49%	1.91
	3	57%	1.82
	4	58%	2.06

Due to the different NH_3 concentrations and positions in the furnace, a series of products with different mass losses were obtained, and their electrochemical performances were investigated. The mass loss results of electrochemical tests are listed in **Table 2.1**, and their polarization curves are shown in **Figure 2.5**b and c. It can be seen clearly that the pure NH_3-treated samples exhibit large differences in mass loss and activity between the different positions in the furnace. The sample located at the entrance (position 4) is almost completely etched by NH_3, thus presenting the worst catalytic activity. On the other hand, the samples treated with 10% NH_3 present closer mass loss, and most importantly, their polarization curves are almost identical. This result proved that decreasing the NH_3 concentration could efficiently improve the diffusion of NH_3 in the tube. Therefore, the samples at different positions in the furnace can be treated evenly. However, samples treated with 10% NH_3 concentration are less active than samples treated in pure NH_3 at position 1 due to insufficient treatment degree. In order to approach the mass loss of the best sample, the treatment time should be prolonged, and we choose 45 min as the appropriate duration.

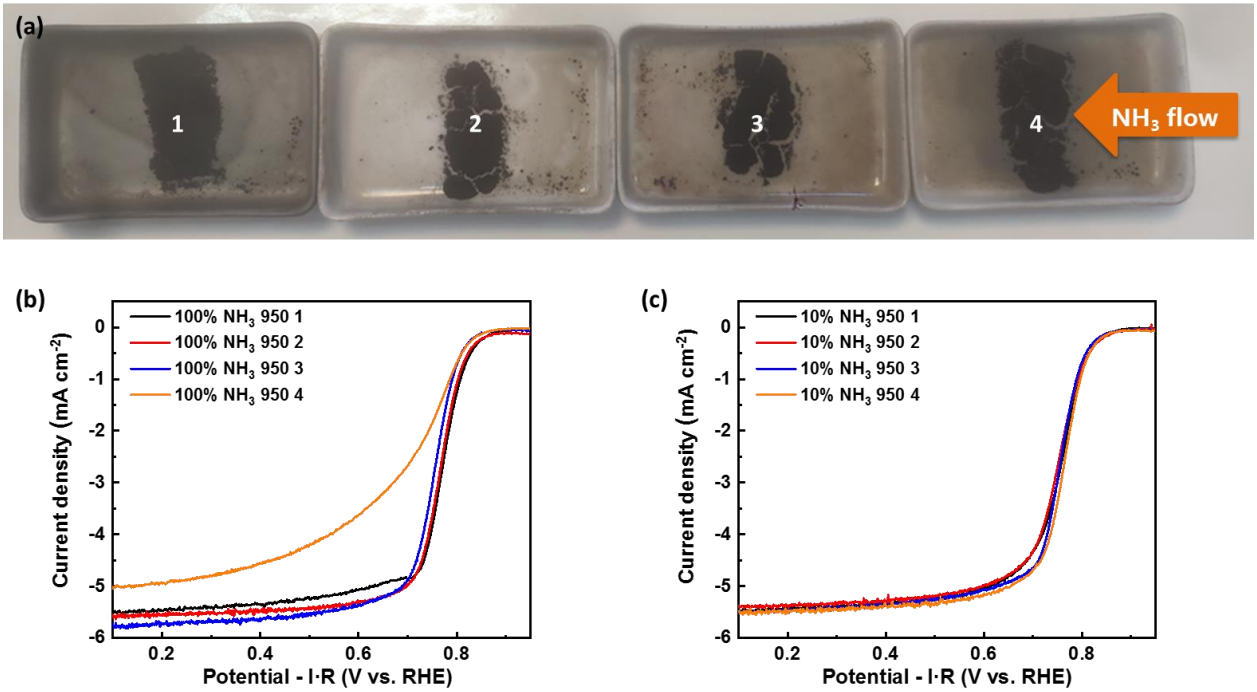

Figure 2.5 **(a)** Positions of samples in tube furnace and direction of NH_3 flow; Polarization curves of samples at different positions treated in **(b)** pure NH_3 and **(c)** 10% NH_3.

In conclusion, the 10% NH_3 can efficiently improve the consistency of treatment degree, thus providing the catalysts with identical activity. Additionally, the decreased concentration also requires longer treatment time to get appropriate activity. Therefore, the final treatment condition was determined as follows: About 1 g of carbon aerogel powder was spread uniformly in two ceramic boats placed in the center of the tube side by side. Raise from room temperature to 950 ℃ with a ramp 4 ℃ min^{-1} and stabilize for 15 min under 0.5 L min^{-1} N_2 flow, then switch the gas to 0.6 L min^{-1} diluted NH_3 flow, dwelling for 45 min. Finally, the system is cooled down under N_2 flow to room temperature.

2.2 Physicochemical characterizations

The morphologies of catalysts were investigated by scanning electron microscopy (SEM) with a MAIA operated at 3.0 kV. The porosity and Brunauer-Emmett-Teller (BET) area were determined by N_2 sorption method at -196 ℃ (seen in annex A.2.2). Transmission electron microscopy (TEM) was used to detect the presence of Fe-based nanoparticles. A JEOL 2010 TEM operated at 200 kV with a resolution of 0.19 nm was used. X-ray diffraction (XRD) of catalyst powder was also performed to verify the existence of crystalline solid (seen in annex A.2.3). The dried organic aerogel was investigated by attenuated total reflection Fourier transform infrared (ATR-FTIR) spectroscopy to determine the integration of RF and MF prepolymers. The measurements were performed in the range of 4000-600 cm^{-1} on a Bruker Tensor 27 machine using OPUS 7.8 software. The graphitic degree of carbon aerogel was evaluated by Raman spectroscopy (seen in annex A.2.4) on a Renishaw InVia instrument in a backscattering configuration (with 532 nm as excitation). The global Fe content in the catalyst was determined by inductively coupled plasma mass spectrometry (ICP-MS) on a PerkinElmer NexION 2000c instrument. X-ray photoelectron spectroscopy (XPS) was used to identify the

surface elemental composition of catalysts (seen in annex A.2.5). Among them, TEM, ICP-MS, and Raman analysis were carried out by LEPMI/CNRS in university Grenoble, France. Other characterizations (XRD, N_2 sorption, and XPS) were performed at Mines Paris in Sophia Antipolis, France. The chemical environment of Fe in catalysts was investigated by ^{57}Fe Mössbauer spectra (seen in annex A.2.6) and X-ray absorption spectroscopy (XAS) (seen in annex A.2.7). The measurements were carried out by ICGM/CNRS in university Montpellier, France and Synchrotron SOLEIL in Saint Aubin, France, respectively.

2.3 Electrochemical characterizations

2.3.1 Rotating Disk Electrode (RDE) tests and ink formulation

The electrochemical tests were carried out in a three-electrode cell with a rotating disk electrode (RDE, OrigaTrod instrument) at room temperature with a potentiostat/galvanostat from Bio-Logic (HCP-803). The setup is shown in **Figure 2.6**.

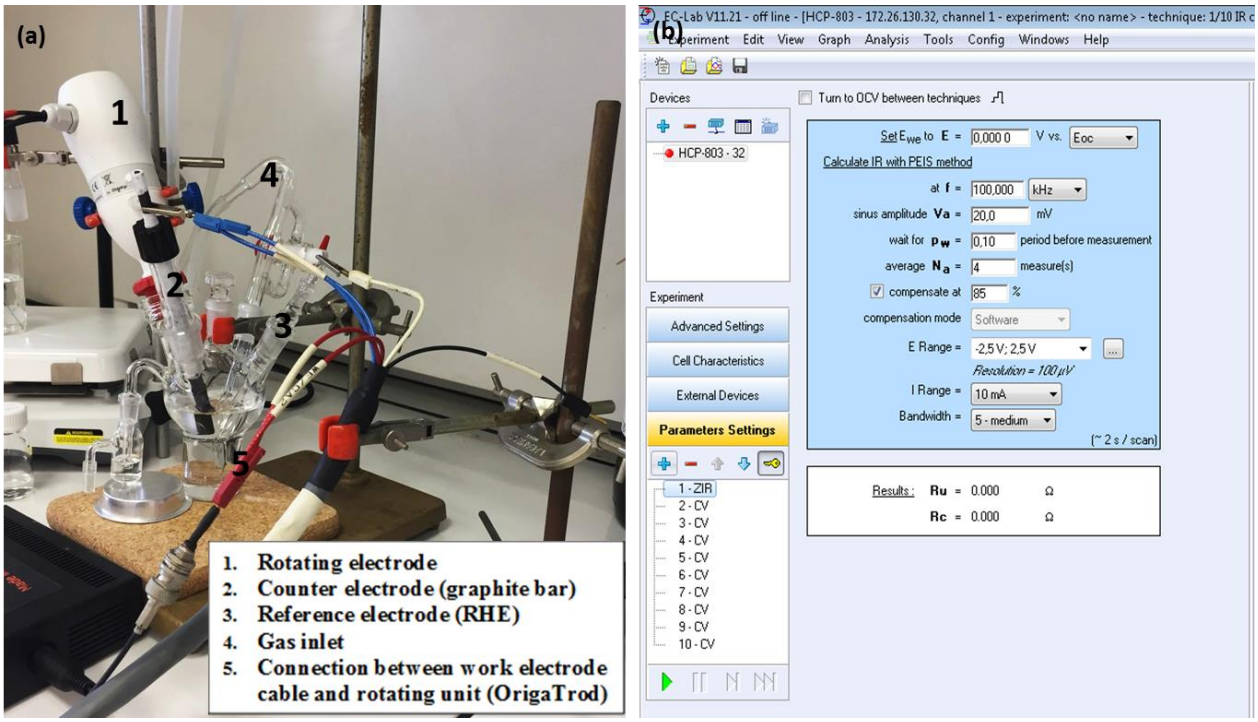

Figure 2.6 **(a)** Three-electrode cell with the rotating disk electrode and **(b)** parameters of ZIR.

2.3.1.1 Description of the cell

The glassware was cleaned by 12 h immersion in Piranha Solution (seen in annex A.1) to clean organic residues off substrates before the first-time use and then thoroughly rinsed with milliQ H_2O (Millipore, 18.2 MΩ cm, 1-3 ppm TOC).

The Reversible Hydrogen Electrode (RHE) is composed of a platinum wire in contact with both gaseous hydrogen (H_2) and electrolyte solution (0.05 mol L^{-1} H_2SO_4). Graphite electrode is used as the counter electrode.

RDE glassy carbon (GC) tips are polished with the diamond paste of 1 μm on a micro-cloth polishing pad following a small "8" pattern for 5 min. The tip was then subjected to washes with acetone, ethanol, and distilled water. For each wash, the electrodes are passed to ultrasound (Elma S40, 140 W) for 15 min. Finally, the electrode is dried by N_2 purge.

2.3.1.2 The preparation of catalyst ink

Prior to the ink preparation, the Fe-N-C catalysts have been well ground by ball milling. The ink was then prepared with obtained powder according to the following steps:

(1) 10 mg Fe-N-C catalyst, 95 μL of 5 wt% Nafion D-520, 752 μL of ethanol, and 46 μL of distilled water were mixed in a microcentrifuge tube of 2 mL.
(2) 30 min of sonication with ultrasound (Elma S40, 120 W) and 10 min of agitation with a vortex mixer was employed to help separate the powder in the suspension, then repeated for more time.
(3) 7 μL of prepared ink was dropped onto the polished GC electrode (5 mm diameter with an area of 0.196 cm^2), which obtained a catalyst loading of 400 μg cm^{-2}

The ratio of ionomer to catalyst (I/C) can be calculated according to formula (2-3):

$$\mathrm{I/C} = \frac{V \times \rho \times 5\%}{mass\ of\ catalyst} \tag{2-3}$$

where V and ρ are the volume and density of the Nafion solution, respectively. Here, V = 95 μL, ρ = 0.93 g cm^{-3}, and the mass of catalyst is 10 mg, thus leading to I/C = 0.44.

An appropriate I/C ratio is crucial for the correct measurement of the catalytic activity. It's important to maintain the catalyst film on the GC surface of RDE, but too much ionomer also increases the resistance of electron transfer on the interface between the catalyst and oxygen.[195] The different formulas of ink and the results of their electrochemical test are listed in **Table 2.2**. According to their polarization curves shown in **Figure 2.7**a, the current density at 0.8 V decreased with increasing the I/C ratio. The increasing Tafel slopes in **Figure 2.7**b indicate an increasing electron transfer resistance due to a thicker Nafion membrane. Therefore, I/C = 0.44 is the appropriate formula for ink.

Table 2.2 Catalytic activity of a catalyst with different ink formula in RDE set up

I/C	Nafion 5 wt% (μL)	Ethanol (μL)	H_2O (μL)	Current density at 0.8 V (A g^{-1})
0.44	95	752	46	2.20
1.4	332	515	46	1.80
2.0	475	372	46	1.18
2.5	594	253	46	0.78

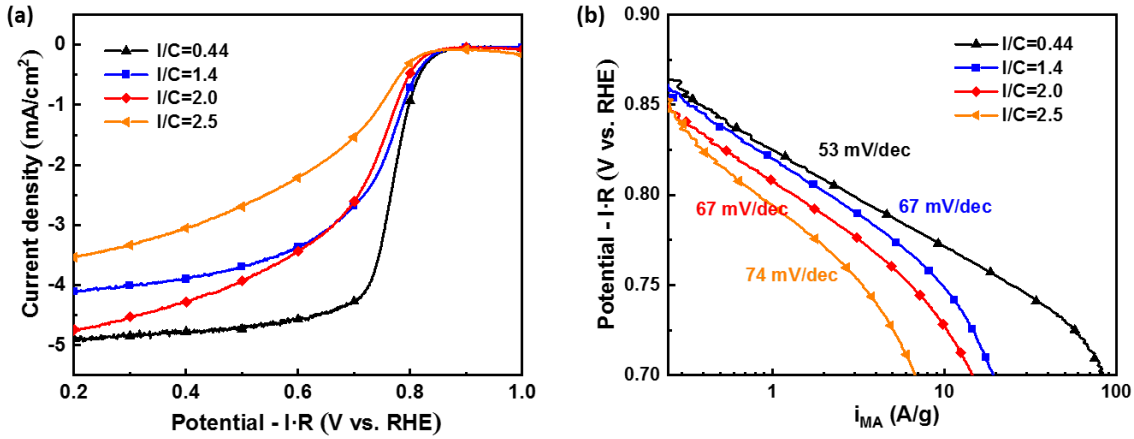

Figure 2.7 **(a)** Polarization curves and **(b)** Tafel slopes of the catalyst prepared with different ink formula.

2.3.1.3 Electrochemical tests

Cyclic voltammetry (CV) and linear scan voltammetry (LSV) tests are done on the Fe-N-C catalyst powders. The obtained data was ohmic-drop (iR-drop) corrected, where ohmic-drop was defined by the solution resistance between the working electrode and the reference electrode. The ohmic drop is determined by performing an impedance measurement at high frequencies before running other experiments (CV or LSV). The magnitude of uncompensated resistance (Ru) is dependent on the concentration of electrolyte, e.g., Ru is approximately 30 Ω in 0.05 M H_2SO_4.

All tests were carried out in 0.05 M H_2SO_4 aqueous solution. The electrolyte solution was previously saturated with O_2 for 15 min. The ORR activity of catalysts was measured by LSV at 1600 rpm, with a scan rate of 10 mV s^{-1} from 1.10 to 0.00 V *vs.* RHE. Oxygen was kept bubbling during the measurement to maintain saturation in the electrolyte. To calculate the electron transfer number during the ORR process, LSV at another 3 different angular velocities (1225, 900, and 625 rpm) were performed under the same condition.

Subsequently, the electrolyte solution was purged with N_2 for 15 min in order to eliminate dissolved O_2 in the electrolyte. Then CV between 0 and 1.0 V *vs.* RHE at 50 mV s^{-1} was carried out in the stagnant (unstirred) solution until stable conditions were obtained, followed by 2 cycles at 10 mV s^{-1} at the same electrochemical window. The N_2 was kept bubbling in the solution during the test but at a slower rate to maintain the atmosphere on the surface of the electrolyte. After CV tests, a LSV with the same condition of oxygen-saturated solution was conducted to determine the background current of the catalysts.

All LSV curves were corrected by subtracting the background current recorded in the N_2-saturated electrolyte. The kinetic current density of the catalyst controlled only by the ORR kinetics was calculated by the Koutecky-Levich equation (2-4):

$$\frac{1}{j_k} = \frac{1}{j_F} - \frac{1}{j_{lim}} \tag{2-4}$$

j_k, j_F *and* j_{lim} are the kinetic current density (in A cm^{-2}), faradic current density (in A cm^{-2}), and limiting current density (in A cm^{-2}), respectively.

The mass activity (in A g^{-1}) is defined by the equation (2-5):

$$j_M = -\frac{i_k}{m} \quad (2\text{-}5)$$

where $j_M > 0$ and m is the catalyst loading (0.4 mg cm^{-2}) on the GC. j_M at 0.8 V was reported and compared.

2.3.1.4 Durability tests

All samples were conducted a primary durability test after LSV measurements. The electrolyte was N_2-saturated before and kept N_2-bubbling during the test. Two CV cycles between 0 and 1.0 V *vs.* RHE at 50 mV s^{-1} were carried out, followed by two cycles under the same electrochemical window at 10 mV s^{-1}. Then 500 CV cycles were conducted between 0.6 and 1.0 V *vs.* RHE with a scan rate of 50 mV s^{-1}. Finally, a CV cycle between 0 and 1.0 V *vs.* RHE at 10 mV s^{-1} was recorded to compare the variation of the electrochemical available area. After the durability test, ORR polarization curves (LSV curve) were recorded with the same electrode in the O_2-saturated electrolyte to compare the degradation of mass activity.

In Chapter 5, the effect of NH_3 treatment on the catalyst stability was investigated by a stronger accelerated stress test (AST) protocol composed of 2000 CV cycles between 0.6 and 1.0 V *vs.* RHE with a scan rate of 50 mV s^{-1}. A CV cycle between 0 and 1.0 V *vs.* RHE at 10 mV s^{-1} was recorded every 500 cycles to investigate the variation of curves. The AST protocol was conducted both in N_2 and O_2-saturated electrolyte to investigate the degradation effects under different atmospheres. During the AST in N_2 saturated electrolyte, the RDE is stationary, whereas, in O_2-saturated electrolyte, the RDE kept a rotation rate of 1600 rpm. The catalysts performed by AST in N_2 or O_2 saturated electrolyte were labeled by AST-N_2 and AST-O_2, respectively. After the AST protocol, LSV curves were recorded in O_2-saturated electrolyte as well to compare the degradation of mass activity.

2.3.2 Single cell tests and ink formulation

The activity of catalysts was further investigated in the single cell of PEMFC to compare the difference with the RDE setup. The experiments were completed in the ICGM/CNRS facilities.

2.3.2.1 Preparation of membrane electrode assembly (MEA)

The measurements were performed on a 5 cm ²MEA. For the preparation of the cathode, 20 mg of catalyst, 915 µL 5 wt. % Nafion (1100W) solution, 300 µL of 1-propanol, and 272 µL of deionized water were mixed and subjected to sonication for 1 hour. Different from RDE, a high I/C ratio is necessary for the MEA since only the active sites attached to the electrolyte network can present activity[195]. The ink was deposited in several batches on a 5 cm^2 gas diffusion layer (GDL S29BC) to make the catalyst layer as even as possible, resulting in a catalyst loading of 4.1 mg cm^{-2}. Then the deposited ink was dried at 80 ℃ overnight to get the cathode, as seen in **Figure 2.8**a. The dried cathode was hot-pressed at 135 ℃ with a Pt/C anode (S28BC, with a Pt load of 0.5 mg cm^{-2}) and a Nafion membrane (NR211, 25 µm) at a pressure of 2 tons for 2 min to get the MEA.

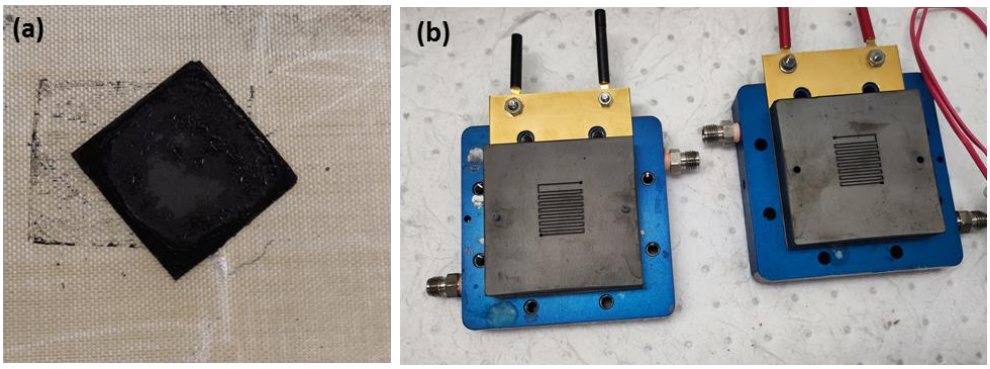

Figure 2.8 (a) 5 cm^2 dried cathode with catalyst (Fe-N-C) loading of 4.1 mg cm^{-2}; (b) Instrument of single cell tests.

2.3.2.2 Electrochemical tests of single cell

The obtained MEA was installed in a fuel cell fixture of Electrochem. Inc, and the experiments are run with a Biologic potentiostat (**Figure 2.8**b). The temperature of the humidifiers and cell was raised to 80 ℃. When the temperature was stable, O_2 and H_2 flows were switched on (150 mL min^{-1}), and gauge pressures were set to 1 bar, leading to the 1.5 bar absolute pressures of O_2 and H_2 since the water vapor saturation pressure is 0.5 bar at 80 ℃. All the pipelines and connectors were wrapped up in thermal insulators to prevent the formation of low-temperature zone, leading to the condensation of water.

The cell was left at an open-circuit voltage (OCV) for about 5 min to record an average value. The CV curve was recorded between 0.9 V and 0.3 V at a scan rate of 1 mV s^{-1}. After, an electrochemical impedance spectroscopy measurement was conducted at OCV, with frequencies from 1kHz – 1Hz. The durability of the catalyst was investigated by Chronoamperometry (CA) spectrum at 0.5 V, which presents the decline of current density with operation hours.

2.3.2.3 Impact of ink formula on single cell test

In the PEMFC environment, the O_2 molecules in direct contact with the catalytic sites are dissolved in the hydrophilic phase of Nafion[195]. Therefore, it is important to cover all the micropore-hosted active sites by the Nafion network to maximize the mass activity of catalysts. On the other hand, the electron transfer resistance can be increased by a too-thick electrolyte layer. An appropriate I/C value should be found to measure the activity correctly. Similar research has been done by Jaouen *et al.*[195]. The optimum I/C value for their catalysts in PEMFC was found between 1.5 and 2, which is higher than the value of carbon-supported Pt catalyst due to a higher BET area (650-1000 m^2 g^{-1}). Our catalysts also present a high BET area after ammonia treatment, typically larger than 1000 m^2 g^{-1}. Therefore, a high I/C value is also expected to get the best activity in PEMFC.

Table 2.3 shows the 4 different formulas of ink and the corresponding current density at 0.8 and 0.5 V from their polarization curves (**Figure 2.9**a). **Figure 2.9**a shows the effect of the Nafion content in the cathode ink formulation, with both the activity and power performance dramatically increasing from I/C =1.0 to I/C =2.0 and thereafter only slightly decreasing from I/C =2.0 to 2.5. Nyquist plots of electrochemical impedance spectroscopy showed little change with I/C (**Figure 2.9**b), while cathode CVs recorded in H_2/N_2 PEMFC mode showed

dramatically increasing capacitive currents from I/C =1.0 to I/C =2.0 and only very slightly increasing from I/C =2 to 2.5 (**Figure 2.9**c). Therefore, the data indicate that the optimum I/C ratio is 2.0 for this catalyst, necessary for covering most of the catalyst surface with ionomer (maximizing the activity) without leading to excessive ionomer thickness (minimizing O_2 diffusion issues through the film and the filling of meso-macropores). This optimum I/C ratio for the Fe-N-C aerogel catalyst in PEMFC is comparable to the one optimized for two other high S_{BET} Fe-N-C catalysts (with similar PEMFC cathode preparation methods)[195]. For the two catalysts labeled as ball milling Fe-N-C catalysts 1 and 2 in that work, the optimum I/C ratio was found to be 1.75 and 2, respectively, while their S_{BET} values were 730 and 1000 $m^2\ g^{-1}$, respectively. The BET area of all catalysts in our work is *ca.* 1100-1600 $m^2\ g^{-1}$, and the optimum ratio I/C of 2.0 is thus in line with previous results. The other catalysts were then investigated with a fixed I/C value of 2.0.

Table 2.3 Catalytic activity of a catalyst with different ink formula in MEA.

I/C	Catalyst (mg)	Nafion 5 wt% (µL)	propanol (µL)	H_2O (µL)	Current density at 0.8 V (mA cm^{-2})	Current density at 0.5 V (mA cm^{-2})
1.0	20	458	300	272	2.39	103.15
1.4	20	641	300	272	11.23	179.26
2.0	20	915	300	272	36.62	580.17
2.5	20	1145	300	272	26.20	472.49

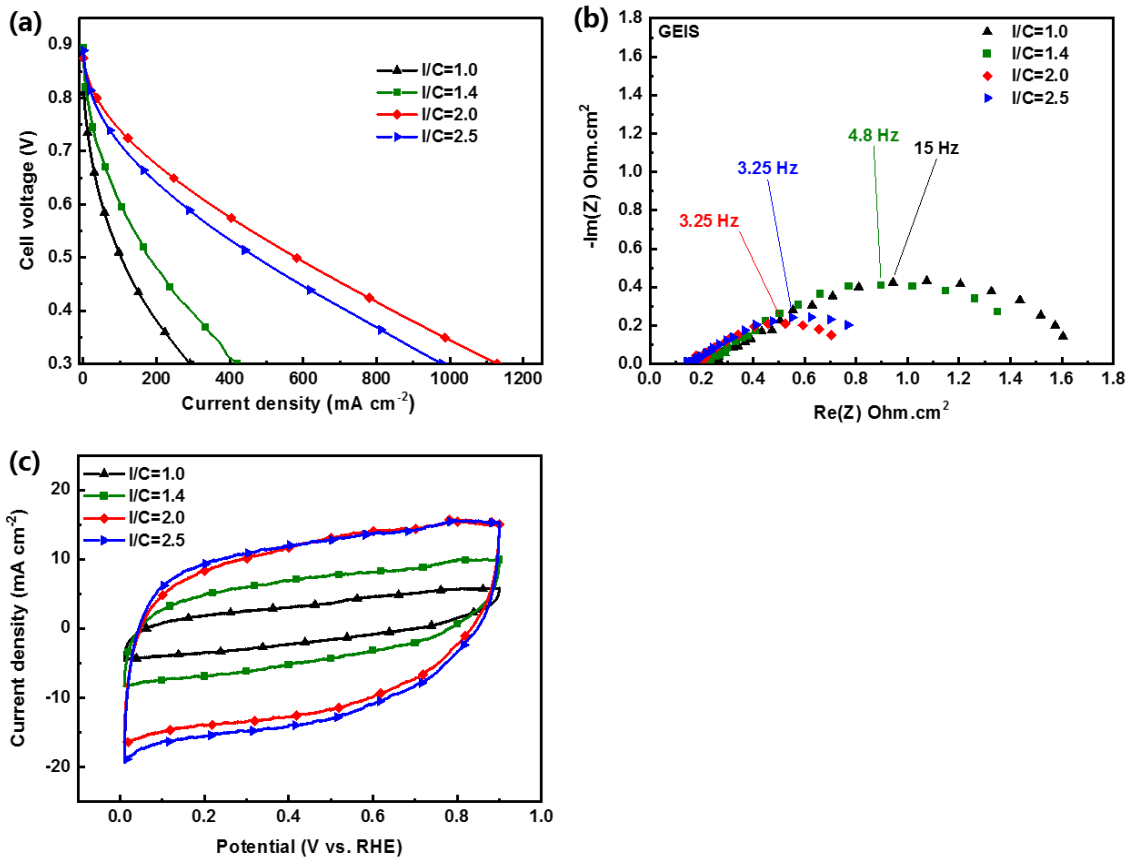

Figure 2.9 Investigation of ink formulations for PEMFC **(a)** H_2-O_2 polarization curves, **(b)** Nyquist plots, and (c) CV curves of catalyst $FeCl_3$-R/M=2/1 with different I/C values.

Chapter 3 Impact of Fe Precursors on the Performance of Fe-N-C Catalysts towards Oxygen Reduction Reaction in Acidic Medium

Résumé Français

Fe est le centre des sites actifs Fe-N_4 dans le catalyseur carboné. La nature de Fe dans la solution de précurseurs joue un rôle crucial lors de la formation de la structure Fe-N_4, affectant ainsi profondément l'activité des catalyseurs. Les facteurs influant sur la dispersion des ions ferreux et ferriques dans la solution de précurseurs doivent être examinés, y compris les états d'oxydation du Fe, le contre-ion des sels de Fe et les ligands attachés. Dans ce chapitre, des catalyseurs ont été synthétisés à partir de différents précurseurs de fer et d'additifs à base de ligands azotés pour établir la relation entre le précurseur de Fe et les performances ORR des catalyseurs. De plus, les impacts des différentes valeurs de pH dans la solution de précurseur et la quantité de précurseur de Fe ont également été discutés.

Dans la section 3.1, la porosité et la performance ORR des catalyseurs Fe-N-C préparés avec différents précurseurs de Fe, y compris le chlorure de fer ($Fe(III)Cl_3$), le nitrate de fer ($Fe(III)(NO_3)_3$), le sel de Mohr ($(NH_4)_2Fe(II)(SO_4)_2$) et la phtalocyanine de fer (II) (Fe(II)Pc), ont été comparées. Les catalyseurs préparés à pH=8 avec $FeCl_3$ et $Fe(NO_3)_3$ (Fe^{3+}) présentent la meilleure activité électrochimique à 0,8 V à la fois dans la configuration RDE et PEMFC, légèrement plus élevée que pour $(NH_4)_2Fe(SO_4)_2$ (Fe^{2+}) en raison à leur excellente solubilité dans la solution de précurseur conduisant à un faible rendement de nanoparticules riches en Fe et à une porosité similaire. Les états d'oxydation de Fe et des contre-ions montrent peu d'effet sur les performances catalytiques finales si le précurseur de Fe est soluble dans l'eau. La phtalocyanine insoluble (FePc, Fe^{2+}) ne semble pas être un bon choix à pH=8 car elle conduit à une faible porosité de l'aérogel de carbone. La faible teneur en Fe dans le catalyseur préparé avec FePc a mis en évidence que le précurseur de Fe insoluble ne peut pas être bien dispersé dans la solution de précurseur, conduisant ainsi à un rendement plus élevé de nanoparticules riches en Fe, qui sont majoritairement éliminées par le lavage à l'acide. La structure Fe-N_4 préexistante dans le précurseur FePc ne peut pas augmenter la densité de sites actifs dans le catalyseur final car cette structure est décomposée au cours de la pyrolyse, avant d'atteindre la température qui crée les sites actifs.

Dans la section 3.2, l'impact d'un faible pH de polycondensation avec un catalyseur FePc a été étudié. Cette recherche vise à augmenter la porosité du catalyseur préparé avec FePc car une concentration plus faible en Na_2CO_3 facilite un volume mésoporeux plus élevé. Les résultats sur FePc avec pH=6 indiquent que la réduction du pH (c'est-à-dire la réduction de la teneur en base en solution) est un moyen efficace d'obtenir un catalyseur avec un volume de mésopores plus élevé. Bien qu'il ne montre qu'une légère amélioration de l'activité électrochimique par rapport à un catalyseur réalisé à pH=8, une grande amélioration des propriétés de transport de matière est observée. Il est à noter que cette modification de pH n'est possible que pour le précurseur de fer FePc car l'ajustement du pH est obligatoire pour les autres précurseurs à base de sel de fer pour dissoudre la précipitation, phénomène préjudiciable à la formation d'un gel tridimensionnel.

Dans les sections 3.3 et 3.4, la modification des précurseurs de Fe, y compris l'introduction d'additifs sous forme de ligand et l'augmentation de la quantité de précurseur de Fe ont été étudiées. Le ligand EDTA augmente la solubilité du précurseur de Fe mais entraîne une perte de Fe lors de l'étape d'échange de solvant. En conséquence, tous les catalyseurs préparés avec un ligand EDTA présentent des teneurs en Fe ultra faibles. La phénentroline (Phen) génère des précipitations insolubles dans la solution mixte de départ, ce qui conduit à une texture différente par rapport au catalyseur sans ligand. Par contre, une teneur élevée en Fe peut être obtenue avec le catalyseur Phen sans aucune nanoparticule observable, indiquant une teneur élevée en sites actifs. Cependant, le faible volume des micropores limite l'amélioration de l'activité

électrochimique. En conclusion, en raison de l'environnement chimique compliqué de la solution mixte de départ, les additifs sous forme de ligands présentent peu d'amélioration de l'activité électrochimique des catalyseurs. Le point crucial parmi ces catalyseurs est que leur activité est étroitement liée à leur teneur en Fe, en particulier la teneur en Fe de surface caractérisée à partir de l'analyse XPS. L'étude menée sur des catalyseurs à base de FePc avec des supports carbonés contenant ou pas de la mélamine dans la solution de départ, indique que la simple augmentation de la quantité de précurseur de Fe ne conduit qu'à des nanoparticules non désirées dans le catalyseur final et plus largement dans les catalyseurs sans mélamine. La structure de coordination préexistante dans FePc présente peu d'influence sur la formation des centres actifs car les macrocycles Fe-N_4 contenus dans le précurseur FePc sont décomposés lors de l'étape de pyrolyse.

Fe is the center of Fe-N_4 active sites in the carbonaceous catalyst. The nature of Fe in the precursor solution plays a crucial role during the formation of the Fe-N_4 structure, thus deeply affecting the activity of catalysts. The factors showing impacts on the dispersion of ferrous and ferric ions in the precursor solution should be concerned, including oxide states of Fe, the counter ion of Fe salts, and the ligands attached. In this chapter, catalysts were synthesized from different iron precursors and nitrogenous ligand additives to find the relationship between the Fe precursor and the ORR performance of catalysts. In addition, the impacts of different pH values in the precursor solution and quantity of Fe precursor were also discussed.

3.1 Impact of different iron precursors

The impact of different Fe precursors will be discussed in this section. Fe precursors with different oxide states or counter ions were selected: iron chloride (Fe(III)Cl_3), iron nitrate (Fe(III)$(NO_3)_3$), Mohr's salt ($(NH_4)_2Fe(II)(SO_4)_2$) and iron (II) phthalocyanine (Fe(II)Pc). Other synthesis conditions were kept constant: the theoretical iron content was 1 wt.%, the mole ratio of resorcinol (R)/melamine (M) was 2/1, and the pH value of polymerization was adjusted to 8 after the addition of Fe precursors. The phenomena during the synthesis, morphologies of carbon aerogel, and electrochemical performance of catalysts were investigated.

3.1.1 Synthesis of catalysts

$FeCl_3$ precursor is a benchmark Fe(III) precursor, which has been used in the previous research of our group[186,187]. $Fe(NO_3)_3$ is another widely applied Fe(III) precursor for preparing Fe-N-C catalysts[196,197]. It is also soluble in water but possesses a different counter ion with $FeCl_3$, which might affect the polymerization process in the precursor solution. The oxide state of Fe is interesting to be investigated because of the considerable difference in solubility between Fe^{3+} and Fe^{2+} at high pH values in the solution. According to the solubility product constant (K_{sp}) of $Fe(OH)_3$ 2.79×10^{-39} and $Fe(OH)_2$ 4.87×10^{-17}, the saturated solubility of Fe^{3+} and Fe^{2+} are 2.79×10^{-21} mol L^{-1} and 4.87×10^{-5} mol L^{-1} at pH=8, respectively[198]. The formation of hydroxide precipitation probably affects the dispersion of Fe in the hydrogel. $(NH_4)_2Fe(SO_4)_2$ was selected as the Fe(II) precursor for its ability to resist oxidation in solution[199]. The precursor FePc is quite special from the other precursors for its preexisting Fe-N_4 structure, which is in favor of synthesizing catalysts with high ORR activity[136].

The phenomena during the preparation of precursor solution with $FeCl_3$ have been described in section 2.1.1. Similar phenomena were observed with $Fe(NO_3)_3$ precursor: red rust precipitation was generated when $Fe(NO_3)_3$ was added and then dissolved after adjusting pH to 8. As for the $(NH_4)_2Fe(SO_4)_2$, dark green precipitation formed initially, then quickly turned to rust red when NaOH solution was added, and finally disappeared at pH=8. Since the FePc is insoluble in water, the precipitation won't form. In this case, the pH adjustment of the mixture solution isn't necessary (but done in order to keep all the synthesis with the same comparable pH), which may lead to different porosity of carbon aerogel. This will be further discussed in section 3.1.2.

The total mass loss was calculated according to the two pyrolysis steps, as shown in **Table 3.1**. The first pyrolysis at 800 ℃ under N_2 flow, also called the carbonization step, transformed the organic aerogel into a relatively pure carbon structure by removing most of the oxide, nitrogen, and hydrogen groups[200]. In this step, the mass loss of all the aerogels prepared with

different iron precursors was around 55%. No significant changes were found because the decomposition of counter ions in the iron precursors was negligible compared to the loss quantity of the organic part. The second thermal treatment at 950 ℃ under N_2/NH_3 flow, which is the activation step, led to different mass loss range from 40% to 50% due to the different etching degree of the carbon aerogels.

The iron contents obtained from ICP-MS of all catalysts are listed in **Table 3.1**. The catalyst prepared with $Fe(NO_3)_3$ precursor presents a slightly higher Fe content than the theoretical value (1 wt.%), whereas that of others is lower. The difference in Fe content between catalysts is more than the variation of total mass loss, indicating a portion of Fe was removed by the acid washing process, such as Fe-rich nanoparticles. Since the $Fe-N_4$ active sites were considered to be resistant to acid washing and preserved in the final catalyst[186], the Fe precursor leading to high Fe content indicates a low yield of Fe-rich nanoparticles. The possible reason is the ferric ions of two precursors ($Fe(NO_3)_3$ and $FeCl_3$) can be better dispersed in the aerogel. Therefore, the Fe atoms are less agglomerated during the pyrolysis. On the contrary, the catalysts prepared with $(NH_4)_2Fe(SO_4)_2$ and FePc precursors possess lower Fe content than the catalyst with Fe(III) precursors, indicating higher yields of Fe-rich nanoparticles of Fe(II) precursors.

Table 3.1 Physicochemical characterization of the catalysts with different Fe precursors.

Fe Precursor	Total mass loss wt.%	ICP Fe		BET surface ($m^2\ g^{-1}$)	Vtotal ($cm^3\ g^{-1}$)	Vmicro ($cm^3\ g^{-1}$)	Vmeso ($cm^3\ g^{-1}$)
		wt.%	at.%				
$FeCl_3$	78	0.85	0.18	1596	2.20	0.44	1.67
FePc	78	0.75	0.16	1318	0.94	0.44	0.44
$Fe(NO_3)_3$	75	1.13	0.24	1498	1.62	0.42	1.09
$(NH_4)_2Fe(SO_4)_2$	81	0.70	0.15	1665	1.92	0.46	1.34

3.1.2 Texture and structure of catalysts

The SEM images displayed in **Figure 3.1**a-d provide a basic view of the morphology of catalysts. According to the figures, the pore size distribution is quite different depending on the solubility of Fe precursors. The catalysts prepared with Fe salts ($FeCl_3$, $Fe(NO_3)_3$, and $(NH_4)_2Fe(SO_4)_2$) show similar porosity on the surface of particles, where the mesopores can be observed clearly. However, the particle surface of the catalyst prepared with FePc seems more compact. The specific surface area and the pore size distribution of the catalysts were then further investigated by the nitrogen adsorption method. **Figure 3.1**e shows the isotherm curves at -196 ℃ of the catalysts, and **Figure 3.1**f gives the curves of pore size distribution, analyzed by using the 2D-NLDFT-Heterogenerous surface calculation method. The results are listed in **Table 3.1**, which confirms the observation under SEM. In the case of pH = 8 and R/M=2/1, the catalyst with insoluble FePc as iron precursor displays the lowest specific surface area and mesopore volume, which differs from those prepared with soluble Fe salts of similar texture. Besides, the mesopore size peak of the FePc catalyst in **Figure 3.1**f is around 5 nm, which is smaller than that of the Fe salts catalysts (around 7 nm). The solubility of iron precursors seems to be determinant for allowing an adequate development of the mesopore structure but exhibits little impact on micropore volume. According to the model of gelation progress proposed by Al-Muhtaseb *et al.*[200,201], the condensation step is realized by the interconnection of prepolymer particles. Therefore, a small condensation unit will reduce the pore size of the hydrogel. The insoluble FePc particles at the micron level can disturb and increase the condensation nucleus to accelerate the interconnection between the prepolymer particles, which limits the growth of condensation units and leads to small mesopore size. On the contrary, the carbon aerogels

prepared with soluble iron salts could be coordinated by the amino group of melamine to slow down the interconnection between the polymer particles, which promotes the growth of condensation units and, consequently, a higher porosity. The soluble iron salts, including $FeCl_3$, $Fe(NO_3)_3$, and $(NH_4)_2Fe(SO_4)_2$, give similar mesopore volume in the final catalysts, indicating different oxide states of iron or counter ions do not significantly affect the polycondensation step.

The distribution of micropores is mainly related to the two different thermal treatments. The micropores are produced by the pyrolysis of the organic aerogel and increased in quantity by the anisotropic NH_3 etching of the carbon matrix[153,194]. The micropore sizes are around 0.75 nm for all catalysts, which perfectly corresponds to the size of the Fe-N_4 macro-cycle proposed by Dodelet *et al.*[88] The micropore volumes of all catalysts are almost identical due to the same heat treatment conditions.

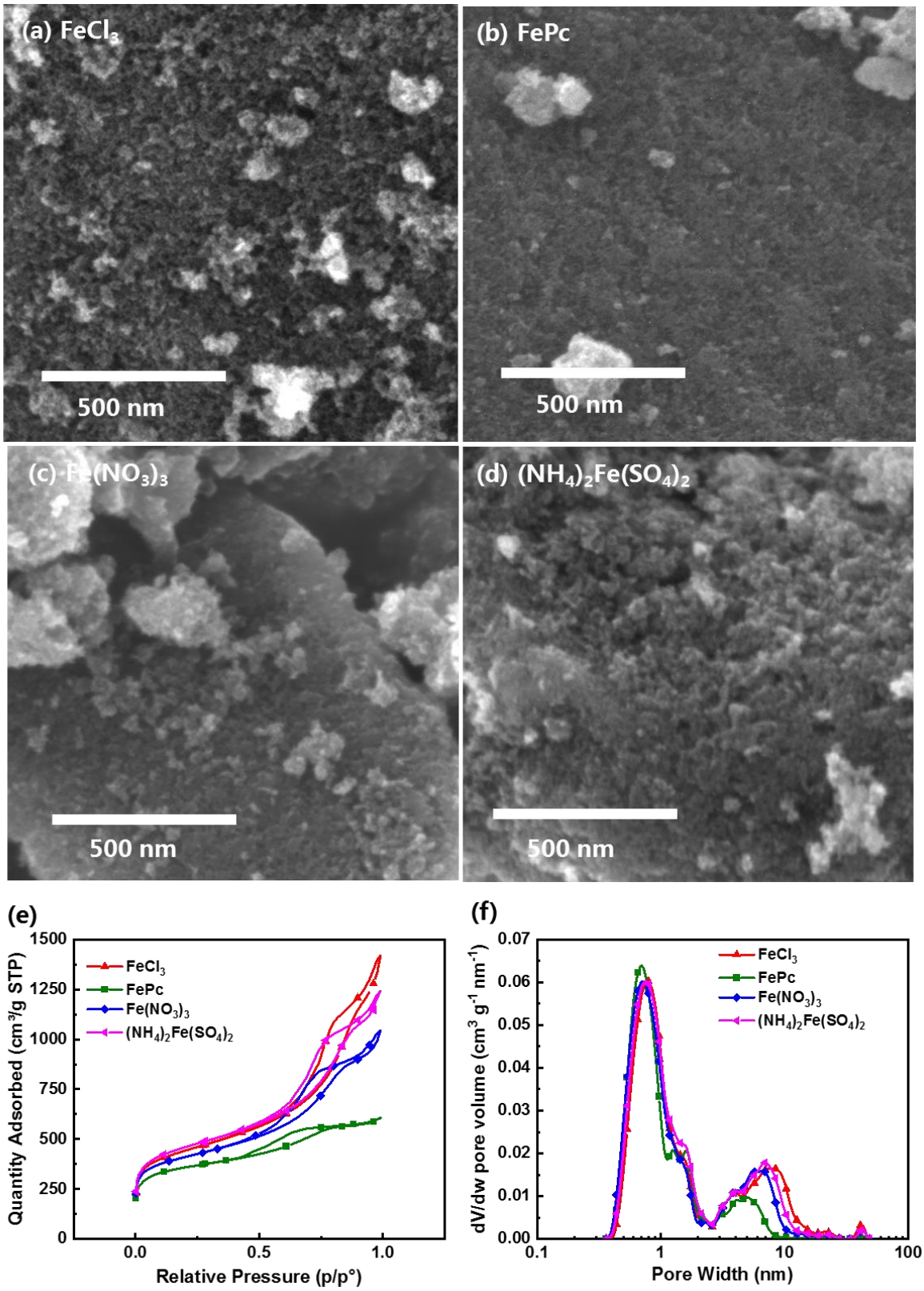

Figure 3.1 **(a)-(d)** SEM and **(e)** N_2 adsorption isotherms at -196 ℃ of the catalysts prepared with different iron precursors; **(f)** pore size distribution plots obtained by using the 2D-NLDFT-Heterogenerous Surface method.

The existence of iron nanoparticles in catalysts was determined by transmission electron microscope (TEM), as shown in **Figure 3.2**a-d. None of the nanoparticles are observed in the images, indicating that all unexpected Fe species can be removed by acid washing. Besides, the carbon substrates are almost amorphous, indicating the aerogel structure can be conserved after heat treatments. The powder X-ray diffraction (PXRD) patterns shown in **Figure 3.2**e confirm the TEM observation. No significant diffraction peak can be indexed to Fe-contained species in all catalysts. The large bump at around 2θ=26 ° and small bump at 2θ=45 ° correspond to the low crystallization carbon, which is observed under TEM. Three weak peaks at 2θ=26.4 °, 34.3 °, and 54.6 ° can be found in some catalysts, but they cannot be assigned to any Fe-contained species.

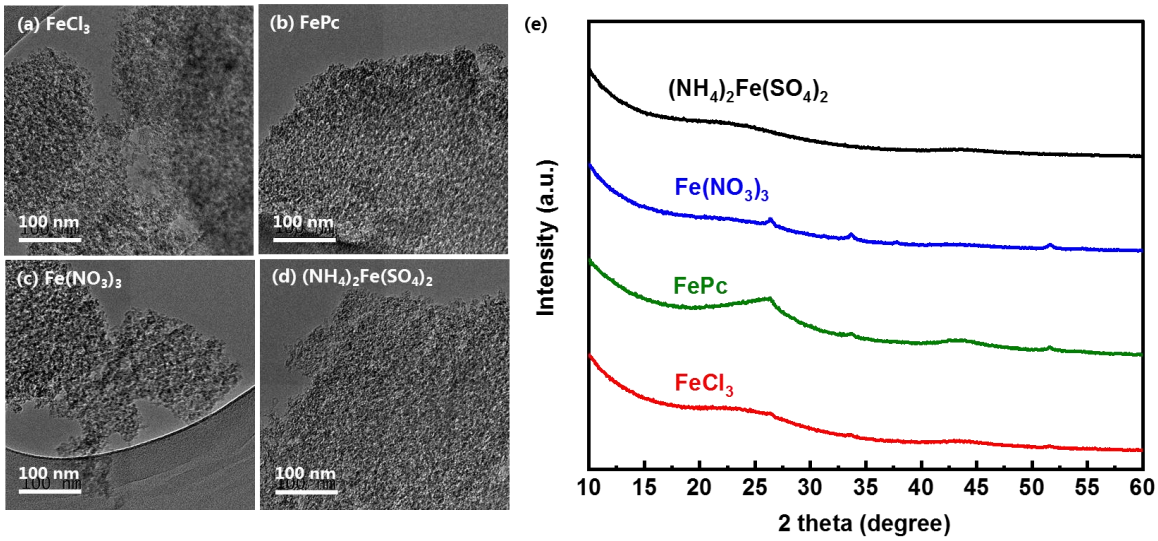

Figure 3.2 **(a)-(d)** TEM images and **(e)** normalized XRD patterns of catalysts prepared from different Fe precursor.

3.1.3 Chemical composition of catalysts

In order to understand the influence of the ion precursor on the activity of the catalysts, it is crucial to investigate the chemical environment on their surface because the active sites exposed on the surface contribute the most to the ORR process. X-ray photoelectron spectroscopy (XPS) studies were performed on the catalysts before electrochemical tests. The analysis is unable to be carried out on the catalysts after electrochemical tests because the quantity on the rotating disk electrode is far from filling up the sample holder of XPS. Besides, the ionomer added in ink can change the element composition as well. The element composition was obtained according to the method in annex A.2.5 and listed in **Table 3.2**. The main substrate C contributes most in the surface component (more than 90 at.%) as expected. All catalysts exhibit a significant amount of N (around 3 at.%), which is the most interesting because it's one of the main elements of active sites. Trace of Fe can also be identified, and the values are close to that of ICP-MS. In general, the XPS is considered to be a surface characterization technology and, ICP-MS presents the global element content. The similar Fe content from the two methods implies a uniform distribution of Fe on the surface and the in bulk of particles. It should also be kept in mind that the measurements made with XPS on Fe are obtained within the detection limits of the equipment and on porous granular materials.

Table 3.2 Surface chemical composition of catalysts prepared with different Fe precursor and deconvolution of their N 1s spectra.

Fe Precursor	C at.%	O at.%	Fe at.%	N at.%	Nitrile at.%	Pyridinic at.%	Fe-Nx at.%	Pyrrolic at.%	Quaternary at.%	Graphitic at.%
					398.0 eV	398.8 eV	399.9 eV	400.9 eV	402.0 eV	403.3 eV
$FeCl_3$	93.69	2.89	0.22	3.21	0.84	0.52	0.52	0.78	0.38	0.18
Fe(II)Pc	93.01	3.78	0.22	3.04	0.87	0.42	0.55	0.72	0.33	0.15
$Fe(NO_3)_3$	95.50	1.62	0.22	2.67	0.63	0.43	0.37	0.70	0.38	0.16
$(NH_4)_2Fe(SO_4)_2$	95.37	1.38	0.18	3.08	0.85	0.50	0.43	0.82	0.35	0.13

In order to figure out the chemical environment of Fe, the deconvolution of XPS spectra was supposed to be conducted for the spectra of N and Fe. However, because the Fe content is close to the detection limit of XPS, the spectra of Fe are too noisy to be analyzed. **Figure 3.3**b gives an example of the Fe 2p spectrum of the catalyst prepared with $FeCl_3$. Only the double peaks of the split Fe 2p spectrum at binding energies (BEs) of 711.1 and 724.3 eV can be identified, which reveals the existence of trivalent iron[202]. Besides, the binding energies are also close to the value of the Fe-N bond identified by Wang *et al.*[203] As an alternative option, the N 1s spectrum is taken into consideration since the states of nitrogen directly relate to the formation of Fe-N_x centers. The deconvolution was followed with the method of Atanassov *et al.*[99] For consistency among all spectra of catalysts, the full width at half-maximum (FWHM) of fitting peaks was constrained between 1.2-1.4 eV as described in annex A.2.5. **Figure 3.3**a shows an example of N 1s spectrum fitted with six peaks. The peak at the lowest BE of 398.0 eV comes from either imine or cyano groups. The peak at 398.8 eV is accepted to be pyridinic N with one electron contributed to the π system, and the pyrrolic N with two π electrons is present at 400.9 eV. These two nitrogen species are most important because they can coordinate with Fe to form active sites. The peaks that appeared at 402.0 eV and 403.3 eV were attributed to quaternary and graphitic nitrogen, respectively. In addition, according to the different test conditions and properties of samples, different deconvolution methods could be used. For example, some research didn't take nitrile species into consideration, thus the BE of pyridinic N moving to 398.3 eV[99,204]. In our analysis, if the peak of nitrile was eliminated, the FWHM of pyrrolic and Fe-N_x fitting peaks should be enlarged to 1.5 eV to get an acceptable residual. Therefore, it is better to conserve the nitrile peak to maintain the consistency of analysis results. When a fixed width of 1.2 eV was used during peak decomposition, another peak at 399.9 eV had to be included in the fit. This peak was confirmed to be the superposition peak of Fe-N_x species by Atanassov's group with density functional theory calculations of binding energy shifts for Fe-N-C graphene-based materials[99,204,205].

The content of different N species obtained from the deconvolution of XPS plots for all catalysts is listed in **Table 3.2**. A significant peak of Fe-N_x at 399.9 eV can be assigned for all catalysts, and the quantity varies with different Fe precursors. The catalysts with $FeCl_3$ and FePc possess higher Fe-N_x content than the others, even though their Fe contents from XPS are similar. One possible reason could be the attenuation lengths of Fe 2p, and N 1s photoelectrons are remarkably different. The atomic percent of nitrogen detected comes from 10 to 15 nm of the top surface of the sample, while the iron is only detected from the top 2-4 nm of the surface[206]. Therefore, the peak at 399.9 eV assigned from the XPS spectrum could be considered as identification of the existence of Fe-N_x active sites. However, for the quantitative study of active site content, more direct characterization of Fe, such as Mossbauer spectroscopy, should be employed. On the other hand, pyridinic and pyrrolic nitrogens also play a crucial role in improving electrochemical activity. As reported in the papers, the graphene enriched with

pyrrolic N or the carbon nano-tubes with high pyridinic N displayed better catalytic activity than the carbon supports without N dopant[207,208]. The catalyst with $(NH_4)_2Fe(SO_4)_2$ precursor presents high content of pyridinic and pyrrolic N, which is also possible to present high activity.

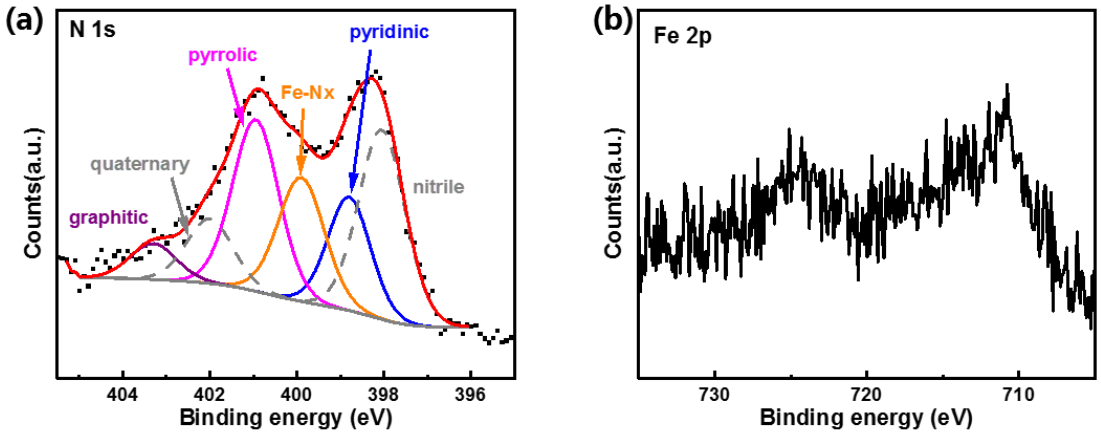

Figure 3.3 **(a)** N 1s and **(b)** Fe 2p XPS spectra of the catalyst prepared with $FeCl_3$ precursor.

3.1.4 Electrochemical characterization of catalysts

The activity of catalysts to ORR was evaluated in a three-electrode setup as presented in section 2.3.1, where electrochemical measurements were performed using a rotating disk electrode. The Fe precursor will be selected for further improvement according to the electrochemical activity. The CV curves in N_2 saturated electrolyte and the polarization curves in O_2 saturated electrolyte at a rotating speed of 1600 rpm of all catalysts are shown in **Figure 3.4**a and b, respectively. The electrolyte is 0.05 mol L^{-1} H_2SO_4, and the scanning rate is 10 mV s^{-1}. The current density values at 0.8 V *vs.* RHE are also listed in **Table 3.3**. These values were extracted from the ORR polarization curves after correction of the Ohmic drop and subtracting the background current measured in N_2 saturated electrolyte, which is accepted to identify the ORR activity[209]. The catalysts prepared with $FeCl_3$ and $Fe(NO_3)_3$ display the highest mass activity at 0.8 V (around 2.0 A g^{-1}) among all, whereas the two others are slightly lower. This result is consistent with the sequence of their Fe content obtained from ICP-MS. The micropore volume exhibits little relationship with activity tendency, where the micropore volumes are almost the same (around 0.44 cm^3 g^{-1}) for all catalysts with mass activities ranging from 1.72 and 2.05 A g^{-1}. Theoretically, the surface composition is more important to determine the activity because the electrochemical reactions mainly conduct on the interface between catalysts and the electrolyte. However, due to the large uncertainty of Fe content from the XPS method, the variation of Fe content cannot be clearly presented. As a result, the ICP-MS results are used instead of the Fe atoms are uniformly distributed on the surface and in bulk. On the contrary, the atomic percentage of Fe-N_x doesn't show an obvious relationship with the electrochemical activities of catalysts. The possible reason is the different attenuation lengths between Fe and N mentioned before that all Fe-N_x nitrogen is not on the surface of the particle to present their electrochemical activity[206]. Besides, the peak at around 400 eV can also be attributed to amine, which also confuses the accurate active site content[99]. The impact of N will be further discussed in chapter 4, where the role of different N species will be clarified.

The limiting current density (obtained from **Figure 3.4**b at 0.2 V) is increased with mesopore volume. Two catalysts ($FeCl_3$ and $(NH_4)_2Fe(SO_4)_2$) which have the largest mesopore volume,

display the highest limiting current density, whereas the FePc catalyst with the lowest mesopore volume shows the lowest current. The same tendency has also been discovered by Carmelo *et al.*, that the carbon support does not influence the onset potential of the catalysts, but its contribution becomes relevant when the rate-determining step is the mass transfer, *i.e.*, at high overpotential[196]. The large mesopore volume contributes to a large electrochemically available surface area for a similar micropore volume, which is consistent with the increase in cyclic voltammetry area in **Figure 3.4**a.

Table 3.3 Electrochemical characteristics of the catalysts with different Fe precursors in RDE setup.

Fe Precursor	$MA_{0.8}$ A g^{-1}	$MA_{0.8}$ after 500 cycles A g^{-1}	Loss ratio	Tafel slope mV dec^{-1}
$FeCl_3$	2.04	1.08	-47%	52
FePc	1.72	1.34	-22%	66
$Fe(NO_3)_3$	2.05	1.24	-40%	60
$(NH_4)_2Fe(SO_4)_2$	1.89	0.84	-56%	55

Figure 3.4c shows the Tafel plots derived from the polarization curves. It seems the Tafel slopes are closely related to the mesopore volume of catalysts, where the catalyst with the lowest mesopore volume (prepared with FePc) corresponds to the highest value (66 mV dec^{-1}) while the catalyst with the highest mesopore volume (prepared with $FeCl_3$) corresponds to the lowest value (52 mV dec^{-1}). With respect to reaction micro-kinetics, lower Tafel slope values correspond to faster reaction rates at the electrode surface[210] because Tafel plots represent the measured current density increase as a function of the overpotential. Therefore, the relationship between the Tafel slope and mesopore volume supports that a high mesopore volume of Fe-N-C aerogel catalyst can facilitate the mass transport in the RDE setup. It should be mentioned that Tafel slopes for all catalysts are essentially the same in acid media (~ 60 mV dec^{-1}), suggesting that the rate-determining step of the ORR mechanism is the same. According to the simulated behavior of the Tafel relation for the oxygen reduction reaction by assuming different elementary steps as the rate-determining step, the Tafel slope around 60 mV dec^{-1} may be associated with the reaction mechanism in which the rate-determining step is affected by the proton-coupled electron transfer (PCET) instead of a single electron transfer reaction, and thus the reaction rate depends on the applied potential[210]. In this case, the different ORR activities are mainly related to the different catalyst-specific active areas for the catalysts prepared with different iron precursors in acid media, thus giving us the activity tendency that coincides with the variation of CV area[211].

The durability tests were carried out for all catalysts with 500 cycles between 0.6-1.0 V in N_2 saturated electrolyte. The activity was then determined by linear scan voltammetry in O_2 saturated electrolyte. The results are shown in **Figure 3.4**d, and the loss ratios are listed in **Table 3.3**. The catalysts display different degrees of degradation after the test. The catalyst prepared with FePc shows the best durability (22% loss of activity after 500 cycles of CV), whereas the others are similar (~ 45% loss). The degradation of Fe-N-C catalysts in an acidic medium is caused by the etching of the carbon matrix and dissolution of Fe, which leads to the loss of active sites[184]. During the CV cycles, the degradation of the Fe-N_4 active sites and of the supporting carbon aerogel occurs in parallel at high potential. Less current density means electrochemical oxidation on carbon, thus less etching. Therefore, it becomes reasonable that the best durability is obtained by FePc, which possesses the lowest electrochemical available area.

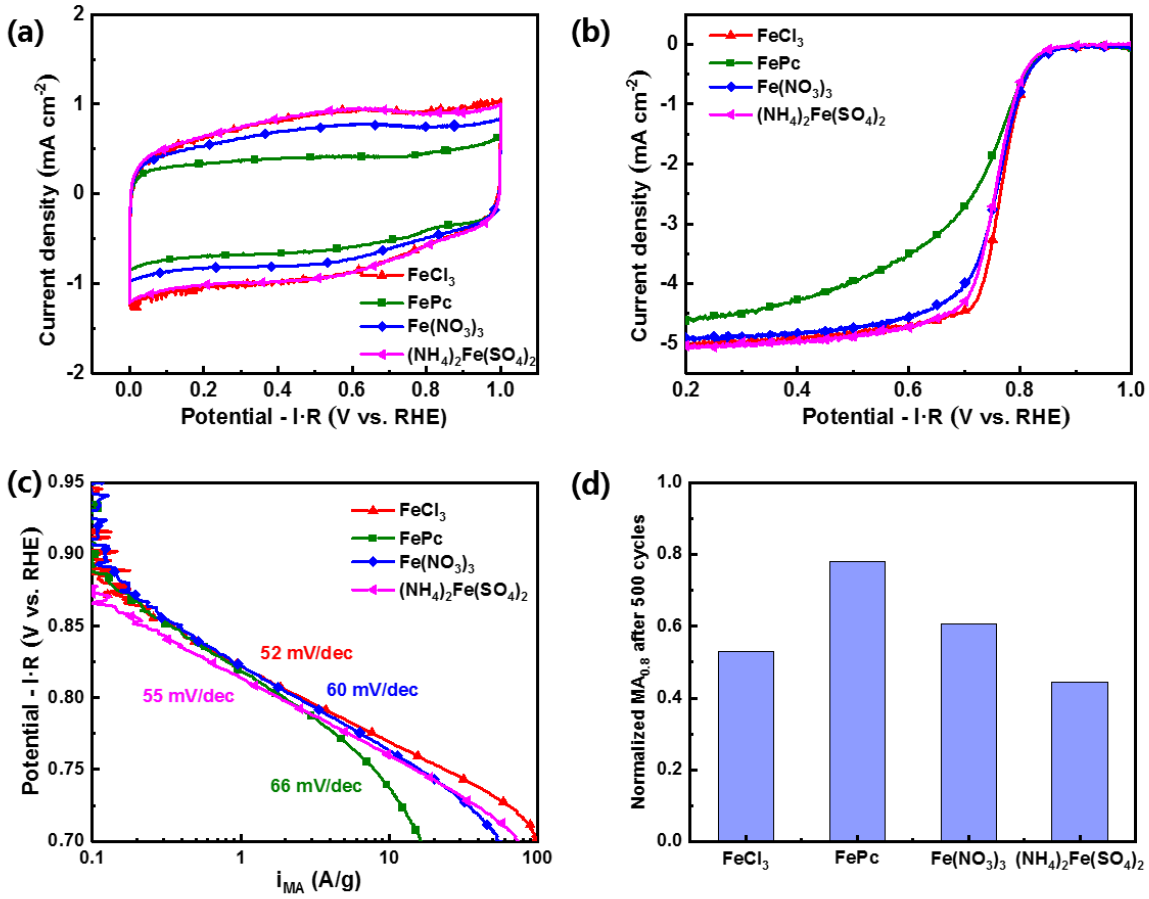

Figure 3.4 **(a)** Cyclic voltammetry curves in N_2-saturated 0.05 mol L^{-1} H_2SO_4; **(b)** Oxygen reduction reaction polarization curves in O_2-saturated 0.05 mol L^{-1} H_2SO_4; **(c)** Tafel plots derived from polarization curves of the catalysts prepared with different iron precursors; and **(d)** normalized current after 500 CV cycles between 0.6-1.0 V in N_2 saturated electrolyte.

Their activities were further investigated in a 5 cm^2 single cell of PEMFC in the conditions described in section 2.3.2, with a scanning rate of 1 mV s^{-1}. As the polarization curves shown in **Figure 3.5**, catalysts show the same trend with RDE tests at 0.8 V. The catalyst prepared with $Fe(NO_3)_3$ displays the best performance, and the catalyst prepared with FePc is less active than the others in the single cell. Besides pure charge-transfer limitations, other characteristics, such as the accessibility of O_2 and proton to the active sites, limit the performance in the single cell. The enlarged difference between catalysts prepared with FePc and the others is probably due to its poor mesopore volume restricting the contact between O_2 and active sites. For all the catalysts, it is important to notice that the polarization curves do not collapse at high current densities (j > 0.5 A cm^{-2}_{geo}), demonstrating the excellent mass transport properties of carbon aerogel catalysts.

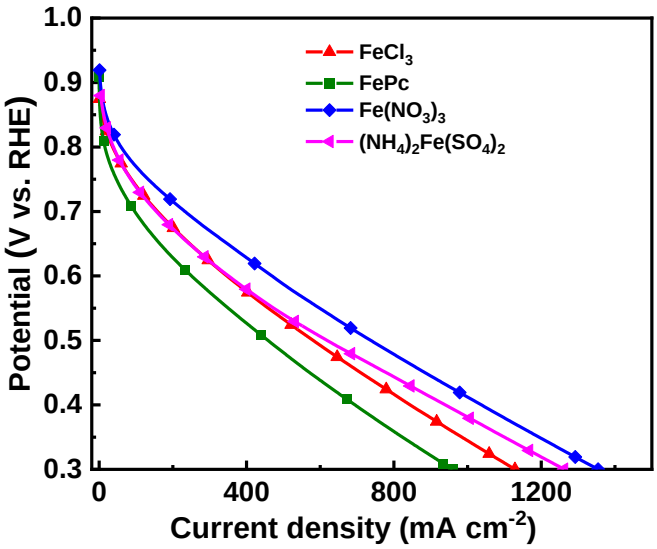

Figure 3.5 Polarization curves of the catalysts prepared with different iron precursors in the single cell. The measurements were performed with T_{cell} = 80 ℃, 100 % RH, *P*cathode = *P*anode = 2 bar_{abs}, the H_2, and O_2 flow rates were 150 mL min^{-1} while the air flow rate was 480 mL min^{-1}.

3.1.5 Conclusion

The impact of four different iron precursors on the porosity and the electrochemical activity of Fe-N-C aerogel catalysts were investigated. The iron salts with different oxide states and counter ions can affect the solubility and the reactivity of iron ions in precursor solution, thus changing the polycondensation reaction during the gelation step, which leads to different porosity and electrochemical activity. We found that the catalysts prepared with Fe(III), $FeCl_3$, and $Fe(NO_3)_3$ display the best electrochemical activity, which corresponds to high mesopore volume and electrochemical available area. The catalyst prepared with $Fe(NO_3)_3$ exhibits the higher current density at 0.8 V both in the RDE setup and single cell associated with the higher Fe content. The catalyst prepared with $(NH_4)_2Fe(SO_4)_2$ possesses an electrochemical activity and porosity slightly lower than those of $FeCl_3$. The insoluble FePc seems not to be a good choice since it leads to a carbon aerogel with a low porosity at pH=8 which seems to limit the performance of the catalyst. However, its insolubility also made the modification of pH possible, which will be discussed in section 3.2

3.2 Impact of different pH with Fe phthalocyanine precursor

The impacts of pH value on porosity and activity will be detailed in this part. The research was focused on the precursor FePc, which is insoluble in water and therefore does not cause the coagulation of prepolymers in the mixed solution. According to the mechanism of gelation, the carbon aerogels prepared at pH=6 show larger development of porosity than their corresponding counterparts obtained at pH 8[212]. Therefore, low pH is in favor of the development of mesoporous structure and obtaining the catalyst with better mass transport properties. To reach pH=6, no extra NaOH was added into the mixture solution A+B, which

corresponded to a ratio of (R+M)/C ~ 100 for pH=6, whereas the value for pH=8 is 10. The phenomena during the synthesis, the morphology of carbon aerogel, and electrochemical performance were investigated.

3.2.1 Synthesis of catalysts

The FePc is a promising iron precursor to prepare the Fe-N-C catalyst with high electrochemical activity due to its pre-existing Fe-N_4 structure[213]. However, rapid polycondensation of the RMF gel happened due to a high amount of the catalyst in the solution at a high pH value. Numerous nuclei form a gel with small construction units. On the contrary, by using a low concentration of catalyst, the particles have enough time to grow up, and the pores between the particles become larger by geometrical effect[200]. As expected, the catalyst prepared in pH=6 took 1 h to form the gel, which is much longer than that in pH=8. The other phenomena during synthesis were essentially the same, as well as the total mass loss after the two pyrolyses (N_2 and N_2/NH_3).

3.2.2 Texture and structure of catalysts

SEM images displayed in **Figure 3.6**a and b provide a basic view of the porosity of catalysts prepared at different pH. It can be seen clearly that catalyst prepared in pH=6 displays a more open porous structure. The BET area and pore size distribution obtained from nitrogen adsorption analysis demonstrate this observation, as shown in **Figure 3.6**c and d. The pore volumes are listed in **Table 3.4**. Catalyst in pH=6 exhibits a larger mesopore size centered around 10 nm (5 nm for pH=8) and mesopore volume (three times higher than in pH=8), indicating that a low pH value favors the development of the mesoporous structure. The Fe content obtained from ICP-MS of the catalyst in pH=6 is lower than the pH=8, which should be further confirmed with the XPS method.

Table 3.4 Physicochemical characteristics of the catalysts in different pH with FePc precursor.

pH	Total mass loss wt.%	ICP Fe		BET surface ($m^2\ g^{-1}$)	Vtotal ($cm^3\ g^{-1}$)	Vmicro ($cm^3\ g^{-1}$)	Vmeso ($cm^3\ g^{-1}$)
		wt.%	at.%				
6	77	0.61	0.13	1424	2.00	0.43	1.51
8	78	0.75	0.16	1318	0.94	0.44	0.44

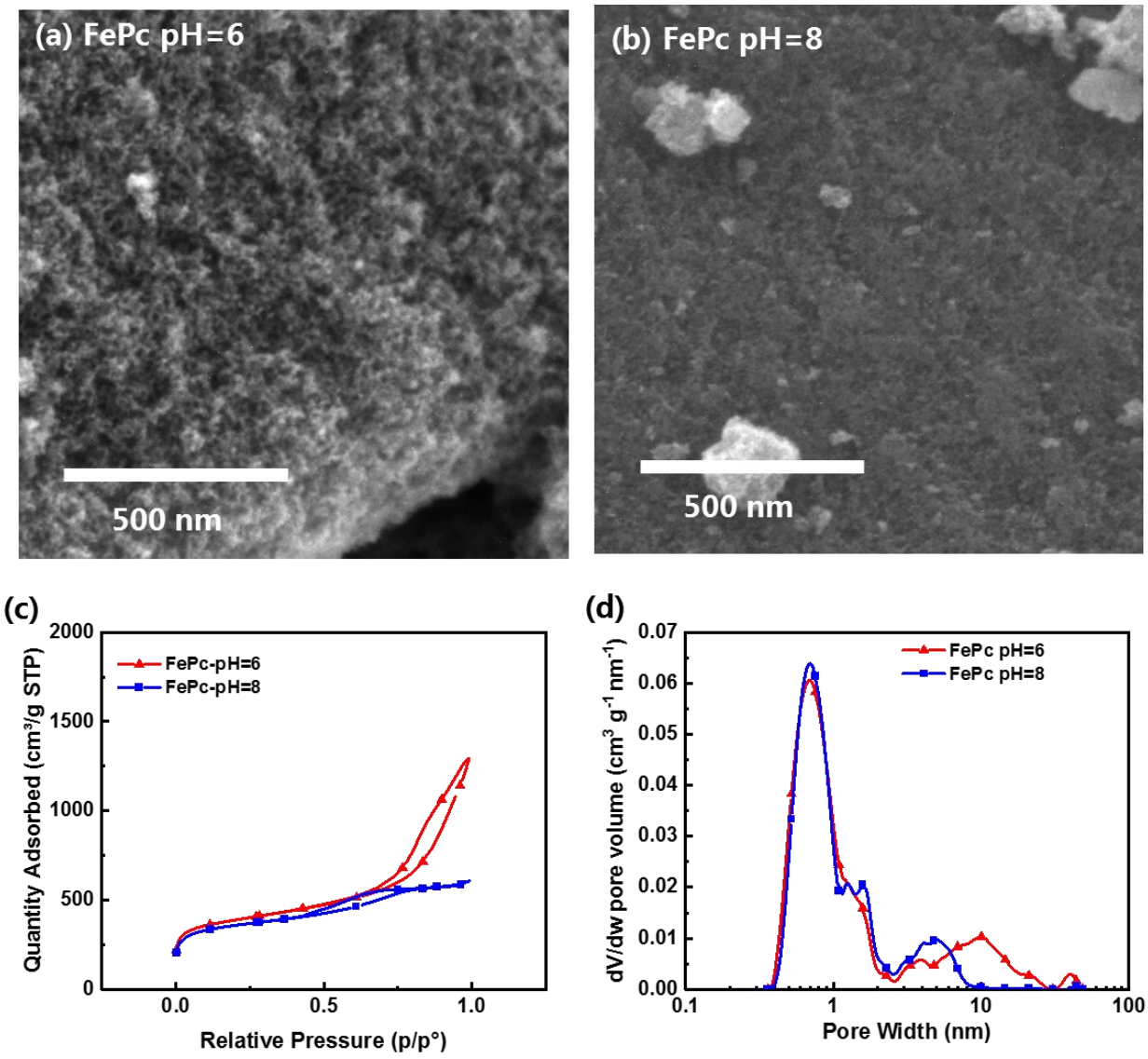

Figure 3.6 **(a), (b)** SEM images of the catalysts prepared in different pH with FePc precursor; **(c)** N_2 adsorption isotherms at -196 ℃ and **(d)** pore size distribution plots obtained by using the 2D-NLDFT-Heterogenerous Surface method.

TEM images are shown in **Figure 3.7**a and b. No Fe-rich nanoparticles are observed on the surface of the two catalysts. Their XRD patterns shown in **Figure 3.7**c confirm this result. For the catalyst prepared in pH=6, no significant diffraction peaks can be identified from the pattern. The bumps of the weakly crystallized carbon are similar to those of the catalyst prepared at pH=8, indicating a similar structure of carbon substrate at different pH values.

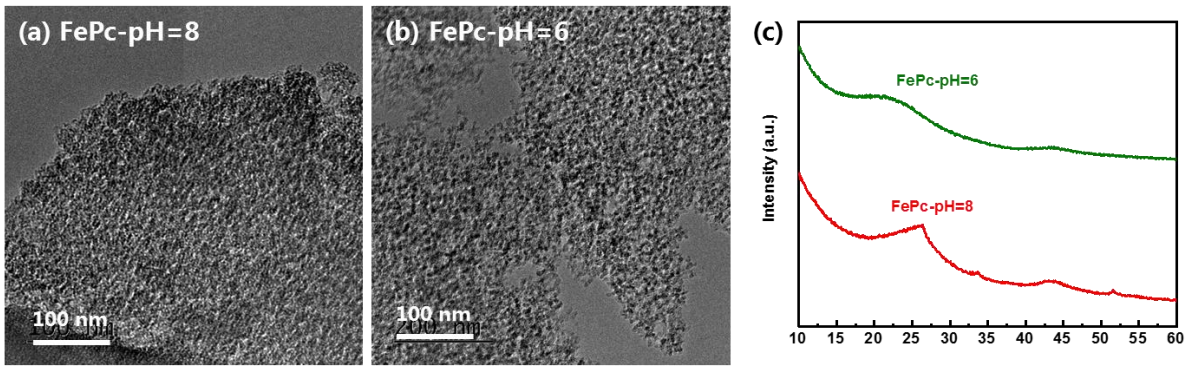

Figure 3.7 **(a), (b)** TEM images and **(c)** normalized XRD patterns of catalysts prepared in different pH with FePc precursor.

3.2.3 Chemical composition of catalysts

The XPS characterization was employed to obtain the chemical environment on the surface of catalysts. The results of elemental composition are listed in **Table 3.5**. The catalysts prepared in pH=6 and 8 possess different iron content on the surface and in bulk, which implies an uneven distribution of Fe. One possible reason for this phenomenon is that the catalyst with a larger mesopore volume is also deeply etched during NH_3 thermal treatment. Therefore, more active sites are exposed on the surface and detected by XPS. In addition, the nitrogen contents of the two catalysts are identical, which implies the limitation of the quantity of active sites and activity by the quantity of Fe. The deconvolution was conducted to figure out the composition of different N species, and the results were listed in **Table 3.5**, along with the results of pH=8 as a comparison. The Fe-N_x content of pH=6 decreased, whereas the other two active N species (pyridinic and pyrrolic N) contents slightly increase.

Table 3.5 Chemical composition of catalyst surface prepared in different pH values with FePc precursor and deconvolution of their N 1s spectra.

Fe Precursor	C at.%	O at.%	Fe at.%	N at.%	Nitrile at.%	Pyridinic at.%	Fe-Nx at.%	Pyrrolic at.%	Quaternary at.%	Graphitic at.%
					398.0 eV	398.8 eV	399.9 eV	400.9 eV	402.0 eV	403.3 eV
6	94.77	1.89	0.26	3.09	0.73	0.55	0.46	0.86	0.36	0.14
8	93.01	3.78	0.22	3.04	0.87	0.42	0.55	0.72	0.33	0.15

3.2.4 Electrochemical characterization of catalysts

The activity of the two catalysts towards ORR was evaluated in the RDE setup. The CV and polarization curves are shown in **Figure 3.8**a and b, respectively. Their current densities at 0.8 V are listed in **Table 3.6**. The catalyst prepared in pH=6 exhibits a larger electrochemical available area according to the CV curves, which is in accord with its larger specific surface area and mesopore volume. According to the results obtained with different Fe precursors, the quantity of Fe-N_x cannot be directly related to the activity. However, their mass activities at 0.8 V are almost the same, indicating that different pH conditions have little influence on the formation of active sites. This result is reasonable because FePc is insoluble in water, and the dispersion of the precursor is only decided by its initial particle size. The larger mesopore volume of pH=6 makes the reactants accessible to the active sites, thus giving a higher limited current. Therefore, both micro- and mesopore volumes are important to obtain catalysts with

high electrochemical activity. The Tafel slopes derived from the polarization curves, as shown in **Figure 3.8**c, are consistent with the trend of activity of samples, indicating a faster reaction rate is obtained with the catalyst prepared in pH=6. Besides, the durability tests in N_2 saturated electrolyte also give similar results, that about 20% loss of activity after 500 cycles.

Table 3.6 Electrochemical characteristics of the catalysts prepared in different pH with FePc precursor in RDE setup.

Fe Precursor	$MA_{0.8}$ A g^{-1}	$MA_{0.8}$ after 500 cycles A g^{-1}	Loss ratio	Tafel slope mV dec^{-1}
6	1.67	1.38	-17%	60
8	1.72	1.34	-22%	68

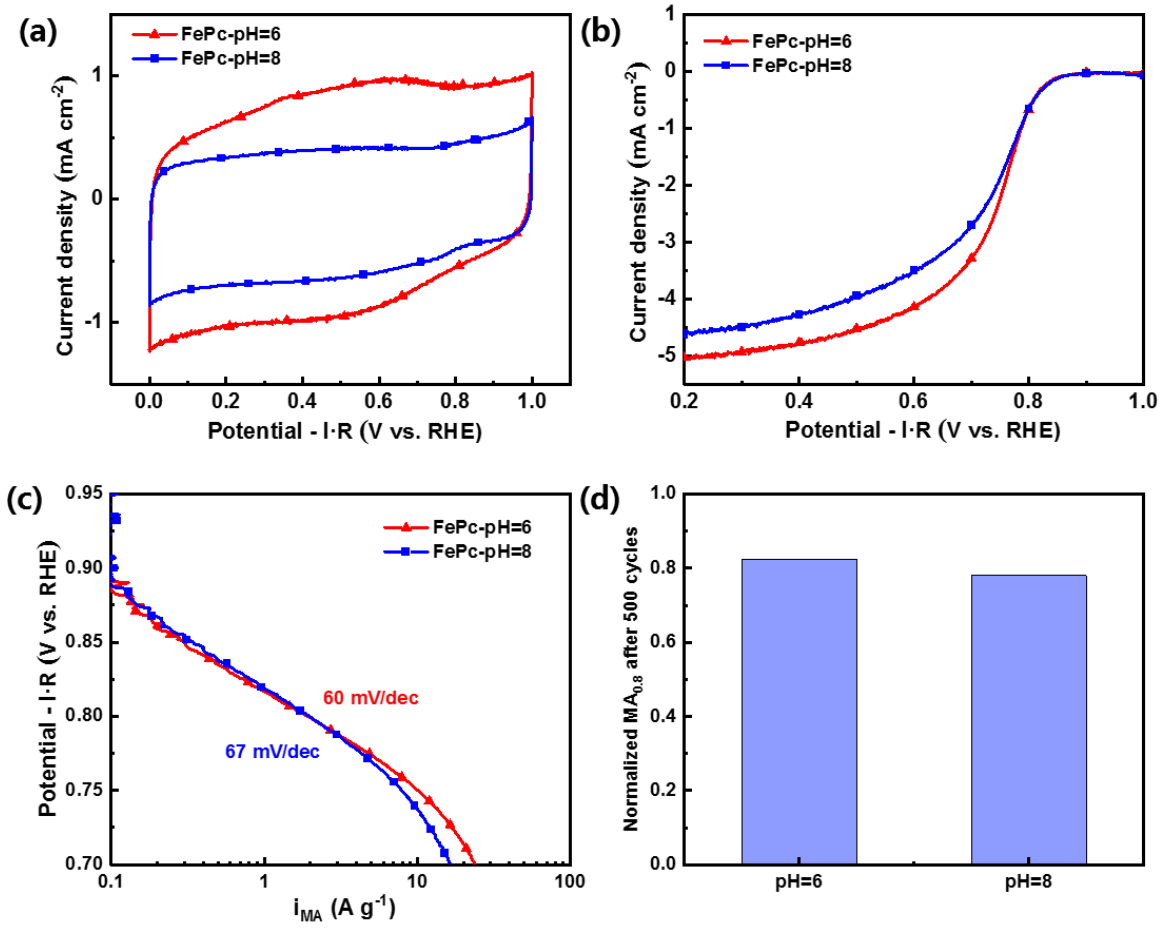

Figure 3.8 **(a)** Cyclic voltammetry curves in N_2 saturated 0.05 mol L^{-1} H_2SO_4; **(b)** Oxygen reduction reaction polarization curves; **(c)** Tafel plots derived from polarization curves of the catalysts prepared in different pH with FePc precursor; and **(d)** normalized current after 500 CV cycles between 0.6-1.0 V in N_2 saturated electrolyte.

Their activity in 5 cm^2 single cell of PEMFC was also investigated. The polarization curves are shown in **Figure 3.9**. Their activities at 0.8 V are similar, which is consistent with the results in the RDE setup. The activity of FePc-pH=6 shows more enhancement at higher overpotential due to a 3 times higher mesopore volume in pH=6 than pH=8.

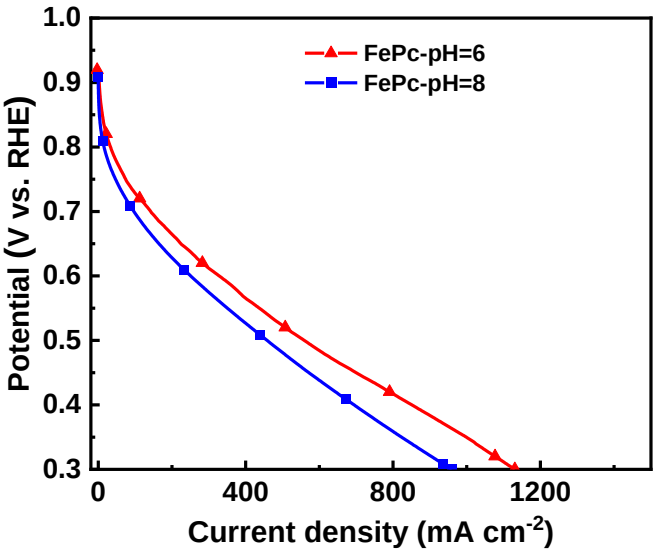

Figure 3.9 Polarization curves of the catalysts prepared in different pH with FePc precursor in the single cell. The measurements were performed with T_{cell} = 80 ℃, 100 % RH, *P*cathode = *P*anode = 2 bar_{abs}, the H_2, and O_2 flow rates were 150 mL min^{-1} while the air flow rate was 480 mL min^{-1}.

3.2.5 Conclusion

The results on FePc with pH=6 indicate that keeping the mixed solution in pH=6 (*i.e.*, reducing the base content in the solution) is an efficient way to get a catalyst with higher mesopore volume. Although it only shows a slight enhancement in electrochemical activity, a large improvement in mass transport properties is observed. It should be noted that this condition is only possible for the iron precursor FePc because adjusting pH is mandatory for other iron precursors to dissolve the precipitation, a phenomenon that is detrimental to the formation of a three-dimensional gel.

3.3 Impact of additive ligands

The impacts of ligand additives in the precursor solution were investigated. According to the literature, the iron precursors with preexisting Fe-N coordination (such as FePc and iron phenanthroline FePhen) could lead to Fe-N-C catalysts with better activity[214]. Besides, the introduced ligand can also improve the solubility of Fe ions in solution and modify the dispersion of Fe atoms in the carbon matrix. Two ligands containing N as the coordination site were selected: ethylenediaminetetraacetic (EDTA) and phenanthroline (Phen). EDTA is a classic chelating ligand that can coordinate with Fe ions at a molar ratio of 1:1 by forming two Fe-N bonds and four Fe-O bonds. The formation constants (K_f) of Fe(II)EDTA and Fe(III) EDTA are 2.0×10^{14} and 1.3×10^{25}, respectively[215]. The chelate with Fe(III) is more stable than Fe(II), which is expected to have better dispersion in the precursor solution. Vecchio *et al.* employed metals (Fe or Co) chelated with EDTA to synthesize M-N-C catalysts with improved activity and stability. The EDTA was used as a low-cost and bio-compound nitrogen precursor to encapsulate the metal center. In their results, the complex ion with high K_f tends to present the highest relative percentage of N-metal interaction[196].

$[FePhen_3]^{2+}$ has been widely used as an indicator in analytical chemistry due to its excellent stability and solubility in water. It is interesting because the formation constant of $[Fe(II)Phen_3]^{2+}$ is larger than $[Fe(III)Phen_3]^{3+}$, 10^{21}, and 10^{14}, respectively, which is contrary to most of the ligands[216]. Abundant Fe-N connections make Phen a promising ligand to prepare the catalysts with better electrochemical activity. Ziloto *et al.* synthesized Co-N-C with improved activity by introducing Phen into Co precursor[217]. Li *et al.* mixed iron acetate (FeAc) with Phen by ball milling method to get the precursor with Fe-N_6 coordination. The obtained catalyst also exhibited better electrochemical activity than the catalyst prepared without Phen[136]. Here, we synthesized the catalysts with two different ligands (EDTA and Phen) and two Fe precursors with different oxide states ($Fe(NO_3)_3$ and $(NH_4)_2Fe(SO_4)_2$), as shown in **Table 3.7**. Their impact during the synthesis on the morphology, the surface chemical composition, and the electrochemical performance were investigated.

3.3.1 Synthesis of catalysts

For preparing the complexes, the ligands and Fe precursor were mixed in 2 mL distilled water and heated at 70 ℃ for 10 min before being added to the resorcinol-melamine-formaldehyde solution. The EDTA can form a light-yellow solution with both Fe precursors, and the precipitation is generated when the precursor solutions have been mixed. After adjusting the pH value to 8 by adding around 3 mL of NaOH solution, the precipitation disappeared, and a maroon solution was obtained. Another noteworthy phenomenon was observed during the solvent exchange (between water and acetone for CO_2 supercritical drying), and the solvent exchanged became light yellow colored. The possible reason is that Fe complexes are more soluble in water than acetone, which may lead to the loss of Fe precursor. The Fe content obtained from ICP-MS demonstrated this negative effect of EDTA. As seen in **Table 3.7**, for both Fe precursors, the Fe contents of the catalysts prepared with EDTA ligand are significantly lower than the catalysts prepared without ligand. This result indicates that the soluble chelated Fe ions are hardly conducive to high Fe content in the catalysts due to the loss of iron during the solvent exchange. The best existing state of Fe in the mixed solution is well-dispersed colloid particles, which can be adsorbed on the skeleton of the hydrogel.

In the case of the Phen ligand, a dark red solution formed with both Fe salts and the orange-red precipitations were generated when complexes were introduced into the mixed solution. However, the precipitation cannot be dissolved by adjusting the pH value. Finally, the suspension took more than 1 hour to finish the gelation. The phenomena during solvent exchange were also different from catalysts prepared with EDTA ligand. The exchanged solvent was colorless, which meant that the $[Fe(II)Phen_3]^{2+}$ and $[Fe(III)Phen_3]^{3+}$ were conserved in the hydrogel. The difference between the two ligands can be attributed to their microstructure. The Phen ligand possesses a conjugation π-system to adsorb onto the organic matrix skeleton by π-π stacking interaction. Therefore, the complexes can be well attached to hydrogel to avoid the loss of Fe during the solvent exchange. The ICP-MS results also demonstrated that the catalysts prepared with Phen ligand have higher Fe content than the catalysts without ligand. However, since Phen led to quite different phenomena during the polycondensation step compared with EDTA, the morphology was supposed to be different from others.

3.3.2 Texture and structure of catalysts

Figure 3.10a and b show the SEM images of the catalysts prepared with the **$Fe(NO_3)_3$** precursor and different ligands alongside the catalyst without ligand as a comparison.

Interesting differences were noticed in the textural variation of the aerogels depending on the ligand additives. The catalysts prepared with ligands seem to have larger mesopore sizes than the catalyst without ligand. **Figure 3.10**d shows the nitrogen adsorption isotherms at -196 ℃ of the catalysts, alongside the pore sizes distribution in **Figure 3.10**e. The pore volumes of catalysts obtained by DFT analysis are listed in **Table 3.7**. It can be clearly seen that both catalysts prepared with ligand additive display larger mesopore volume than catalysts without ligand and centered at a larger mesopore size. However, this result should be attributed to different reasons for the two ligands according to their different phenomena observed during synthesis. A similar phenomenon was observed in the catalysts prepared with EDTA and without ligand. The maroon precipitation was generated when Fe precursor was introduced, and then it was dissolved after adjusting pH. On the basis of the polycondensation mechanism of RMF hydrogel, EDTA may increase the solubility of Fe ion, thus reducing the nuclei number in the mixed solution and leading to larger mesopore volume[218]. As for the catalyst prepared with Phen, since precipitation cannot be dissolved by adjusting pH, the final catalyst is more likely to be a stack of large particles instead of an integrated network of aerogel. The mesopore volume may be contributed by the space between these large particles.

In contrast to the variation of mesopore volume, the micropore volumes and BET surface were significantly decreased for the catalysts prepared with ligand, although the same heat treatment conditions were used (both in N_2 and N_2/NH_3). Since micropores are widely considered to be the containers of Fe-N_4 active sites, decreased micropore volume may lead to weak ORR activity.

Table 3.7 Physicochemical characterization of the catalysts prepared with $Fe(NO_3)_3$ or $(NH_4)_2Fe(SO_4)_2$ and different ligand additives.

Fe Precursor	Ligand	Total mass loss wt.%	ICP Fe		BET surface ($m^2\ g^{-1}$)	Vtotal ($cm^3\ g^{-1}$)	Vmicro ($cm^3\ g^{-1}$)	Vmeso ($cm^3\ g^{-1}$)
			wt.%	at.%				
$Fe(NO_3)_3$	EDTA	73	0.36	0.08	1263	2.59	0.33	2.22
	Phen	74	0.86	0.18	1226	2.62	0.34	2.23
	-	75	1.13	0.25	1498	1.62	0.42	1.09
$(NH_4)_2Fe(SO_4)_2$	EDTA	72	0.16	0.03	1274	1.63	0.37	1.21
	Phen	74	0.73	0.16	1455	2.32	0.43	1.83
	-	81	0.70	0.15	1665	1.92	0.46	1.34

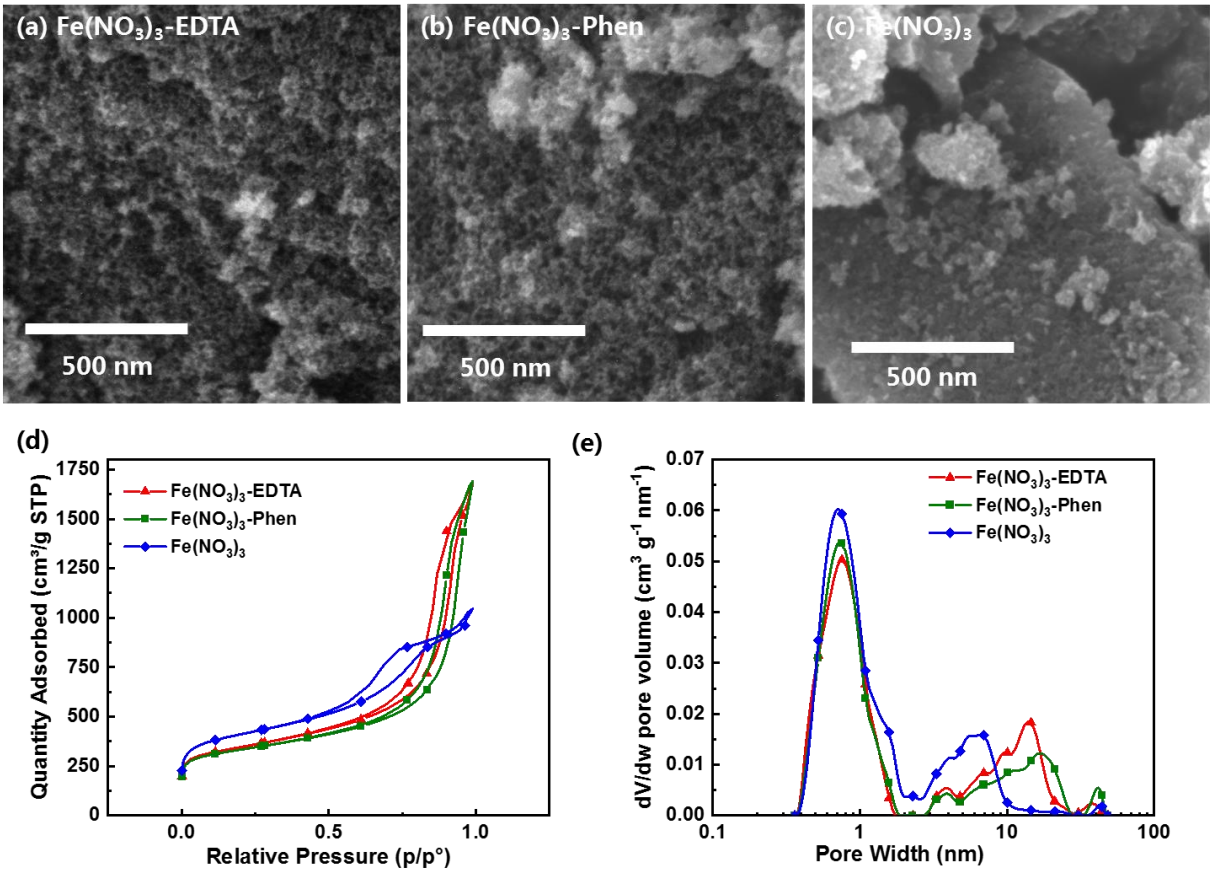

Figure 3.10 **(a), (b)** SEM images of the catalysts prepared with $Fe(NO_3)_3$ precursor and different ligand additives; **(c)** N_2 adsorption isotherms at -196 ℃ and **(d)** pore size distribution plots obtained by using the 2D-NLDFT-Heterogenerous Surface method.

The SEM images in **Figure 3.11**a-c give a general view of the porosity of the catalysts prepared with **$(NH_4)_2Fe(SO_4)_2$** precursor and different ligands alongside the catalyst without ligand as the comparison. The EDTA ligand leads to a similar morphology with the catalyst without ligand under SEM, whereas the Phen ligand changes the texture of aerogel due to undissolved precipitation in the mixed solution. Their nitrogen adsorption isotherms at -196 ℃ and distribution of pore sizes are shown in **Figure 3.11**d and e, respectively. The catalyst prepared with EDTA exhibits a similar mesopore volume to the catalyst without ligand (mesopore size around 6-10 nm), which may be attributed to the lower formation constant of Fe(II)EDTA complex than Fe(III)EDTA. Phen ligand leads to a larger mesopore size (peak at around 20 nm) and mesopore volume, which is similar to the results of $Fe(NO_3)_3$ precursor. SEM image **Figure 3.11**b exhibits its texture seems like a stack of large particles instead of a porous network. The micropore volume of catalysts prepared with the ligand is decreased, which is similar to the situation of $Fe(NO_3)_3$ precursor. This result implies a reduced ORR activity, which will be discussed later.

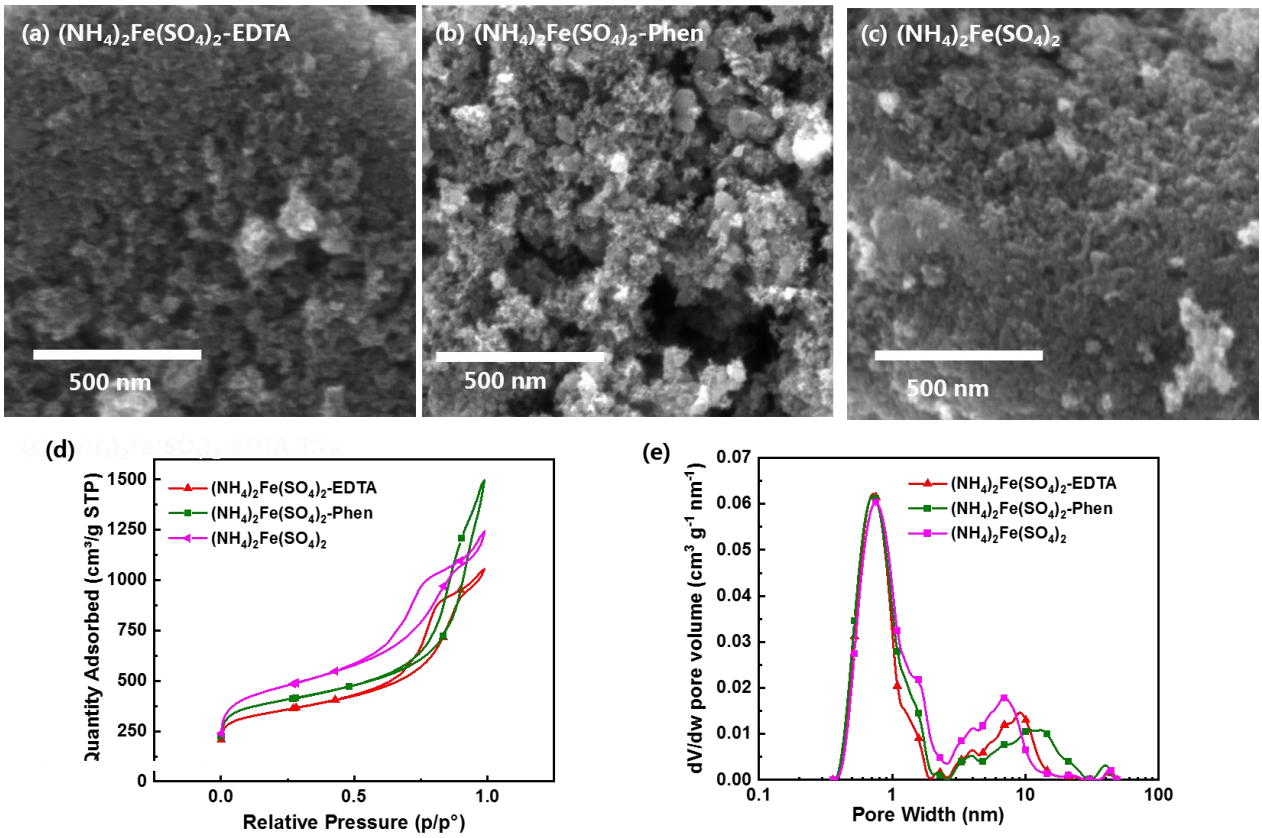

Figure 3.11 **(a)-(d)** SEM images of the catalysts prepared with $(NH_4)_2Fe(SO_4)_2$ precursor and different ligand additives; **(e)** N_2 adsorption isotherms at -196 ℃ and **(f)** pore size distribution plots obtained by using the 2D-NLDFT-Heterogenerous Surface method.

The TEM and XRD were employed to determine the existence of Fe nanoparticles. **Figure 3.12**a-c and **Figure 3.13**a-c summarize the TEM images for catalysts synthesized with ligand additives. As for the catalysts prepared without ligand, no Fe-rich nanoparticle can be observed under the view of TEM, indicating that Fe atoms are well dispersed in the carbon matrix. Besides, no significant peak of Fe-containing species can be identified from XRD patterns of catalysts, as shown in **Figure 3.12**d and **Figure 3.13**d, confirming the observation of TEM. As for the catalysts prepared with Phen ligand, the same peaks with at 2θ=26.4 °, 34.3 °, and 54.6 ° can be found, but they cannot be identified to any Fe-contained species.

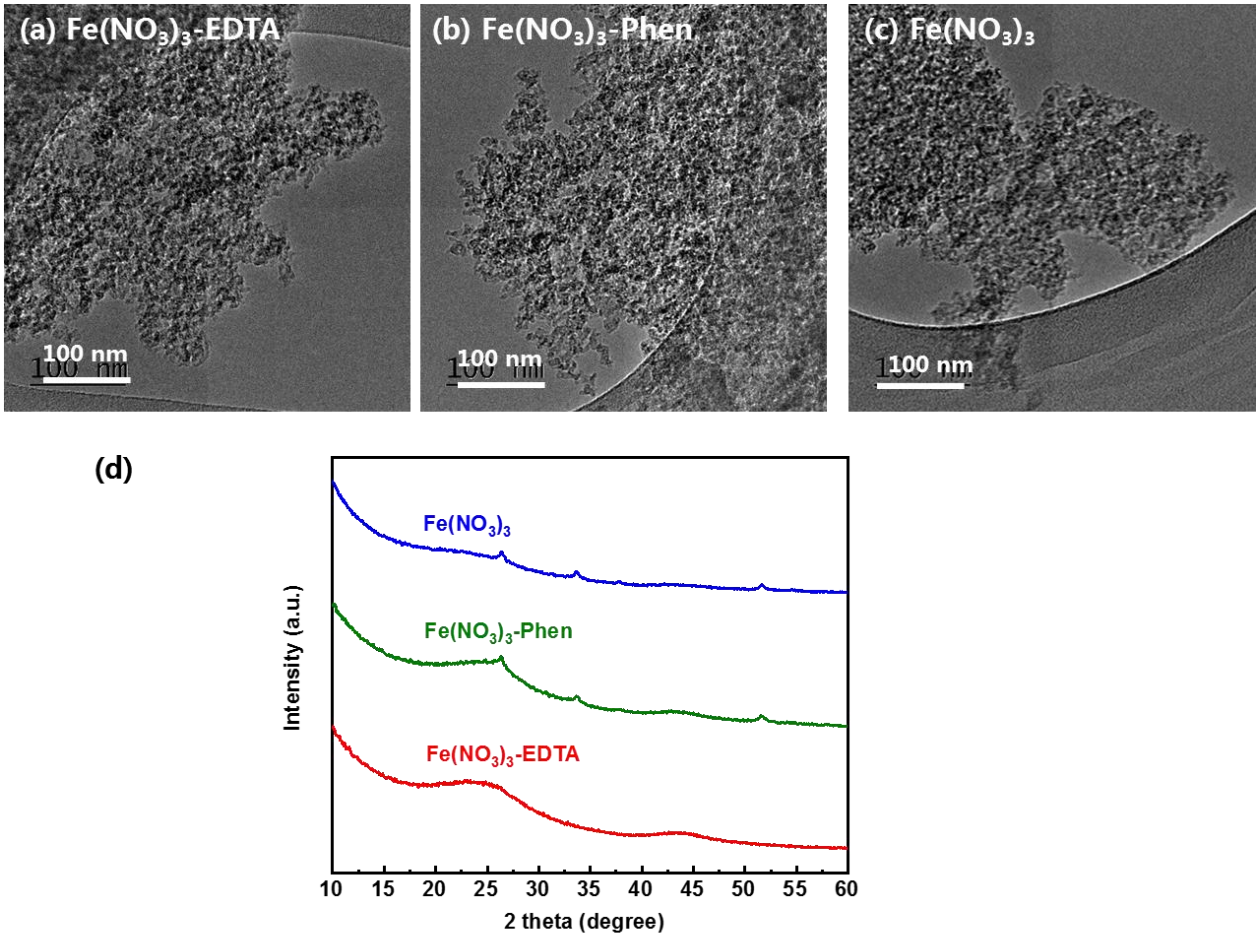

Figure 3.12 **(a)-(c)** TEM images and **(d)** normalized XRD patterns of catalysts prepared with $Fe(NO_3)_3$ and different ligand additives.

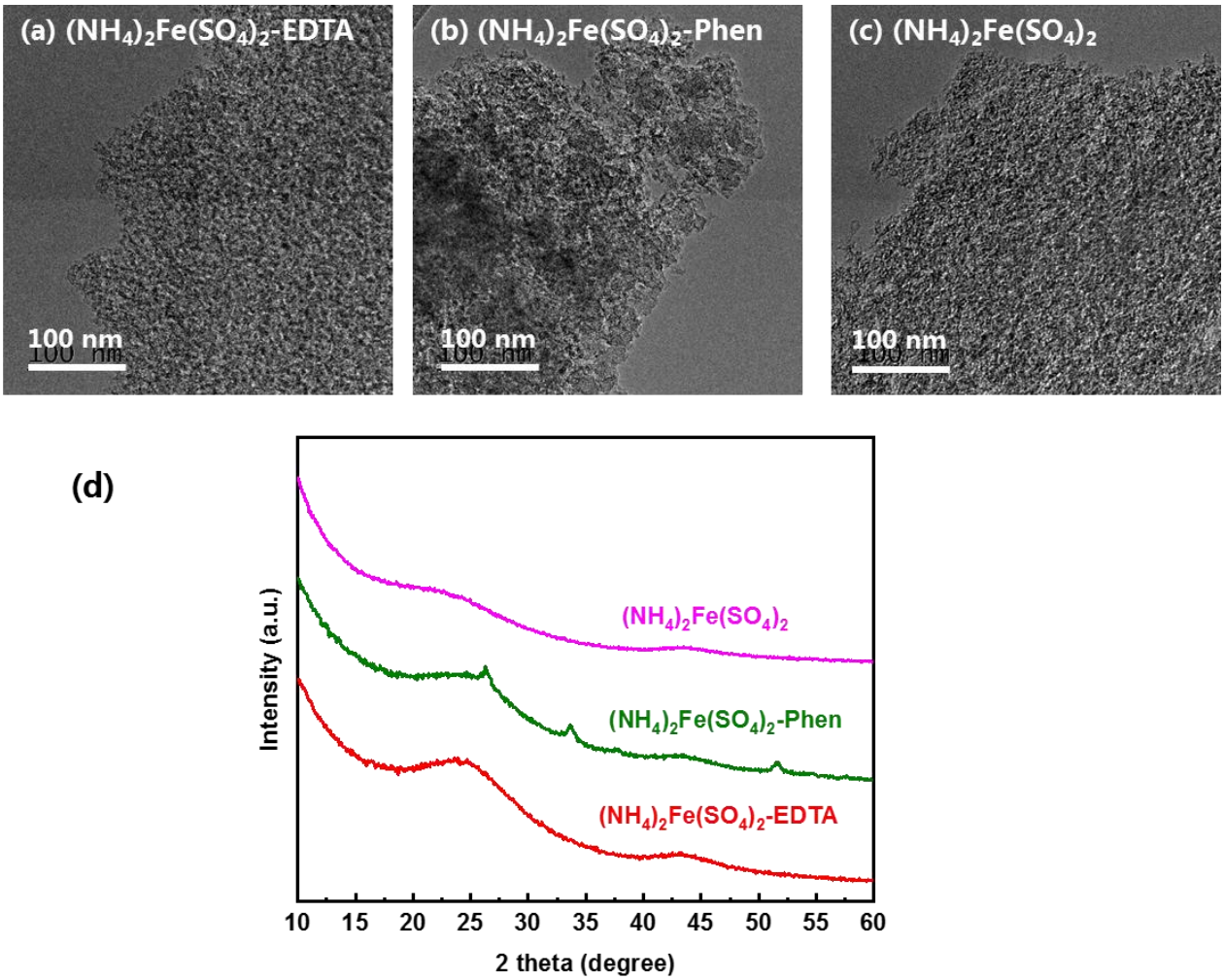

Figure 3.13 **(a)-(c)** TEM images and **(d)** normalized XRD patterns of catalysts prepared with $(NH_4)_2Fe(SO_4)_2$ and different ligand additives.

3.3.3 Chemical composition of catalysts

The surface chemical environment of catalysts was investigated by XPS. The results of catalysts prepared with $Fe(NO_3)_3$ and ligands are listed in **Table 3.8**, along with the catalyst without ligand as a comparison. The Fe contents of the catalyst prepared with the ligand are close to the results of ICP-MS, indicating a uniform distribution of Fe in bulk and on the surface.

The details on the chemical bonding states of the surface N-groups are provided by deconvolution of N 1s spectra with the method of Atanassov *et al.*, as discussed in section 3.1[99]. The atomic percentages of different N groups on the surface are listed in **Table 3.8**. The peak at 399.9 eV can be assigned for all catalysts, whereas, for the catalyst with EDTA ligand, the atomic percentage ratio of Fe-N_x/Fe is larger than the maximum coordination number of Fe (Fe-N_4). As we mentioned before, this peak may be attributed to other N species, such as amines [206]. Therefore, this peak cannot be simply attributed to N coordinated with Fe due to the different synthesis methods of catalysts. The pyridinic N of the EDTA catalyst is decreased compared to a non-ligand catalyst, but that of the Phen catalyst slightly increases. The pyrrolic N contents for all catalysts are almost identical. Their impacts on electrochemical activity will be discussed in the next section.

Table 3.8 Chemical composition of catalyst surface prepared with $Fe(NO_3)_3$ and different ligand additives and deconvolution of their N 1s spectra.

Ligand	C at.%	O at.%	Fe at.%	N at.%	Nitrile at.%	Pyridinic at.%	Fe-Nx at.%	Pyrrolic at.%	Quaternary at.%	Graphitic at.%
					398.0 eV	398.8 eV	399.9 eV	400.9 eV	402.0 eV	403.3 eV
EDTA	94.07	3.19	0.11	2.63	0.73	0.35	0.48	0.66	0.31	0.10
Phen	92.66	4.40	0.23	2.72	0.66	0.47	0.57	0.67	0.24	0.10
-	95.50	1.62	0.22	2.67	0.63	0.43	0.37	0.70	0.38	0.16

The XPS analysis results of catalysts prepared with $(NH_4)_2Fe(SO_4)_2$ and different ligand additives are listed in **Table 3.9**, as well as the deconvolution results of N 1s spectra. Similar to the Fe content obtained from ICP-MS, XPS analysis also reveals low Fe content on the surface. The Fe atoms are uniformly dispersed in the carbon aerogel, but the low Fe content of the catalysts prepared with EDTA ligand suggests a low concentration of active sites. For the catalyst prepared with EDTA ligand, Fe-N_x content obtained from deconvolution of N 1s spectra is much higher than the maximum value (Fe-N_x/Fe > 4), which also proves that this peak may be attributed to other N species. The N content of catalyst prepared with Phen ligand is decreased compared to non-ligand catalyst. The impacts on their activity will be discussed later.

Table 3.9 Chemical composition of catalyst surface prepared with $(NH_4)_2Fe(SO_4)_2$ and different ligand additives and deconvolution of their N 1s spectra.

Ligand	C at.%	O at.%	Fe at.%	N at.%	Nitrile at.%	Pyridinic at.%	Fe-Nx at.%	Pyrrolic at.%	Quaternary at.%	Graphitic at.%
					398.0 eV	398.8 eV	399.9 eV	400.9 eV	402.0 eV	403.3 eV
EDTA	93.92	2.72	0.06	3.30	0.95	0.45	0.51	0.80	0.40	0.19
Phen	93.20	3.85	0.20	2.76	0.74	0.40	0.45	0.66	0.36	0.15
-	95.37	1.38	0.18	3.08	0.85	0.50	0.43	0.82	0.35	0.13

3.3.4 Electrochemical characterization of catalysts

The impacts of ligand additives on the electrochemical activity of two series catalysts were evaluated in a three-electrode RDE setup. The CV and polarization curves of $Fe(NO_3)_3$–based catalysts are shown in **Figure 3.14**a and b, respectively. The curves of catalyst without ligand are also plotted as a comparison. The corresponding current density values at 0.8 V *vs.* RHE are listed in **Table 3.10**. The catalyst prepared without ligand displays the best electrochemical activity and the stability after 500 cycles in N_2 saturated electrolyte. The CV areas are correlated to the specific surface area of the catalysts of the samples, which shows that the surface is accessible to the electrolyte. The non-ligand catalyst shows the largest CV area, corresponding to its largest BET area. The catalysts prepared with ligand show a lower BET area (**Table 3.7**), thus presenting a lower CV area.

The mass activity at 0.8 V of catalysts increases with their Fe content, indicating an increased density of active sites. This result confirmed the guess before that low micropore volume of catalysts prepared with ligand show weak ORR activity. The limit current at 0.2 V of the catalysts prepared with the ligand is slightly higher than the non-ligand catalyst due to higher mesopore volume improving the mass transport property in the RDE setup. The Tafel slopes shown in **Figure 3.14**c are similar for all catalysts, indicating that they have the same ORR

mechanism. Therefore, ligand additives do not affect the properties of Fe-N_4 active sites. **Figure 3.14**d shows the normalized current density at 0.8 V after the durability test. The EDTA catalyst lost most of the activity because its ultra-low Fe loading and high mesopore volume made the demetallation effect more significant than the others.

Table 3.10 Electrochemical characteristics of the catalysts with $Fe(NO_3)_3$ or $(NH_4)_2Fe(SO_4)_2$ and different ligand additives in RDE setup.

Fe Precursor	Ligand	$MA_{0.8}$ A g^{-1}	$MA_{0.8}$ after 500 cycles A g^{-1}	Loss ratio	Tafel slope mV dec^{-1}
$Fe(NO_3)_3$	EDTA	0.80	0.27	-67%	67
	Phen	1.32	0.73	-48%	63
	-	2.05	1.24	-40%	60
$(NH_4)_2Fe(SO_4)_2$	EDTA	1.01	0.64	-39%	68
	Phen	1.74	1.08	-40%	63
	-	1.89	0.84	-56%	55

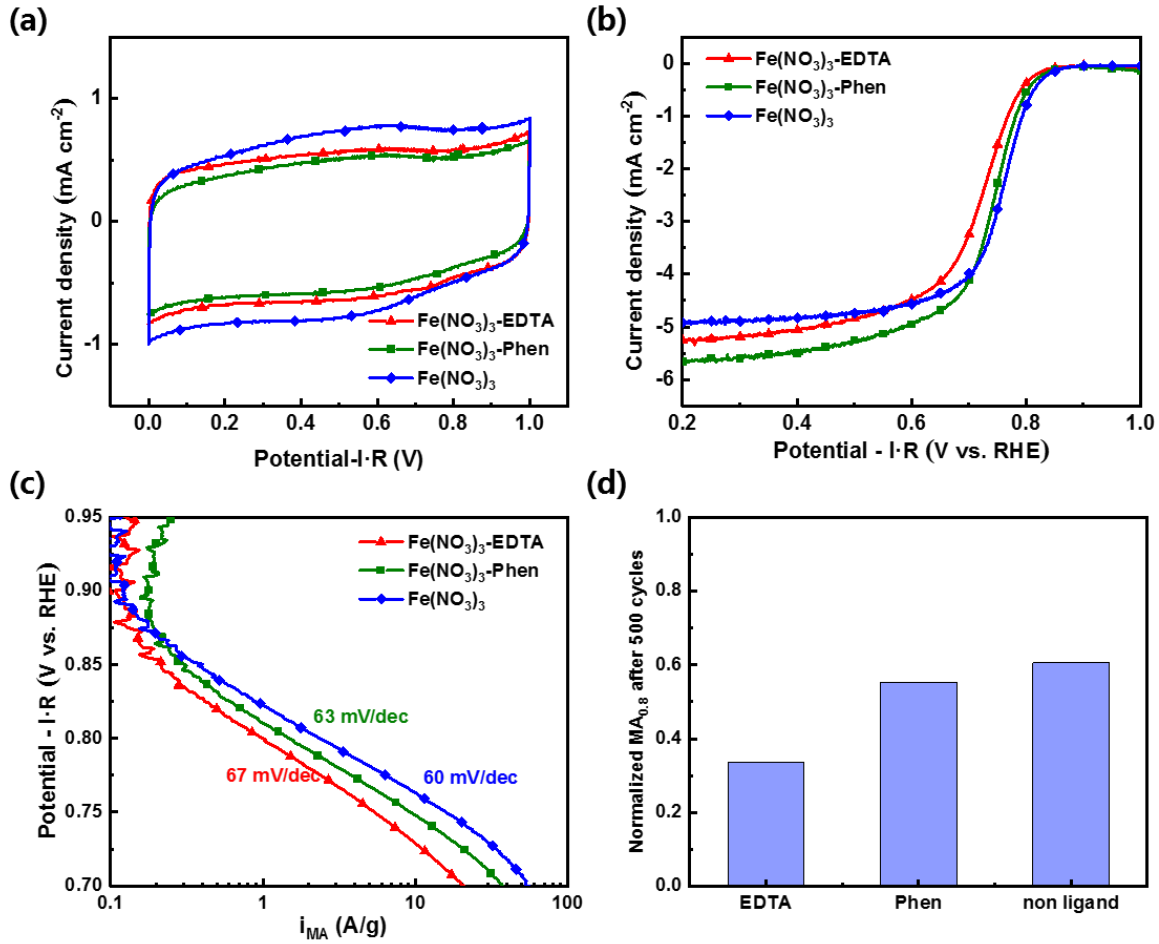

Figure 3.14 **(a)** Cyclic voltammetry curves in N_2 saturated 0.05 mol L^{-1} H_2SO_4; **(b)** Oxygen reduction reaction polarization curves; **(c)** Tafel plots derived from polarization curves of the catalysts prepared with $Fe(NO_3)_3$ and different ligand additives; and **(d)** normalized current after 500 CV cycles between 0.6-1.0 V in N_2 saturated electrolyte.

The same tendency can be found when $(NH_4)_2Fe(SO_4)_2$ is used as the Fe precursor. As the CV and polarization curves shown in **Figure 3.15**a and b, the catalyst prepared without ligand additive displays the best mass activity according to the current density at 0.8 V. The electrochemical available areas obtained from CV curves exhibit the same tendency with the electrochemical activity and Fe content of catalysts. EDTA leads to low Fe content and micropore volume in the final catalyst, thus weak ORR activity. Non-ligand and phen catalysts possess similar Fe content, thus presenting similar mass activity. Their Tafel slopes are shown in **Figure 3.15**c also indicate that all catalysts have the same ORR mechanism, which is not affected by different ligands or Fe precursors. **Figure 3.15**d shows that catalysts prepared with ligands exhibit slightly higher durability than that without ligand after 500 CV cycles, which is opposite to $Fe(NO_3)_3$ precursor.

It is interesting to remark on the different effects between the two ligands. The EDTA ligand leads to a decreased Fe content because the $[Fe(II)EDTA]^{2-}$ and $[Fe(III)EDTA]^{-}$ complexes can be removed during the solvent exchange step. On the contrary, phen shows much less effect on the Fe content than EDTA but significantly changes the morphology of aerogel under SEM. Comparing their different effects on electrochemical activity, the Fe content seems more critical than morphology, which is always proportional to the mass activity of catalysts regardless of the variation of mesopore volume. Besides, since the electrochemical reaction occurs on the interface between catalyst and electrolyte, the surface Fe content obtained from XPS should be a relatively accurate parameter to determine the activity. However, due to the high uncertainty of XPS analysis, the ICP-MS can be used if the Fe distribution is uniform. The XPS value becomes more important when the difference between ICP-MS and XPS cannot be ignored, *i.e.*, an uneven distribution of Fe occurs.

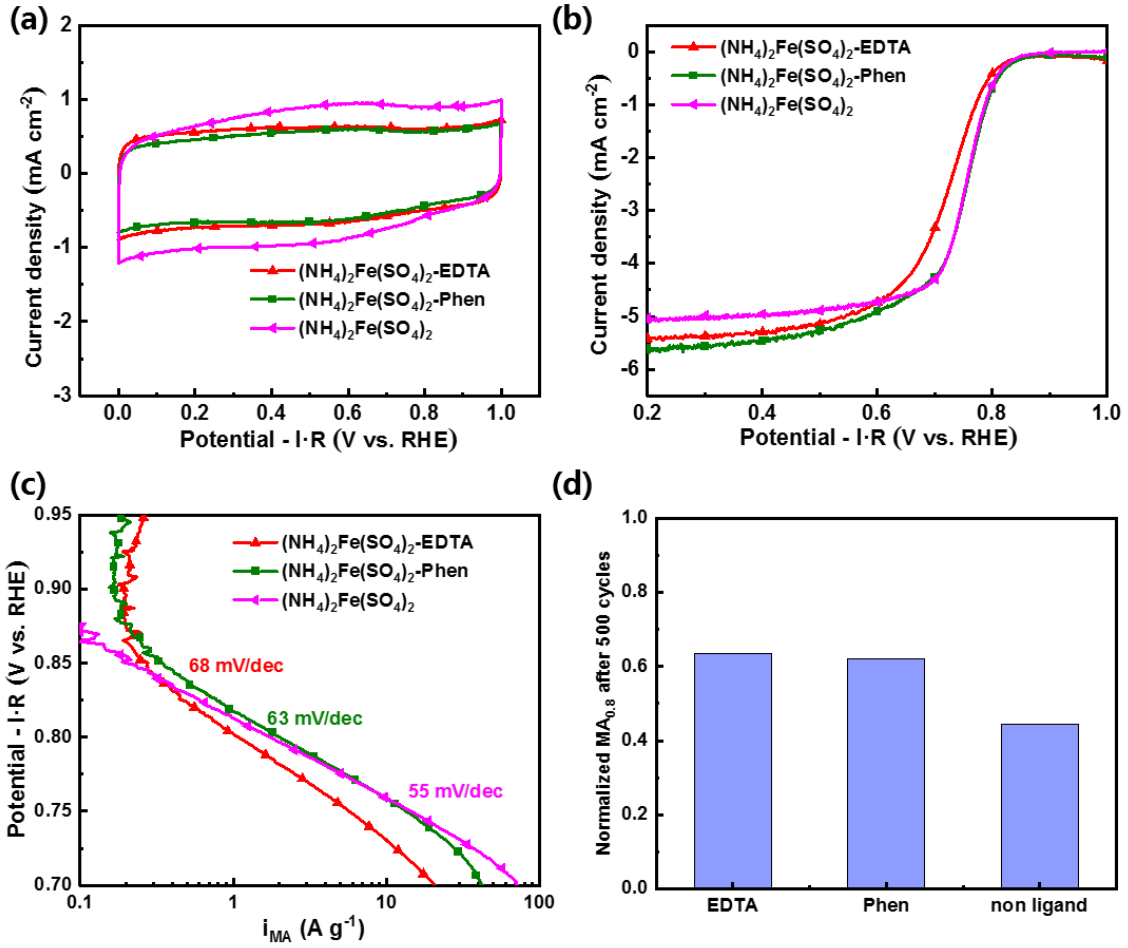

Figure 3.15 **(a)** Cyclic voltammetry curves in N_2 saturated 0.05 mol L^{-1} H_2SO_4; **(b)** Oxygen reduction reaction polarization curves; **(c)** Tafel plots derived from polarization curves of the catalysts prepared with $(NH_4)_2Fe(SO_4)_2$ and different ligand additives; and **(d)** normalized current after 500 CV cycles between 0.6-1.0 V in N_2 saturated electrolyte.

The activity in the 5 cm^2 single cell PEMFC of catalysts prepared with different ligand additives was investigated (method described in section 2.3.2). The polarization curves of the catalysts prepared with $Fe(NO_3)_3$ or $(NH_4)_2Fe(SO_4)_2$ precursor are shown in **Figure 3.16**a and b, respectively. For the $Fe(NO_3)_3$ precursor, the activities of the catalyst prepared with EDTA or phen ligand are almost identical, whereas both significantly declined compared with the non-ligand catalyst. Their difference in micropore volume can be the explanation. The non-ligand catalyst has the largest micropore volume thus, the most active. Two catalysts prepared with ligands show identical polarization curves due to their similar micropore volume. The catalysts prepared with $(NH_4)_2Fe(SO_4)_2$ precursor present the same tendency, which is also in accord with the variation of their micropore volume.

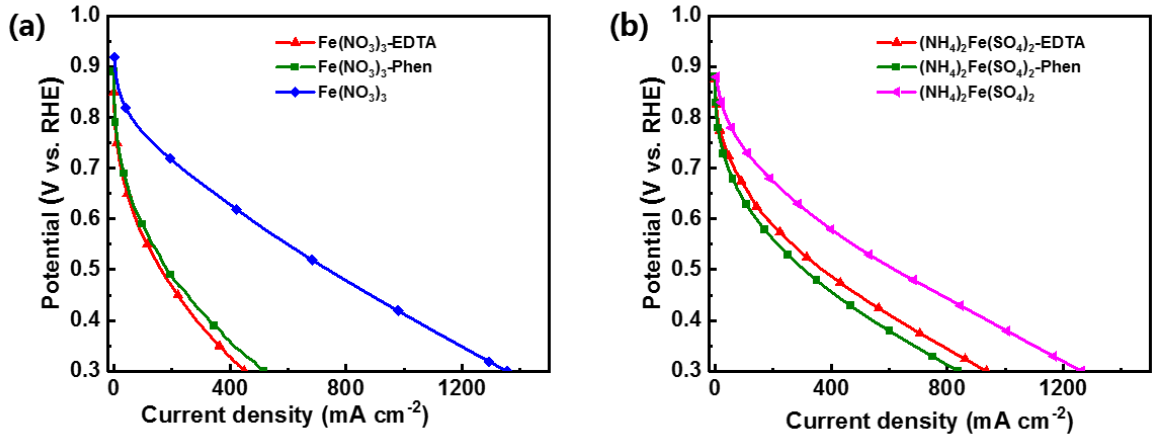

Figure 3.16 Polarization curves of the catalysts prepared with **(a)** $Fe(NO_3)_3$ or **(b)** $(NH_4)_2Fe(SO_4)_2$ and different ligand additives in the single cell. The measurements were performed with T_{cell} = 80 ℃, 100 % RH, *P*cathode = *P*anode = 2 bar_{abs}, the H_2, and O_2 flow rates were 150 mL min^{-1} while the air flow rate was 480 mL min^{-1}.

3.3.5 Conclusion

The impacts of two classic N-containing ligands on the porosity and activity of catalysts have been investigated. The impacts of ligands are similar for the two Fe precursors with different oxide states. The possible reason is that Fe^{2+} is easy to be oxidized in the solution at pH=8. Therefore, the oxide states show little influence during synthesis. The EDTA can greatly increase the solubility of Fe ions, which leads to loss of iron during solvent exchange step. Therefore, all catalysts prepared with EDTA display poor electrochemical activity. Phen generates indissoluble precipitation in the mixed solution, which leads to a different texture from the non-ligand catalyst. High Fe content can be obtained in Phen catalyst without any observable nanoparticles, indicating a high content of active sites. However, the low micropore volume limits the improvement of electrochemical activity. In conclusion, due to the complicated chemical environment of mixed solution, the ligand additives exhibit slight improvement in the electrochemical activity of catalysts.

The crucial point among these catalysts is that their activity is closely related to their Fe content, especially the surface Fe content obtained from XPS analysis. However, due to the Fe content in the Fe-N-C catalyst approaching the detection limit of XPS (less than 1 wt.%), the uncertainty is too large to analyze quantity. Therefore, if ICP-MS and XPS values are close, the bulk Fe content obtained from ICP-MS could be used as a more precise value to be analyzed. Suppose the difference between two values cannot be ignored due to uneven distribution of Fe. In that case, the XPS value seems to be more reliable, even though a larger uncertainty should be tolerated. Besides, since the Fe content is the only important factor we found here, the impacts of increasing Fe content will be further investigated in the next section.

3.4 Impact of different Fe content

As discussed in section 3.3, the Fe contents in the catalyst significantly influence the electrochemical activity and thus should be further investigated. If all the Fe are atomically

dispersed in the carbon aerogel, the activity is supposed to show a linear relationship with Fe content. However, in order to form more Fe-N_4 active sites, the N content should be increased simultaneously, otherwise, the nanoparticles of Fe may be found in the catalyst[219]. The FePc precursor possesses a pre-existing coordination structure, which can ensure the supplementation of N while increasing the Fe content. Therefore, the melamine content can remain constant. The catalysts with different theoretical Fe content were synthesized with FePc precursor, as shown in **Table 3.11**. The pH value of the mixed solution was controlled at around 6 according to the results in section 3.2. The solid content of hydrogel is 20 wt.%. Two different R/M ratios were selected to investigate the impact of the N source content for the Fe precursor with pre-existing coordination structure. If the pre-existing coordination structure can be preserved in the final catalyst, the existence of an extra N source is unnecessary. Therefore, we removed the N source in the carbon aerogel to compare the difference between two series of catalysts, with and without melamine.

3.4.1 Texture and structure of catalysts

The phenomena during synthesis were essentially the same as discussed in section 3.2. The black suspension was obtained when FePc precursor was added, then the hydrogel formed after around 40 minutes. Their iron contents were determined by the ICP-MS method, as shown in **Table 3.11**. For the composition R/M=2/1, the catalyst with low theoretical Fe content (0.5 wt.%) presents an identical value, whereas, for the catalysts with more Fe precursor, the ICP-MS results are lower than theoretical values. It is possible that more nanoparticles were generated with increasing of FePc quantity, which was then removed by acid leaching. A similar tendency is observed with the catalysts with composition R/M=2/0, in which no melamine is introduced. The melamine exhibits little impact on the total Fe content of final catalysts (atomically dispersed and nanoparticles) that we have 0.61 wt.% *vs.* 0.56 wt.% for the 1 wt.% theoretical content and 1.51 wt.% *vs.* 1.86 wt.% for the 2 wt.% theoretical content. However, these results cannot lead to the conclusion that the pre-existing structure can be preserved before the chemical environments of Fe are determined.

Table 3.11 Physicochemical characteristics of the catalysts with different quantities of Fe precursors and different R/M ratio.

Name	R/M	Theoretical Fe content wt.%	Total mass loss wt.%	ICP Fe		BET surface $m^2 g^{-1}$	Vtotal $cm^3 g^{-1}$	Vmicro $cm^3 g^{-1}$	Vmeso $cm^3 g^{-1}$
				wt.%	at.%				
FePc 0.5wt.% R/M=2/1	2/1	0.5	80%	0.50	0.11	1574	2.06	0.47	1.51
FePc 1wt.% R/M=2/1		1	77%	0.61	0.13	1424	2.00	0.43	1.51
FePc 1.5wt.% R/M=2/1		2	74%	1.51	0.33	1282	2.39	0.37	1.97
FePc 0.5wt.% R/M=2/0	2/0	1	73%	0.56	0.12	1533	2.78	0.41	2.28
FePc 1wt.% R/M=2/0		2	66%	1.86	0.41	1300	2.53	0.35	2.13
FePc 1.5wt.% R/M=2/0		3	68%	2.33	0.51	1147	2.13	0.31	1.77

The SEM images shown in **Figure 3.17**a-c exhibit that all the catalysts prepared with composition R/M=2/1 display similar mesopore size. The N_2 adsorption isotherm curves at -196 ℃ and corresponding pore size distribution plots are shown in **Figure 3.17**d and **Figure 3.17**e, respectively. The corresponding pore volumes are listed in **Table 3.11**. The mesopore

volumes are almost identical and the distribution of mesopore size is centered around 10 nm for all catalyst, which is consistent with the observation from SEM images.

The micropore volumes of the catalyst also decrease with the increase of FePc quantity. If we suppose that all Fe ions are atomically dispersed in the catalyst, since the Fe-N_4 active sites are hosted in the micropores, the micropore volume should increase with Fe content rather than the other way around. This inversed tendency suggests the existence of unexpected Fe contained species in the catalysts. Except for small amounts of iron (0.5wt.%), the Fe contents of catalysts prepared with high Fe precursor quantity are less than the theoretical values. For larger amounts of Fe precursor, the iron atoms can be quite close and coalesce with the heat treatments. In fact, nanoparticles larger than 2 nm can block access to micropores and small mesopores, which explains the variation of micropore volume.

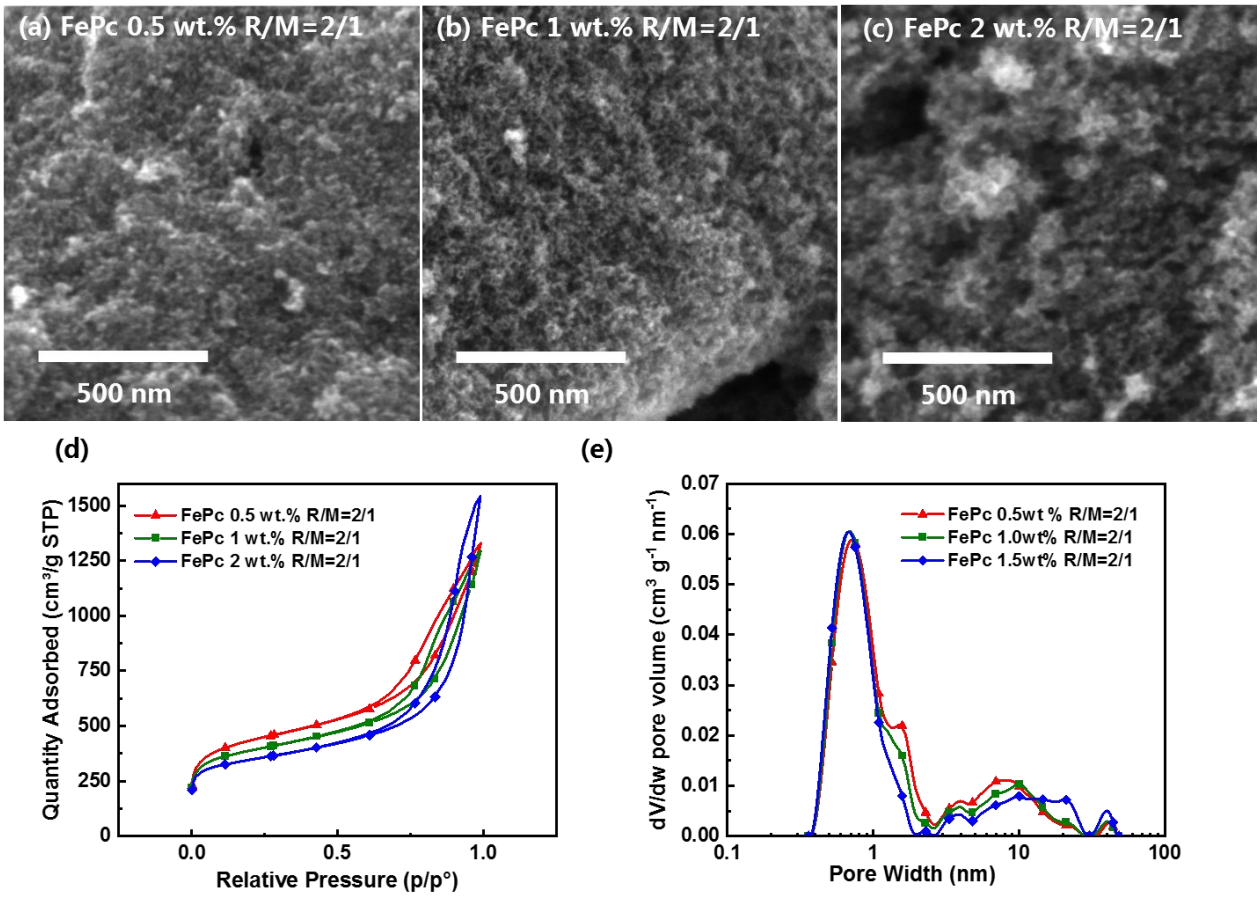

Figure 3.17 **(a), (b)** SEM images of the catalysts prepared with different quantities of Fe precursors at R/M=2/1; **(c)** N_2 adsorption isotherms at -196 ℃ and **(d)** pore size distribution plots obtained by using the 2D-NLDFT-Heterogenerous Surface method.

The SEM images of catalysts prepared without melamine (R/M=2/0) are shown in **Figure 3.18**a-c. The morphology of catalysts with 1 wt.% and 2 wt.% Fe content is similar, whereas the catalyst with 3 wt.% seems to be constituted by larger compact particles. **Figure 3.18**d and e show the N_2 adsorption isotherm curves at -196 ℃ and corresponding pore size distribution plots. The pore volumes are listed in the **Table 3.11**, which proves the observation from SEM images. The mesopore volume decreases with the increase of FePc quantity. The phthalocyanine (Pc) in the precursor is another carbon source during the synthesis, whereas it is non-porous. One thing should be noted for the catalysts prepared with the same quantity of

FePc but different R/M, the catalyst with low M content always has a larger mesopore volume, which is in accord with the results in the literature[58]. In this series, the micropore volume also decreases while increasing Fe content due to the formation of Fe-rich nanoparticles.

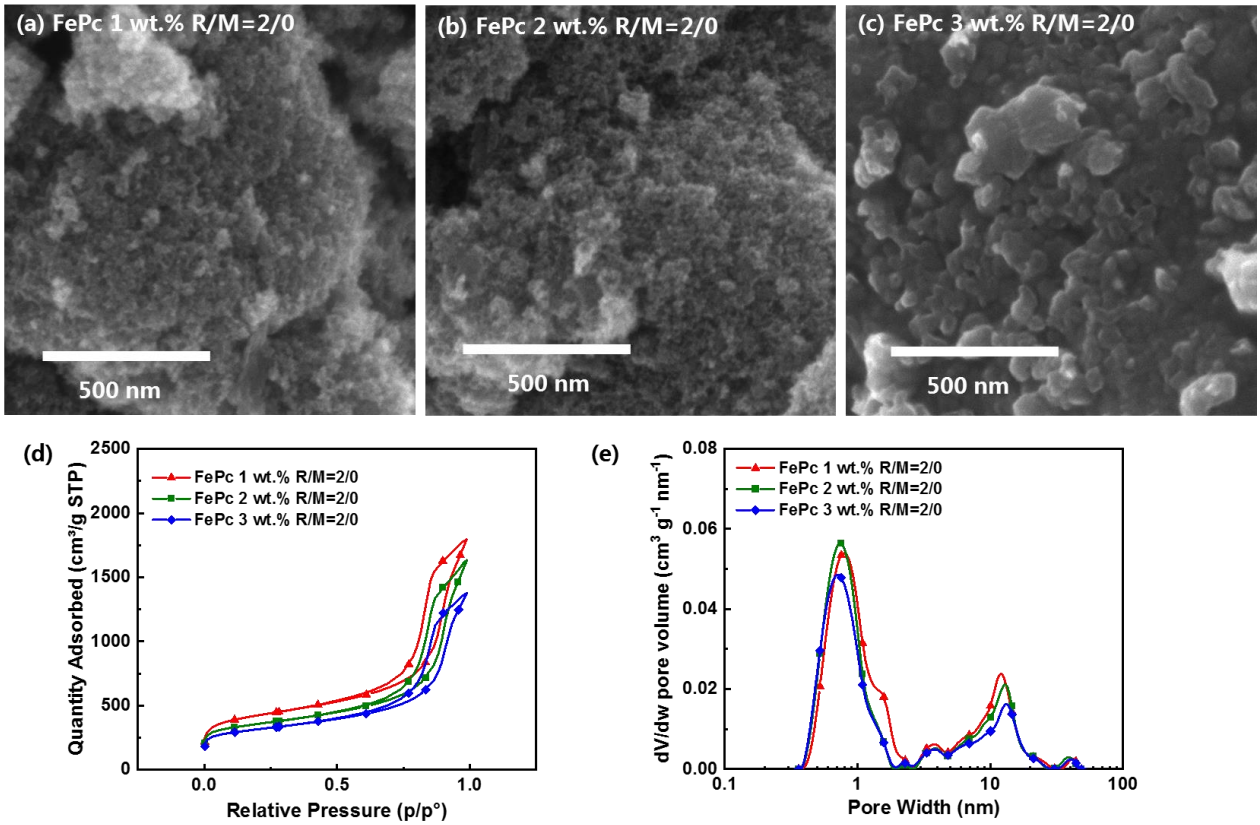

Figure 3.18 **(a), (b)** SEM images of the catalysts prepared with different quantities of Fe precursors at R/M=2/0; **(c)** N_2 adsorption isotherms at -196 ℃ and **(d)** pore size distribution plots obtained by using the 2D-NLDFT-Heterogenerous Surface method.

The TEM images of catalysts prepared with different quantities of FePc at R/M=2/1 are shown in **Figure 3.19**a-c, respectively. No iron nanoparticles are detectable (>1-2 nm) for all catalysts, which means the Fe atoms can be well dispersed in the carbon matrix even if the Fe content is increased to 1.5 wt%. For the catalyst with 2wt% Fe theoretical, the presence of some Fe nanoparticles not detectable by TEM because they are very small. Meanwhile, no significant diffraction peak can be identified from their XRD patterns (**Figure 3.19**d) also demonstrate no crystalline detectable iron phases in the catalysts. The atomically dispersed Fe suggests their Fe contents directly relate to their activity.

The situation is different with the catalyst prepared at R/M=2/0, as shown in **Figure 3.20**a-c. Nanoparticles can be observed by TEM in all catalysts, as seen in the white frame of figures. As the quantity of FePc increases, more and more nanoparticles can be observed. Meanwhile, from the XRD patterns of the catalysts, as seen in **Figure 3.20**d, a small peak at around 2θ=44° gradually appears with an increasing amount of FePc, which can be indexed to the (111) diffraction of γ-Fe. The same acid washing treatment was conducted on all catalysts, but the dissolution of the larger nanoparticles was not fully achieved. Therefore, these Fe nanoparticles are encapsulated in the carbon sheets, protecting the larger one eliminated from acid washing. In this case, the quantity of atomically dispersed Fe in the catalysts cannot be counted by their total Fe content, suggesting the activity show a weak relationship with ICP-MS results. The variation in micropore volume can be explained by their low quantity of active sites.

The difference between the two series concerning the presence or not of visible Fe nanoparticles can be linked to the presence of nitrogen (brought by melamine) which can attract the iron and avoid its coalescence into large nanoparticles during the heat treatments.

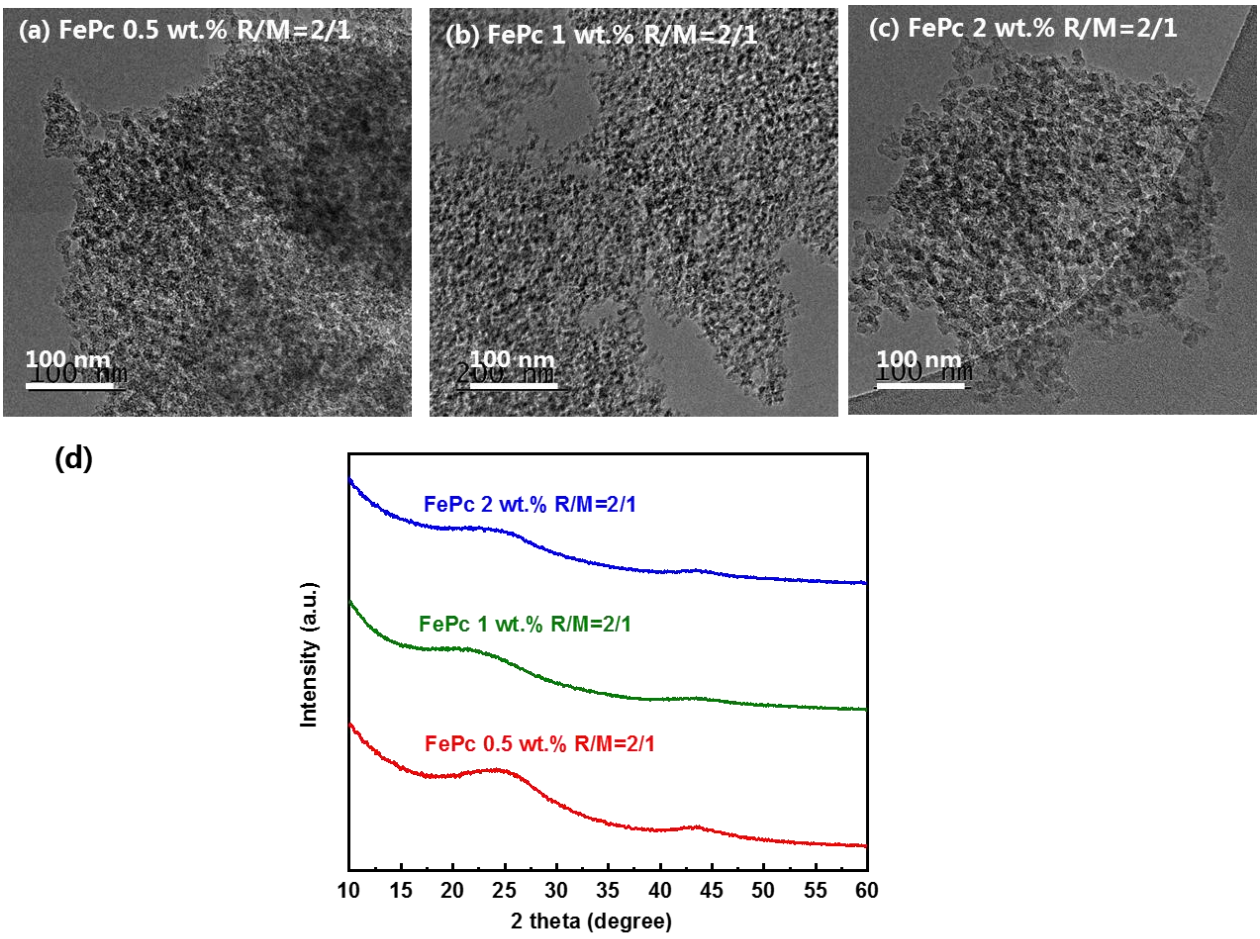

Figure 3.19 **(a)-(d)** TEM images and **(e)** normalized XRD patterns of catalysts prepared with different quantities of Fe precursors at R/M=2/1.

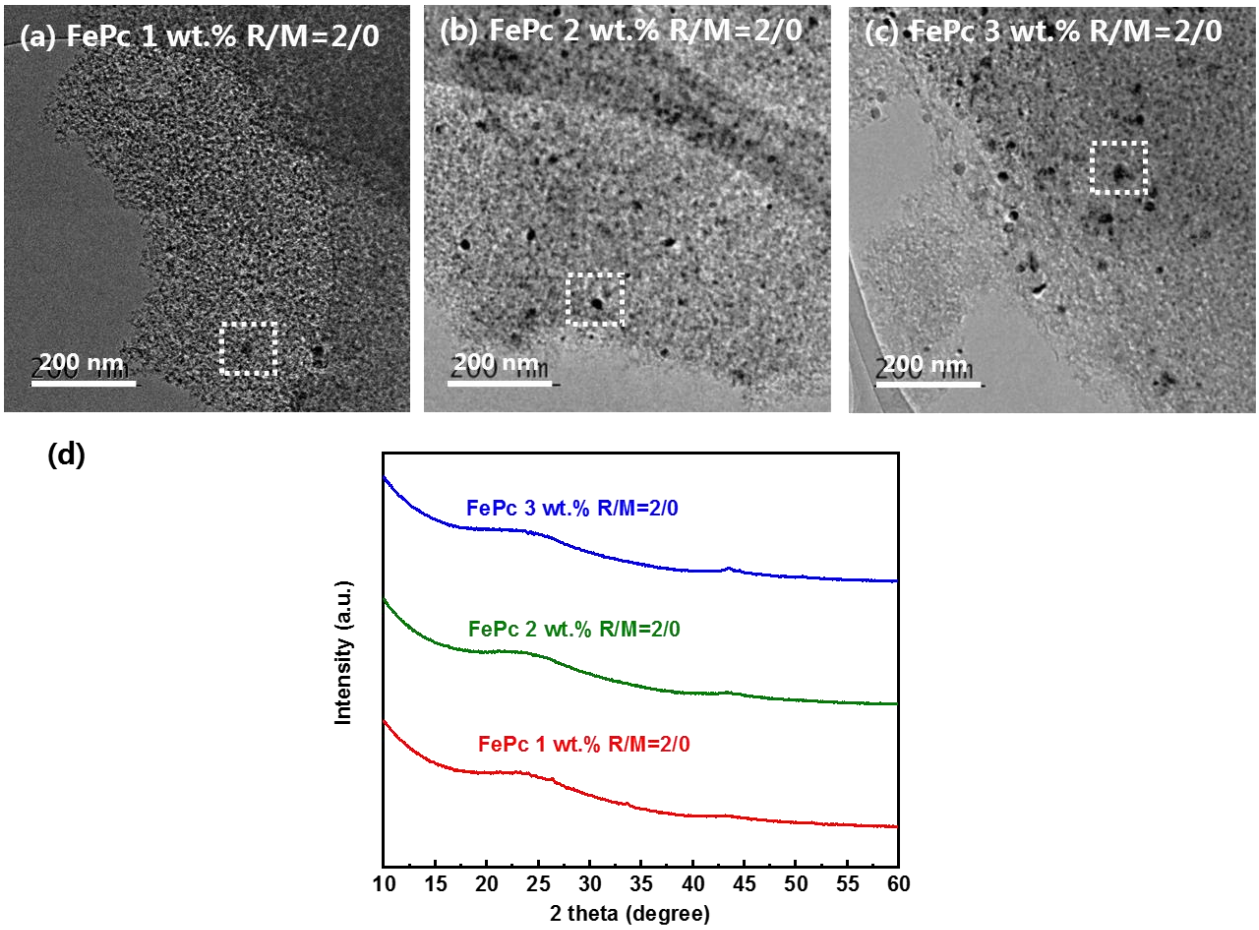

Figure 3.20 **(a)-(d)** TEM images and **(e)** normalized XRD patterns of catalysts prepared with different quantities of Fe precursors at R/M=2/0.

3.4.2 Chemical composition of catalysts

The chemical compositions of catalyst surface were investigated by XPS method. The results of catalysts prepared with different quantities of FePc at **R/M=2/1** are listed in **Table 3.12**. The Fe content on the surface of catalysts increases with the increase of the FePc quantity introduced in the sol from 0.5 wt.% to 1 wt.%, then keeps constant from 1 wt.% to 2 wt.%. In fact, both 0.5 wt.% and 1 wt.% show uneven distribution of Fe on the surface and in bulk. The Fe in the 0.5 and 1 wt.% catalysts is more concentrated on the surface (ex: 0.13 at.% in bulk vs. 0.26 at.% on the surface for 1wt%), whereas the 2 wt.% catalyst is more homogeneous (0.33 at.% in bulk vs. 0.27 at.% on the surface). The former situation can be attributed to the etching of carbon during NH_3 treatment, which removes the carbon but preserves the Fe to form active sites. The 2 wt.% catalyst has similar surface Fe content to 1 wt.% catalyst but significantly increased in bulk. The possible reason is a small amount of Fe nanoparticles are sparsely dispersed in the carbon, which are hard to find under TEM. The nanoparticles are encapsulated by carbon sheets that cannot be detected by XPS, whereas ICP-MS can give the whole Fe content regardless of if they are on the surface or in bulk.

The N content decreases with increasing Fe content, as shown in **Table 3.12**. The deconvolution results of their N 1s spectra show more than 40% loss of pyridinic N and almost

30% loss of pyrrolic N. The Fe-N_x composition decreases the least among three active N species. The impacts on their activity will be investigated.

Table 3.12 Chemical composition of catalysts surface prepared with different quantities of Fe precursors at R/M=2/1 and deconvolution of their N 1s spectra.

Theoretical Fe content wt.%	C at.%	O at.%	Fe at.%	N at.%	Nitrile at.%	Pyridinic at.%	Fe-Nx at.%	Pyrrolic at.%	Quaternary at.%	Graphitic at.%
					398.0 eV	398.8 eV	399.9 eV	400.9 eV	402.0 eV	403.3 eV
0.5	94.38	1.98	0.20	3.45	0.86	0.60	0.56	0.92	0.36	0.15
1	94.77	1.89	0.26	3.09	0.73	0.55	0.46	0.86	0.36	0.14
2	93.33	3.85	0.27	2.55	0.62	0.35	0.43	0.66	0.32	0.16

The XPS results of catalysts prepared with different quantities of FePc at **R/M=2/0** are listed in **Table 3.13**. The Fe content of all catalysts is almost identical regardless of their quantity of FePc. This result demonstrates the Fe nanoparticles observed under TEM are encapsulated because they cannot be detected by XPS. Therefore, these nanoparticles are not formed during NH_3 treatment but originally after the first pyrolysis. It should be noted that even though the catalysts with the same FePc content possess similar Fe content in ICP-MS results for two R/M series, the series without melamine (R/M=2/0) always show lower Fe content in XPS results due to the formation of Fe nanoparticles. This result emphasizes the importance of melamine during the formation of active sites. Although all Fe atoms are located in the Fe-N_4 coordination structure in FePc precursor, the Fe nanoparticles can still form during the carbonization step, which means the pre-existing active site structure cannot be preserved. In this case, melamine becomes the true N source of active sites, which provides abundant active N to coordinate with Fe during pyrolysis. The surface N contents of series R/M=2/0 don't show a significant relationship with Fe content, whereas they are always lower than the series R/M=2/1 due to the lack of melamine. According to the deconvolution of their N 1s spectra, the pyrrolic N component of series R/M=2/0 is only half the content of series R/M=2/1, but the pyridinic N almost keeps constant. The different variation of N components implies that melamine is a source of pyrrolic N. In summary, the melamine content seems to be the crucial factor that affects the formation of Fe-N_4 active sites. Besides, melamine tends to form pyrrolic N in the final catalyst, which is possible to propose that the Fe atoms are coordinated with pyrrolic N to form the active sites. The impacts of melamine content will be further investigated in chapter 4.

Table 3.13 Surface chemical composition of catalysts prepared with different quantities of Fe precursors at R/M=2/0 and deconvolution of their N 1s spectra.

Theoretical Fe content wt.%	C at.%	O at.%	Fe at.%	N at.%	Nitrile at.%	Pyridinic at.%	Fe-Nx at.%	Pyrrolic at.%	Quaternary at.%	Graphitic at.%
					398.0 eV	398.8 eV	399.9 eV	400.9 eV	402.0 eV	403.3 eV
1	94.87	2.04	0.18	2.72	0.84	0.55	0.51	0.48	0.24	0.10
2	96.22	1.69	0.21	1.87	0.54	0.34	0.30	0.41	0.21	0.08
3	96.09	1.74	0.22	1.95	0.56	0.36	0.32	0.41	0.21	0.09

3.4.3 Electrochemical characterization of catalysts

The CV and polarization curves tested in the RDE setup of catalysts at **R/M=2/1** are shown in **Figure 3.21**a and b, respectively. Their current densities at 0.8 V are listed in **Table 3.14**. As

expected, the current density increases with Fe content but exhibits a nonlinear relationship. The $MA_{0.8}$ is almost doubled when theoretical Fe content is increased from 0.5 wt.% to 1.0 wt.%, but only a 30% increase when it is further increased to 2 wt.%. The outstanding enhancement of activity can be explained by the uneven distribution of Fe in the 1 wt.% catalyst, as discussed before, that the XPS result presents 0.26 at.% (~1.19 wt.%) of Fe on the surface, which is twice the 0.5 wt.% catalyst, corresponding to the increase of $MA_{0.8}$. When the FePc is further increased to 2 wt.%, the surface Fe content remains constant, implying the formation of less active Fe species. Therefore, the current density doesn't show a linear relationship with Fe content.

Their electrochemical available area obtained from CV curves decreases with increasing Fe content, which is different from the tendency observed with different ligands in section 3.3. However, the variation of CV areas closely relates to the N content here, that the electrochemical available area decreases with the total N content of catalysts. The CV area in N_2 saturated electrolyte contains both the redox of active N species (pyridinic and pyrrolic N) as well as Fe-N_4 active sites. For the catalysts prepared with different FePc quantities, the redox of N species dominates surface reactions because there are more than ten times more abundant than Fe, and all catalysts show similar morphology. The catalysts prepared with different ligands cannot show the same tendency because their different morphologies lead to different activities of surface N groups.

The Tafel slopes derived from polarization curves are shown in **Figure 3.21**c. The values of all catalysts are in the range of 60-70 mV dec^{-1}, corresponding to the classic atomically dispersed Fe-N-C catalyst. For the catalysts based on nanoparticles, the Tafel slopes are usually in the range of 90-100 mV dec^{-1}.[219] Therefore, the less active nanoparticles found in 2 wt.% catalyst have little contribution to the activity. The normalized current densities after 500 cycles in N_2 saturated electrolyte are shown in **Figure 3.21**d. The catalysts with 0.5 wt.% and 1 wt.% FePc exhibited a similar loss ratio after 500 cycles, around 33%, while the 2 wt.% catalyst showed almost double the loss. The possible reason for the huge decline is that the less active nanoparticles can be dissolved into electrolyte during CV test.

Table 3.14 RDE tests of the catalysts with different quantities of Fe precursors at different R/M ratio.

R/M	Theoretical Fe content wt.%	$MA_{0.8}$ A g^{-1}	$MA_{0.8}$ after 500 cycles A g^{-1}	Loss ratio	Tafel slope mV dec^{-1}
2/1	0.5	0.85	0.56	-34%	65
	1	1.67	1.09	-35%	61
	2	2.16	0.85	-66%	60
2/0	1	0.67	0.32	-52%	55
	2	0.51	0.26	-49%	66
	3	0.89	0.49	-45%	62

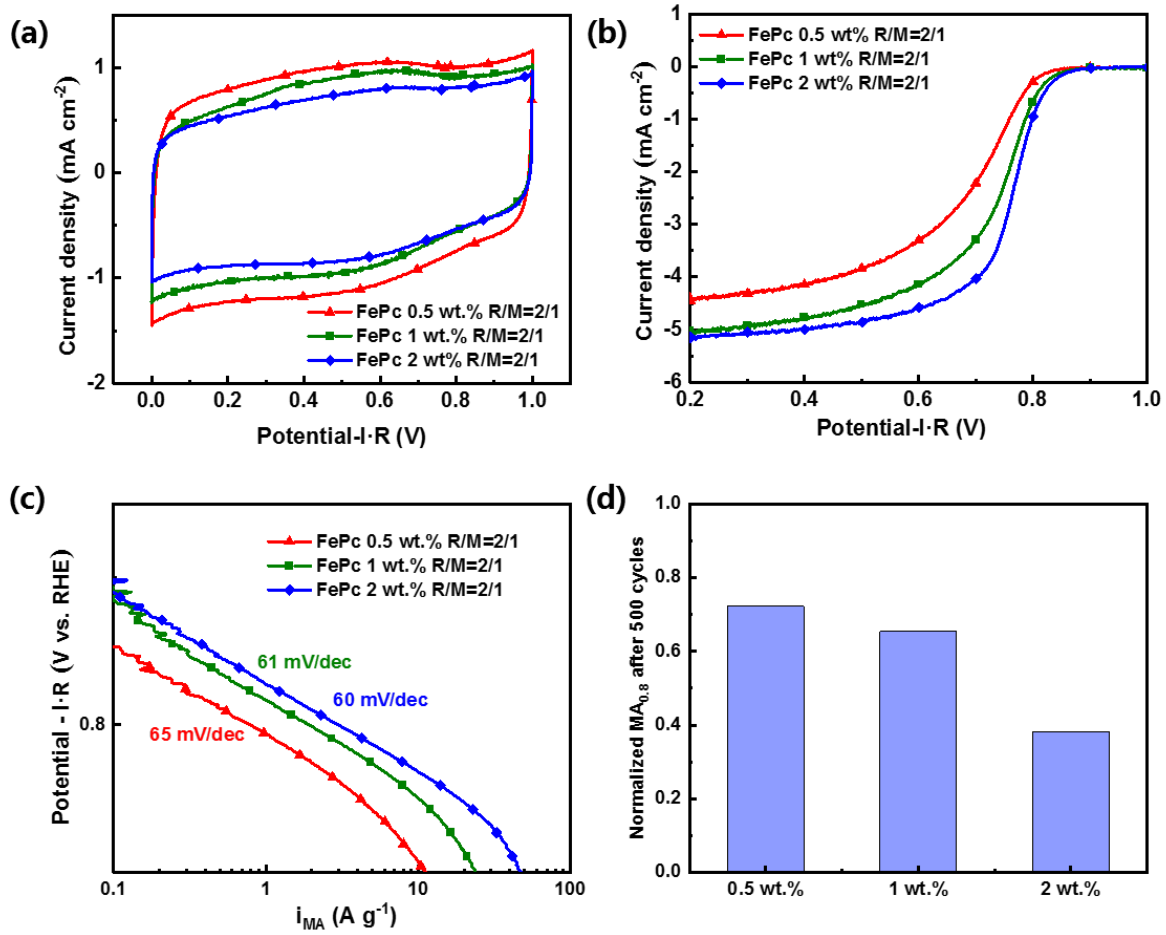

Figure 3.21 **(a)** Cyclic voltammetry curves in N_2 saturated 0.05 mol L^{-1} H_2SO_4; **(b)** Oxygen reduction reaction polarization curves; **(c)** Tafel plots derived from polarization curves of the catalysts prepared with different quantities of Fe precursors at R/M=2/1; and **(d)** normalized current after 500 CV cycles between 0.6-1.0 V in N_2 saturated electrolyte.

The CV and polarization curves tested in the RDE setup of catalysts at **R/M=2/0** are shown in **Figure 3.22**a and b, respectively. Their current densities at 0.8 V are also listed in **Table 3.14**. The CV areas also increase with surface N content obtained from XPS spectra. Their current densities at 0.8 V are almost identical, corresponding to their similar surface Fe content (0.18 at.%, 0.21 at.%, and 0.22 at.%). The Tafel slopes derived from their polarization curves are shown in **Figure 3.22**c. The values are around 60 mV des^{-1}, corresponding to the behavior of atomically dispersed active sites. Despite their Fe content in bulk ranging from 0.56 wt.% to 2.33 wt.%, the nanoparticles encapsulated in the carbon sheets are non-active to ORR. All the catalysts prepared at R/M=2/0 are less active than the series R/M=2/1, in agreement with the tendency of their surface Fe content. As we have mentioned in the section of chemical composition, melamine plays a crucial role during the formation of active sites, which cannot be replaced by pre-existing Fe-N_4 structure in the precursor. The normalized current densities after 500 cycles in N_2 saturated electrolyte are shown in **Figure 3.22**d. All the catalysts show a similar loss ratio (around 50%), which is greater than the catalyst without metallic Fe (R/M=2/1, 0.5 wt.%, and 1 wt.%). The same explanation of R/M=2/1, 2 wt.% catalysts can be employed, that the Fe particles are dissolved into electrolyte during CV test, which leads to the loss of active center.

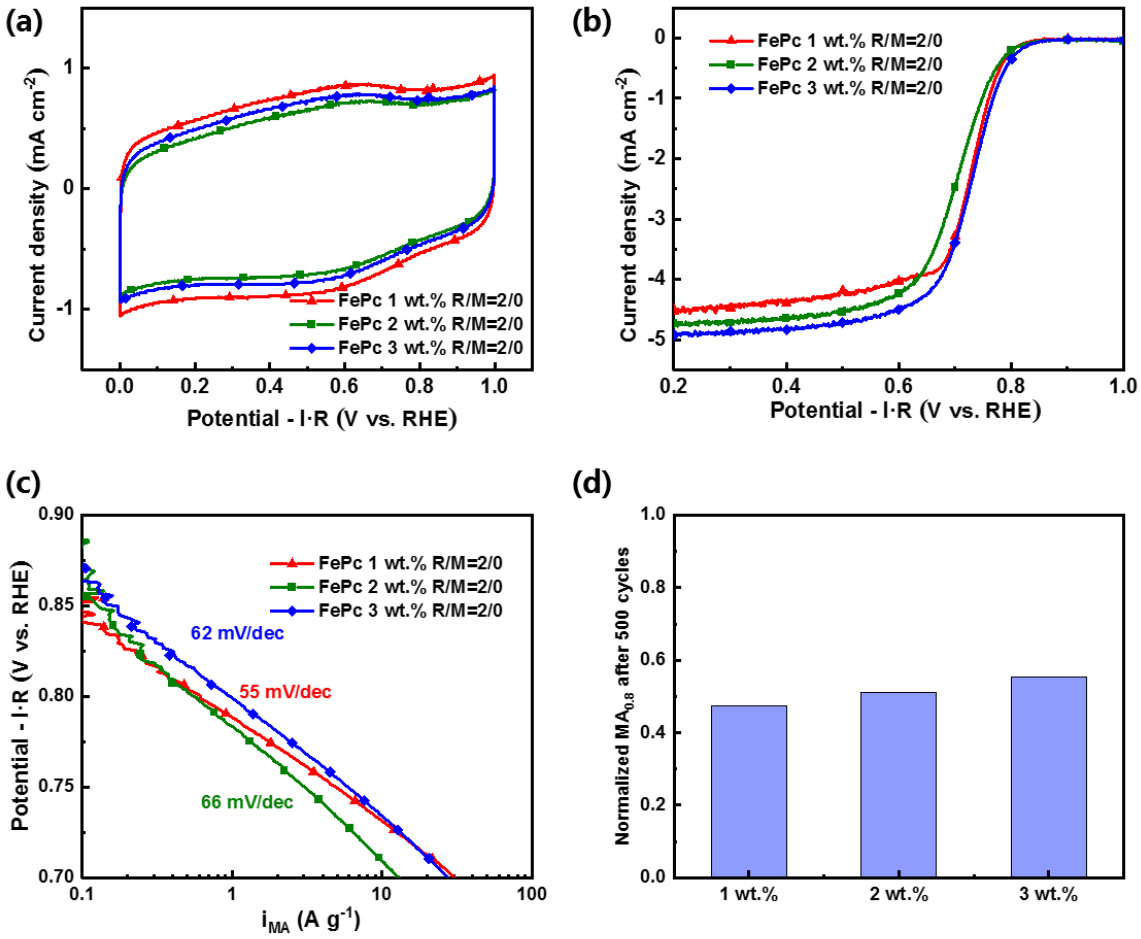

Figure 3.22 **(a)** Cyclic voltammetry curves in N_2 saturated 0.05 mol L^{-1} H_2SO_4; **(b)** Oxygen reduction reaction polarization curves; **(c)** Tafel plots derived from polarization curves of the catalysts prepared with different quantities of Fe precursors at R/M=2/0; and **(d)** normalized current after 500 CV cycles between 0.6-1.0 V in N_2 saturated electrolyte.

3.4.4 Conclusion

The catalysts with different quantities of FePc precursor were prepared to investigate the impacts on activity. Two series with different R/M ratios are prepared to investigate the effect of pre-existing coordination structure. For the series prepared at R/M=2/1, the activity increases with Fe content but shows a non-linear relationship due to the formation of Fe nanoparticles at high Fe content. The Fe nanoparticles can be found in all the catalysts prepared at R/M=2/0. Their activities are independent of their Fe contents and are almost identical. In fact, the activity of all the catalysts closely relates to their Fe content on the surface instead of in bulk. In the series R/M=2/0, no matter how much the quantity of FePc increases, the limit of surface Fe content is around 0.22 at.%, and for the series R/M=2/1, the limit seems to be increased to 0.27 at.%. Otherwise, unexpected nanoparticles appear in the catalyst.

In conclusion, increasing the quantity of Fe precursor increases the activity, but too much is not beneficial. Simply increasing Fe content only leads to nanoparticles instead of atomic iron in the final catalyst. On the other hand, the melamine content seems very important because the limit of atomic surface Fe content can be increased by melamine, which is directly related to the activity. Besides, the pre-existing coordination structure presents little impact on forming

active centers. Even though all Fe atoms are contained in the Fe-N_4 macrocycles in the FePc precursor, the microstructure will be decomposed during the carbonization step. Therefore, the undissolved FePc powders are more likely to form nanoparticles because they are easier to agglomerate than the soluble Fe salts. In the next chapter, the impact of melamine content will be further investigated, promising to improve the activity of catalysts.

Chapter 4 Impact of Melamine Content on the Performance of Fe-N-C Catalysts towards Oxygen Reduction Reaction Activity

Résumé Français

Dans ce chapitre, les impacts de la teneur en mélamine sur l'activité ORR et les propriétés de transport de masse des catalyseurs à base d'aérogel Fe-N-C ont été systématiquement étudiés.

Dans la section 4.1, une série de catalyseurs Fe-N-C ont été synthétisés en modulant la teneur en mélamine (M), afin de définir les limites des paramètres de gélification et d'explorer les relations entre les paramètres de gélification, la texture des matériaux, et l'activité ORR. Avec $FeCl_3$ comme précurseur de fer, avec l'augmentation de la teneur en M, le volume des mésopores varie non linéairement avec un maximum à R/M=2/1. Il diminue ensuite rapidement à haute teneur en M en raison de la réorganisation du squelette carboné avec un départ massif d'azote au cours de la pyrolyse. La quantité absolue de Fe augmente avec la teneur en M, ainsi que la teneur en N. Les spectres XAS et Mössbauer du ^{57}Fe montrent la présence de rares nanoparticules riches en Fe et que le site D1 est la configuration majoritaire des sites actifs Fe-N_4. D'après l'analyse des spectres XPS, la teneur en N pyrrolique est positivement corrélée avec l'augmentation de la teneur en M, ce qui confirme que la plupart des atomes de Fe actifs sont coordonnés par l'azote pyrrolique, en accord avec les spectres Mössbauer. L'azote atomiquement dispersé dans la mélamine peut stabiliser le Fe pendant la pyrolyse, évitant ou minimisant la formation de nanoparticules de fer. Les tests électrochimiques en RDE montrent une relation linéaire entre l'activité massique et la teneur en Fe jusqu'à 0.3 at.% ($FeCl_3$-R/M=2/2), avec l'activité massique ($MA_{0.8}$) la plus élevée de 3.0 A g^{-1} à 0.8 V. Cette tendance est conforme à la caractérisation XPS indiquant que la plupart du Fe est présent sous forme de sites Fe-N_x dispersés atomiquement. Une augmentation supplémentaire de la teneur en mélamine a réduit l'activité massique car le faible volume de mésopores limite les propriétés de transport de matière. Leurs performances ORR en PEMFC présentent une tendance similaire qu'en configuration RDE, à savoir que le $FeCl_3$-R/M = 2/2 présente les meilleures performances. Toutes les courbes de polarisation sous H_2-air en PEMFC ne s'effondrent pas, ce qui indique d'excellentes propriétés de transport de masse des catalyseurs à base d'aérogel.

Dans la section 4.2, les catalyseurs Fe-N-C sont synthétisés avec différents précurseurs de Fe (FePc et $Fe(NO_3)_3$) et une teneur en M élevée pour confirmer si la tendance précédente convient à d'autres précurseurs de Fe. A haute teneur en M, pour le précurseur $Fe(NO_3)_3$, l'activité ORR du catalyseur est significativement augmentée, alors que pour le précurseur FePc, elle n'est que légèrement augmentée car ce précurseur, insoluble ne peut pas être bien dispersé dans l'aérogel. En combinant le meilleur précurseur ($Fe(NO_3)_3$) et une haute teneur en M (R/M=2/2), le meilleur catalyseur a été obtenu avec une $MA_{0.8}$=3.58 A g^{-1} en configuration RDE qui est proche de la poudre de Pajarito commerciale (PMF D1240). En PEMFC, sous H_2/O_2, $Fe(NO_3)_3$-R/M=2/2 montre également la densité de courant la plus élevée, de 113 mA cm^{-2} à 0,8 V, et de 44 mA cm^{-2} à 0.85 V. Cette valeur n'est que de 0.05 V inférieur à l'objectif DOE 2025 défini pour des catalyseurs sans métal du groupe du platine. En outre, la courbe de polarisation ne s'effondre pas à haute densité de courant, indiquant ses bonnes propriétés de transport de masse. Ces catalyseurs sont donc très prometteurs.

The discussion in Chapter 3 reveals a positive relationship between atomically dispersed Fe content and ORR activity of Fe-N-C catalyst. The mass activity of Fe-N-C catalysts relates to the number of accessible Fe-N_4 sites per mass of catalyst (site density, SD) and the average ORR turnover frequency (TOF) of all accessible sites[70]. In the absence of pathways to increase the TOF, increasing the absolute amount of atomically dispersed Fe is an efficient way to increase the SD, thus the mass activity of the Fe-N-C catalysts[70]. However, simply increasing the quantity of Fe precursor in the preparation of aerogel precursor only increases the yield of less active Fe-rich nanoparticles instead of atomically dispersed Fe, as discussed in section 3.4. On the contrary, the melamine content affects significantly the ORR activity of Fe-N-C aerogel catalysts. The presence of well-dispersed N and Fe sources in the aerogel precursor can promote the formation of Fe-N_4 active sites and reduce the yield of Fe-rich nanoparticles during pyrolysis[220,221]. As seen in section 3.4, all catalysts prepared with R/M=2/1 show a clear view of carbon aerogel substrate under TEM, whereas the nanoparticles can be observed for those prepared without melamine (R/M=2/0). However, excessive M content can decrease the porosity of the aerogel and even impede the gelation process, which may lead to the problem of mass transport[58,222].

In this chapter, a series of Fe-N-C catalysts were synthesized by modulating the M content, with $FeCl_3$ as benchmark Fe precursor, to define the limits of the gelation parameters and to identify the relationships between the gelation parameters, materials' structure, porosity, activity, and mass-transport properties. Subsequently, the impacts of melamine content (M) on the other Fe precursors, including FePc and $Fe(NO_3)_3$, were investigated as well.

4.1 Impact of melamine content with $FeCl_3$ precursor

4.1.1 Synthesis of catalysts

The Fe-N-C catalysts were prepared according to the protocol described in Chapter 2. The M content was modulated according to the molar ratio of R/M=2/*x* at the aerogel preparation stage and the molar ratio of reactants is 2:(4+3*x*):*x*:(0.017+0.016*x*):60 for R:F:M:NaC:W. The final catalysts were named by $FeCl_3$-R/M=2/*x*, with the M content *x* ranging from 0 to 2.5. The molar ratio (R+M):Fe was kept constant with a value of 1:0.01, targeting *ca*. 1 wt. % Fe in the final catalysts by assuming no iron was removed during the acid leaching step and around 70% mass loss of (R+M+F) after pyrolysis. The specific quantities of products were listed in **Table 4.1**.

Table 4.1 Specific quantities of reagents for preparing Fe-N-C aerogel catalysts with different R/M ratios and $FeCl_3$ precursor.

R/M	Resorcinol	Melamine	Formaldehyde	$FeCl_3$	Na_2CO_3
	g	g	mL	g	g
2/0	3.6	0	5.00	0.066	0.030
2/0.5	3.6	1	6.75	0.075	0.044
2/1	3.6	2	8.50	0.080	0.058
2/1.5	3.6	3	10.25	0.095	0.072
2/2	3.6	4	12.00	0.110	0.086
2/2.5	3.6	5	13.75	0.124	0.100

The composition of Fe-doped organic aerogels before pyrolysis was characterized by Fourier transform infrared (FTIR) spectroscopy (**Figure 4.1**) to follow the variation of their composition. The assignments of absorption bands are listed in **Table 4.2**. The spectra of RF and MF aerogel without Fe were also plotted in the same figure as the reference. For the catalyst $FeCl_3$-R/M=2/0 (no melamine), the FTIR spectrum is similar to that of RF aerogel. The absorption bands at 1479 cm^{-1} belong to the CH_2 scissor vibrations, which derive from the condensation of formaldehyde.[223] The absorption band at 1614 cm^{-1} corresponds to stretching vibrations of benzene ring in resorcinol.[223,224] The two absorption bands at 1222 and 1092 cm^{-1} are associated with C-O-C asymmetric and symmetric stretching vibrations of methylene ether bridges, respectively, which have been previously identified in the FTIR spectra of RF aerogels.[223] This bond demonstrates the existence of benzylether structures, which are typically derived from the polycondensation between methylol and resorcinol in basic conditions.[200,201] With increasing melamine content, the absorptions derived from MF aerogel become more intense. Two sharp absorption bands at 1544 and 810 cm^{-1} can be unambiguously assigned to vibration modes specific to the melamine triazine ring.[225] The relatively broad absorption band at 1350 cm^{-1} can be assigned to the stretching vibration of C-N bond between aromatic carbon and amine function.[225] An additional absorption band is visible at around 1000 cm^{-1}, which cannot be assigned to RF or MF aerogel. It can instead be assigned to a N-CH_2-O stretching mode, indicative of crosslinking between resorcinol and melamine with methylene derived from formaldehyde as the linker.[226] The peak intensity increases with melamine content, indicating the proper integration of nitrogen atoms in the RMF aerogel backbone.

Table 4.2 FTIR band assignment of Fe doped RMF aerogel spectra.

Frequency Wavenumber cm^{-1}	Assignment
1614	Benzene ring stretching vibration of resorcinol[223,227]
1544	Triazine ring stretching vibration of melamine[225]
1479	CH_2 scissor vibration of condensation of formaldehyde[223]
1350	Aromatic C-N stretching vibration of melamine[225]
1222	C-O-C asymmetric vibration of methylene ether bridges between resorcinols[223,227]
1092	C-O-C symmetric vibration of methylene ether bridges between resorcinols[223,227]
1000	N-CH_2-O stretching vibration of methylene ether bridges between melamine and resorcinol[225,226]
810	Triazine ring[225]

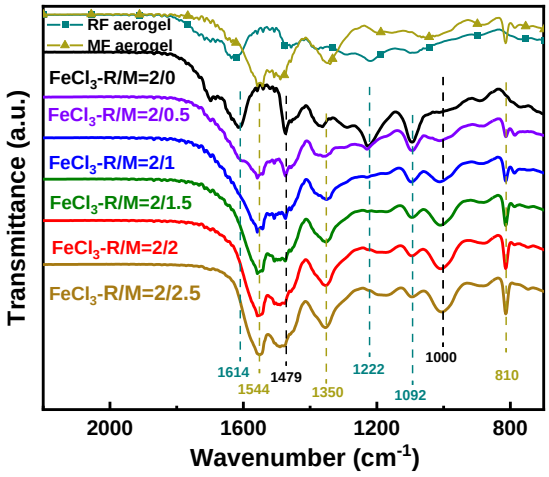

Figure 4.1 FTIR spectrum of organic aerogel prepared with different R/M ratios and $FeCl_3$ precursor. The spectra were normalized by the absorption peak at 1614 cm^{-1}.

4.1.2 Texture and structure of catalysts

Further characterizations were then conducted on the final catalysts after the two thermal treatments (N_2 and N_2/NH_3). Their total mass loss after two pyrolysis steps almost keeps constant with increasing melamine content (around 80% in **Table 4.3**), whereas their morphologies are dramatically changed. As seen by SEM in **Figure 4.2**, the catalysts prepared with low M content (x<1, **Figure 4.2**a-c) display the familiar stacking appearance of covalently linked spherical units, and porous texture on the surface of particles can be observed. However, with the increasing of M content, a more compact texture appears at x=1.5 (**Figure 4.2**d), then completely occupies the view at x=2.5 (**Figure 4.2**f).

Table 4.3 Physicochemical characterization of the catalysts with different R/M ratios and $FeCl_3$ precursor.

R/M	Total mass loss wt.%	ICP Fe		BET surface ($m^2\ g^{-1}$)	Vtotal ($cm^3\ g^{-1}$)	Vmicro ($cm^3\ g^{-1}$)	Vmeso ($cm^3\ g^{-1}$)
		wt.%	at.%				
2/0	74%	0.33	0.07	1481	1.37	0.44	0.83
2/0.5	78%	0.49	0.10	1595	2.13	0.43	1.60
2/1	78%	0.85	0.18	1596	2.20	0.44	1.67
2/1.5	77%	1.17	0.25	1256	0.87	0.42	0.38
2/2	81%	1.36	0.30	1271	0.78	0.45	0.25
2/2.5	80%	1.57	0.34	1099	0.46	0.42	0.02

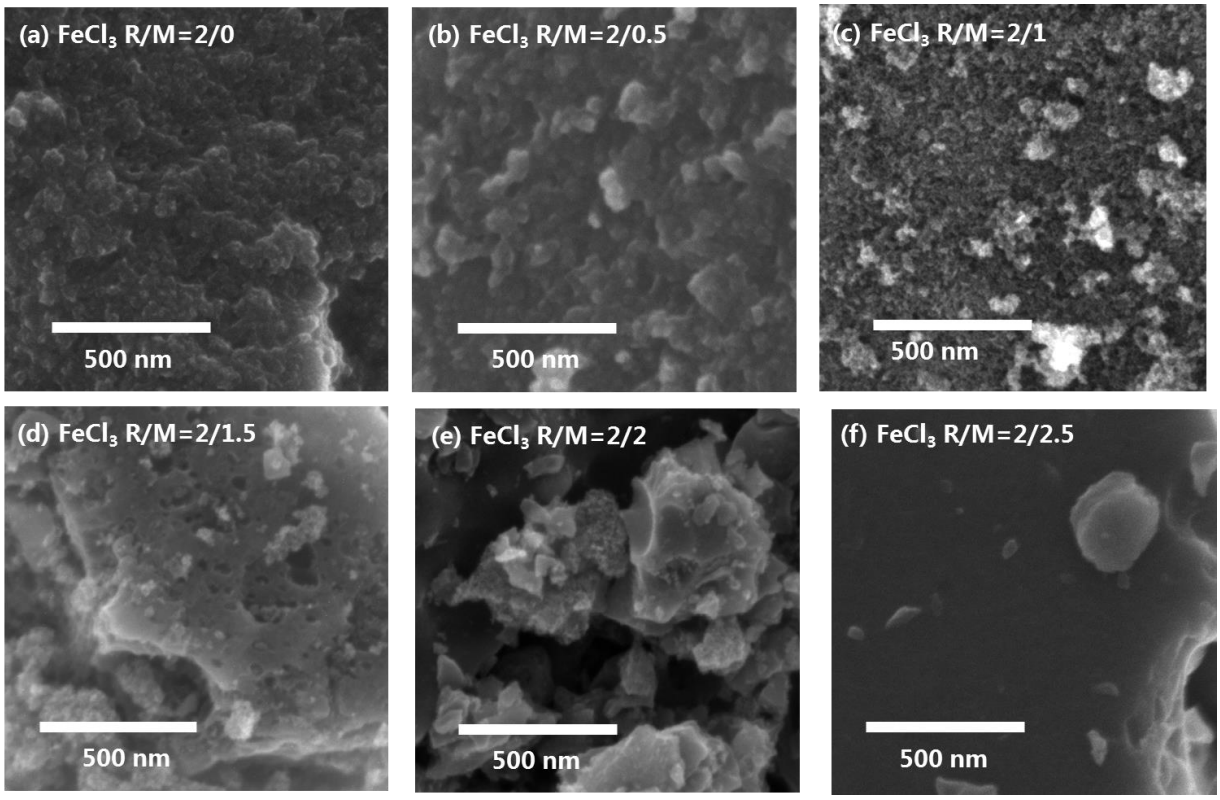

Figure 4.2 **(a)-(f)** SEM images of the catalysts prepared with different R/M ratios and $FeCl_3$ precursor.

TEM shows a similar evolution. For the catalysts prepared with low M content, R/M ranging from 2/0 to 2/1, their TEM images (**Figure 4.3**) show a highly porous texture, which is similar

to those reported for RMF aerogel without Fe.[58,228] When R/M reaches 2/1.5, some pore-less platelets can be observed and finally become the dominant morphology at R/M=2/2.5. This result implies the decrease in the porosity of carbon aerogel as M content increases.

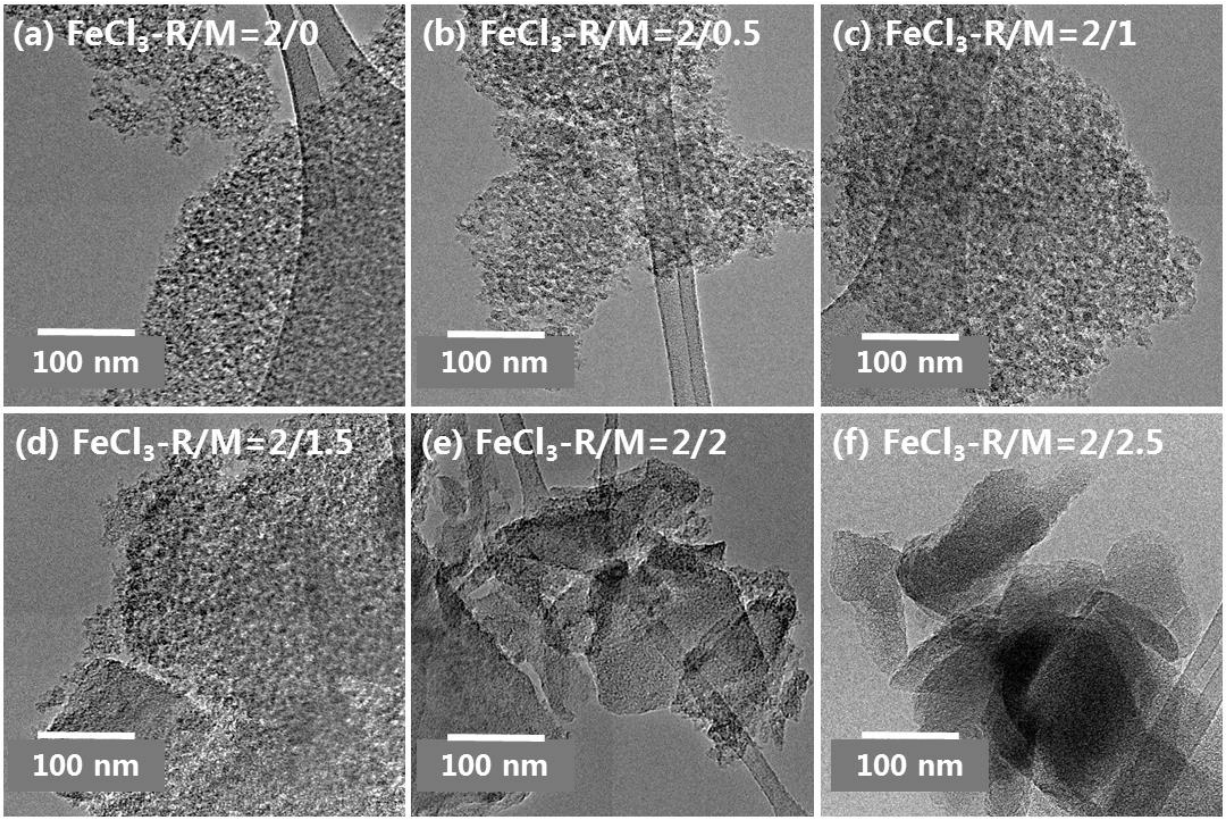

Figure 4.3 **(a)-(f)** TEM images of the catalysts prepared with different R/M ratios and $FeCl_3$ precursor.

The adsorption isotherms analyses and the pore size distribution curves obtained by N_2 sorption are shown in **Figure 4.4**. The results of BET surface area and pore volume are listed in **Table 4.3**. The catalysts with low melamine content ($FeCl_3$-R/M=2/0-2/1) present relatively higher BET surface and mesopore volume than those prepared with high melamine content ($FeCl_3$-R/M=2/1.5-2/2.5). This trend is consistent with the observation by SEM. It should be noted that the mesopore volume does not vary linearly with melamine content. It slightly increases at R/M=2/0 to 2/1, from 0.83 to 1.67 $cm^3\ g^{-1}$, then sharply decreases to only 0.02 $cm^3\ g^{-1}$ at R/M=2/2.5 (**Table 4.3**). The explanation of this tendency should be found in the micro-structure of the aerogel. The skeleton of RMF hydrogel was constructed by linking the RF and MF units in the precursor solution, and a part of the interspace between these units became the mesopores after drying and pyrolysis.[200,201] Different from thermally stable benzene rings in R, the triazine rings in M were decomposed during pyrolysis. At low M content, the venting of M decomposition products helps create mesopores without destroying the skeleton of the aerogel. However, when this decomposition becomes dominant in RMF aerogel, the skeleton collapses, thus presenting a more compact morphology and lower porosity.[228–230] In contrast to the mesopore volume, the micropore volume is almost constant with the R/M ratio at 0.42-0.45 $cm^3\ g^{-1}$. The micropores are mainly formed during pyrolysis and mainly by the reaction between NH_3 and carbon matrix, indicating a similar etching degree of carbon aerogel substrate.

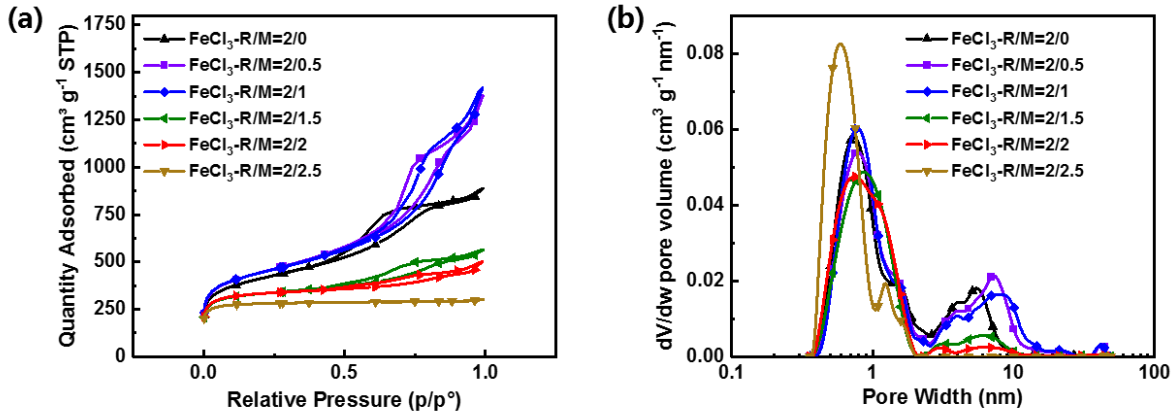

Figure 4.4 **(a)** N_2 adsorption isotherms at -196 ℃ and **(b)** pore size distribution plots obtained by using the 2D-NLDFT-Heterogenerous Surface method of the catalysts prepared with different R/M ratios and $FeCl_3$ precursor.

The minimum crystallite size of catalysts can be obtained from XRD and Raman spectroscopy, as shown in **Figure 4.5**a and b, respectively. The XRD patterns and Raman spectra show that the carbon matrix is poorly organized for all R/M values, as indicated by their large peak width at 2θ=25.6º in XRD patterns, a peak assigned to the (002) diffraction of graphite, and as indicated by a high ratio of the D_1 to G band intensities (I_{D1}/I_G around 4.7) from Raman spectra.[231,232] The average values of graphite crystallite thickness (L_c) and the in-plane graphite crystallite size (L_a) were derived from the full width at half-maximum (fwhm) of the peak at 2θ=25.6º in XRD patterns (corresponding to d_{002}=0.36 nm) and I_D/I_G of Raman spectra, respectively (**Figure 4.5**c and d). The results listed in **Table 4.4** show that both L_a and L_c values are very small. The changes in L_a and L_c are however moderate, with the L_c values ranging from 1.7 to 1.1 nm and L_a ranging from 1.11 to 0.89 nm. The global trend is a slight decrease of both L_a and L_c when R/M increase. This indicates a moderately increasing average structural disorder of the graphite matrix in the final catalysts with increasing melamine content at the aerogel preparation stage. Since the carbon atoms situated on the edge of graphite particles are preferentially etched by ammonia compared to carbon atoms located in the plane of the graphite crystallites,[184,194] the etching process trend to start at the margin between two minimum crystallite particles and the melamine content does not affects the phenomena. The catalysts prepared with different melamine content present a similar etching degree by NH_3 and micropore volume.

Table 4.4 L_a and L_c values of the catalysts prepared with different R/M ratios and $FeCl_3$ precursor.

R/M	L_a nm	L_c nm
2/0	1.11	1.7
2/0.5	1.06	1.5
2/1	0.93	1.2
2/1.5	0.95	1.2
2/2	0.93	1.2
2/2.5	0.89	1.1

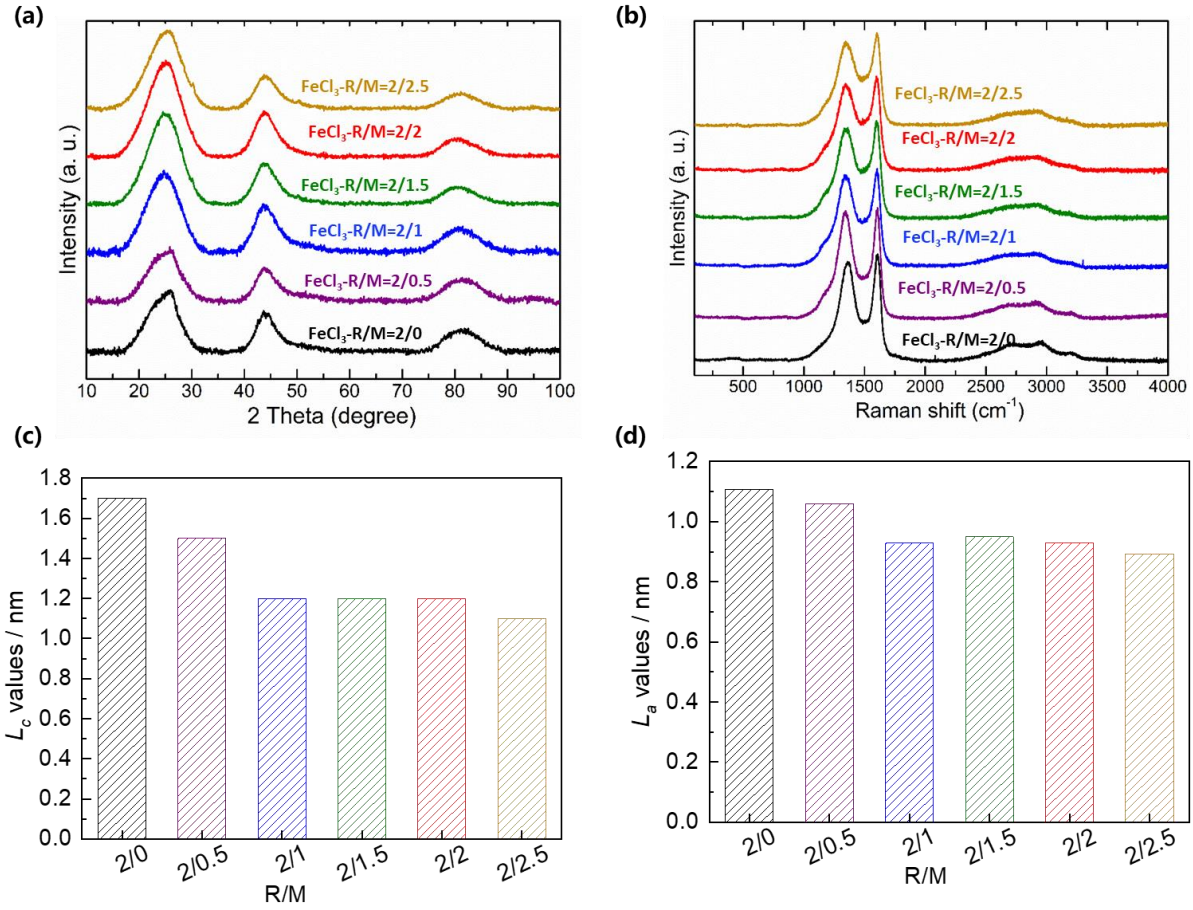

Figure 4.5 Structural and textural characterization of the catalysts prepared with different R/M ratios and $FeCl_3$ precursor. **(a)** XRD patterns and **(b)** Raman spectra; **(c)** Graphite crystalline thickness in the direction perpendicular to the graphene layers obtained from XRD (L_c) and **(d)** in-plane graphite crystallite size obtained from Raman spectroscopy (L_a).

The Fe content of catalysts was determined by ICP-MS, as listed in **Table 4.3**. A similar tendency with FePc precursor in section 3.4 is observed that Fe content increases with M content, even though the initial quantity of $FeCl_3$ is targeting to around 1 wt.% Fe content in the final catalysts. Two main hypotheses can explain this. In the first one, adding melamine helps coordinate and disperse iron in the aerogel before pyrolysis, decreasing the amount of metallic iron or iron oxide particles formed during or after pyrolysis, and therefore minimizing the amount of iron leached during the acid washing step. In the second hypothesis, the increasing amount of melamine increases mass loss of C and N as volatile products during pyrolysis, indirectly increasing the iron content in final catalysts. However, the very low Fe amount measured with R/M = 2/0 supports that our first hypothesis is the main factor accounting for the Fe content in the final catalysts. Moreover, no Fe-rich particles can be observed from TEM images or identified from XRD patterns, suggesting that Fe exists as atomically dispersed Fe-N_4 sites. However, nanometric particles of iron or iron oxides are difficult to track with TEM or XRD. Therefore, and Fe coordination was characterized by dedicated spectroscopies, as discussed in the next section.

In summary, all the catalysts in this series present a high specific surface area (>1000 m $^2g^{-1}$) and high micropore volume, which is usually considered necessary to reach a high ORR activity with Fe-N-C catalysts. However, their very different iron contents are possible to dominate their

activities instead. The relationship between micropore volume, Fe content and activity will be clarified later.

4.1.3 Chemical composition of catalysts and investigation of active site structure

The chemical composition of catalysts was investigated by XPS (**Table 4.5**). The Fe content measured by XPS is similar to that measured with ICP-MS, indicating a uniform distribution of Fe in bulk and on the surface of catalysts. The N content also shows an increasing trend with increasing M, although the relative increase is less than that of Fe content. These results indicate only a portion of nitrogen atoms in catalysts participate in the forming of Fe-N_4 active sites.

The N 1s narrow scan spectra identify a dramatic change in the type of N-groups present, the catalysts prepared with R/M = 2/0 showing a very weak signal at *ca.* 401 eV while the relative intensity of this signal increases with increasing melamine content (**Figure 4.6**a). The spectra were then analyzed by the deconvolution method used in Chapter 3. As the results in **Table 4.5**, the increasing peak at 401 eV corresponds to the component of pyrrolic N. **Figure 4.6**b presents the variation of different N species with increasing M content. It shows that only the pyrrolic N content is positively correlated with the M content. In contrast, the other N-species are almost constant or only increase slightly with increasing M content. Moreover, the molar ratio of pyrrolic N/Fe is close to 5.4 at R/M=2/0, then decreases with increasing M content, and finally, the values are stable at around 4 until $FeCl_3$-R/M=2/1.5. This number corresponds well to the stoichiometry in Fe-N_4 sites, suggesting all nitrogen atoms involved in the ligation of Fe are pyrrolic N. The values are decreased to around 3 for $FeCl_3$-R/M=2/2 and $FeCl_3$-R/M=2/2.5, suggesting the existence of other Fe species. The possible reason of relatively high pyrrolic N/Fe values at low M content is the Fe content is too low to full fill all N_4C_{12} macrocycles. It should be noted that all N atoms in catalyst $FeCl_3$-R/M=2/0 were introduced by ammonia treatment, whereas the absolute contents of all N species are almost unchanged, except pyrrolic N. These results imply M content mainly affects the pyrrolic N content, which relates to the Fe content, whereas the condition of NH_3 treatment modulates the other N components.

Table 4.5 Surface chemical composition of catalysts prepared with different R/M ratios and deconvolution of their N 1s spectra.

R/M	C at.%	O at.%	Fe at.%	N at.%	Nitrile at.%	Pyridinic at.%	Fe-Nx at.%	Pyrrolic at.%	Quaternary at.%	Graphitic at.%	Pyrrolic/Fe
					398.0 eV	398.8 eV	399.9 eV	400.9 eV	402.0 eV	403.3 eV	
2/0	95.57	1.39	0.10	2.94	1.05	0.50	0.45	0.54	0.28	0.12	5.4
2/0.5	95.22	1.63	0.16	3.00	0.94	0.55	0.43	0.61	0.35	0.13	3.8
2/1	93.69	2.89	0.22	3.21	0.84	0.52	0.52	0.78	0.38	0.18	3.5
2/1.5	94.32	1.97	0.27	3.44	0.79	0.52	0.45	1.00	0.46	0.22	3.7
2/2	93.54	2.32	0.36	3.76	0.94	0.57	0.50	1.14	0.43	0.18	3.2
2/2.5	92.91	2.49	0.43	4.17	1.01	0.66	0.53	1.30	0.48	0.19	3.0

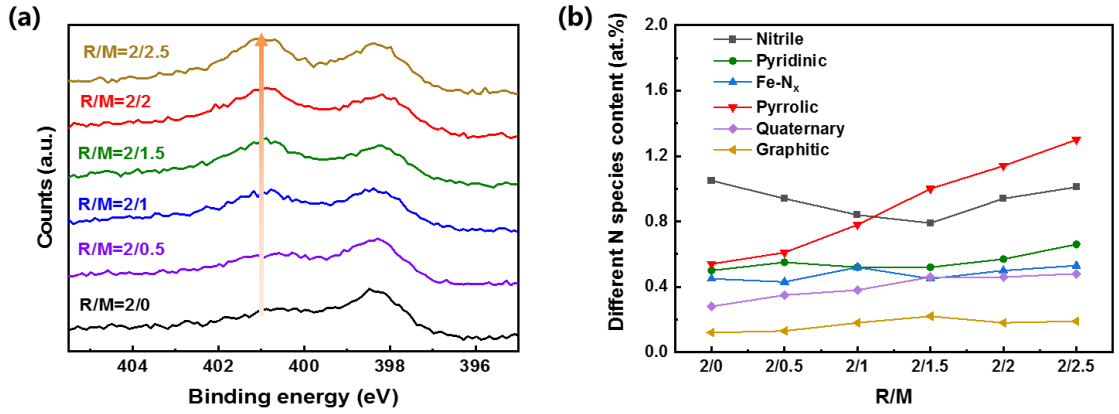

Figure 4.6 **(a)** N 1s XPS spetra of the catalysts prepared with different R/M ratios and $FeCl_3$ precursor; **(b)** Evolution of different N species content with R/M.

Insights into the type of Fe species present were obtained from Fe K-edge XAS and ^{57}Fe Mössbauer spectroscopies (from Synchrotron Soleil facilities and ICGM, respectively). **Figure 4.7**a shows selected XANES spectra for three catalysts in the series and the XANES spectrum of a reference Fe-N-C catalyst derived from ZIF-8 (labeled $Fe_{0.5}$ from ICGM laboratory) for which Fe is known to be present as Fe-N_x active sites only[98]. The spectra show high similarities, suggesting Fe is mainly present as Fe-N_x coordination structures[98,233]. However, the presence of nanometric iron oxides cannot be excluded due to similar XANES spectra with Fe-N_4 sites.[105] The Fourier transform of the EXAFS signals of down-selected catalysts (**Figure 4.7**b) are also similar to that of $Fe_{0.5}$, with a main signal at *ca.* 1.5 Å, assigned to Fe-N or Fe-O bonds.[98,187,233,234] As for XANES, the presence of nanometric iron oxide cannot be excluded since the signal from Fe-N bonds in Fe-N_x sites and Fe-O from oxides cannot be distinguished. The signal from Fe-Fe backscattering is not always discernible in nanometric oxides due to the size and/or amorphous character of nano-oxides.[105] The iron coordination was further investigated with ^{57}Fe Mössbauer spectra collected at -268 °C. Low-temperature acquisition enables distinguishing in particular nanometric iron oxides, contributing with a sextet component from atomically dispersed Fe-N_x sites contributing with quadrupole doublets.[105] The spectra of selected catalysts (**Figure 4.7**c-e) could be well fitted with appropriate combinations of doublet and sextet components. The main signal in all catalysts is a quadrupole doublet with quadrupole splitting (QS) values of 0.98-1.13 mm s^{-1}, and isomer shift (IS) value of 0.46-0.47 mm s^{-1}, which is assigned to a high-spin O-Fe(III)N_4C_{12} configuration (D1), with O representing an oxygenated species adsorbed on the metal center (**Table 4.6**).[98,105,235] A second quadrupole doublet with a high IS and QS is identified, and labeled as D3. On the basis of its distinct IS values (0.97-1.20 mm s^{-1}), this component can be unambiguously assigned to high-spin ferrous centers. While the existence of high spin Fe(II)-N_x sites cannot be excluded, the recent observation that the presence of this D3 component in Fe-N-C materials coincides with the use of Fe-chloride salts for their synthesis suggests that D3 is due to the presence of ferrous-chloride, with the quadrupole doublet signal of $FeCl_2 \cdot 4H_2O$ having Mössbauer parameters (IS and QS values) matching those of D3[70]. As the present series of catalysts is prepared with $FeCl_3$, we assign D3 in the current work to $FeCl_2 \cdot 4H_2O$[70]. Independent experimental evidence for the presence of $FeCl_2$ after $FeCl_3$ chemical vapor deposition on Zn-N-C also supported the assignment of D3[70]. The relative contribution of D3 to the absorption signal in the present work is however small, 5-8% in $FeCl_3$-R/M=2/0.5 and $FeCl_3$-R/M=2/1 and is not observed in $FeCl_3$-R/M=2/2 or $FeCl_3$-R/M=2/2.5. For the latter two, another quadrupole doublet with IS

comparable to D1 but with higher QS (2.85 mm s^{-1}) is observed, labeled D2, accounting for 16% of the signal. This doublet is commonly co-observed with the D1 component in Mössbauer spectra of Fe-N-C catalysts and assigned to a low or medium spin $Fe(II)N_4$ configuration[235]. The ferrous state of D2 may be explained by its location in the bulk of the carbon matrix or by a low affinity with O_2. The presence of D2 in the catalyst prepared with the highest melamine content coincides with a decreasing BET area (**Table 4.3**), supporting that the minor D2 contribution may result from the non-accessibility of O_2 to some $Fe\text{-}N_x$ sites. Mössbauer spectroscopy also identifies an important contribution from a broad sextet in $FeCl_3$-R/M=2/0.5, which is assigned to high-spin ferric oxide[187]. The high linewidth (3.19 mm s^{-1}, **Table 4.6**) supports ultra-small clusters that are not fully magnetically ordered at -268 °C. No sextet is detected in the spectra of $FeCl_3$-R/M=2/1 and $FeCl_3$-R/M=2/2, while two well-defined sextets (LW of only 0.27 mm s^{-1}) are identified in the spectrum of $FeCl_3$-R/M=2/2.5, assigned to ferric oxides, but accounting for only 8% of the signal (**Table 4.6**). Therefore, Mössbauer spectroscopy confirms the XANES and EXAFS results but also provides more quantitative insights, especially identifying an important contribution from ultra-small iron oxide clusters for samples prepared at low R/M value. This shows that the addition of melamine is critical to forming $Fe\text{-}N_x$ sites during the first pyrolysis. Without melamine or with too little melamine, iron probably mainly forms metallic or metal carbide species during pyrolysis. Upon exposure to air or to acid washing, these particles can remain in zerovalent state if they are perfectly covered by a graphite shell, or they can be converted partially or fully to iron oxides, depending on oxygen/proton accessibility to the surface of these particles and depending on the particle size. The iron oxide signal in $FeCl_3$-R/M=2/0.5 must thus be a consequence of the presence of iron zerovalent particles after the first pyrolysis stage. Fe cations in an acid solution can indeed partially reprecipitate, depending on the acid nature, temperature, and local iron concentration.

Table 4.6 Spectral parameters derived from the fitting of Mössbauer spectra. Isomer shift (IS), quadrupole splitting (QS), Linewidth (LW), Hyperfine Field (H) and relative signal area (%).

R/M	component	IS mm s^{-1}	QS mm s^{-1}	LW mm s^{-1}	H T	Relative area%
2/0.5	D1	0.47	0.98	1.26	-	54
	D3	1.20	2.72	0.50	-	5
	Sextet 1	1.19	-	3.19	43	41
2/1	D1	0.47	1.10	1.25	-	92
	D3	0.97	2.90	0.69	-	8
2/2	D1	0.32	1.07	0.89	-	76
	D2	0.56	2.62	1.44	-	24
2/2.5	D1	0.46	1.13	1.04	-	76
	D2	0.45	2.85	2.41	-	16
	Sextet 1	0.69	-0.1	0.27	43.5	3
	Sextet 2	0.65	+0.1	0.27	53.7	5

Together with the ICP-MS data, we can conclude that nitrogen introduced by M can bind the iron atoms and stabilize them to avoid the formation of iron nanoparticles with optimized M content. Last but not least, the signal/noise ratio and absolute signal intensity of the Mössbauer absorption spectra also reflect the Fe content in the sample, with low signal and high noise for the sample with low melamine content (R/M=2/0.5). The major contribution of D1 in this series of catalysts (increasing absolute absorption intensity of D1 with the melamine content) also suggests that the nitrogen species involved in coordinating iron in D1 sites is pyrrolic nitrogen. Pyrrolic nitrogen was indeed shown by XPS to be absent in the sample prepared with R/M =2/0 and to increase with increasing M content continuously. Moreover, the presence of D2 sites at high M content can explain decreased pyrrolic N/Fe value because Fe atoms in D2 sites are

coordinated by pyridinic N. After correcting the Fe content by percentage of D1 in **Table 4.6**, the pyrrolic N/Fe values of $FeCl_3$-R/M=2/2 and $FeCl_3$-R/M=2/2.5 in **Table 4.5** are 4.2 and 4.0, respectively, which correspond well to the stoichiometry in Fe-N_4 sites.

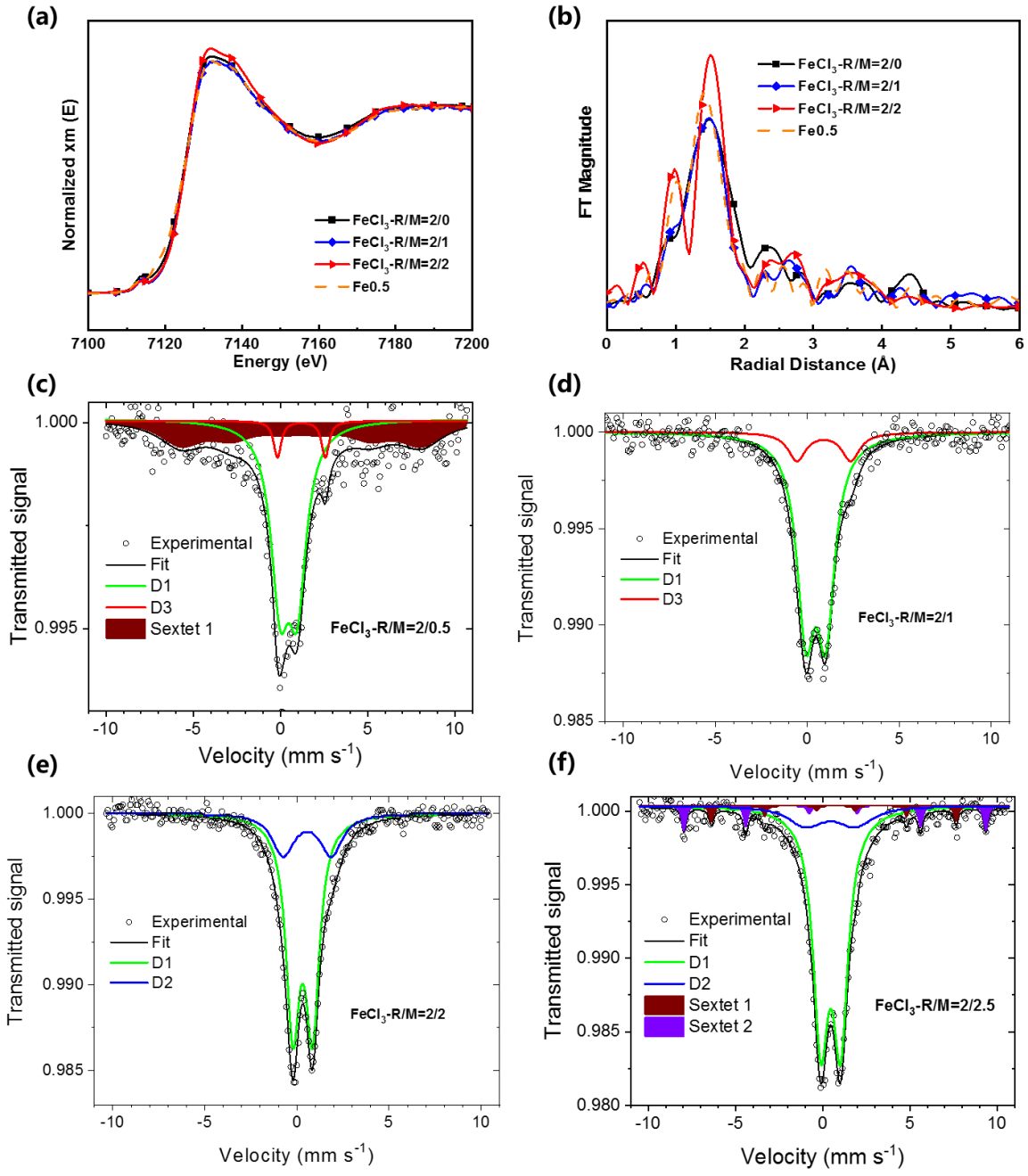

Figure 4.7 **(a)** XANES and **(b)** Fourier transforms of the EXAFS spectra measured at Fe K-edge. Mössbauer spectroscopy characterization of selected catalysts. **(c)** $FeCl_3$-R/M = 2/0.5, **(d)** $FeCl_3$-R/M = 2/1, **(e)** $FeCl_3$-R/M = 2/2, and **(f)** $FeCl_3$-R/M = 2/2.5. The spectra were acquired at -268 ℃.

4.1.4 Electrochemical characterization of catalysts

The CV curves of catalysts prepared with different M content are shown in **Figure 4.8**a. $FeCl_3$-R/M=2/2.5 has the lowest electrochemical active area, whereas $FeCl_3$-R/M=2/1 has the largest surface area. This agrees with tendency that the larger specific surface area and

mesopore volume lead to a larger electrochemical available area (**Table 4.3**)[233]. However, the variation of their CV areas is moderate, even though their BET areas are reduced by *ca.* 1/3 and mesopore volume almost disappeared when M content increased from R/M=2/1 to 2/2.5 (from 1.67 to 0.02 $cm^3\ g^{-1}$). The possible reason is the catalysts with higher M content also possess higher Fe content, which contributes more electrochemical active surface that compensates for their lower specific surface area.

The polarization curves show increasing half-wave potential with increasing M content up to R/M = 2/2, while at R/M = 2/2.5, the activity seems to achieve a plateau or even to decrease slightly (**Figure 4.8**b). All polarization curves except those of $FeCl_3$-R/M=2/0 and $FeCl_3$-R/M=2/2.5 present a sharp kinetic-to-diffusion transition region, indicative of adequate mass-transport properties, at least in RDE setup[187]. The catalysts exhibit similar Tafel slopes around 60 mV dec^{-1} (**Figure 4.8**c), consistent with the literature and demonstrating that the rate-determining step of the ORR mechanism is the same in this series of catalysts.[64,210,233,236] This is in line with the dominant signal from the component D1 in the Mössbauer spectra, supporting that the change in ORR activity is mainly due to a change in the number of sites, while the fundamental ORR mechanism on the active sites is unmodified. The mass activity increases by *ca* 4-fold from R/M = 2/0 to 2/1 (0.47 to 2.04 A g^{-1}), then increases slowly from 2/1 to 2/2 (2.04 to 3.00 A g^{-1}), and decreases slightly at R/M = 2/2.5 (2.22 A g^{-1}). The mass activity for the optimized material, $FeCl_3$-R/M=2/2, is only slightly lower than that of the commercial Fe-N-C catalyst (Pajarito powder PMF D14401, 4.04 A g^{-1} as seen in **Figure 4.8**b).

Table 4.7 RDE tests of the catalysts prepared with different R/M ratios and $FeCl_3$ precursor. The mass activity was measured in O_2-saturated 0.05 M H_2SO_4 at 1600 rpm and scan rate of 10 mV s^{-1}. The SD and the TOF values were determined by nitrite stripping method considering a 3 electrons process (A.2.8)

R/M	$MA_{0.8}$ A g^{-1}	$MA_{0.8}$ after 500 cycles A g^{-1}	Loss ratio	Tafel slope mV dec^{-1}	SD×10^{18} g^{-1}	TOF *e* s^{-1} $site^{-1}$
2/0	0.47	0.26	-47%	59	4.52	0.65
2/0.5	0.79	0.39	-51%	60	6.02	0.82
2/1	2.04	1.08	-47%	52	8.04	1.58
2/1.5	2.34	1.73	-26%	60	6.30	2.32
2/2	3.00	2.22	-26%	60	5.66	3.31
2/2.5	2.22	1.59	-28%	69	5.95	2.33

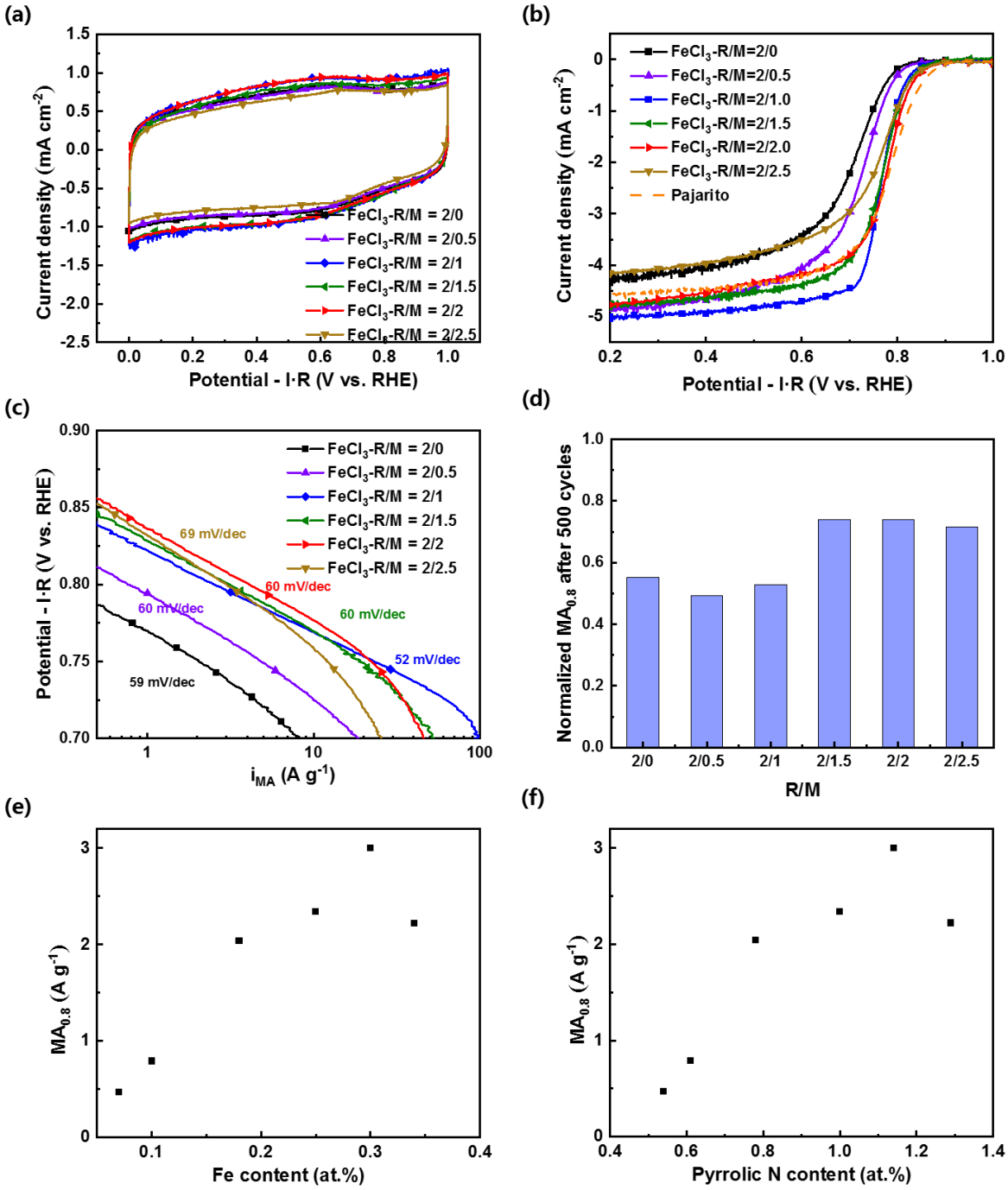

Figure 4.8 Electrochemical characterization of catalysts prepared from different R/M ratio and $FeCl_3$ precursor recorded in 0.05 M H_2SO_4. **(a)** CV curves in N_2-saturated electrolyte; **(b)** Polarization curves in O_2-saturated electrolyte at ω = 1600 rpm and v = 10 mV s^{-1}; **(c)** Tafel plots of the O_2-transport and background-current corrected kinetic current obtained from the steady-state Ohmic drop-corrected *I–E* curves at ω= 1600 rpm; **(d)** normalized current after 500 CV cycles between 0.6-1.0 V in N_2 saturated electrolyte; relationships between **(e)** mass activity in RDE setup and Fe content, **(f)** mass activity in RDE setup and pyrrolic N content.

In the search for structure-property relationships, **Figure 4.8**e plots the mass activity of catalysts as a function of their Fe content obtained from ICP-MS. A linear trend can be observed up to the Fe content of 0.3 at.% (1.36 wt.%), corresponding to the catalyst $FeCl_3$-R/M=2/2, with the highest mass activity 3.0 A g^{-1} for this series. This trend is explained by Mössbauer

spectroscopy, showing that most of Fe atoms are present as atomically dispersed Fe-N_x sites, except at low melamine content. Therefore, the site density also increases with the bulk Fe content. Further increasing the M content (and the Fe content) results in a slight decline of the activity due to the restricted mass transfer. The very low mesopore volume in $FeCl_3$-R/M=2/2.5 prevents reactants in electrolyte from accessing the active sites. This can be demonstrated by its higher Tafel slope (79 mV dec^{-1}), representing a slow kinetic-to-diffusion transition region[187]. The mass activity also shows a positive correlation with the pyrrolic N content obtained from XPS analysis (**Figure 4.8**f), which further demonstrates the Fe-N_4 active sites are constructed by pyrrolic N. It should be noticed that the activity of our catalysts shows little relationship with micropore volume, which is generally considered an index of the number of active sites[61,64,105,194]. This lack of correlation is due to the limitation of active Fe at low M content, not by micropores, in the present synthetic approach. **Figure 4.9** provides a further description of the formation pathway of Fe-N_4 active sites. The organic aerogel was first carbonized to form N-doped carbon layers at around 500 ℃, and Fe precursor was transformed to nanoparticles simultaneously. When further increasing the temperature, the Fe atoms are released from Fe-rich nanoparticles. In the rich melamine aerogel base, the free Fe atoms have more chance to be captured into a neighbor NC defect during the pyrolysis, thus forming more Fe-N_4 active sites[213]. On the contrary, in the poor melamine aerogel base, few Fe atoms can be hosted, thus leading to a low density of active sites.

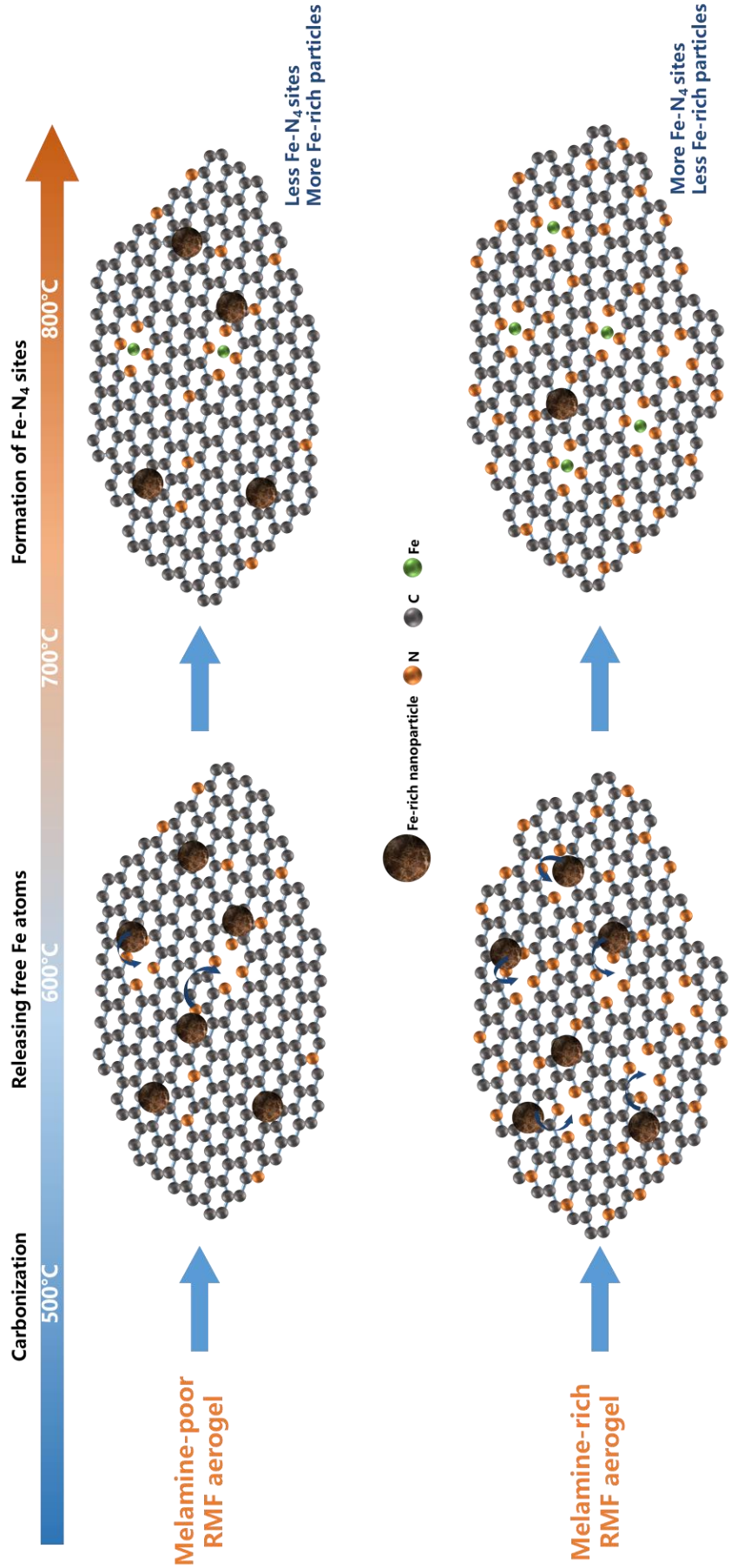

Figure 4.9 Evaluation pathway of Fe-rich nanoparticles to Fe-N_4 active site during the pyrolysis in poor/rich melamine content aerogel.

Figure 4.8d shows the normalized ORR mass activities after 500 cycles of CV between 0.6 and 1.0 V *vs*. RHE in N_2 saturated 0.05 M H_2SO_4. The MA values of catalysts prepared with low M content (R/M=2/0-2/1) drop around 50%, whereas activity loss is less than 30% for the catalysts prepared with high M content (R/M=2/1.5-2/2.5). Better durability is accompanied by a sharp decrease of their mesopore volume when M content increases from R/M=2/1 to 2/2.5 associated with a high Fe amount. This coincidence implies a potential relationship between durability and mesopore volume and Fe content of the catalyst. The carbon oxidation reaction occurs at high potential during CV cycles and amorphous carbon domains that are preferentially corroded[231]. The characterizations of XRD and Raman spectra show that average minimum crystallite sizes are almost identical for all catalysts, indicating that the degree of graphitization of the carbon matrix is similar. In this case, the reason is linked to the presence of Fe. The degradation of catalysts may be explained because the catalysts with low M content have Fe-rich nanoparticles that are unstable during CV cycles in an acidic medium. The existence of Fe oxides has been demonstrated by the Mössbauer spectrum in the sample $FeCl_3$-R/M=2/0.5 (**Figure 4.7**c), and more Fe oxides can be expected in $FeCl_3$-R/M=2/0 due to its lower M content. As discussed before, these oxides are converted from the Fe nanoparticles perfectly covered by a graphite shell to survive from acid leaching. During the CV cycles, the protective layers of graphite are corroded to expose Fe oxide nanoparticles so that they can be eliminated by acidic electrolyte. As a result, not only the activity from micropore-hosted Fe-N_4 sites but the contribution of Fe oxides is eliminated compared with catalysts prepared with high M content (M more than R/M=2/1.5). Therefore, the catalysts containing oxide nanoparticles lose more activity than those with pure Fe-N_4 active sites. However, this explanation does not adapt to the sample $FeCl_3$-R/M=2/1, in which no Fe oxide is detected by the Mössbauer spectrum (**Figure 4.7**d). Because the carbon oxidation rate is faster on the edge of carbon sheets than on the basal plane, the etching of carbon starts from the boundary between crystallite, where the micropores created by NH_3 treatment situate as well[184]. Therefore, it can be inferred that the Fe-N_4 sites hosted between boundaries are eliminated faster than graphene-defect sites[184]. The possible reason for the relatively low durability of $FeCl_3$-R/M=2/1 is its high mesopore volume helps increase the accessibility of electrolyte to the edge of crystallite, thus leading to more electrochemical oxidation.

To gain further insights into the fundamental reasons for the evolution of the mass activity with the melamine content, the SD and the TOF (**Table 4.7**) were evaluated using the nitrite adsorption/reduction electrochemical method[231]. The SD value increases with M content from R/M=2/0 to 2/1, reaching the maximum value of 8.04×10^{18} sites g^{-1}, whereas it declines when further increasing M content. These results are not in agreement with the previous conclusion that the increasing mass activity is because the increasing Fe content leads to higher SD values instead of TOF. To explain this discrepancy, note that the decline of SD when M content increased from R/M=2/1 to 2/1.5 coincides with a sharp decrease of mesopore volume, which may limit the accessibility of reductive NO_2^- to active sites[231]. Therefore, the SD values at high M content are possibly underestimated. This agrees with the research of Strasser *et al.* that the SD (CO) values derived from gaseous CO cryo chemisorption were 2-8 folds greater than the SD (NO_2^-) values[237]. This is largely attributed to the fact that Fe surface sites located inside micropores are less accessible for reductive NO_2^- adsorption, whereas gaseous CO has facile accessibility to those sites. Hence, these sites are not probed by the nitrite stripping technique, and the SD values obtained from nitrite stripping should be regarded as the low bound of the surface Fe site density of the catalyst. The precaution of the SD result of nitrite stripping was also proposed in previous research on ammonia treated Fe-N-C catalyst[231]. Two main issues related to the nitrite stripping method were proposed to explain the discrepancy: (i) the measurement of NO_2^- adsorption/desorption needs to be performed at pH=5.2, which is less acidic than the normal conditions of RDE tests; (ii) even if most of the ORR activity is lost

during the NO_2^- adsorption, a non-negligible activity remains, suggesting that NO_2^- could not be adsorbed into all exposed sites because of their very high chemical specificity[231,237]. Thus, this method cannot be applied for all Fe-N-C catalysts, in particular for those treated by NH_3-based second pyrolysis, as the chemisorption of NO_2^- might be impacted by the basicity of N-groups. This NH_3 treatment can enormously increase the basicity of the N-C matrix and consequently reduce the interaction strength between the NO_2^- and the Fe-N_4 active sites because of the electron-donating properties of the neighboring nitrogen groups. It should be mentioned that even though our SD values are underestimated, they are still comparable with the catalysts measured under the same conditions. In the work of Kumar *et al.*[231], their catalyst labeled as Fe-HT_2 reaches the SD value of 2.6×10^{18} sites g^{-1} ($MA_{0.8}$= 4.2 A g^{-1}), which is only half of $FeCl_3$-R/M=2/2 with similar mass activity ($MA_{0.8}$=3.0 A g^{-1}).

On the contrary, the SD value measured at low M content is possible to be relatively overestimated because the increase of SD value is much lower than mass activity from R/M = 2/0 to 2/1 (*ca.*2 folds of SD *vs. ca.* 4 folds of mass activity). The unexpectedly high SD measured at low R/M can be explained by the lack of selectivity of the nitrite stripping method, which counts not only Fe-N_x sites on the surface but also Fe oxides. This caveat of the nitrite stripping method had been unveiled in the frame of a study on the degradation mechanisms of Fe-N-C in O_2 saturated acidic solution[238]. The significant presence of Fe oxides is detected by ^{57}Fe Mössbauer spectroscopy in $FeCl_3$-R/M=2/0.5 (accounting for 41 % of the signal intensity), and it can be hypothesized that even more Fe oxides would be present in $FeCl_3$-R/M=2/0. Combining the two factors, the variation of SD with M content becomes moderate and seems uncorrelated with mass activity. The TOF values are calculated by using the SD values measured at pH=5.2 and the mass activity measured in 0.05 M H_2SO_4. The TOF values seem consistent with the mass activity variation, which keeps increasing from R/M=2/0 to 2/2 then declining at R/M=2/2.5. However, this coincidence cannot be the explanation of mass activity because ^{57}Fe Mössbauer spectroscopy has demonstrated the nature of the main active sites are D1 when M content is more than R/M=2/1. Hence the TOF values should keep constant. The variation of SD values is too moderate to affect the tendency of calculation results of TOF values.

The ORR activity and power performance of these catalysts were then investigated in a 5 cm^2 single cell PEMFC. **Figure 4.10**a shows the H_2/O_2 polarization curves of all catalysts, with trends in activity at 0.8 V and overall cell performance in line with the trends observed in RDE. For a quantitative comparison of ORR activity trend with the melamine content, **Figure 4.10**b reports the current density at 0.8 V in PEMFC (a voltage at which the current density is mostly controlled by ORR kinetics) as a function of the melamine content. It can be seen that the trend and proportional change of activity with M is similar to that observed in RDE (**Figure 4.8**b), increasing by a factor 4 from R/M = 2/0 to 2/2 and thereafter decreasing by about 35% from R/M = 2/2 to 2/2.5. The similar activity trends observed in RDE and PEMFC support that the I/C ratio of 2 for the PEMFC cathode is appropriate for all catalysts of the present series. Otherwise, lower-than-expected activity would have been observed for some materials in PEMFC. For assessing the oxygen-transport properties of the different Fe-N-C cathodes (different R/M values for aerogel preparation), we compare the current densities measured at 0.3 V (voltage at which mass-transport plays a key role on the current density achieved) with pure O_2 or with air (**Figure 4.10**d). The figure shows that the magnitude of the decrease in current density when switching from O_2 to air is comparable for all catalysts, despite huge differences in the mesopore volume of this series of catalysts. Therefore, mesopores are not a necessary criterion to reach high PEMFC performance of Fe-N-C catalysts. For the current synthesis approach, the addition of melamine is therefore critical to increase the Fe content, SD,

and ORR activity. In contrast, the impact is less significant on the mass-transport properties of the cathode active layers.

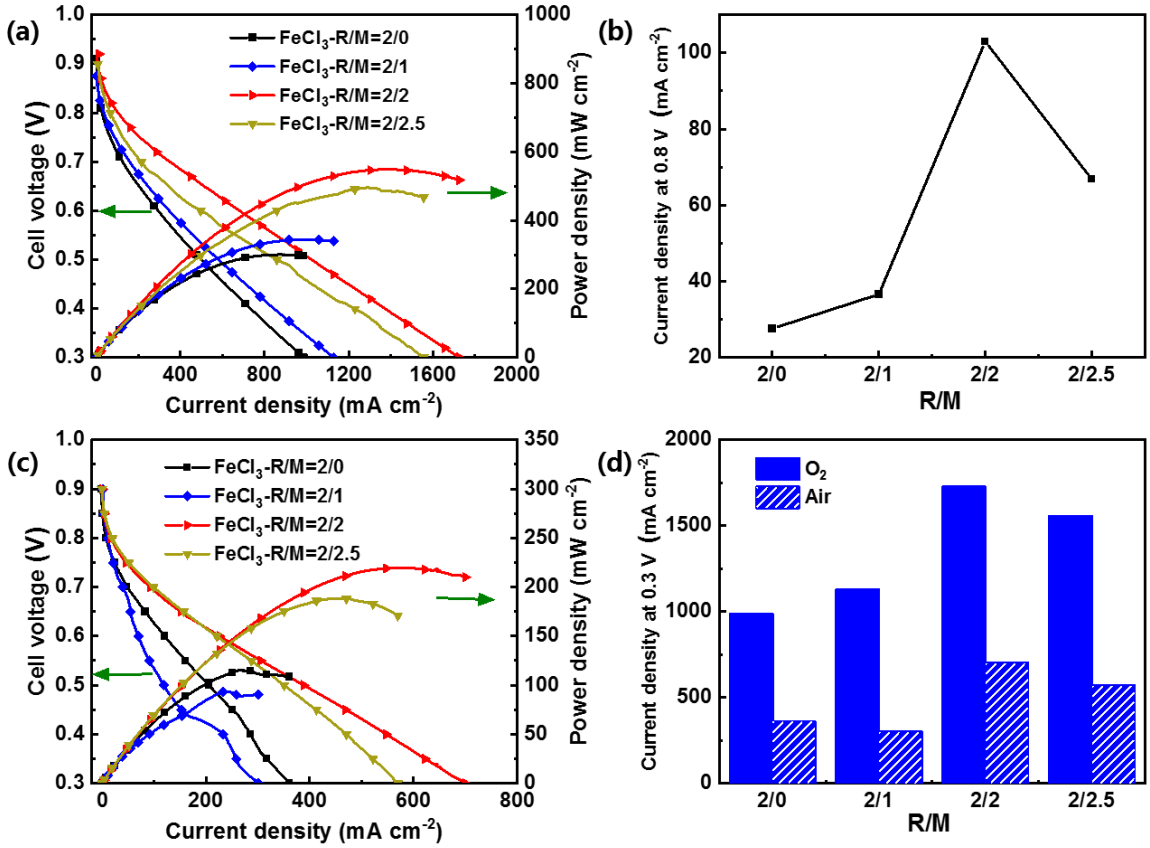

Figure 4.10 Investigation of the set of aerogel Fe-N-C catalysts as PEMFC cathodes. **(a)** H_2/O_2 PEMFC polarization curves. **(b)** Current density at 0.8 V as a function of the melamine content at the aerogel preparation stage. **(c)** H_2-air PEMFC polarization curves. **(d)** Comparison of the current density at 0.3 V measured with O_2 or air, for each catalyst. The measurements were performed with T_{cell} = 80 °C, 100 % RH, *P*cathode = *P*anode = 2 bar_{abs}, the H_2, and O_2 flow rates were 150 mL min^{-1} while the air flow rate was 480 mL min^{-1}.

4.1.5 Conclusion

In conclusion, the impacts of melamine content on the ORR activity and mass transport properties of Fe-N-C aerogel catalysts were systematically investigated. The mesopore volume of aerogel catalysts slightly increased at low M content (from R/M=2/0 to 2/1) due to the decomposition of M during pyrolysis, then sharply decreased at higher M content because too many bond ruptures collapse the skeleton of aerogel. In contrast, the average graphite crystallite size and the micropore volume were almost unaffected by the change in M content. The absolute amount of Fe increased with M content, and the absolute amount of Fe-N_4 sites also increased with M content. From the analysis of XPS spectra, the pyrrolic N content is positively correlated with the increasing M content, supporting that most active Fe atoms are ligated by pyrrolic nitrogen. This is in line with Mössbauer spectra, identifying that most of the Fe sites are D1 sites, assigned to porphyrinic type FeN_4C_{12} structures. The atomically dispersed nitrogen in melamine can stabilize the Fe during pyrolysis, avoiding or minimizing the formation of iron nanoparticles. The electrochemical tests in RDE show a linear relationship between mass activity and Fe content up to 0.3 at.% ($FeCl_3$-R/M=2/2), with the highest mass activity of 3.0 A

g^{-1} at 0.8 V. This trend is in line with the physico-chemical characterization that most of Fe atoms exist as atomically dispersed Fe-N_x sites. Further increase of melamine content reduces the mass activity due to low accessibility to the active sites. Their ORR performance in PEMFC exhibits a similar trend with RDE setup using adapted ink formula. All polarization curves in H_2-air PEMFC do not collapse, indicating excellent mass transport properties of aerogel-based catalysts.

4.2 Impact of melamine content with different Fe precursors

In this section, the Fe-N-C catalysts were synthesized with modulated M content and different Fe precursors (FePc and $Fe(NO_3)_3$) in order to compare the results obtained with $FeCl_3$ and to see if the previous conclusion can be generalized to another salt or iron precursor with preexisting active sites (section 3.1). Therefore, it is expected to obtain the best catalyst with adapted M content and $Fe(NO_3)_3$ precursor. The two catalysts were prepared following the same gel composition with $FeCl_3$-R/M=2/2, and the quantity of Fe precursor was decided by molar ratio (R+M):Fe=1:0.01 to gain *ca.*1 wt.% Fe in the final catalysts as well. As for the FePc precursor, the pH value of polycondensation process was controlled at around 6 to preserve as many mesopores as possible, according to the discussion in section 3.2. The pH value of polycondensation process with $Fe(NO_3)_3$ precursor was adjusted to 8 to dissolve the precipitation generated after introducing iron salt as for $FeCl_3$. The two catalysts are noted by FePc-R/M=2/2 and $Fe(NO_3)_3$-R/M=2/2, respectively. After two pyrolysis steps, their total mass loss is almost constant for different Fe precursors (around 80% in **Table 4.8**), which is consistent with other catalysts. The Fe contents determined by ICP-MS are similar to $FeCl_3$-R/M=2/2, which are higher than the value of catalyst prepared with the same iron precursor at low M content (R/M=2/1). These results further confirm the stabilization effect of M on the atomically dispersed Fe in the carbon aerogel. Meanwhile, their high Fe content also implies a higher activity.

4.2.1 Texture and structure of catalysts

The morphologies of two catalysts are dramatically changed under SEM. As seen in **Figure 4.11**a and b, the catalysts prepared with FePc precursor display a porous structure. In contrast, the particle surface of $Fe(NO_3)_3$-R/M=2/2 is more compact, and no significant mesopore can be observed. The N_2 adsorption isotherm curves at -196 ℃ and corresponding pore size distribution plots are shown in **Figure 4.11**c and d, respectively, and the corresponding pore volumes are listed in **Table 4.8**. In according with the observation under SEM, even though the R/M value was constant, the different Fe precursor and pH conditions still affect the porosity of the final catalyst. Compared with the catalysts prepared with iron salts ($FeCl_3$ and $Fe(NO_3)_3$), FePc-R/M=2/2 has the highest mesopore volume (0.73 cm^3 g^{-1}), which is far over the others. The mesopore volume in $FeCl_3$-R/M=2/2 (0.25 cm^3 g^{-1}) declines to one-third of FePc-R/M=2/2 and almost disappears in $Fe(NO_3)_3$-R/M=2/2 (0.04 cm^3 g^{-1}). The negative effect on mesopore volume of increasing M content is confirmed for all catalysts, whereas the degree of decline is different. The possible reason for this discrepancy is their different pH values during polycondensation. According to the discussion in section 3.2, the mesopore volume of the catalyst prepared at pH=6 is much higher than at pH=8 with FePc as the precursor. NaOH solution is not only a reagent of pH adjustment for the solubilization of the precipitates but also a catalyst for polycondensation of RMF hydrogel. Using a high concentration of catalyst causes the formation of many small network clusters during gelation step. The pores between clusters

are also small as a result[200]. Therefore, the catalyst FePc-R/M=2/2 prepared at pH=6 gives a much higher mesopore volume than the catalyst prepared at pH=8. Moreover, this explanation is also appropriate for the difference between $FeCl_3$-R/M=2/2 and $Fe(NO_3)_3$-R/M=2/2. Since the target of pH adjustment is to dissolve the precipitation after introducing the iron salt precursors, the quantity of NaOH is decided by the point that the precipitation disappears and the transparent solution is obtained. The catalyst $Fe(NO_3)_3$-R/M=2/2 consumed more NaOH to dissolve the precipitation thus the final pH value is slightly higher than $FeCl_3$-R/M=2/2. On the contrary, even though the mesopore volume of catalyst $Fe(NO_3)_3$-R/M=2/2 is small, it possesses a similar BET surface area with FePc-R/M=2/2 due to higher micropore volume. This result indicates the mesopore volume does not affect the accessibility of NH_3 to the carbon aerogel.

Table 4.8 Physicochemical characterization of the catalysts with different Fe precursors at R/M=2/2.

Fe precursor	Total mass loss wt.%	ICP Fe		BET surface ($m^2\ g^{-1}$)	Vtotal ($cm^3\ g^{-1}$)	Vmicro ($cm^3\ g^{-1}$)	Vmeso ($cm^3\ g^{-1}$)
		wt.%	at.%				
FePc	78%	1.42	0.31	1180	1.22.	0.40	0.73
$Fe(NO_3)_3$	79%	1.31	0.28	1221	0.55	0.47	0.04
$FeCl_3$	81%	1.36	0.30	1271	0.78	0.45	0.25

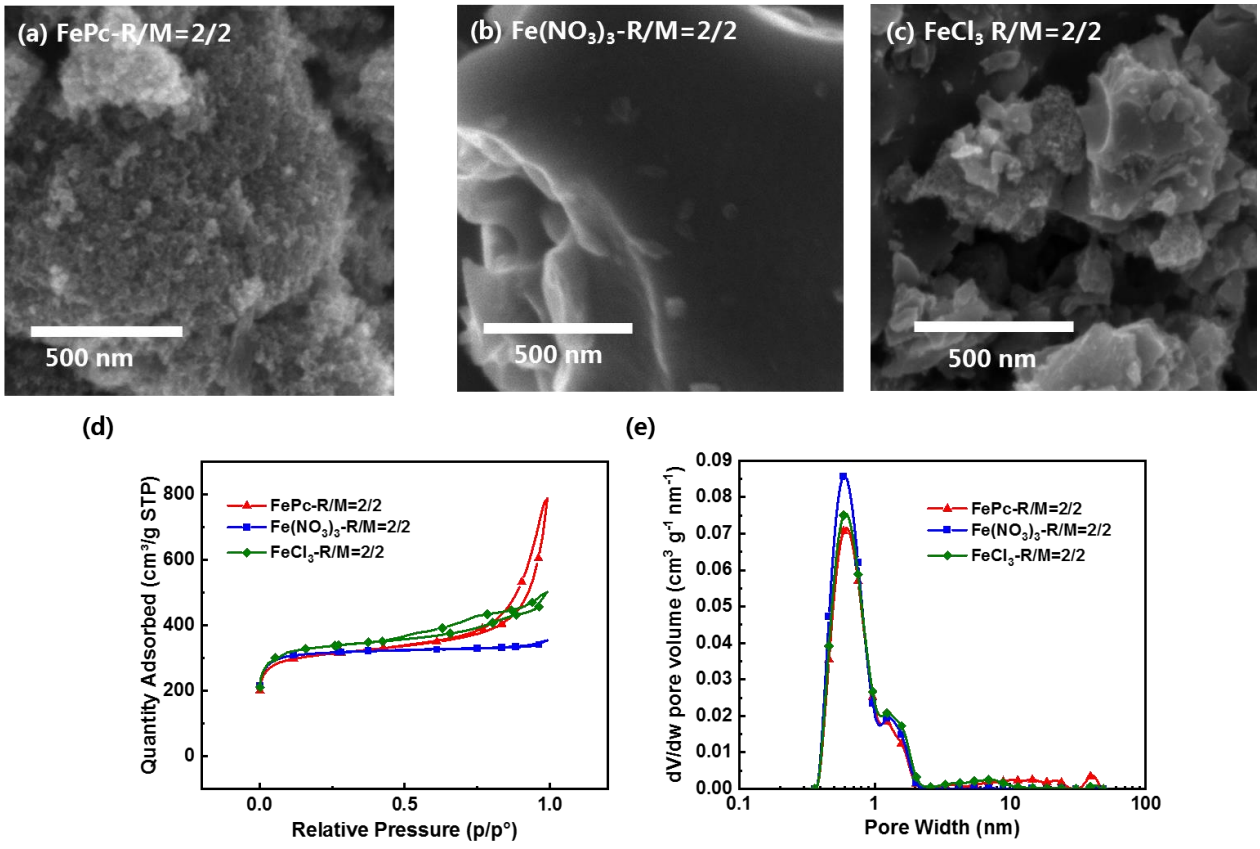

Figure 4.11 **(a)-(c)** SEM images of the catalysts prepared with different Fe precursors **(d)** N_2 adsorption isotherms at -196 ℃ and **(e)** pore size distribution plots obtained by using the 2D-NLDFT-Heterogenerous Surface method.

The TEM images of two catalysts (**Figure 4.12**) show a similar trend with SEM on mesopore volume with N_2 sorption results. **Figure 4.12**a presents a high porous carbon layers for FePc

(as $FeCl_3$), whereas the carbon in **Figure 4.12**b is more compact for $Fe(NO_3)_3$). No nanoparticles can be observed in both figures, indicating most of Fe is atomically dispersed in carbon aerogel. **Figure 4.12**c shows the XRD patterns of two catalysts. Similar to our previous discussion, no significant peak belonging to iron oxide or metallic iron can be indexed. Two bumps at around 2θ=26 °and 45 °correspond to the diffraction of low crystalized carbon. Three weak peaks at 2θ=26.4 °, 34.3 °, and 54.6 °that are not able to index can be found in $Fe(NO_3)_3$-R/M=2/2, which may relate to the by-products of iron salt.

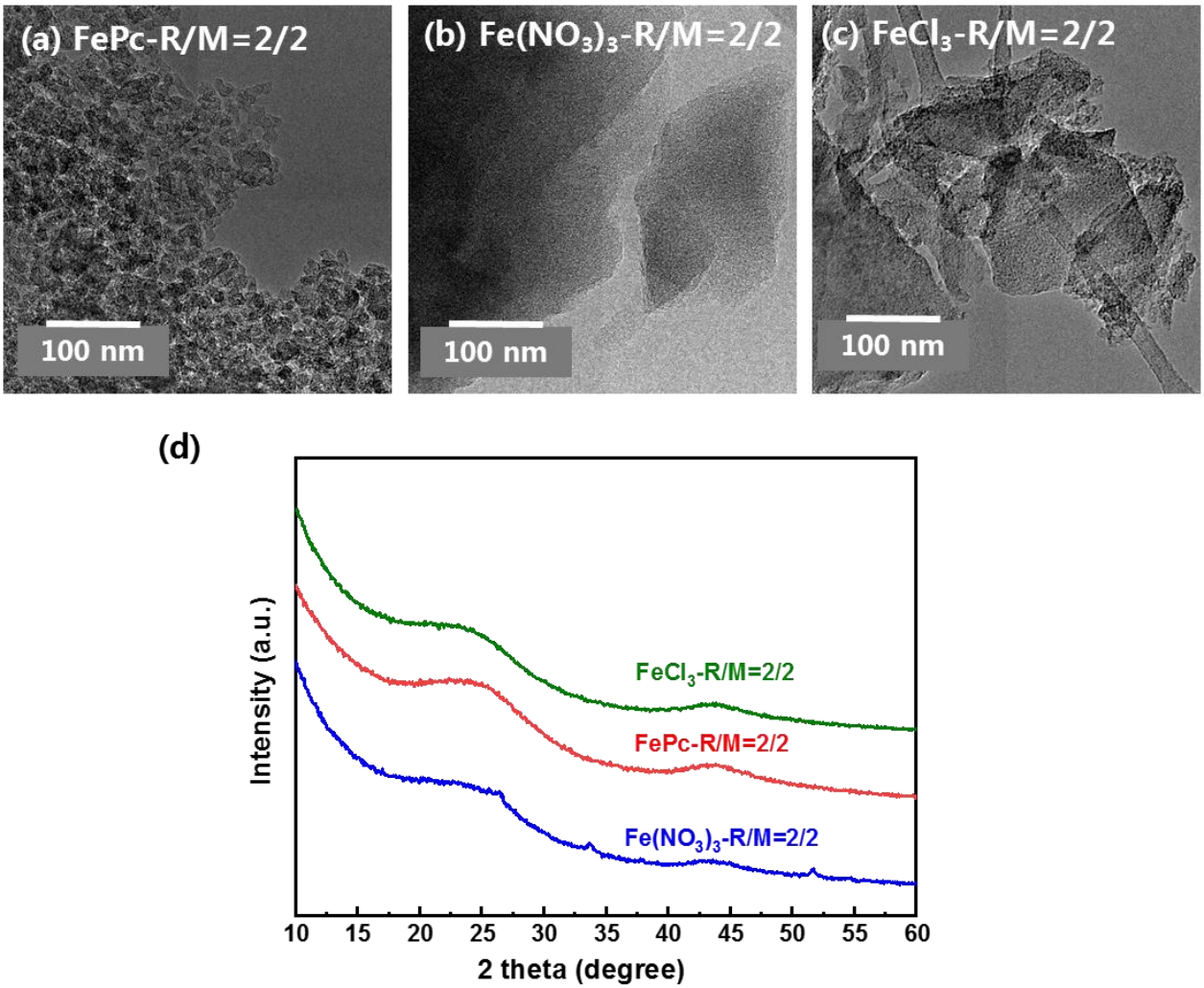

Figure 4.12 **(a)-(c)** TEM images and **(d)** normalized XRD patterns of the catalysts prepared with different Fe precursors at R/M=2/2.

4.2.2 Chemical composition of catalysts

The chemical composition of catalysts was investigated by XPS (**Table 4.9**). The surface Fe content of FePc-R/M=2/2 measured by XPS is close to that measured with ICP-MS, indicating a uniform distribution of Fe in bulk and on the surface of catalysts, whereas the bulk Fe contents of FePc-R/M=2/0 and FePc-R/M=2/1 are much lower than the surface Fe content. In section 3.4, higher Fe content on the surface of later catalysts is attributed to more Fe atoms being exposed by NH_3 treatment. This phenomenon can be explained by two possible hypotheses: (i) with the etching of carbon during NH_3 treatment, the Fe atoms detached from edge of carbon layers are left and reform Fe-N_4 centers on the surface to realize the enrichment of Fe; (ii) some

encapsulated Fe-rich nanoparticles are exposed after the above carbon layers are removed by NH_3. The first hypothesis can be verified by the variation of Fe content before and after pyrolysis, which will be further discussed in Chapter 5. The similar Fe contents of FePc-R/M=2/2 obtained from ICP-MS and XPS maybe support the second hypothesis. As discussed in section 4.1, the addition of melamine is crucial for the formation of atomically dispersed Fe. Therefore, high melamine content in FePc-R/M=2/2 can reduce the yield of Fe-rich nanoparticles, thus promoting the uniform distribution of Fe, whereas FePc-R/M=2/0 and FePc-R/M=2/1 with relatively low M contents are more likely to exist Fe-rich nanoparticles, which leads to uneven distribution of Fe. However, this should be further discussed with the results of electrochemical tests. The XPS value of $Fe(NO_3)_3$-R/M=2/2 is slightly higher than the result of ICP-MS, indicating a higher concentration of Fe on the surface (as for $FeCl_3$). It should be noted that the FePc precursor has a stronger trend to form Fe-rich nanoparticles than the other Fe salt precursors. The possible reason is that insoluble FePc powder is less dispersed than soluble Fe salts, thus tending to agglomerate during pyrolysis. This result implies that the preexisting active site structure in Fe precursor cannot be conserved during the first carbonization step. by The research of Li *et al.* can support this guess, that no Fe-N_4 sites can be found if the pyrolysis temperature is lower than 600 ℃, much higher than the decomposition temperature of FePc[213]. The coordination structure in the FePc decomposed at high temperature and released free Fe atoms, which may form Fe-N_4 active sites if they were captured by the N-C defect nearby or sintered and aggregated into Fe clusters in the absence of nitrogen defects in the carbon aerogel. The N content also shows an increasing trend with increasing M content, especially the pyrrolic N. The molar ratios of pyrrolic N/Fe are close to 4 for FePc catalysts, indicating a high proportion of D1 site, whereas the $Fe(NO_3)_3$ catalyst has a similar ratio to the $FeCl_3$ catalyst, implying the formation of D2 site. These results suggest that the mesopores are still important in exposing more D1 sites on the catalyst surface, although they exhibit little effect on mass transport properties.

Table 4.9 Surface chemical composition of catalysts prepared with different Fe precursors and deconvolution of their N 1s spectra.

Fe precursor	C at.%	O at.%	Fe at.%	N at.%	Nitrile at.%	Pyridinic at.%	Fe-Nx at.%	Pyrrolic at.%	Quaternary at.%	Graphitic at.%	Pyrrolic/Fe
					398.0 eV	398.8 eV	399.9 eV	400.9 eV	402.0 eV	403.3 eV	
FePc	93.90	2.33	0.30	3.47	0.80	0.51	0.45	1.12	0.39	0.20	3.7
$Fe(NO_3)_3$	93.24	2.44	0.39	3.94	0.93	0.64	0.48	1.25	0.46	0.18	3.2
$FeCl_3$	93.54	2.32	0.36	3.76	0.94	0.57	0.50	1.14	0.43	0.18	3.2

4.2.3 Electrochemical characterization of catalysts

The CV curves of catalysts prepared with different Fe precursors at R/M=2/2 are shown in **Figure 4.13**a, along with two samples prepared at low M content as the comparison. It is interesting to see that among three catalysts prepared with FePc precursor and different R/M values, the FePc-R/M=2/1 has the largest electrochemical available area, corresponding well to its largest BET area and micropore volume (refer to **Table 3.11**). Although the FePc-R/M=2/0 has the largest mesopore volume, it contributes less to both BET and electrochemical available areas than micropore. The BET area of $Fe(NO_3)_3$-R/M=2/2 is also slightly higher than that of FePc-R/M=2/2, thus giving a slightly larger CV area (**Table 4.9**).

Table 4.10 RDE tests of the catalysts prepared with different Fe precursors at R/M=2/2.

Fe precursor	R/M	$MA_{0.8}$ A g^{-1}	$MA_{0.8}$ after 500 cycles A g^{-1}	Loss ratio	Tafel slope mV dec^{-1}
FePc	2/2	2.12	1.21	-43%	66
$Fe(NO_3)_3$	2/2	3.58	2.74	-23%	61
$FeCl_3$	2/2	3.00	2.22	-26%	60

The polarization curves of catalysts prepared with FePc precursor in **Figure 4.13**b show an increasing tendency of half-wave potential with increasing M content up to R/M = 2/2. They all present a sharp kinetic-to-diffusion transition region, indicating their adequate mass-transport properties in RDE setup[187]. The catalysts exhibit similar Tafel slopes around 60 mV dec^{-1}(**Figure 4.13**c), which means their ORR mechanism is similar to $FeCl_3$-R/M=2/2[64,210,233,236]. This aligns with the increasing pyridinic N content in XPS, suggesting the primary active sites are D1 configuration as well. The mass activities of the catalysts at 0.8 V *vs.* RHE are derived from their polarization curves, as listed in **Table 4.10**. Different from the series with $FeCl_3$ precursor, the mass activity of the FePc series shows a linear relationship with Fe content determined by XPS instead of the Fe content determined by ICP-MS, as seen in **Figure 4.13**e. The mass activity sharply increases by *ca.* 2.5-fold from R/M = 2/0 to 2/1 (0.67 to 1.67 A g^{-1} *vs.*0.61 refer in **Table 3.14**), then only slightly increases from 2/1 to 2/2 (1.67 to 2.12 A g^{-1}). This discrepancy is due to the uneven distribution of Fe in bulk and on the surface for the catalysts prepared with FePc precursor. According to the discussion before, the catalytic activity directly relates to the accessible SD and TOF of the active site, which relates to the number of active Fe atoms exposed on the surface and the property of active sites. Therefore, the mass activity should be more closely associated with surface Fe content, which is obtained from XPS instead of the ICP-MS method. In section 4.1, the ICP-MS results are used to plot the relationship between mass activity and Fe content because the uncertainty of the ICP-MS method is lower than that of the XPS method at the detection limit of XPS. However, a linear relationship can still be found due to the uniform distribution of Fe in the catalysts prepared with $FeCl_3$ precursor. In contrast, the catalysts prepared with FePc precursor have more Fe atoms on the surface. Therefore, the mass activity only presents a linear relationship with the XPS value. According to the results in section 4.1, increasing Fe content directly relates to increasing SD instead of TOF. Therefore, the surface Fe atoms should possess similar properties. It should be clarified that this inference does not mean the second hypothesis proposed in section 4.2.2 should be denied because the iron oxide nanoparticles exposed to NH_3 can be further transformed to Fe-N_4 active sites[194]. In **Figure 4.13**f, a linear relationship between mass activity and pyrrolic N content can also be found, which demonstrates that Fe-N_4 active sites are constructed by pyrrolic N. The mass activity for the optimized material, $Fe(NO_3)_3$-R/M=2/2, reaches 3.58 A g^{-1}, the highest among all catalysts. The polarization curve of $Fe(NO_3)_3$-R/M=2/2 also shows a sharp kinetic-to-diffusion transition and a flatter plateau at high overpotential, indicating the catalyst has good mass transport properties even though the mesopores are quasi-absent.

Figure 4.13d shows the normalized ORR mass activities after 500 cycles of CV between 0.6 and 1.0 V *vs.* RHE in N_2 saturated 0.05 M H_2SO_4. The MA values dropped by 43% and 23% after the durability test for FePc-R/M=2/2 and $Fe(NO_3)_3$-R/M=2/2, respectively. This discrepancy may be due to the higher mesopore volume of FePc-R/M=2/2, which increases the

proportion of D1 site. Since D1 sites exposed on the surface of catalysts are considered less stable than D2 covered by few layers of carbon, $Fe(NO_3)_3$-R/M=2/2 with a small portion of D2 sites preserved more activity[239].

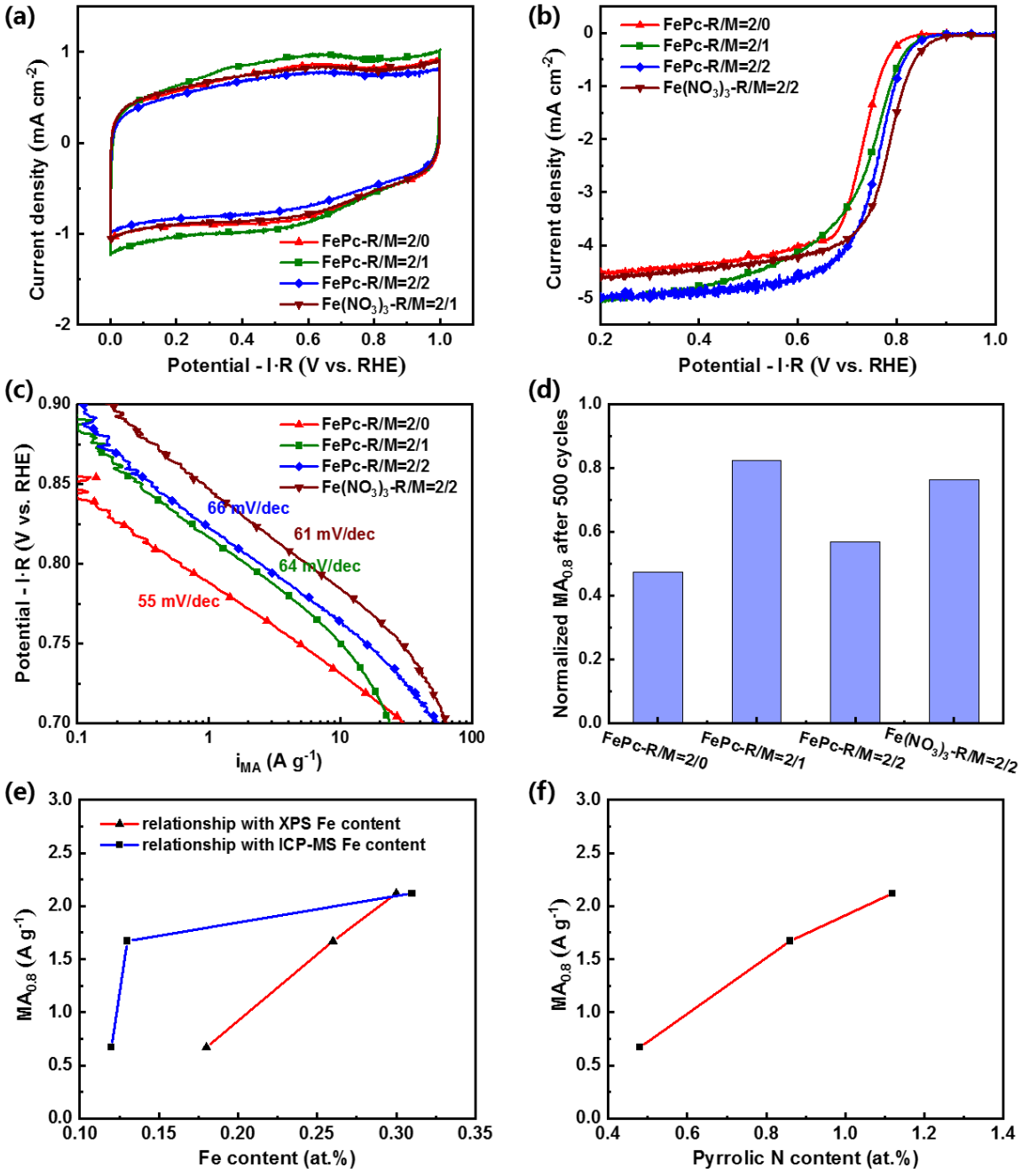

Figure 4.13 Electrochemical characterization of catalysts prepared with different Fe precursors with R/M=2/2. The catalysts prepared with low M content and FePc precursor were also presented as the comparison. **(a)** CV curves in N_2-saturated electrolyte; **(b)** polarization curves in O_2-saturated electrolyte at ω = 1600 rpm and v = 10 mV s^{-1}; **(c)** Tafel plots derived from polarization curves; and (d) normalized mass activity after 500 CV cycles between 0.6-1.0 V in N_2 saturated electrolyte; **(e)** relationships between mass activity in RDE setup and Fe content determined by XPS or ICP-MS respectively; (f) relationships between mass activity in RDE setup and pyrrolic N content.

Figure 4.14a compares the polarization curves in the RDE setup of all catalysts prepared with different Fe precursors at R/M=2/2, along with the curve of commercial Pajarito catalyst (Pajarito powder PMF D14401). All catalysts show good mass-transport properties which is verified by their sharp kinetic-to-diffusion regions. Among all, $Fe(NO_3)_3$-R/M=2/2 presents the highest half-wave potential and mass activity at 0.8 V, consistent with the result in section 3.1 that $Fe(NO_3)_3$ precursor shows the best activity among the catalysts prepared with different precursors at R/M=2/1. FePc-R/M=2/2 has the highest limited current density at the diffusion-controlled region, corresponding to its highest mesopore volume. **Figure 4.14**b shows the polarization curves of these catalysts in H_2/O_2 PEMFC, with the ink formulation keeping the I/C ratio of 2. The trend of mass activity is in line with the trends observed in RDE that the $Fe(NO_3)_3$-R/M=2/2 shows the highest current density of 113 mA cm^{-2} at 0.8 V and the current density of 44 mA cm^{-2} is reached at 0.85 V, which is only 0.05 V lower than the DOE 2025 target for platinum group metal-free electrocatalysts[156]. Meanwhile, no polarization curve is collapsed even for the current density reaches *ca*. 1700 mA cm^{-2} at 0.3 V, indicating the excellent mass transport properties of $Fe(NO_3)_3$-R/M=2/2. Similar to the observation in the series of $FeCl_3$ precursor, the quasi-absence of mesopores in $Fe(NO_3)_3$-R/M=2/2 (0.02 cm^3 g^{-1}) does not affect the accessibility of gaseous oxygen and evacuation of water, indicating the mesopores are not necessary for the catalyst to reach high H_2/O_2 PEMFC performance.

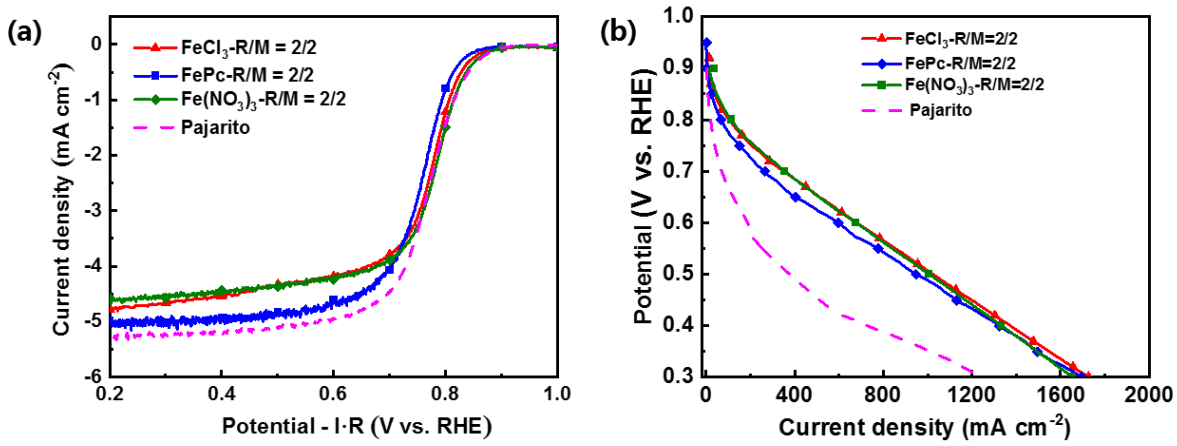

Figure 4.14 Polarization curves in **(a)** RDE setup and **(b)** H_2/O_2 PEMFC of catalysts prepared with different Fe precursors at R/M=2/2. The commercial catalyst Pajarito powder is presented as the comparison.

In summary, this section further expands the conclusion in section 4.1 that high melamine content promotes the formation of Fe-N_4 active sites regardless of the properties of Fe precursor. The preexisting Fe-N_4 coordination structure in the precursor cannot reduce the yield of Fe-rich nanoparticles because it cannot be directly transformed to Fe-N_4 active sites anchored on the carbon substrate. The evolution of Fe atoms in FePc is similar to those in iron salt precursors in which high temperature decomposes the initial structure and release free Fe atoms. They are captured by the N-C defect nearby to form Fe-N_4 active sites or sintered into aggregated Fe clusters. This evolution pathway is in line with our results. In the end, by combining the best precursor ($Fe(NO_3)_3$) and high M content (R/M=2/2), the best catalyst was obtained with a $MA_{0.8}$=3.58 A g^{-1} in RDE setup, which is close to the commercial Pajarito powder (PMF D14401). In H_2/O_2 PEMFC, $Fe(NO_3)_3$-R/M=2/2 also shows the highest current density of 113 mA cm^{-2} at 0.8 V, and the current density of 44 mA cm^{-2} is reached at 0.85 V, which is only 0.05 V lower than the DOE 2025 target for platinum group metal-free catalyst[156]. Besides, the

polarization curve does not collapse at high current density, indicating its good mass transport properties, promising to be widely used in the future.

Chapter 5 Impact of Ammonia Treatment on the Active Sites of Fe-N-C Catalysts

Résumé Français

Dans ce chapitre, les impacts des différentes étapes de synthèse ont été étudiés sur l'activité catalytique et la durabilité des catalyseurs. La discussion porte principalement sur les effets du traitement au NH_3 sur les aérogels de carbone en comparant les caractéristiques du catalyseur après deux conditions différentes de second traitement thermique, soit sous atmosphère de N_2 soit sous NH_3 dilué. Outre la mélamine, le traitement NH_3 est une autre source importante d'azote dans le catalyseur final. Par conséquent, étudier la variation des espèces N après traitement dans NH_3 aiderait à comprendre le mécanisme d'activation des catalyseurs.

Après le processus de lavage à l'acide, la teneur en Fe a diminué en raison de l'élimination des nanoparticules riches en Fe, puis a montré différents degrés d'augmentation après le deuxième traitement thermique en fonction du flux gazeux. Le catalyseur traité dans NH_3 dilué a une teneur en Fe plus faible que celle du catalyseur traité dans N_2 car une partie de Fe est perdue avec l'attaque du carbone.

En ce qui concerne la variation des espèces N, leurs spectres XPS révèlent que le traitement NH_3 présente des effets différents de ceux dus à un accroissement de la teneur en mélamine, où le pourcentage atomique de N pyridinique a été significativement augmenté avec NH_3 au lieu de N pyrrolique pour une augmentation de M. Puisque la configuration D1 est le principal site actif dans nos catalyseurs à base d'aérogel, où le N pyrrolique est impliqué dans la première couche de coordination, le traitement NH_3 peut ne pas introduire de nouveaux sites actifs mais augmenter l'activité des sites existants, c'est-à-dire augmenter la valeur du TOF. Une première étude a été menée pour élucider l'effet du traitement NH_3 sur l'augmentation de l'activité massique du catalyseur Fe-N-C. En conséquence, deux fonctions principales du traitement au NH_3 peuvent être déduites de leurs différents spectres XPS et de leurs courbes de polarisation: (i) Lorsque les couches de carbone sont corrodées par le NH_3, davantage de sites actifs sont exposés. Pendant ce temps, certains atomes de Fe libérés réagissent avec le N pyrrolique et sont ancrés à la surface du carbone. La réaction entre NH_3 et Fe est exclue car le N pyridinique n'est pas impliqué dans la formation de sites actifs Fe-N_4. (ii) Le N pyridinique introduit par le traitement NH_3 augmente la basicité à la surface des catalyseurs, ce qui peut améliorer considérablement le TOF des sites actifs. Il serait nécessaire de caractériser la variation du centre Fe avant et après traitement par des spectres Mössbauer pour confirmer les résultats de l'XPS.

Le catalyseur traité au NH_3 présente une durabilité réduite lors des tests accélérés de durabilité (AST) dans un électrolyte saturé en O_2, probablement en raison des groupes azotés hautement basiques introduits par le NH_3 augmentant le taux de démétallisation des catalyseurs Fe-N-C en milieu acide. Il serait nécessaire de caractériser l'évolution de la SD et de la valeur TOF des catalyseurs par une méthode adaptée avant et après les différents AST.

In this chapter, the impacts of different synthesis steps will be investigated. The discussion focuses on the effects of NH_3 treatment by comparing the characteristics of the catalyst after two different second heat treatment conditions, under N_2 or diluted NH_3 (NH_3/N_2 = 10/90) atmosphere, on the catalytic active sites and the durability. Throughout the synthesis protocol of Fe-N-C aerogel catalysts, there are mainly two nitrogen sources for the formation of Fe-N_4 active sites, including melamine in precursor solution and NH_3 during the second heat treatment. The effects of melamine content have been discussed in Chapter 4, that the content of Fe-N_4 active site increase with melamine content. Both XPS and ^{57}Fe Mössbauer spectra demonstrated that melamine mainly incorporated pyrrolic N into the carbon matrix, which constructed the high-spin O-Fe(III)N_4C_{12} configuration. This conclusion raises a question: do the N atoms incorporated by NH_3 treatment participate in the formation of active sites? Previous research has revealed that a second heat treatment under NH_3 atmosphere usually results in a 3-fold increase in ORR mass activity versus a N_2 second heat treatment under the same conditions[194,231,240].

Thereafter, efforts have been made to elucidate the microscopic mechanism of ammonia treatment. Jaouen *et al.* proposed an activation process comprising three consecutive steps: (i) incorporation of nitrogen atoms in the carbon, (ii) micropore formation through the reaction between carbon and NH_3, and (iii) completion of active sites in the micropores by reaction of Fe with NH_3[194]. The first two steps are the preconditions for the formation of new active sites, which can be demonstrated by increasing N content and micropore volume of catalysts after NH_3 treatment, respectively[194,240]. The last step was used to be considered as the main reason of increasing mass activity because additional active sites were generated at the carbon surface[240]. However, this hypothesis is insufficient to be compatible with the previous conclusion in Chapter 4 that the active sites are mainly generated during the first pyrolysis by the reaction between released Fe atoms and N-C defects nearby. Since most Fe-rich nanoparticles were removed by acid washing, it was impossible to generate a large number of active site during the second NH_3 treatment. Recent research of Kumar *et al.* proposed different insights on the reason of increasing mass activity based on the site density values determined by nitrite adsorption/reduction method[231]. In their research, although a 1.8-fold increase in mass activity was assessed after NH_3 treatment, the SD values of the catalysts are almost unchanged, indicating no significant increase of active sites at the carbon surface. On the contrary, they found a 1.3-fold increase of TOF value, indicating the possible effects of neighbor nitrogen atoms incorporated by NH_3 treatment. Herein, we try to elucidate the variation of Fe and N contents after the second heat treatment by XPS method and further investigate their electrochemical performance. The effect of acid washing will be discussed as well.

5.1 Synthesis of catalysts

Figure 5.1 schematically illustrates the samples extracted at different steps of synthesis. The aerogel was prepared with FePc as the Fe precursor, R/M=2/1, and pH=6. The carbon aerogel blocks were obtained by pyrolyzing RMF aerogels at 800 ℃ in N_2 flow for 1 hour. They were then ball milled to fine powder labeled as FePc BM. The conditions were detailed in section 2.1.2. The obtained powder was then subjected to acid leaching with 0.5 M H_2SO_4 at 80 ℃ for 7 h in a refluxing device to remove the iron nanoparticles that were possibly generated during the pyrolysis[187]. The obtained powder was labeled as FePc AW. In order to investigate the effect of NH_3 treatment, the powder was separated into two parts and then subjected to a second pyrolysis under different atmospheres. The sample labeled as FePc NH_3 was treated at 950 ℃ in NH_3 diluted flow, as the condition described in section 2.1.3. The sample labeled as FePc N_2 was prepared as the comparison following the same heating program under N_2 flow. As seen in **Table 5.1**, the aerogel lost around 56% of mass after the first pyrolysis due to the decomposition

of melamine and ether groups. After the second pyrolysis under N_2 (FePc N_2), the carbon aerogel lost another 16% of weight, reaching a total mass loss of 63%, due to further organization of the carbon matrix at higher temperature. As for the sample treated with diluted NH_3 (FePc NH_3), the mass loss during the second pyrolysis was 47%, reaching a total mass loss of 77%. This discrepancy demonstrated the chemical etching of NH_3 at high temperature. The carbon gasification process comprises the main reaction ($C+NH_3 \rightarrow HCN+H_2$) and minor reaction ($C+2H_2 \rightarrow CH_4$)[187]. The difference in their morphologies and chemical compositions will be discussed later.

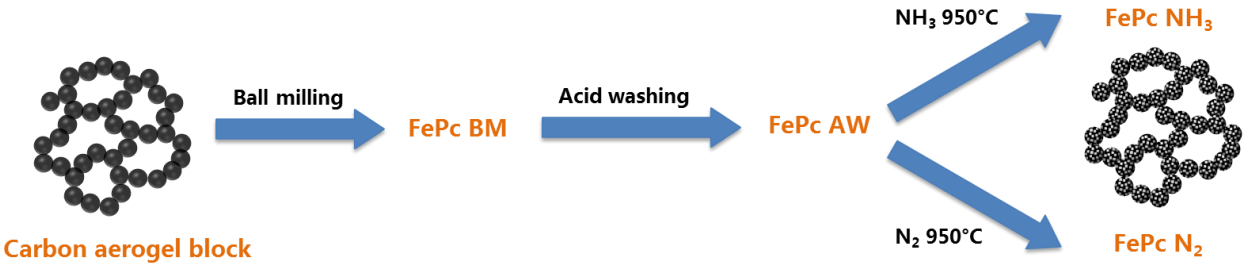

Figure 5.1 Schematic illustration of samples extracted at different synthesis procedure.

5.2 Texture and structure of catalysts

Figure 5.2 a and b show the SEM images of catalysts prepared by different second heat treatment conditions. Both catalysts exhibit a highly porous structure and similar mesopore size, indicating that mesopores have been generated during the first pyrolysis. The specific surface area and the pore size distribution of catalysts were then further investigated by nitrogen adsorption method. **Figure 5.2**c shows the isotherm curves measured at -196 ℃. If we ignore the adsorption quantity, the catalysts treated under different atmospheres show similar isotherm curves, including features associated with micro/mesoporous materials. Both curves present a steep rise at low relative pressures, indicating the presence of micropores. At higher relative pressures, a hysteresis loop appears due to the capillary condensation of mesopores. The difference between two isothermal curves is that FePc NH_3 has a much higher adsorption quantity than FePc N_2, especially in the region of low relative pressures, indicating a larger micropore volume. Thus, FePc NH_3 also has a larger BET area than FePc N_2 (**Table 5.1**). The pore size distribution curves analyzed using the 2D-NLDFT-Heterogenerous surface calculation method are shown in **Figure 5.2**d, and the corresponding textural characteristics are listed in **Table 5.1**. In line with the observation from isothermal curves and SEM images, the micropore volume of FePc NH_3 is more than 2-fold that of FePc N_2 (0.43 *vs.* 0.18 $cm^3\ g^{-1}$), while the mesopore volume only increases *ca.* 1.5-fold (1.51 *vs.* 1.01 $cm^3\ g^{-1}$). Since N_2 is inert to carbon at 950 ℃, it can be considered that the mesopores in FePc N_2 are mainly inherited from gel formation and particle organization. The micropores in FePc N_2 come from the reorganization of carbon atoms during pyrolysis. The difference in pore size distribution between FePc NH_3 and FePc N_2 can be attributed to the pure effect of NH_3 etching. According to **Figure 5.2**d, the peak of micropore size increases from 0.5 nm to 1.0 nm after NH_3 treatment due to the gasification of amorphous carbon. On the contrary, the mesopore size is almost identical (around 10 nm), and the volume of mesopores is less impacted because the mesopore walls are constructed by small graphitic domains with more sluggish kinetic on the reaction with NH_3. Since the amorphous carbon can be located between graphitic domains on the walls, the mesopore volumes can be slightly increased by removing these areas, and micropores are then created on the mesopore walls[187,194,231].

Table 5.1 Physicochemical characterization of the catalysts with different R/M ratios and $FeCl_3$ precursor.

Sample	Total mass loss wt.%	ICP Fe		BET surface ($m^2\ g^{-1}$)	Vtotal ($cm^3\ g^{-1}$)	Vmicro ($cm^3\ g^{-1}$)	Vmeso ($cm^3\ g^{-1}$)
		wt.%	at.%				
FePc BM	56%	0.92	0.20	-	-	-	-
FePc AW	-	0.58	0.12	-	-	-	-
FePc N_2	63%	0.76	0.16	635	1.21	0.18	1.01
FePc NH_3	77%	0.61	0.13	1424	2.00	0.43	1.51

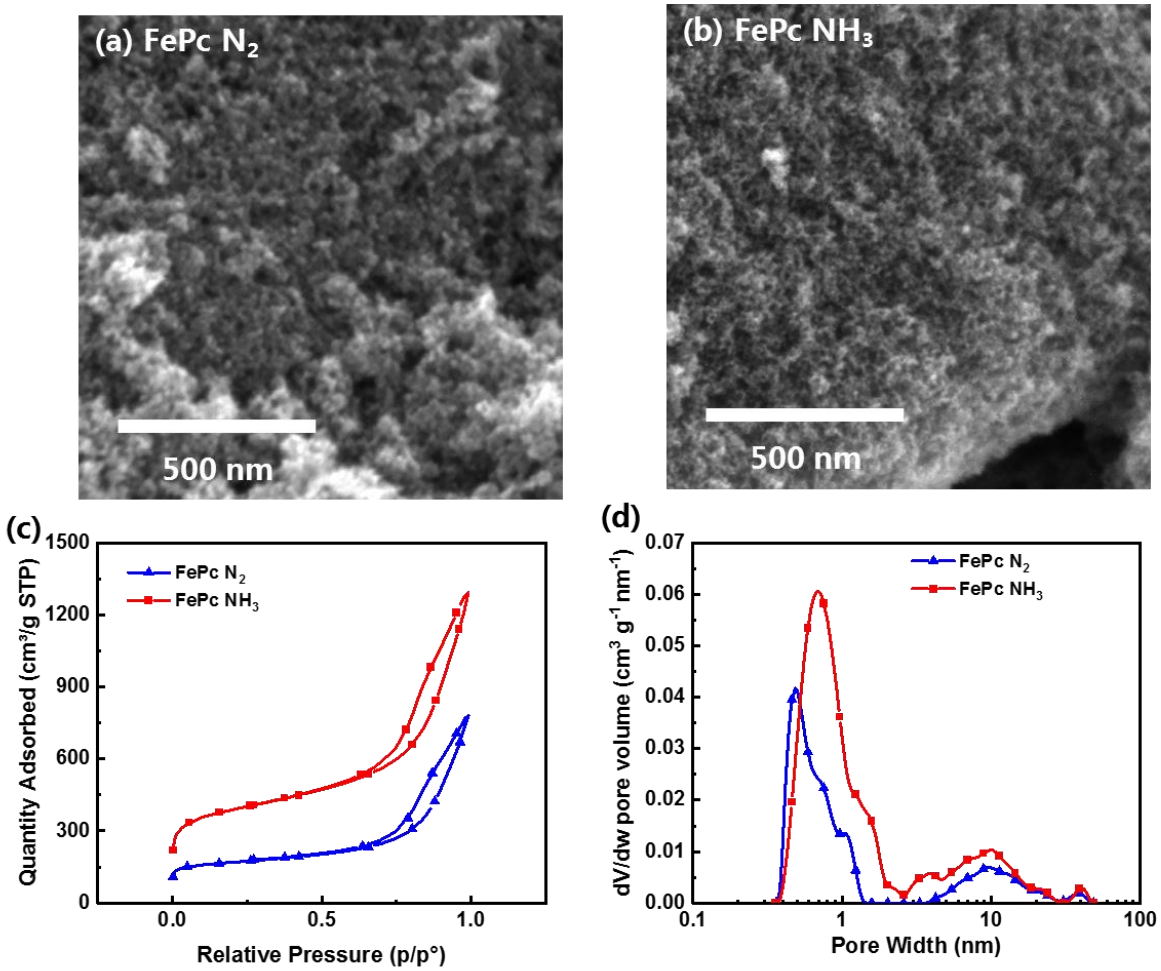

Figure 5.2 SEM images of the catalysts prepared with different second heat treatment conditions **(a)** in N_2, **(b)** in diluted NH_3; **(c)** N_2 adsorption isotherms at -196 ℃ and **(d)** pore size distribution plots obtained by using the 2D-NLDFT-Heterogenerous Surface method.

The Fe contents of all samples extracted at different stages were determined by ICP-MS method, as listed in **Table 5.1**. FePc BM shows the highest Fe content, then decreases after the acid washing due to the removal of acid-soluble Fe compounds. This result explains the lower Fe content than the theoretical value in the catalysts with low melamine content. It confirms the conclusion of Chapter 4 that melamine can reduce the yield of Fe-rich nanoparticles during the first pyrolysis. After the second heat treatment, Fe contents in FePc N_2 and FePc NH_3 increase again with the loss of materials. However, the increasing degrees are inconsistent with their mass loss during the second heat treatment, that the FePc NH_3 loses more carbon due to the

etching of NH_3 but contains less Fe than FePc N_2. We can then recall hypothesis (i) in section 4.2.2 and further discuss that with the etching of carbon during NH_3 treatment, the Fe atoms detached from edge of carbon layers are left and reform Fe-N_4 centers on the surface to realize the enrichment of Fe. The variation of Fe in FePc N_2 can be considered the benchmark without any extra loss of carbon except further graphitization at 950 ℃. The Fe content in FePc NH_3 is lower than FePc N_2 and slightly higher than FePc AW, indicating that although most of the Fe was lost with the etching of carbon, a small portion of Fe atoms remained and accumulated on the surface to form new active sites with NH_3. Therefore, hypothesis (i) is correct in explaining the uneven distribution of Fe in the catalysts prepared with FePc.

The TEM images of all samples extracted at different steps are shown in **Figure 5.3**a-d. Although the existence of acid-soluble Fe compounds can be inferred from the reduced Fe content after acid washing, the quantity of Fe-rich nanoparticles is not enough to be directly observed under TEM. Meanwhile, no significant diffraction peak of Fe-contained species can be identified from their XRD patterns (**Figure 5.3**e) because the quantity of nanoparticles is very low and the particle size is small. In this case, the intensity of diffraction peaks is too weak to be identified, and the width of peaks is enlarged and easily hidden in the background.

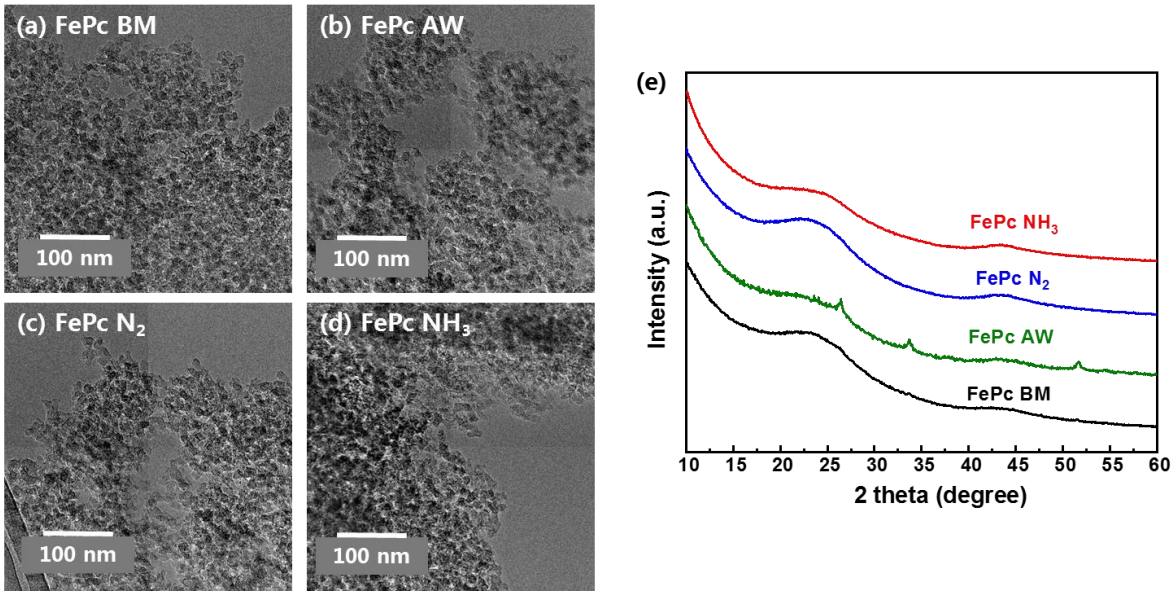

Figure 5.3 (a)-(d) TEM images of the samples extracted at different steps and **(e)** normalized XRD patterns.

5.3 Chemical composition of catalysts

The surface chemical compositions of samples were investigated by the XPS method, as listed in **Table 5.2**. The Fe content of FePc BM determined by XPS (0.13 at.%) is lower than that of ICP-MS (0.20 at.%), indicating an uneven distribution of Fe on the surface and in bulk. The possible reason is Fe-rich nanoparticles filled in mesopores or encapsulated by carbon layers cannot be detected by XPS. After acid washing, FePc AW shows uniform distribution of Fe, suggesting most of the nanoparticles have been removed. In contrast, the Fe-N_4 sites are stable to acid washing and uniformly distributed in the whole carbon matrix. This result also confirms that most active sites have been generated during the first pyrolysis. After the second heat treatment, the Fe content on the surface of FePc N_2 increased by 2 folds and even more for FePc NH_3. The N_2 heat treatment enhances the graphitic degree of carbon layers while removing heteroatoms on the margins. Thus, the relative content of Fe increases. Since N_2 is

inert during heat treatment, the carbon etching process is inhibited. No free Fe atoms are released in this step to form new active sites on the surface, thus the distribution of Fe is still uniform. In contrast, the catalyst treated in NH_3 exhibited an uneven distribution of Fe due to the release of free Fe atoms accumulated on the surface by etching amorphous carbon.

The Fe K-edge XAS spectra were used to investigate the evolution of Fe at different steps. The XANES data (**Figure 5.4**) for all samples are similar to the reference Fe-N-C catalyst ($Fe_{0.5}$) with almost pure Fe-N_x active sites shown in Chapter 4, indicating Fe is mainly present as Fe(II)/(III) oxidation states[219]. Their Fourier transform of the EXAFS signals are also similar to that of the reference $Fe_{0.5}$, with a main signal at *ca.* 1.5 Å, assigned to Fe-N or Fe-O bonds,[98,187,233,234] and a minor signal at *ca.* 2.4 Å, assigned to Fe-C backscattering from the second coordination sphere[219]. The absence of signals at *ca.* 2.2 Å and 2.7 Å, corresponding to the Fe-Fe bond length in metallic Fe and oxides, respectively, indicates all samples are free of metallic Fe particles and well-ordered Fe oxides, which is consistent with the observation in XANES and XRD patterns[62,187]. The Fe-N_4 sites thus can be considered as the main contributor to the signal at 1.5 Å. However, the presence of nanometric Fe oxides cannot be excluded in FePc BM since the signal at *ca.* 2.7 Å is indiscernible in nanometric oxides due to the size and/or amorphous character of nanoparticles[105]. The intensities of XANES spectra are slightly stronger for FePc NH_3 than FePc N_2. The research of Santori *et al.* interpreted this by a higher coordination number in the first coordination sphere surrounding Fe (either N or O atoms), relating to the interaction between Fe-N_4 moieties and axial O_2[62]. However, the relative intensity in their research shows an inverse trend to our results, that the sample treated in NH_3 showed a lower intensity than that treated in argon. This discrepancy might be elucidated by the uneven distribution of Fe in FePc NH_3. In general, the samples treated in argon/N_2 are considered to have a higher average oxidation state of Fe, thus showing a stronger FeN_4-O_2 interaction and higher coordination number. The lower oxidation state of Fe in the NH_3 treated sample is due to the presence of highly basic nitrogen groups that are directly involved in Fe cation ligation[62]. On the contrary, the more concentrated Fe atoms on the surface in FePc NH_3 are oxidized easily to a higher oxidation state during the conservation under air, thus exhibiting a higher coordination number than FePc N_2.

Table 5.2 Surface chemical composition of the samples extracted at different synthesis steps.

Sample	C at.%	O at.%	Fe at.%	N at.%	Nitrile at.%	Pyridinic at.%	Fe-Nx at.%	Pyrrolic at.%	Quaternary at.%	Graphitic at.%
					398.0 eV	398.8 eV	399.9 eV	400.9 eV	402.0 eV	403.3 eV
FePc BM	95.57	1.39	0.13	3.72	1.10	0.48	0.55	1.12	0.34	0.13
FePc AW	95.22	1.63	0.11	3.73	1.05	0.36	0.65	1.10	0.42	0.15
FePc N_2	93.69	2.89	0.20	2.99	0.65	0.36	0.37	1.05	0.39	0.16
FePc NH_3	92.91	2.49	0.26	3.09	0.73	0.51	0.45	0.86	0.36	0.14

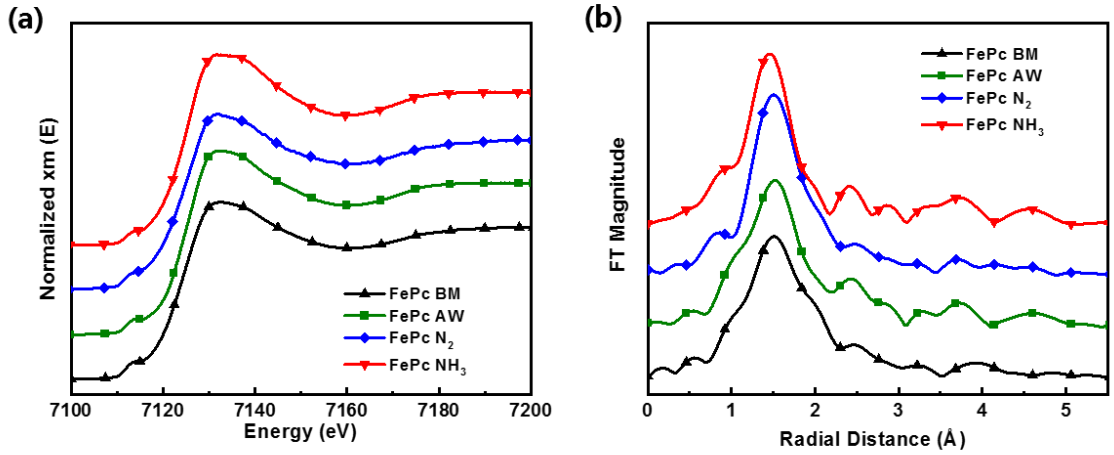

Figure 5.4 **(a)** XANES and **(b)** Fourier transforms of the EXAFS spectra measured at Fe K-edge of the samples extracted at different steps.

The N 1s narrow scan spectra of all samples are shown in **Figure 5.5**a. FePc BM and FePc AW show similar spectra, whereas FePc NH_3 shows a more intense signal at *ca.* 398.8 eV instead of 400.9 eV. The spectra were then analyzed by the deconvolution method used in Chapter 3 to further elucidated the variation of N species during the second heat treatment. As the results listed in **Table 5.2**, the content of all N species was almost kept constant after acid washing, whereas it significantly changed after the second heat treatment regardless of N_2 or diluted NH_3 atmosphere. The content of thermally unstable nitrile N was greatly decreased for both FePc N_2 and FePc NH_3, which confirms our previous description of increasing graphitic degree during second heat treatment by losing thermally unstable ingredients. The variation of three active N species content was plotted in **Figure 5.5**b. Comparing two samples treated under different atmospheres, FePc NH_3 shows a lower pyrrolic N content (0.86 at.% *vs.* 1.05 at.%) but a higher pyridinic N content (0.51 at.% *vs.* 0.36 at.%), which exhibits a different effect from melamine. This trend is consistent with the research of Kumar *et al.* that the pyridinic N content increased after NH_3 treatment[231]. The variation of Fe-N_x content is explained by the contribution of the amine peak at 399.9 eV is predominant instead of Fe-N_x. It should be noted that in Chapter 4, we mentioned that all N species in catalyst $FeCl_3$-R/M=2/0 were introduced by ammonia treatment. The absolute contents of all N species are almost unchanged with melamine content, except pyrrolic N. Herein, we can further conclude that the pyridinic N species content is not affected by different Fe precursors by comparing the deconvolution results in **Table 5.2** and **Table 4.5**. According to these phenomena, it can be deduced that a dynamic equilibrium exists between gaseous NH_3 and different N species anchored on carbon under certain conditions, regardless of the Fe and melamine content. Since the research in Chapter 4 has demonstrated that major active sites are constructed by pyrrolic N, whereas NH_3 treatment mainly introduces pyridinic N, it is possible that NH_3 can only modify the N species on the carbon instead of reacting with Fe to form new active sites.

Moreover, the molar ratio of pyrrolic N/Fe is close to 5 in FePc N_2, which is over the stoichiometric number in Fe-N_4 sites, indicating the existence of uncoordinated pyrrolic N on the surface. This value decreases to 3.3 in FePc NH_3, indicating excessive Fe appears on the surface because the pyrrolic N is insufficient to coordinate all free Fe atoms released by the etching of carbon. This ratio is similar to the $FeCl_3$-R/M=2/2, suggesting a small part of Fe atoms are coordinated by pyridinic N. Besides the number of active sites, many publications

reported a positive effect on the TOF of active sites due to highly basic N groups introduced by NH_3 pyrolysis[105,194,231]. This may be demonstrated by increasing pyridinic N content after NH_3 treatment since pyridinic N is a stronger base than pyrrolic N. The basic character of pyridinic N is attributed to the remaining two nonbonded electrons in the sp^2 orbital, which do not participate in the 6π-electron conjugated system[241].

In summary, NH_3 treatment draws our attention back to the pyridinic N, which is not considered involved in the Fe cation ligation in Chapter 4. This section deduced the same conclusion according to the invariable pyridinic N content with Fe content. Therefore, the reaction between free Fe atoms and pyrrolic N on the surface should generate new active sites. However, our inference related to the evolution of active sites requires more evidence on the chemical environment of Fe, such as the ^{57}Fe Mössbauer spectra. The increasing basicity on the surface is demonstrated by increasing pyridinic N content, which is related to the increasing TOF value of Fe-N_4 sites.

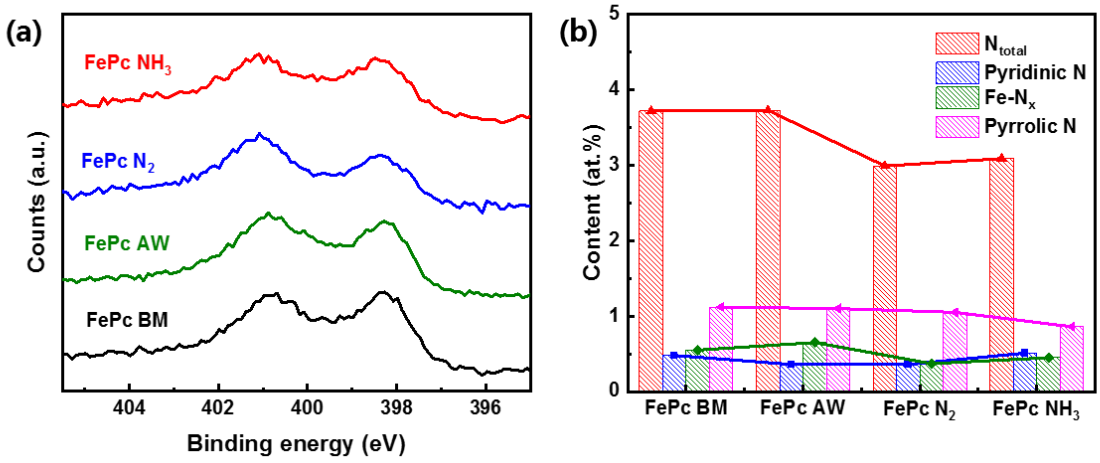

Figure 5.5 a) N 1s XPS spetra of the samples extracted at different steps; (b) Evolution of different N species content with the different synthesis steps.

5.4 Electrochemical characterization of catalysts

The CV curves obtained in the RDE setup of samples extracted from different steps are shown in **Figure 5.6**a. All the CV curves exhibit a typical profile characteristic of carbonaceous materials. FePc NH_3 presents the largest electrochemical available area, in agreement with its highest BET area. **Figure 5.6**b exhibits the corrected ORR polarization curves recorded in O_2 saturated electrolyte. The corresponding normalized mass activities at 0.8 V *vs.* RHE are listed in **Table 5.3**. As can be seen, the samples at different steps present different activities. Although the active sites are supposed to be created during the first heat treatment, FePc BM exhibits a low ORR activity. According to its low Fe content from XPS, it is possible that these active sites are hidden under carbon layer. In addition, Wu *et al.* also proposed another explanation for highly porous catalysts: the Fe-rich nanoparticles on the catalyst surface impeded the accessibility of oxygen to active sites,[89] even if, in our case, no Fe based nanoparticles are detected by XDR or TEM. After acid washing, the mass activity of FePc AW is slightly reduced, which can be attributed to two factors: (i) the contribution of less active Fe-rich nanoparticles is removed by acid washing; (ii) the acid washing results in a partly oxidized catalyst surface, which could disrupt ORR active sites. The reduced Fe content from ICP-MS after acid washing (from 0.20 to 0.12 at.% seems to support the hypothesis (i) Moreover, the removal of unstable

Fe-rich nanoparticles from the catalyst surface presumably exposes more Fe-N_4 active sites, which should result in a higher ORR activity[89]. This inversed variation of mass activity suggests a considerable contribution of mass activity by Fe oxides. The increasing mass activity of FePc N_2 demonstrates hypothesis (ii) because the second heat treatment in N_2 can be envisioned to "repair" the partially oxidized surface by removing some heteroatoms. The mass activity of FePc N_2 is *ca.* 2.5 times higher than FePc BM, indicative of new active sites exposed after removing Fe oxides on the catalyst surface.

Table 5.3 RDE tests of the samples extracted at different steps.

Sample	$MA_{0.8}$ A g^{-1}	$MA_{0.8}$ after N_2 AST A g^{-1}	Loss ratio (N_2)	$MA_{0.8}$ after O_2 AST A g^{-1}	Loss ratio (O_2)	Tafel slope mV dec^{-1}
FePc BM	0.20	-	-	-	-	89
FePc AW	0.07	-	-	-	-	94
FePc N_2	0.65	0.32	-50%	0.20	-70%	85
FePc NH_3	1.67	1.05	-37%	0.38	-77%	64

The NH_3 treated catalyst (FePc NH_3) exhibits a 3-fold increase in mass activity than FePc N_2. According to the discussion in the previous section, the NH_3 treatment caused a burn-off of the catalyst material, which leads to a higher specific surface area and exposal of active sites buried by low crystalized carbon. Meantime, the Fe atoms released from destroyed active sites accumulate on the surface and react with pyrrolic N to form new catalytic centers. However, the high mass activity of FePc NH_3 cannot be simply explained by the increase of the active sites (0.26 at.% for FePc NH_3 *vs.* 0.20 at.% for FePc N_2), even though we assume all Fe atoms on the surface are atomically dispersed. This result indicates the active sites of FePc NH_3 present a higher TOF value than those of FePc N_2. The Tafel plots derived from polarization curves are shown in **Figure 5.6**c. The FePc NH_3 shows a much lower Tafel slope than the others (*ca.* 60 mV dec^{-1} for FePc NH_3 *vs. ca.* 90 mV dec^{-1} for the others), indicating a different property of active sites. This discrepancy might be evidence that NH_3 treatment increases the TOF value of Fe-N_4 sites by introducing highly basic nitrogen groups[105].

The NH_3 treatment is known to lead to less durable catalyst[231]. Here, the effect of NH_3 treatment on the catalyst stability was investigated by a stronger accelerated stress test (AST) protocol composed of 2000 CV cycles between 0.6 and 1.0 V *vs.* RHE with a scan rate of 50 mV s^{-1}. The catalysts performed by AST in N_2 or O_2 saturated 0.05 M H_2SO_4 were labeled by AST-N_2 and AST-O_2, respectively. The polarization curves of catalysts after AST are shown in **Figure 5.6**d and e. **Figure 5.6**f shows the normalized ORR mass activities at 0.8 V of catalysts extracted from their polarization curves after AST. MA values dropped by 50% after AST in N_2-saturated electrolyte for FePc N_2 and % for FePc NH_3, whereas the difference in O_2-saturated electrolyte was significantly increased (-70% for FePc N_2 *vs.* -77% for FePc NH_3). The loss of activity in N_2-saturated is mainly caused by cleaving the Fe-N bonds at high potentials, thus promoting the displacement of Fe atoms onto the basal planes. Eventually, these Fe atoms agglomerate nanoclusters after AST[231]. A similar loss ratio after AST N_2 for FePc N_2 and FePc NH_3 suggests that their active sites have the same property. Since the major active sites in our aerogel catalysts are D1 configuration, which has been identified to be a non-durable FeN_x site to O_2 in Fe-N-C materials during the electrochemical tests[105], higher loss ratios of mass activity for both FePc N_2 and FePc NH_3 thus can be expected, in agreement with the results shown in **Table 5.3**. Fe-N_4 sites can also be transformed to Fe oxides by oxygen during AST O_2. The different loss ratio after AST O_2 between two catalysts was recently explained by

higher demetallation rates for NH_3 treated Fe-N-C catalysts in an acid medium. The involvement of highly basic nitrogen groups neighbor to Fe-N_4 sites leads to higher TOF but also fast protonation of N groups in acid medium, thus leading to demetallation of the most active sites[105]. In order to further demonstrate our inference, the active SD and TOF before and after different AST should be determined for both catalysts. The demetallation of catalysts is supposed to be validated by a decreased SD value. **Figure 5.7** shows the H_2/O_2 polarization curves in a single cell of catalysts treated in different atmospheres. FePc NH_3 presents a higher activity than FePc N_2 in PEMFC, indicating that NH_3 treatment is an efficient way to increase the activity of Fe-N-C catalysts in RDE setup and PEMFC.

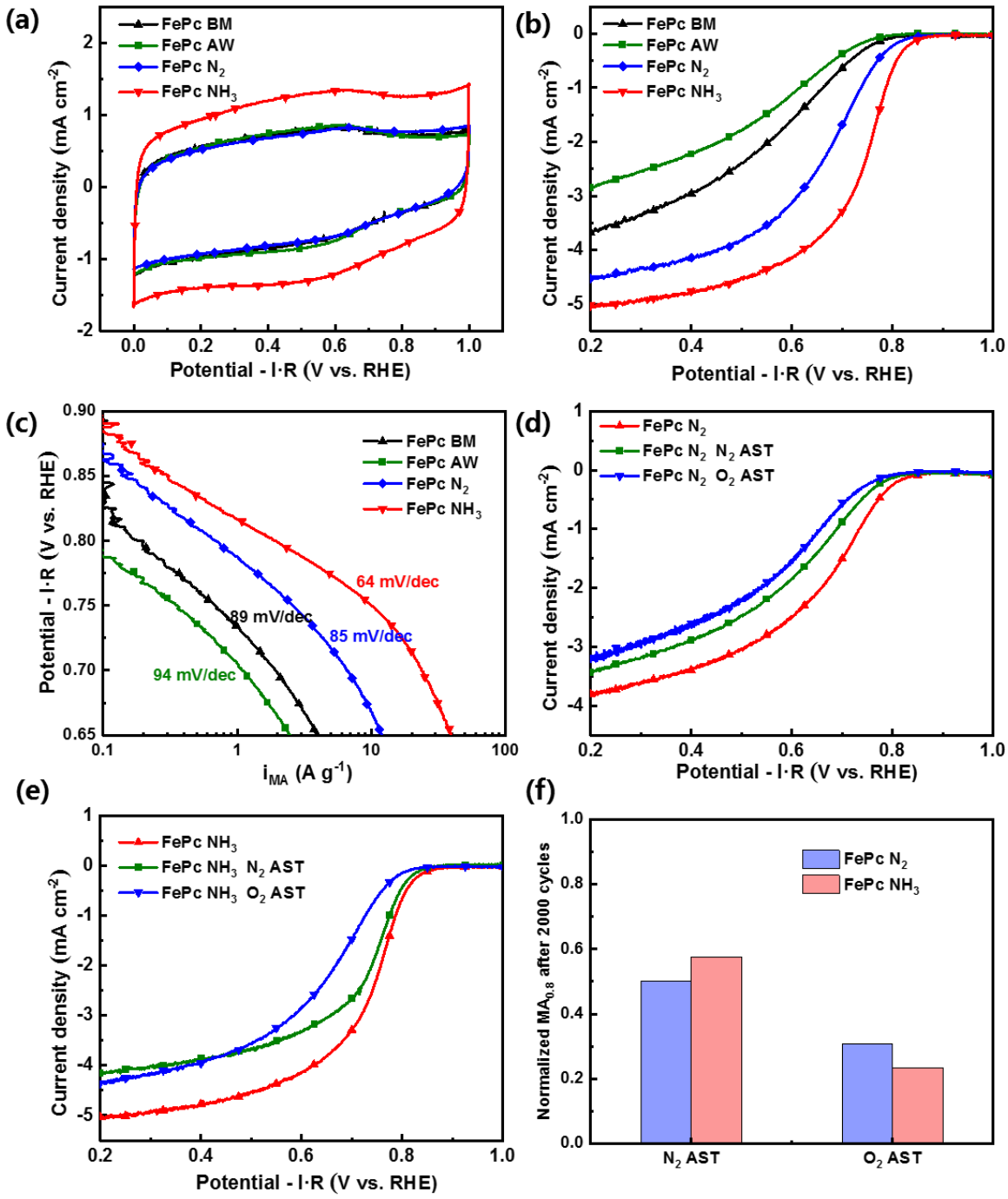

Figure 5.6 Electrochemical characterization of the samples extracted at different steps recorded in 0.05 M H_2SO_4. **(a)** CV curves in N_2-saturated electrolyte; **(b)** Polarization curves in O_2-saturated electrolyte at ω = 1600 rpm and v = 10 mV s^{-1}; **(c)** Tafel plots of the O_2-transport and background-current corrected kinetic current obtained from the steady-state Ohmic drop-corrected *I–E* curves at ω= 1600 rpm; Polarization curves of catalysts before/after 2000 CV cycles between 0.6-1.0 V in N_2 and O_2-saturated electrolyte respectively **(d)** FePc N_2 and **(e)** FePc NH_3; **(f)** normalized mass activity at 0.8 V after durability test.

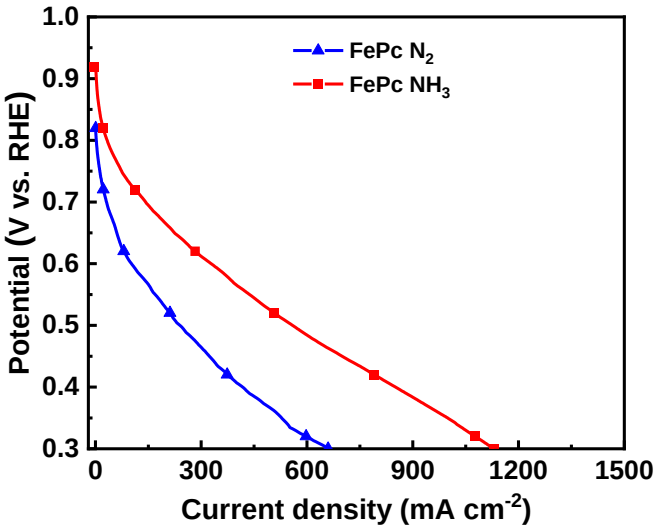

Figure 5.7 H_2/O_2 PEMFC polarization curves of the catalysts prepared with different second heat treatment conditions. The measurements were performed with T_{cell} = 80 °C, 100 % RH, *P*cathode = *P*anode = 2 bar_{abs}, the H_2, and O_2 flow rates were 150 mL min^{-1} while the air flow rate was 480 mL min^{-1}.

In summary, two main functions of NH_3 treatment on increasing the mass activity of Fe-N-C catalyst can be inferred from their different XPS spectra and polarization curves:

(i) As NH_3 corrodes the carbon layers, more active sites are exposed, as seen in **Figure 5.8**. Meantime, some released free Fe atoms are reacted with pyrrolic N and anchored on the carbon surface. The reaction between NH_3 and Fe is excluded because pyridinic N is not involved in the formation of Fe-N_4 active sites. However, this conclusion should be further demonstrated by the characterization of the chemical environment of Fe, such as the Mössbauer spectrum.

(ii) (ii) The pyridinic N introduced by NH_3 treatment increases the basicity on the surface of catalyst, which can significantly enhance the TOF of the sites. The NH_3 treated catalyst exhibits a decreased durability during AST in O_2-saturated electrolyte due to the highly basic nitrogen groups introduced by NH_3 increasing the demetallation rate of Fe-N-C catalysts in an acid medium. An adapted method for aerogel catalysts should be performed before and after the different AST of both FePc N_2 and FePc NH_3 catalysts to observe the evolution of the SD and the TOF values.

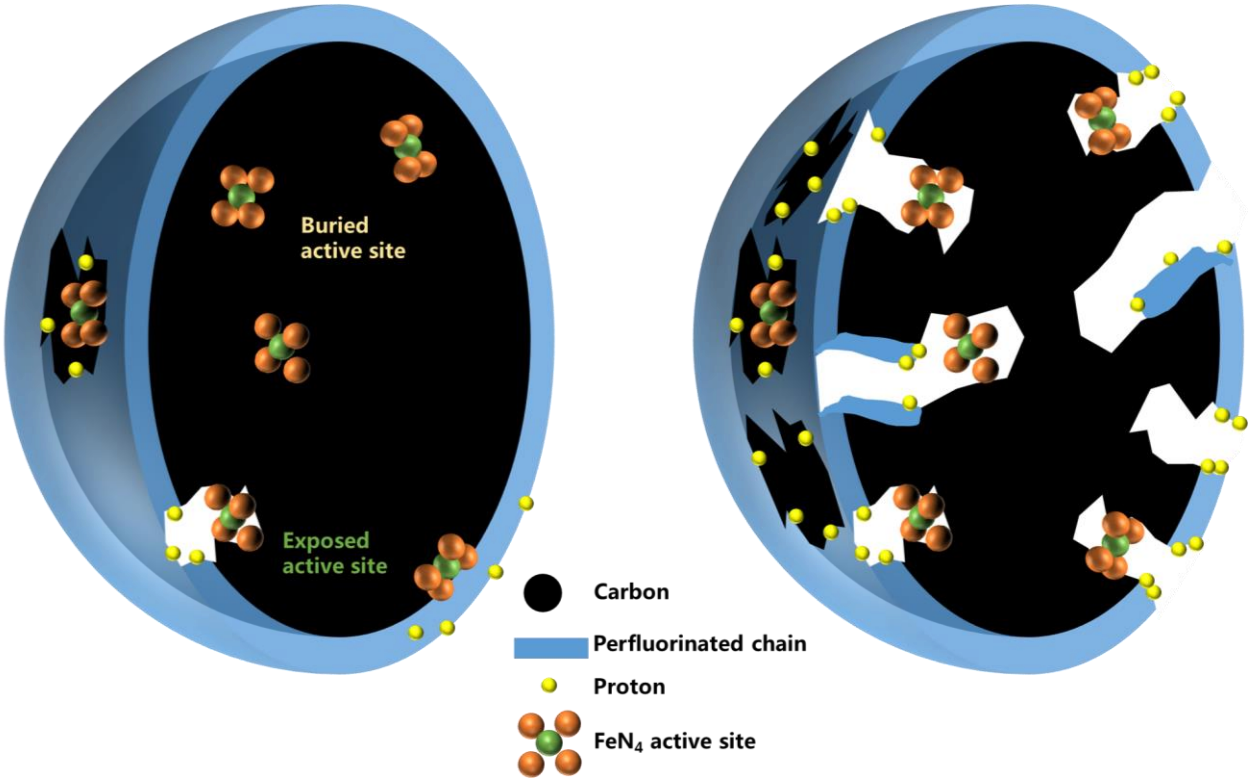

Figure 5.8 Comparison between carbon substrates before and after NH_3 treatment.

Chapter 6 Impact of Cerium Dioxide on the Durability of Fe-N-C Catalysts

Résumé Français

La principale source de désactivation des catalyseurs Fe-N-C en électrolyte saturé en O_2 est principalement causée par le H_2O_2 produit pendant l'ORR impliquant la voie à $2e^-$. Différent des catalyseurs à base de Pt, les catalyseurs Fe-N-C ont une activité extrêmement faible pour la réduction de H_2O_2. Par conséquent, un piégeur de H_2O_2 supplémentaire pourrait être judicieux pour aider à améliorer la durabilité des catalyseurs Fe-N-C. Dans ce chapitre, les catalyseurs à base d'aérogel Fe-N-C chargés de CeO_2 avec différentes teneurs en CeO_2 ont été synthétisés pour étudier les impacts sur la durabilité des catalyseurs Fe-N-C. L'échantillon $FeCl_3$-R/M=2/2 a été sélectionné comme catalyseur Fe-N-C de référence. Deux précurseurs de Ce ont été choisis, $CeCl_3 \cdot 7H_2O$ et la nanopoudre de CeO_2, pour étudier les impacts de la solubilité des précurseurs et de leur intégration au sein du catalyseur final.

Dans la section 6.1, $CeCl_3$ a été utilisé comme précurseur de CeO_2 soluble dans l'eau et introduit dans la solution mixte de départ simultanément avec le précurseur de Fe. Le volume mésoporeux du catalyseur Fe-N-C dopé au CeO_2 a été significativement diminué car la présence de $CeCl_3$ dans la solution de précurseur nécessite plus de NaOH pour dissoudre la précipitation modifiant la formation du gel. Les teneurs finales en Ce de tous les échantillons sont inférieures aux valeurs théoriques de Fe/Ce en raison de la perte de précurseur de Ce lors de l'étape d'échange de solvant. Lorsque la charge de Ce est inférieure à 0.11 at.% (~1 wt.%), des impacts négligeables sur les performances de l'ORR peuvent être observés. Cependant, lors de l'augmentation supplémentaire de la teneur en CeO_2, un excès de CeO_2 peut entraver la formation et l'exposition de sites actifs Fe-N_4, entraînant une diminution du volume des micropores et des performances ORR. Bien que la capacité particulière du CeO_2 à piéger les peroxydes ait été rapportée dans des publications précédentes, les catalyseurs Fe-N-C dopés au CeO_2 ne présentent pas une meilleure durabilité par rapport au catalyseur de référence dans notre test de durabilité. La raison possible est que les nanoparticules de CeO_2 ne sont déposées qu'à la surface du carbone, ce qui entraîne une faible interaction avec les sites actifs Fe-N_4.

Dans la section 6.2, des nanoparticules de CeO_2 ont été utilisées comme précurseur de Ce pour obtenir une distribution plus uniforme de la taille des particules de CeO_2. Cependant, en raison d'une faible interaction entre les nanoparticules de CeO_2 et le squelette de l'hydrogel, la plupart d'entre elles ont été perdues lors de l'étape d'échange de solvant et une très faible teneur en Ce a été obtenue dans le catalyseur final. En comparaison, l'introduction de nanoparticules de CeO_2 par broyage à billes des nanoparticules de CeO_2 avec notre catalyseur $FeCl_3$-R/M=2/2 après l'étape de lavage à l'acide et avant l'étape de traitement sous NH_3 dilué, permet de bien préserver le précurseur de Ce. Semblable au précurseur $CeCl_3$, une teneur élevée en CeO_2 entraîne également un volume de micropores et une activité ORR inférieurs, et présente des impacts négligeables sur la durabilité.

Par conséquent, la méthode de dopage CeO_2 doit être encore modifiée pour obtenir une meilleure synergie entre les sites actifs CeO_2 et Fe-N_4, par exemple en préparant du CeO_2 encapsulé par quelques couches de carbone pour combiner étroitement deux types de sites.

Besides the investigation of the ORR performance of Fe-N-C catalyst, the durability during the catalytic processes is also an important indicator for evaluating the catalysts. However, the inherent stability of most Fe-N-C catalysts is significantly attenuated with the increased operating time of tests. According to the 2025 DOE technical targets of PEMFC, the loss in initial catalytic mass activity should be less than 40% after their accelerated stress test (AST) in a H_2/N_2 single cell of 25-50 cm^2. The DOE's AST protocol contains 30,000 square wave cycles between 0.6 V and 0.95 V[156,242]. In contrast, most of our aerogel-based Fe-N-C catalysts reach the DOE-target limit of mass activity loss after only 500 cycles in RDE setup under similar test conditions. As a result, It is urgent to find new strategies that can effectively prevent the loss of mass activity.

As discussed in Chapter 5, the main source of deactivation of Fe-N-C catalysts in N_2 saturated electrolyte is the demetallation of Fe-N_4 active sites[184], mainly caused by carbon corrosion when subjected to potentials above *ca.* 1.0 V[184,243,244]. Since the electrochemical oxidation is fast on the edges of carbon layer, in which micropore-hosted Fe-N_4 sites are located, the loss of ligand environment of Fe ions leads to their solvation and elimination of active sites on the surface simultaneously[184,245]. In the presence of O_2, the loss of mass activity of Fe-N-C catalysts becomes more severe due to the H_2O_2 or radical oxygen species (ROS) produced during ORR via $2e^-$ pathway[246]. Although the percentages of H_2O_2 formation for atomically dispersed Fe-N-C catalysts is not significantly higher than that of Pt-based catalyst[233], the residence time of H_2O_2 on the electrode may be longer with Fe-N-C catalysts due to their extremely poor activity for the electro-reduction of H_2O_2 to H_2O and the chemical disproportionation of H_2O_2 [246]. In contrast, platinum is an excellent catalyst for both $4e^-$ reduction of O_2 to H_2O and $2e^-$ reduction of H_2O_2 to H_2O [247]. As a result, H_2O_2 and ROS are pointed as the key degradation source for Fe-N-C catalysts during the ORR. Choi *et al.* found the ORR activity decay by H_2O_2 origins from reduced TOF value of active sites[248], which is different from the destruction of Fe-N_4 active sites resulting from the electrochemical oxidation of the surrounding carbon support, inducing a decreased number of active sites. Goellner *et al.* found when H_2O_2 reacts with Fe^{2+} species, such as those in Fe-N_4 moieties, ROS are generated via Fenton-like reactions, promoting the formation of oxygen functionalities on the carbon matrix, especially epoxy groups. The formation of such oxidized groups decreases the electron density around the Fe center, weakening the O_2-binding energy in Fe-N_4 ensembles and decreasing the TOF of the ORR[243,246,248]. A more careful investigation with ^{57}Fe Mössbauer spectroscopy was carried out by Li *et al.*, in which the durable and non-durable Fe-N_4 sites were identified[105]. The high-spin D1 site is not durable in operating PEMFC, quickly transforming to ferric oxides due to the localized carbon surface oxidation or protonation of highly basic N atoms involved in active sites. In contrast, the D2 site is shown to be more durable due to its lower amount of ROS produced during ORR or its subsurface location. This discrepancy was also demonstrated by the variation of N1s spectra from XPS after AST. The signal for pyrrolic N, including Fe-N_4 in pyrrolic environment (corresponding to D1 site), is almost absent in the spectrum collected after the AST in acid electrolyte. On the contrary, the signal of pyridinic N, including Fe-N_4 in pyridinic environment (corresponding to D2 site), still exists after AST, indicating a higher durability[243]. Considering the major active sites in our Fe-N-C aerogel catalysts are D1 configuration, the durability of catalysts might be increased by adding cocatalysts to scavenge H_2O_2 or ROS generated during ORR in acid medium.

As a widely-recognized rare earth oxide, cerium oxide (CeO_2) has a unique oxygen storage and release capacity, prominent reversible redox property (Ce^{4+}/Ce^{3+}), and possesses a large number of oxygen vacancies, which are beneficial to ORR catalytic process[249,250]. Wei *et al.* first reported that eliminating H_2O_2 by the cocatalyst of CeO_2 in Fe-N-C catalysts could improve

their durability[251]. They found that Ce^{3+} can reduce H_2O_2 quickly by following reactions, protecting the catalyst from being attacked by H_2O_2:

$$O_2 + 2H^+ + 2e^- \rightarrow H_2O_2$$

$$2CeO_2 + 2H^+ + 2e^- \rightarrow Ce_2O_3 + H_2O$$

$$Ce_2O_3 + H_2O_2 \rightarrow 2CeO_2 + H_2O$$

As the CeO_2 mass ratio increases, the yield of H_2O_2 decreases and the durability increases. However, the initial mass activity of Fe-N-C catalysts decreases at high CeO_2 content. As reported by Lv *et al.*, the electronic interaction between CeO_2 and metal in the co-synthesized catalyst may enhance the oxygen absorption on the catalyst to improve ORR activity[252]. In contrast, the excessive loading amount (>1 wt.%) may lead to the aggregation of CeO_2 nanoparticles and hinder the exposure of Fe-N_4 active sites, resulting in a decrease of the catalytic performance on the contrary[253]. Therefore, the CeO_2 loading should be carefully controlled to preserve the ORR activity with increased durability.

Herein, we synthesized CeO_2-loaded Fe-N-C aerogel catalysts with varying CeO_2 contents. $FeCl_3$-R/M=2/2 was selected as the pristine Fe-N-C catalyst and two Ce precursors were tested, $CeCl_3 \cdot 7H_2O$ (99.9% from Sigma-Aldrich) and CeO_2 nanopowder (<25 nm particle size from Sigma-Aldrich), to investigate the impact of precursor solubility. The Ce precursors were introduced in the solution with Fe precursor, the solubility of Ce precursor thus affecting the polycondensation process of hydrogel. The catalysts prepared with different Ce precursors and Ce content were labeled as "$FeCl_3$/Ce precursor = molar ratio of Fe/Ce". For example, $FeCl_3/CeCl_3$=1/1 representing $CeCl_3$ as the precursor and the targeted molar ratio of Fe/Ce=1/1.

6.1 $CeCl_3$ precursor

$CeCl_3$ is a commonly used water soluble Ce^{3+} precursor. In this section, the content of CeO_2 cocatalyst was adjusted by different molar ratios of $FeCl_3/CeCl_3$, including 1/0.5, 1/1, and 1/1.5. In the presence of $CeCl_3$, more NaOH solution is required to dissolve the rust-red precipitation. The final pH of the polycondensation step is slightly higher than 8, which may result in different porosity of carbon aerogel compared to the pristine sample. The electrochemical performances and durability of catalysts in RDE setup and single cell were investigated.

6.1.1 Texture and structure of catalysts

The SEM images shown in **Figure 6.1**a-c provide a basic view of the morphology of catalysts prepared with different $CeCl_3$ contents. All samples present a more compacted texture than the pristine catalyst $FeCl_3$-R/M=2/2 (**Figure 4.2**e) and are similar to the catalyst prepared with higher melamine content ($FeCl_3$-R/M=2/2.5, **Figure 4.2**f). This result is consistent with our previous research on the effect of pH value (section 3.2) that a higher pH value leads to smaller condensation units during the condensation step, thus reducing the pore size of aerogel.

Their N_2 sorption results confirmed the observation under SEM. **Figure 6.1**d and e exhibit the N_2 adsorption-desorption isotherms and corresponding pore size distribution curves, respectively. All samples present a steep rise at low relative pressures, indicating the presence of micropores. In contrast, at higher relative pressures, all curves show a platform instead of a hysteresis loop, suggesting the absence of mesopores in catalysts. The textural properties

calculated from the nitrogen sorption isotherms are listed in **Table 6.1**. The mesopores are absent in all catalysts due to their high melamine content and pH value. Their BET areas and total pore volumes present decreasing trends as the Ce content increases, mainly caused by the decrease in micropore volume. In previous research on Fe precursor and melamine content, the micropore volumes are almost unchanged due to the same NH_3 treatment condition. However, the micropore volume significantly decreases in the presence of Ce, suggesting the existence of CeO_2 can prevent the gasification reaction between NH_3 and the carbon matrix. The NH_3 is possible to be consumed by reducing Ce^{4+} to Ce^{3+}, which protects the carbon layer from being attacked[251].

Table 6.1 Physicochemical characterization of catalysts doped by different molar ratios of Ce. $CeCl_3$ was used as the Ce precursor.

Fe/Ce	Total mass loss wt.%	ICP Fe		ICP Ce		BET surface ($m^2\ g^{-1}$)	Vtotal ($cm^3\ g^{-1}$)	Vmicro ($cm^3\ g^{-1}$)	Vmeso ($cm^3\ g^{-1}$)
		wt.%	at.%	wt.%	at.%				
pristine	81%	1.36	0.30	-	-	1271	0.78	0.45	0.25
1/0.5	79%	1.09	0.24	0.32	0.03	1155	0.51	0.45	0.03
1/1	81%	1.10	0.24	1.28	0.11	1034	0.46	0.40	0.03
1/1.5	74%	0.96	0.21	2.75	0.25	564	0.32	0.20	0.10

The Fe and Ce contents were determined by ICP-MS method, and the results are listed in **Table 6.1**. Two samples with relatively low Ce content, $FeCl_3/CeCl_3$=1/0.5 and 1/1, show similar Fe content, whereas that of the sample with higher Ce content ($FeCl_3/CeCl_3$=1/1.5) is slightly decreased. Moreover, the Fe contents of all samples are slightly lower than that of pristine catalyst ($FeCl_3$-R/M=2/2 with 0.30 at.% of Fe in **Table 4.3**). Since the total mass loss of $FeCl_3/CeCl_3$=1/0.5 and 1/1 are close to the pristine catalyst, the discrepancy in Fe content might be explained by their higher yield of Fe-rich nanoparticles during the first pyrolysis in N_2, which were then removed by acid washing. In the presence of $CeCl_3$ in the precursor solution, more NaOH was required to dissolve the precipitation. However, a higher pH value is possible to promote the formation of larger precipitation particles of iron hydroxide, thereby slowing the release of single free Fe atoms during the pyrolysis. Another possible reason for the higher yield of Fe-rich nanoparticles is that CeO_2 impedes the transformation from the free Fe atom to the Fe-N_4 site. The reactive N-C defect nearby the Fe might be hidden by CeO_2 nanoparticles, thus reducing the chance of free Fe atoms being captured by N-C defects. Since the Fe content decreases with increasing Ce content, whereas the consumption of NaOH solution is kept constant, the second hypothesis could be the main reason for the high yield of Fe-rich nanoparticles. This hypothesis might be demonstrated by preparing Fe-N-C catalyst without CeO_2 precursor at the same pH value, *i.e.*, using the same quantity of NaOH solution, and comparing their Fe content in the final catalysts.

Although the Ce content in the final catalyst presents an increasing tendency with the quantity of $CeCl_3$, the absolute content is far less than the expected value. In $FeCl_3/CeCl_3$=1/0.5, only 0.03 at.% was obtained, only reaching a Fe/Ce value of 8/1. This result indicates a considerable loss of Ce precursor during the solvent exchange and/or acid-washing steps. $FeCl_3/CeCl_3$=1/1 and $FeCl_3/CeCl_3$=1/1.5 also present lower Ce contents than expected values, reaching Fe/Ce values of 1/0.5 and 1/1, respectively. It seems the absolute loss of Ce for all samples is around 0.1 at.% regardless of the initial quantity of $CeCl_3$. This result suggests the Ce precursor is mainly lost in the solvent exchange step, and the unprecipitated $CeCl_3$ is removed with water. The loss quantity is decided by pH value and its impact on the solubility of cerium hydroxide, thus similar pH value leading to a similar loss of Ce.

On the other hand, if CeO_2 could be removed by acid leaching, the catalyst with higher Ce content shall exhibit a higher loss of Ce because more CeO_2 nanoparticles are exposed to acid, which is not the case. It should be noticed that the effect of CeO_2 on the texture of the catalyst, including BET area and micropore volume, is more significant when Ce content is higher than 0.11 at.% (corresponding to 1.28 wt.%). The micropore volumes of $FeCl_3/CeCl_3$=1/0.5 and 1/1 are still close to the pristine catalyst, whereas the sharply decreased to only half the value in $FeCl_3/CeCl_3$=1/1.5. Therefore, the $FeCl_3/CeCl_3$=1/1 is possible to present similar activity with the pristine catalyst with enhanced durability.

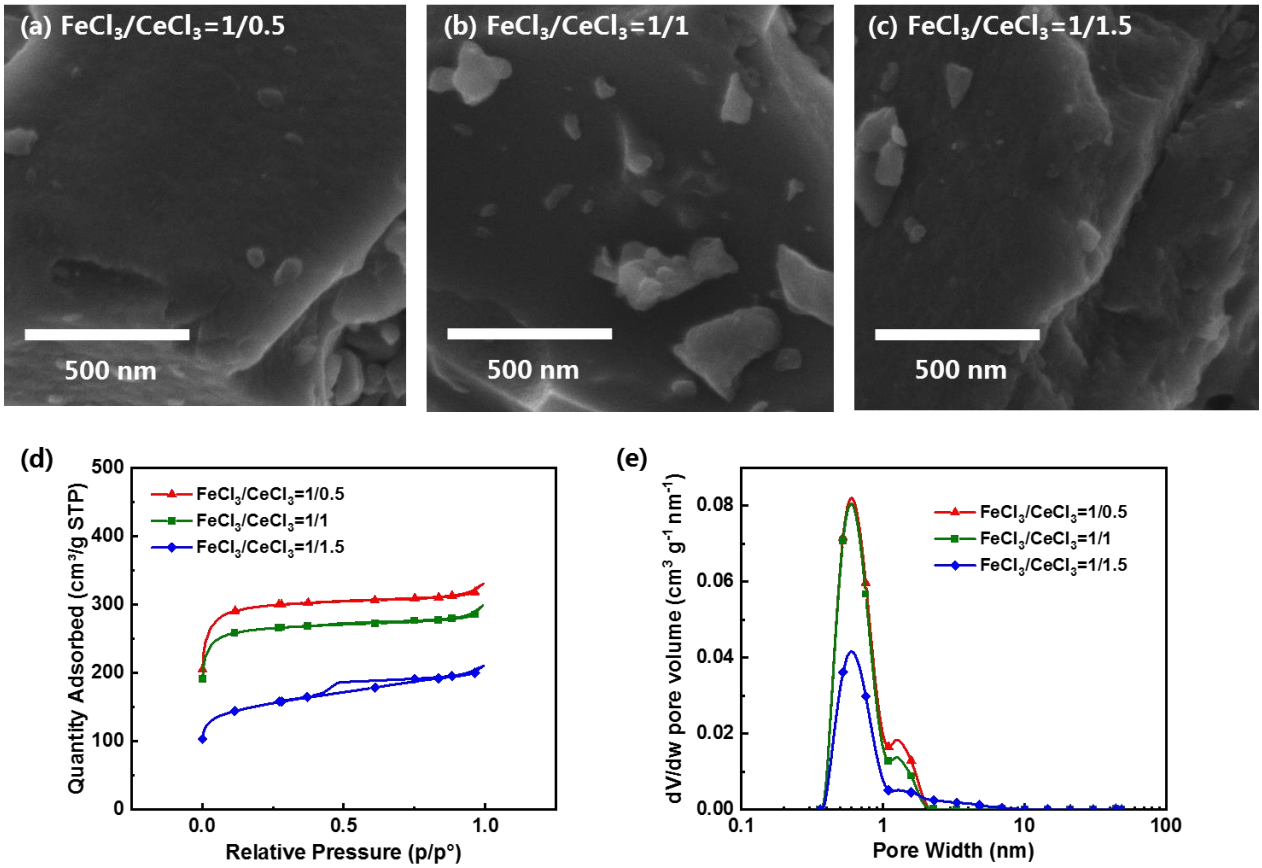

Figure 6.1 **(a)-(c)** SEM images of the catalysts doped by different molar ratios of Ce; **(d)** N_2 adsorption isotherms at -196 ℃ and **(e)** pore size distribution plots obtained by using the 2D-NLDFT-Heterogenerous Surface.

The CeO_2 nanoparticles can be observed clearly under TEM images. As seen in **Figure 6.2**a-c, more and more CeO_2 nanoclusters were deposited onto the catalyst surface with increasing quantities of $CeCl_3$. The distribution of CeO_2 particle size is uneven, with particle size varying from a few nanometers to tens of nanometers. Their carbon layers are similar to the pristine catalyst, which shows a pore-less morphology. X-ray diffraction patterns of the catalysts are shown in **Figure 6.2**d. Two lumps at around 2θ=26.0 ° and 43.6 ° correspond to the low crystalized carbon. It can be observed that two lumps become narrower at high Ce content, suggesting CeO_2 can increase the graphitic degree of carbon matrix, probably by limiting etching during the diluted NH_3 thermal treatment to the low crystallized carbon parts. Meanwhile, two weak peaks at 2θ=28.5 °and 47.3 ° can be observed in the pattern of $FeCl_3/CeCl_3$=1/1.5, which can be assigned to (111) and (220) crystal planes of CeO_2, respectively[253]. However, the diffraction peaks of CeO_2 in $FeCl_3/CeCl_3$=1/0.5 and 1/1 are hidden in the background due to their low Ce content.

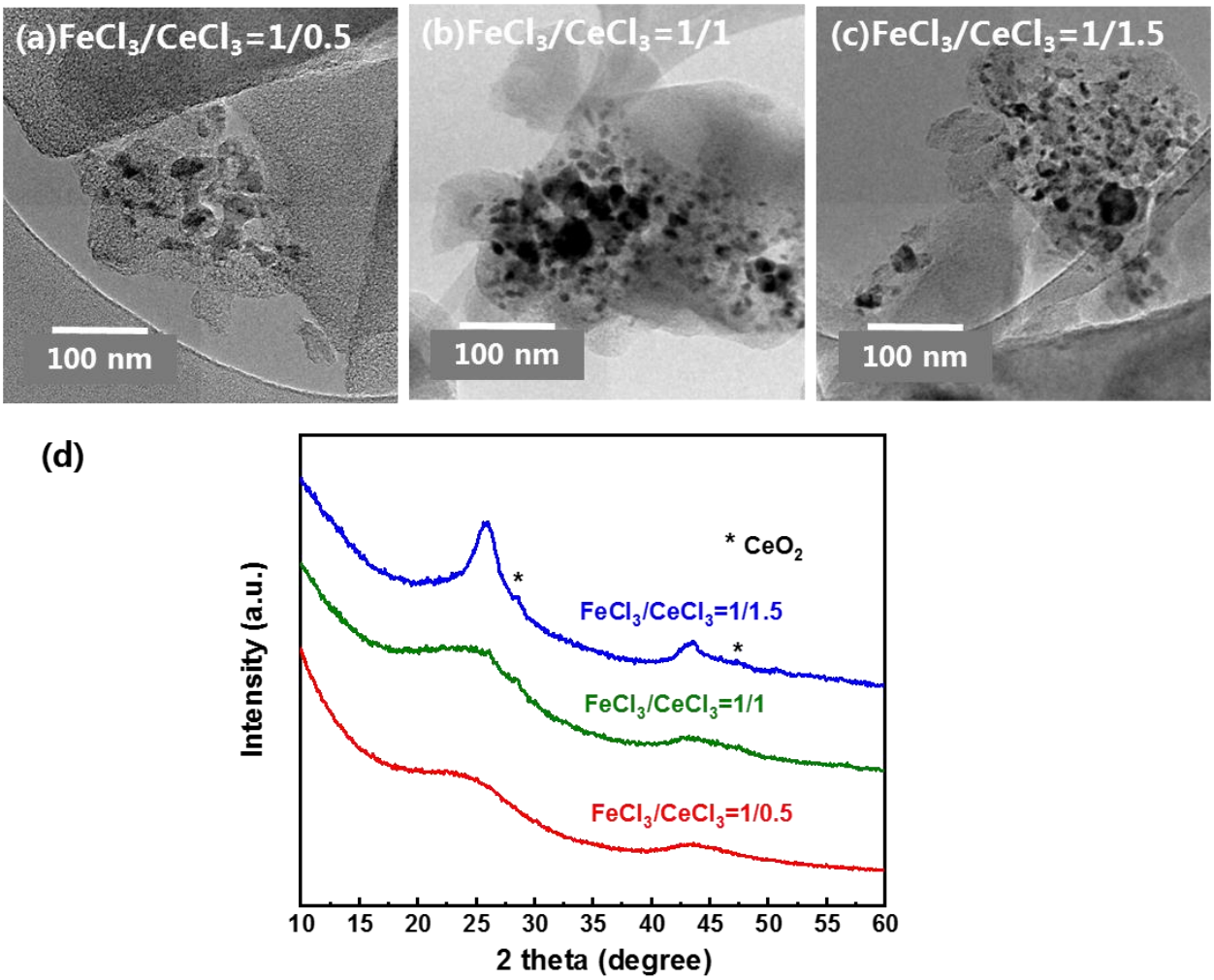

Figure 6.2 **(a)-(c)** TEM images of the catalysts doped by different molar ratios of Ce and **(d)** normalized XRD patterns.

6.1.2 Chemical composition of catalysts

The XPS characterization was employed to obtain the chemical environment on the surface of catalysts. The chemical compositions of all elements identified are listed in **Table 6.2**. The Fe contents of XPS are slightly higher than that of ICP-MS for all catalysts, indicating Fe atoms are more concentrated on the surface. Moreover, the Ce content exhibits a similar tendency with Fe, that all Ce contents on the surface is higher than that in bulk. In this case, the surface oxygen content also increases with Ce due to the contribution of metal oxide. The total N contents of $FeCl_3/CeCl_3$=1/0.5 and 1/1 are slightly higher than the pristine catalyst (3.76 at.% in **Table 4.5**). This phenomenon was mentioned by Bai *et al.* that the addition of CeO_2 could facilitate the fixation of N during pyrolysis of the precursors[253]. However, this does not mean more Fe-N_4 active sites can be obtained because these extra N atoms should preferentially be located around CeO_2. On the contrary, $FeCl_3/CeCl_3$=1/1.5 exhibits a lower total N content than the pristine catalyst because high CeO_2 content limits the reaction between carbon layers and NH_3, as confirmed by its low micropore volume. The deconvolution results of their N1s spectra are shown in **Table 6.2**. The pyrrolic N, which is considered to coordinate with iron in Fe-N_4 active sites, gradually decreases with the increase of Ce content. This result implies a decreasing trend of active site number on the surface, which may lead to low catalytic performance.

Table 6.2 Surface chemical composition of catalysts doped by different molar ratios of Ce.

Fe/Ce	C at.%	O at.%	Fe at.%	Ce at.%	N at.%	Nitrile at.%	Pyridinic at.%	Fe-Nx at.%	Pyrrolic at.%	Quaternary at.%	Graphitic at.%
						398.0 eV	398.8 eV	399.9 eV	400.9 eV	402.0 eV	403.3 eV
pristine	93.54	2.32	0.36	-	3.76	0.94	0.57	0.50	1.14	0.43	0.18
1/0.5	92.55	2.65	0.38	0.10	4.32	1.07	0.70	0.59	1.32	0.44	0.20
1/1	91.79	3.43	0.35	0.20	4.22	1.13	0.60	0.64	1.24	0.45	0.18
1/1.5	91.59	4.09	0.33	0.45	3.56	0.84	0.61	0.53	1.05	0.37	0.15

6.1.3 Electrochemical characterization of catalysts

In order to investigate the effects of Ce doping on ORR activity and stability of the pristine catalyst, the catalysts with different Ce loading amounts were measured in 0.05 M H_2SO_4 electrolyte in RDE setup. **Figure 6.3**a shows the CV tests of catalysts in N_2 saturated electrolyte, along with the pristine catalyst as the comparison. Comparing all CV curves of the samples, two catalysts with low Ce content ($FeCl_3/CeCl_3$=1/0.5 and 1/1) present similar electrochemical available areas with the pristine, indicating low CeO_2 doping content does not affect the exposure of active sites. In contrast, the catalyst with high Ce content ($FeCl_3/CeCl_3$=1/1.5) exhibits a much lower CV area due to its lower BET area and micropore volume. This discrepancy indicates high CeO_2 content may hinder the formation and exposure of Fe-N_4 active sites.

Table 6.3 RDE tests of the catalysts doped by different molar ratios of Ce.

Fe/Ce	$MA_{0.8}$ A g^{-1}	$MA_{0.8}$ after 500 cycles A g^{-1}	Loss ratio	Tafel slope mV dec^{-1}
1/0.5	2.35	1.65	-30%	59
1/1	2.57	1.60	-38%	63
1/1.5	0.69	0.44	-36%	70
Pristine	3.00	2.22	-26%	60

Figure 6.3b shows the ORR polarization curves of catalysts measured in O_2 saturated electrolyte. As expected, $FeCl_3/CeCl_3$=1/0.5 and 1/1 show similar mass activity with the pristine catalyst, indicating a weak impact on the properties of Fe-N_4 active sites at low Ce content. The possible explanation of these results is these CeO_2 nanoparticles, obtained by co-precipitation with Fe precursor, are only deposited on the carbon surface instead of encapsulated or embedded into carbon layers. In this case, the distance between CeO_2 particles and Fe cores is too long to affect the electron density of Fe-N_4 moieties[253]. Moreover, the large particle size of CeO_2 also limits the unveiling of oxygen defects in CeO_2, and thus they cannot well integrate with Fe-N_4 active sites. At high CeO_2 content, the mass activity of $FeCl_3/CeCl_3$=1/1.5 is sharply decreased, indicating a loading limit of CeO_2 is around 0.11 at.% (1.28 wt.%). When the content of CeO_2 is further increased, excessive CeO_2 hinders the Fe-N_4 active sites. However, it should be noted that this limit is only appropriate for the weakly attached CeO_2 particles. It is possible to enhance the loading limit by adjusting the doping method of Ce to realize a stronger integration between CeO_2 and Fe-N_4 moieties. The Tafel plots drawn from the corrected polarization curves are shown in **Figure 6.3**c. It is clear that $FeCl_3/CeCl_3$=1/0.5 and 1/1 show similar Tafel slopes around 60 mV dec^{-1}, which is consistent with the literature and demonstrates that the rate-determining step of the ORR mechanism is the same[64,210,233,236].

However, the value of $FeCl_3/CeCl_3$=1/1.5 is increased to 70 mV dec^{-1}, indicating a different ORR mechanism which may be caused by the presence of CeO_2 nanoparticles.

The durability tests of CeO_2 doped catalysts were conducted in N_2 saturated electrolyte in the RDE setup. **Figure 6.3**d shows the mass activity after 500 CV cycles between 0.6 and 1.0 V. No significant difference between CeO_2-doped catalysts and the pristine catalyst can be observed, with mass activity loss for all catalysts ranging from 30% to 40%. As discussed before, the loss of mass activity in the N_2 saturated electrolyte is mainly caused by the electrochemical oxidation of carbon at high potential, leading to the Fe solvation. Therefore, similar durability of CeO_2 doped catalysts indicates CeO_2 cannot help reducing the electrochemical oxidation of carbon. Since no H_2O_2 or ROS was produced in our durability test condition, the effect of CeO_2 as a scavenger of H_2O_2 should be further investigated.

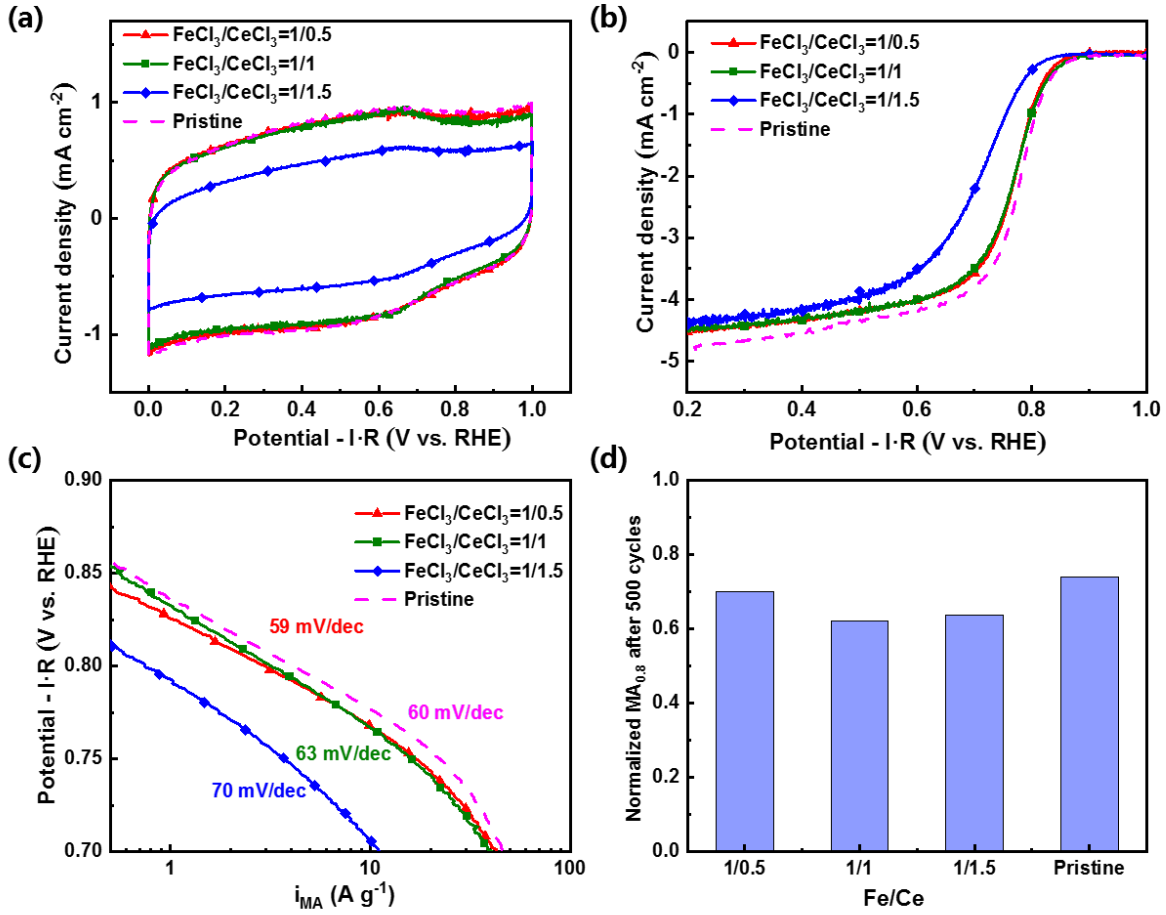

Figure 6.3 Electrochemical characterization of the catalysts doped by different molar ratios of Ce recorded in 0.05 M H_2SO_4. **(a)** CV curves in N_2-saturated electrolyte; **(b)** Polarization curves in O_2-saturated electrolyte at ω = 1600 rpm and v = 10 mV s^{-1}; **(c)** Tafel plots of the O_2-transport and background-current corrected kinetic current obtained from the steady-state Ohmic drop-corrected *I–E* curves at ω= 1600 rpm; **(d)** normalized mass activity at 0.8 V after 500 CV cycles between 0.6-1.0 V in N_2-saturated electrolyte.

The ORR activity and durability of these catalysts were then investigated in a 5 cm^2 single cell PEMFC. The ink formulation was determined in section 2.3, with N/C=2. **Figure 6.4**a shows the H_2/O_2 polarization curves of all catalysts. It can be seen that the trend of activity with Ce content is similar to that observed in RDE. Two catalysts with low Ce content

($FeCl_3/CeCl_3$=1/0.5 and 1/1) show slightly lower activities than the pristine catalyst, whereas that of the catalyst with high Ce content ($FeCl_3/CeCl_3$=1/1.5) is much lower than the pristine catalyst. To get a view of the effect of CeO_2 in H_2/O_2 PEMFC, the corresponding cathodes were operated at 0.5 V in the cell for about 20 h. All catalysts present a quick decline in the first 2 hours, and then the slope becomes flatter. The CeO_2 exhibits a poor effect on scavenging peroxides due to a weak interaction between Fe-N_4 sites and CeO_2.

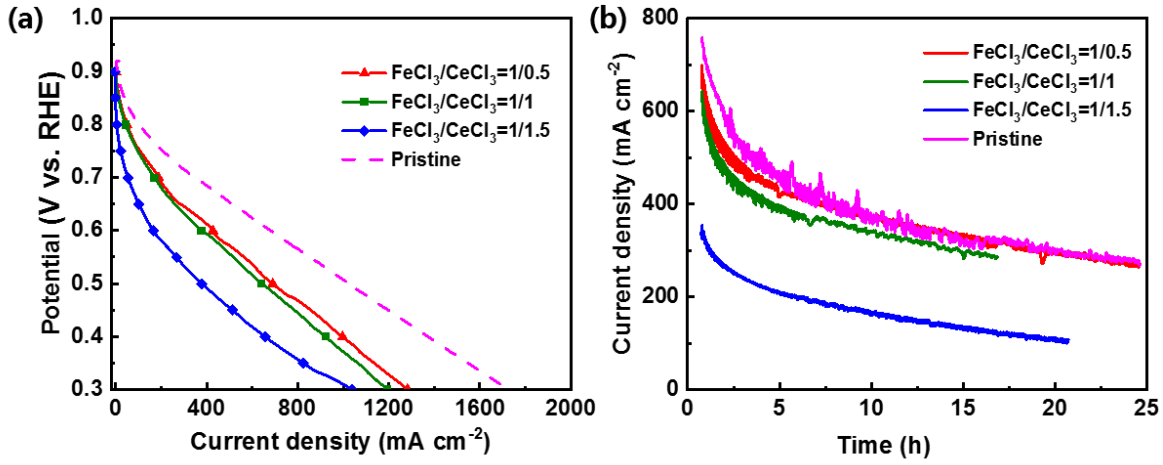

Figure 6.4 **(a)** Polarization curves and **(b)** durability tests in H_2/O_2 PEMFC of catalysts doped by different molar ratios of Ce. The measurements were performed with T_{cell} = 80 ℃, 100 % RH, *P*cathode = *P*anode = 2 bar_{abs}, the H_2, and O_2 flow rates were 150 mL min^{-1} while the air flow rate was 480 mL min^{-1}.

It should be noted that different decay rates may suggest different deactivation mechanisms of active sites in PEMFC. The flatter decay after 2 hours is supposed to be caused by H_2O_2 produced during the ORR, which is considered to be a non-recoverable activity decay, whereas the reason for rapid decay in the first 2 hours is still controversial. Jaouen *et al.* initially proposed a mechanism relating to the nitrogen-protonation and anion-binding effects in Fe-N-C catalysts[107,195]. **Figure 6.6** shows the initial spatial relations between Fe-N_4 active site and highly basic N group were shown in the as-prepared catalyst. The active site is assumed to possess a high TOF value for the ORR as long as nearby basic N-groups are protonated but not bound to an anion. However, when these protonated NH^+ groups are bound by anions, the TOF of active sites becomes "normal" again. The HSO_4^- anion adsorption is fast in RDE since the anions can diffuse freely, while it is probably much slower in PEMFC since the sulfonate anions are bound to the polymeric backbone of the Nafion surrounding the catalyst in the PEMFC electrode.

In a fully humidified PEMFC cathode, the protons can swiftly access the basic N-groups to get high TOF active sites. However, they would later switch to the low TOF state when polymeric chains slowly approach the NH^+ groups, resulting in anion binding. This effect can explain the sharp activity decay in the first 2 hours, and this part is recoverable by removal of counter anions by chemical or heat treatment[107]. If this hypothesis is correct, the rate of decay of the current density should relate to the size of pendent chains of ionomer. However, when Nafion is replaced by other ionomers bearing shorter pendant chains, such as Flemion, or those with pendant chains too big to enter into micropores, such as tetrasulfonate hydrogen porphyrins, no effect on the initial decay rate can be observed[254]. In this case, a new hypothesis was proposed that the first decay of the current density is related to water flooding of the micropores,

and the rate at which water flooding occurs depends on the hydrophilicity of the micropore walls, the latter varying with the heteroatom content on the catalyst surface[254]. For the hydrophobic catalyst layer, the fast decay rate can be slowed down, but with elapsed time, the carbonaceous cathode is slowly oxidizing and becomes more and more hydrophilic. However, this hypothesis was latterly argued by Choi *et al.* that the majority of the micropores were wetted at the beginning of life. Although some degree of additional catalyst layer wetting occurred during the stability test, such a small increase could not explain the significant performance loss that was observed[255,256]. Therefore, the reason for the rapid decay at the beginning of the durability test should be further explored.

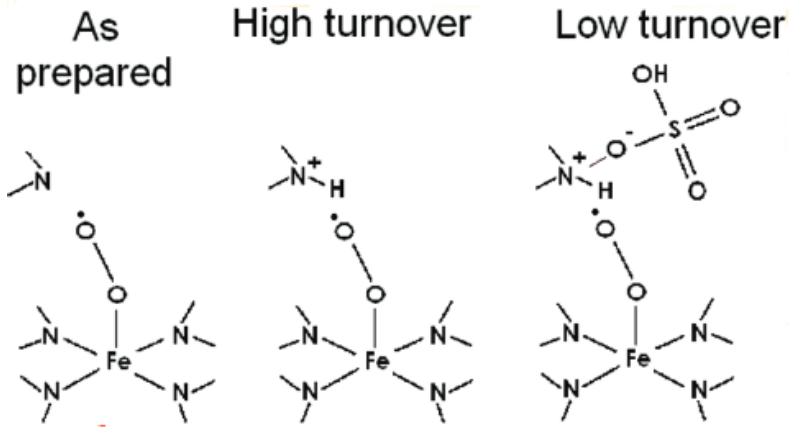

Figure 6.5 Change of the chemical state of protonable N-groups and simultaneous change of the TOF for the ORR of Fe-N_4 active sites when the Fe-N-C catalyst is in H_2SO_4 electrolyte[107].

In summary, CeO_2 doped Fe-N-C samples with different CeO_2 content were prepared with $CeCl_3$ precursor. The composition of $FeCl_3$-R/M=2/2 was used as the pristine catalyst. The final Ce contents of all samples are lower than the theoretical Fe/Ce values due to the loss of Ce precursor during the solvent exchange step. The mesopore volume of CeO_2 doped Fe-N-C catalyst was significantly decreased because the presence of $CeCl_3$ in the precursor solution requires more NaOH to dissolve the precipitation modifying the gel formation. Appropriate low Ce loading (0.11 at.%) does not affect the micropore volume and ORR activity. However, when the content of CeO_2 is further increased, excessive CeO_2 limits the effect of the NH_3 thermal treatment. It may hinder the formation and exposure of Fe-N_4 active sites, resulting in a decline in the micropore volume and ORR performance. Although the special ability of CeO_2 to scavenge peroxides has been reported in previous publications, the CeO_2 doped Fe-N-C catalysts based on the insertion of Ce precursor in the gel do not exhibit better durability than the pristine catalyst in our durability test. The possible reason is CeO_2 nanoparticles are only attached to the carbon surface, resulting in a weak interaction with Fe-N_4 active sites. Therefore, the synthesis method should be modified to realize a better integration between CeO_2 and Fe center.

6.2 CeO_2 nanoparticle precursor

6.2.1 Texture and structure of catalysts

In this section, CeO_2 nanoparticles were used as the Ce precursor. Compared with $CeCl_3$, it is supposed to obtain a more uniform particle size of CeO_2 because the size is given by the supplier as less than 25 nm. For comparison, we also tried to introduce the CeO_2 nanoparticles into pristine catalyst by ball milling method, after the acid washing step but before NH_3 treatment, which is supposed to reduce the loss of Ce. The CeO_2 nanopowder and $FeCl_3$-R/M=2/2 were ground with ZrO_2 balls of 5 mm diameter at 400 rpm for 2 h. The samples were collected, and then conducted to NH_3 treatment. The initial molar ratio of $FeCl_3/CeO_2$ is 1/1, and the sample is labeled as $FeCl_3/CeO_2$=1/1 BM.

The SEM images shown in **Figure 6.6**a-d show a basic view of the morphology of catalysts prepared with different CeO_2 contents or introduction methods. Similar to the catalysts prepared with $CeCl_3$ precursor, all samples present a more compacted texture than the pristine catalyst $FeCl_3$-R/M=2/2 (**Figure 4.2**e). Some small holes can be observed on $FeCl_3/CeO_2$=1/1 BM, which may be caused by mechanical milling with CeO_2 nanoparticles. Their N_2 sorption results confirmed the observation under SEM. **Figure 6.6**d and e exhibit the N_2 adsorption-desorption isotherms and pore size distribution curves, respectively. Similar to the series of $CeCl_3$, the isothermal curves of all samples exhibit a quasi-absence of mesopore volume. Their texture characteristics calculated from nitrogen sorption isotherms are listed in **Table 6.4**. It seems the CeO_2 nanoparticles introduced in the precursor solution do not affect the morphology of catalysts. All samples ($FeCl_3/CeO_2$=1/0.5, 1/1, and 1/1.5) show similar specific surface area and micropore volume. On the contrary, if the CeO_2 is introduced by ball milling after acid washing of pristine catalyst, the specific surface area and micropore volume are halved.

Table 6.4 Physicochemical characterization of catalysts doped by different molar ratios of Ce. CeO_2 nanoparticles were used as the Ce precursor.

Fe/Ce	Total mass loss wt.%	ICP Fe		ICP Ce		BET surface ($m^2\ g^{-1}$)	Vtotal ($cm^3\ g^{-1}$)	Vmicro ($cm^3\ g^{-1}$)	Vmeso ($cm^3\ g^{-1}$)
		wt.%	at.%	wt.%	at.%				
pristine	81%	1.36	0.30	-	-	1271	0.78	0.45	0.25
1/0.5	79%	1.19	0.26	0.12	0.01	1185	0.51	0.46	0.02
1/1	84%	1.20	0.26	0.77	0.07	1151	0.51	0.44	0.04
1/1.5	80%	1.22	0.27	0.60	0.07	1089	0.50	0.42	0.05
1/1 BM	74%	1.00	0.22	3.71	0.33	578	0.32	0.21	0.09

To gain further insight into the effects of the introduction method on the catalyst morphology, the Fe and Ce contents were determined by the ICP-MS method, and the results are listed in **Table 6.4**. Samples with CeO_2 introduced in precursor solution ($FeCl_3/CeO_2$=1/0.5, 1/1, and 1/1.5) show very low Ce content (less than 0.1 at.%), far less than the designed value. The possible reason is electrically neutral CeO_2 nanoparticles cannot be well adsorbed onto the RMF hydrogel. In contrast, the $CeCl_3$ precursor can reach a higher Ce content in the final catalyst because the fresh cerium hydroxide precipitation can form hydrogen bonds to anchor on the skeleton of hydrogel. In this case, CeO_2 nanoparticles are easier to remove during solvent exchange. Since the Ce content is less than 0.1 at.%, the negative effects of CeO_2 on micropore volume and BET area are negligible. In contrast, $FeCl_3/CeO_2$=1/1 BM shows a high Ce content in the final catalyst due to no Ce loss during NH_3 treatment. The final Ce content is higher than the designed value (molar ratio of Fe/Ce=1/1.5) due to the loss of Fe during the acid-washing

step. Moreover, the micropore volume and BET area of $FeCl_3/CeO_2$=1/1 BM is halved due to its high Ce content. This result is in agreement with the previous result with $CeCl_3$, that the limit of Ce content should be lower than 0.11 at.%. Otherwise, the presence of excessive CeO_2 may prevent the gasification reaction between carbon and NH_3.

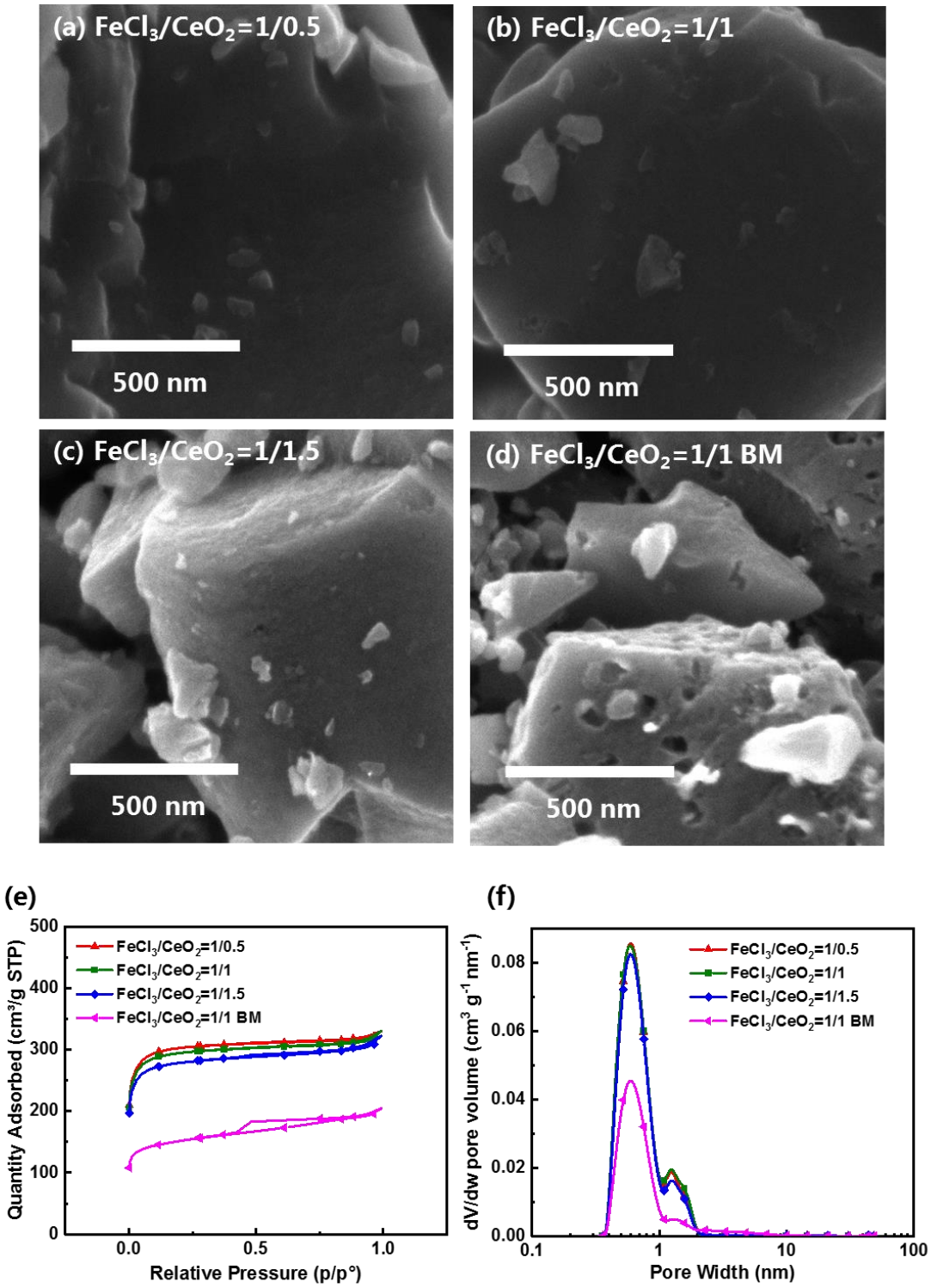

Figure 6.6 **(a)-(d)** SEM images of the catalysts doped by different molar ratios of Ce; **(e)** N_2 adsorption isotherms at -196 ℃ and **(f)** pore size distribution plots obtained by using the 2D-NLDFT-Heterogenerous Surface.

The CeO_2 nanoparticles can also be observed under TEM images (**Figure 6.7**a-c). However, due to their low Ce content, only some small CeO_2 nanoparticles are sparsely dotted on the carbon. More and larger CeO_2 particles can be found in $FeCl_3/CeO_2$=1/1 BM (**Figure 6.7**d). Their carbons also show a pore-less morphology, in agreement with their poor mesopore volume. **Figure 6.7**e shows the X-ray diffraction patterns of catalysts. $FeCl_3/CeO_2$=1/0.5, 1/1, and 1/1.5 show two lumps at around 2θ=26.0 °and 43.6 °, corresponding to the low graphitized carbon. These two peaks become more intense for $FeCl_3/CeO_2$=1/0.5 BM, confirming that high CeO_2 content can promote the graphitization of carbon at high temperature. Therefore, the micropore volume of $FeCl_3/CeO_2$=1/0.5 BM is only half the others. Two peaks of CeO_2 at 2θ=28.5 °and 47.3 ° can be observed in the patterns of $FeCl_3/CeO_2$=1/1 and 1/1.5[253]. The diffraction peaks of CeO_2 are more intense than those in the $CeCl_3$ series because commercial CeO_2 nanoparticles have larger and well crystallized particles. In the pattern of $FeCl_3/CeO_2$=1/1 BM, two more peaks at 2θ=33.0 °and 56.3 ° can be identified, which can be assigned to (200) and (311) crystal planes of CeO_2.

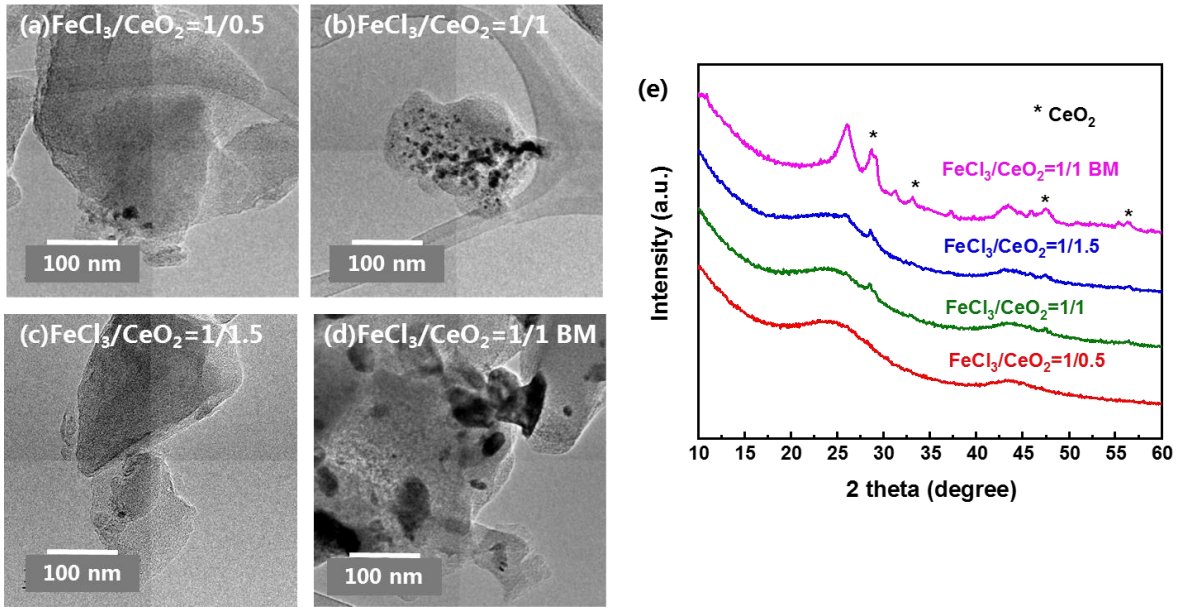

Figure 6.7 (a)-(d) TEM images of the catalysts doped by different molar ratios of Ce and **(e)** normalized XRD patterns.

6.2.2 Chemical composition of catalysts

The surface chemical compositions of catalysts were investigated by XPS characterization. As the results listed in **Table 6.5**, the Fe and N contents of CeO_2 doped catalysts ($FeCl_3/CeO_2$=1/0.5, 1/1, and 1/1.5) obtained from XPS are similar to the pristine catalyst, indicating the structural composition of Fe-N_4 sites are still well preserved in the existence of low content CeO_2. However, the total N content of $FeCl_3/CeO_2$=1/1 BM is significantly decreased, which is in agreement with the previous conclusion that high CeO_2 content prevents the formation of Fe-N_4 active sites. The deconvolution results of N1s spectra are listed in **Table 6.5**. Catalysts with low Ce content show similar pyrrolic N content with pristine catalyst, whereas the value decreases in $FeCl_3/CeO_2$=1/1 BM because CeO_2 impedes the formation of Fe-N_4 sites. The Ce contents obtained from XPS of $FeCl_3/CeO_2$=1/0.5, 1/1, and 1/1.5 are similar to the results of ICP-MS. In contrast, the value in $FeCl_3/CeO_2$=1/1 BM is much higher than ICP-MS method because the CeO_2 introduced by BM can only deposit on the surface of carbon aerogel particles.

Table 6.5 Surface chemical composition of catalysts doped by different molar ratios of Ce.

Fe/Ce	C at.%	O at.%	Fe at.%	Ce at.%	N at.%	Nitrile at.%	Pyridinic at.%	Fe-Nx at.%	Pyrrolic at.%	Quaternary at.%	Graphitic at.%
						398.0 eV	398.8 eV	399.9 eV	400.9 eV	402.0 eV	403.3 eV
pristine	93.54	2.32	0.36	-	3.76	0.94	0.57	0.50	1.14	0.43	0.18
1/0.5	92.25	3.35	0.35	0.10	3.96	0.93	0.65	0.62	1.21	0.40	0.15
1/1	91.92	3.40	0.36	0.16	4.15	1.02	0.67	0.61	1.22	0.44	0.19
1/1.5	92.33	3.56	0.34	0.12	3.65	0.87	0.59	0.58	1.07	0.39	0.15
1/1 BM	91.09	4.52	0.33	0.79	3.28	0.84	0.47	0.48	0.93	0.41	0.16

6.2.3 Electrochemical characterization of catalysts

In order to test and verify the effect of CeO_2 on ORR activity and stability, the catalysts with different Ce loading amounts were measured in 0.05 M H_2SO_4 electrolyte in the RDE setup. **Figure 6.8**a shows the CV curves of catalysts recorded in N_2 saturated electrolyte, along with the pristine catalyst as the comparison. As expected, the catalysts with low Ce content ($FeCl_3/CeO_2$=1/0.5, 1/1, and 1/1.5) present similar electrochemical available area with the pristine catalyst, whereas $FeCl_3/CeO_2$=1/1 BM shows very low CV area due to its low BET area at high CeO_2 content. Their polarization curves in the O_2 saturated electrolyte are shown in **Figure 6.8**b, and corresponding mass activities at 0.8 V are listed in **Table 6.6**. The mass activity of the catalyst is comparable with the pristine catalyst at low Ce content, whereas it dramatically drops at high Ce content ($FeCl_3/CeO_2$=1/1 BM with Ce more than 0.11 at.%). This result is consistent with previous research on $CeCl_3$ precursor. Therefore, it might be concluded that different Ce precursors and introduction methods of Ce do not change the property of CeO_2 nanoparticles and Fe-N_4 sites in the final catalyst but only affect the loading of CeO_2, which presents a crucial effect on the mass activity of the catalyst.

Table 6.6 RDE tests of the catalysts doped by different molar ratios of Ce.

Fe/Ce	$MA_{0.8}$ A g^{-1}	$MA_{0.8}$ after 500 cycles A g^{-1}	Loss ratio	Tafel slope mV dec^{-1}
1/0.5	2.60	1.85	-29%	68
1/1	3.16	2.36	-25%	66
1/1.5	2.70	1.95	-28%	68
1/1 BM	1.21	0.79	-35%	75
pristine	3.00	2.22	-26%	60

The Tafel plots of catalysts derived from the polarization curves are shown in **Figure 6.8**c. The Tafel slopes of samples with low CeO_2 content ($FeCl_3/CeO_2$=1/0.5, 1/1, and 1/1.5) are slightly higher than that of pristine catalyst, suggesting the oxygen is reduced by a different mechanism in the presence of CeO_2[187,210]. The value is further increased at higher CeO_2 content in $FeCl_3/CeO_2$=1/1 BM, indicating the contribution of CeO_2 to ORR activity is also increased. The durability tests were carried out for all catalysts with 500 CV cycles between 0.6-1.0 V in N_2 saturated electrolyte. The mass activities after the durability test and the loss ratio are listed in **Table 6.6**. Catalysts with low CeO_2 content ($FeCl_3/CeO_2$=1/0.5, 1/1, and 1/1.5) exhibit loss ratios in the range of 25%-29%. These results are similar to those of pristine catalyst and $CeCl_3$ series, indicating the change of Ce precursor to CeO_2 cannot enhance the interaction between Ce and Fe-N_4 sites. The loss ratio of $FeCl_3/CeO_2$=1/1 BM with higher Ce content is even

increased, indicating that excessive CeO_2 can lead to more severe carbon corrode by electrochemical oxidation.

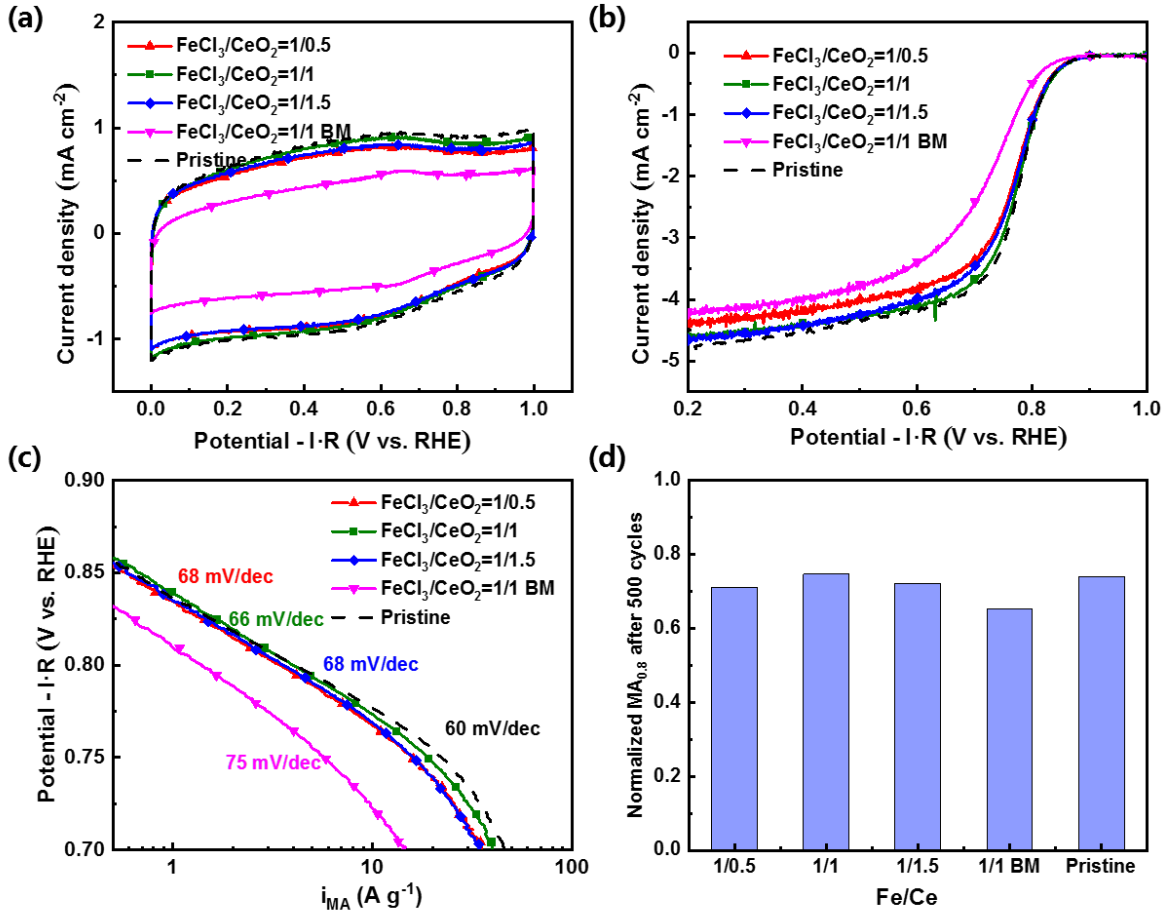

Figure 6.8 Electrochemical characterization of the catalysts doped by different molar ratios of Ce recorded in 0.05 M H_2SO_4. **(a)** CV curves in N_2-saturated electrolyte; **(b)** Polarization curves in O_2-saturated electrolyte at ω = 1600 rpm and v = 10 mV s^{-1}; **(c)** Tafel plots of the O_2-transport and background-current corrected kinetic current obtained from the steady-state Ohmic drop-corrected *I–E* curves at ω= 1600 rpm; **(d)** normalized mass activity at 0.8 V after 500 CV cycles between 0.6-1.0 V in N_2-saturated electrolyte.

The activity and durability of catalysts with low Ce content ($FeCl_3/CeO_2$=1/0.5, 1/1, and 1/1.5) were further investigated in a 5 cm^2 single cell PEMFC. The tests were not conducted on $FeCl_3/CeO_2$=1/1 BM due to poor ORR activity. **Figure 6.9**a shows their H_2/O_2 polarization curves, along with the pristine as the comparison. Their curves present a similar trend with the result in RDE setup that the activity of $FeCl_3/CeO_2$=1/1 is slightly higher than the other two. However, the difference is too small to say $FeCl_3/CeO_2$=1/1 is the best composition. To further investigate their durability in H_2/O_2 PEMFC, the corresponding cathodes were operated at 0.5 V in the cell for about 20 h. As seen in **Figure 6.9**b, all catalysts present similar decline behavior with $CeCl_3$ series, that a sharp decrease at the beginning followed by a flatter decline. According to the discussion in section 6.1, the latter is non-recoverable decay due to the loss of Fe sites. Since the H_2O_2 scavenger mainly affects the slope of non-recoverable decay, the similar decline slope indicates the presence of CeO_2 in the pristine catalyst cannot inverse the attenuation trend of Fe-N_4 sites with increasing operation time. The poor effect of CeO_2 on scavenging peroxides can also be attributed to a weak interaction between Fe-N_4 sites and CeO_2.

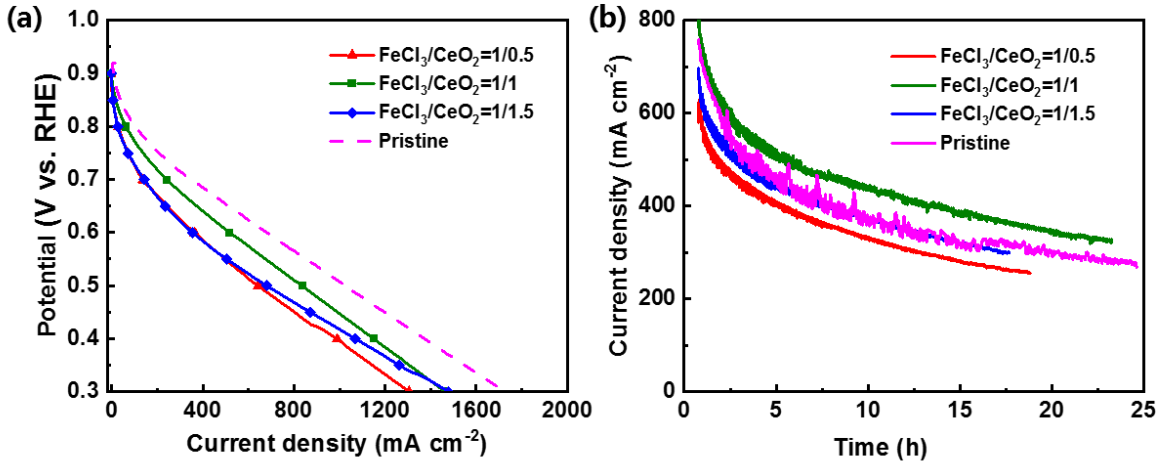

Figure 6.9 **(a)** Polarization curves and **(b)** durability tests in H_2/O_2 PEMFC of catalysts doped by different molar ratios of Ce. The measurements were performed with T_{cell} = 80 ℃, 100 % RH, *P*cathode = *P*anode = 2 bar_{abs}, the H_2, and O_2 flow rates were 150 mL min^{-1} while the air flow rate was 480 mL min^{-1}.

In summary, an alternative Ce precursor (CeO_2 nanopowder) was used to prepare CeO_2 doped Fe-N-C samples to achieve a more uniform particle size distribution. Different from the $CeCl_3$ precursor, which can be transformed to cerium hydroxide to anchor on the RMF hydrogel, CeO_2 nanoparticles are only deposited on the hydrogel surface, thus leading to a high loss ratio CeO_2 during the solvent exchange step and very low Ce content in the final catalyst. In comparison, introducing CeO_2 nanoparticles by ball milling after the acid washing step can preserve the Ce precursor well. Similar to the $CeCl_3$ series, low Ce loading does not affect the micropore volume and ORR activity. In contrast, these are significantly decreased at high Ce content because the presence of excessive CeO_2 may hinder the formation and exposure of Fe-N_4 active sites. The series CeO_2 nanopowder does not exhibit better durability than the pristine catalyst in our test conditions, indicating different Ce precursor does not affect the properties of CeO_2 in the final catalyst. Therefore, the interaction between CeO_2 and Fe-N_4 active sites is still too weak to scavenge the peroxide nearby. The function of CeO_2 is possible to be highlighted by approaching the CeO_2 to Fe-N_4 sites. To achieve this, the particle size of CeO_2 should be further reduced to have more chance to meet Fe-N_4 sites. It is also possible to directly graft carbon layers around CeO_2 nanoparticles with new synthesis methods, which is supposed to improve both activity and durability of the Fe-N-C catalyst.

Conclusion and Perspective

Proton exchange membrane fuel cells (PEMFCs) are considered promising technology for stationary and mobile applications because of their high energy conversion efficiency and power density. These devices promote the possibility of establishing a clean and sustainable society. Due to sluggish oxygen reduction reaction (ORR) on the cathode and the acidic environment of PEMFC, large quantities of Pt-based electrocatalysts are necessary to reach the acceptable power performance of PEMFCs, which impedes their broader commercialization and threatens their sustainability. Therefore, developing platinum-group metal-free catalysts for the ORR in acid media is highly desirable. In this manuscript, a series of state-of-art Fe-N-C aerogel catalysts were synthesized and characterized.

The impacts of different iron precursors on the porosity and electrochemical activity of Fe-N-C catalysts were investigated. The iron salts with different oxide states and counter ions were selected to investigate the impacts on porosity and electrochemical activity. The catalysts prepared at pH=8 with $FeCl_3$ and $Fe(NO_3)_3$ (Fe^{3+}) display the best electrochemical activity at 0.8 V both in the RDE setup and PEMFC, slightly higher than for $(NH_4)_2Fe(SO_4)_2$ (Fe^{2+}) due to their excellent solubility in precursor solution leading to a low yield of Fe-rich nanoparticles and similar porosity. The oxide states of Fe and counter ions show little effect on final catalytic performance if the Fe precursor is soluble in water. The insoluble phthalocyanine (FePc, Fe^{2+}) is not a good choice at pH=8 since it led to low porosity of carbon aerogel. Although the porosity could be increased at a lower pH value, the current density at 0.8 V was only slightly increased. The low Fe content in the catalyst prepared with FePc evidenced that insoluble Fe precursor cannot be well dispersed in the precursor solution, thus leading to a higher yield of Fe-rich nanoparticles, which can be eliminated by acid washing. The pre-existing Fe-N_4 structure in the FePc precursor cannot increase the density of active sites in the final catalyst because this structure is decomposed before reaching the temperature that creates active sites.

The modification of Fe precursors, including the introduction of ligand additives and increase of Fe precursor quantity, did not receive expected results. EDTA ligand increases the solubility of Fe precursor but leads to a loss of Fe during the solvent exchange step. As a result, all catalysts prepared with EDTA ligand exhibit ultra-low Fe contents. Phenentroline (Phen) generates insoluble precipitations in the mixed solution, which leads to a different texture from the non-ligand catalyst. High Fe content can be obtained in Phen catalyst without any observable nanoparticles, indicating a high content of active sites. However, the low micropore volume limits the improvement of electrochemical activity. In conclusion, due to the complicated chemical environment of mixed solution, the ligand additives exhibit little improvement in the electrochemical activity of catalysts. The crucial point among these catalysts is their activity is closely related to their Fe content, especially the surface Fe content obtained from XPS analysis. However, simply increasing the quantity of Fe precursor only leads to more unexpected nanoparticles in the final catalyst. The pre-existing coordination structure presents little impact on forming active centers. Even though all Fe atoms are contained in the Fe-N_4 macrocycle in the FePc precursor, the microstructure will be decomposed during the carbonization step.

The impacts of melamine content on the ORR activity and mass transport properties of Fe-N-C aerogel catalysts were systematically investigated. The absolute amount of Fe was found to increase with M content, and the absolute amount of Fe-N_4 sites also increased with M content. The atomically dispersed nitrogen in melamine can stabilize the Fe during pyrolysis, avoiding or minimizing the formation of iron nanoparticles. From the analysis of XPS spectra, the pyrrolic N content is positively correlated with the increase of the M content, supporting

that most of the active Fe atoms are coordinated by pyrrolic nitrogen, in agreement with Mössbauer spectra. Electrochemical tests in RDE show a linear relationship between mass activity up to a Fe content of 0.3 at.%, corresponding to the catalyst $FeCl_3$-R/M=2/2, with the highest mass activity of 3.0 A g^{-1}. This trend is in line with the physicochemical characterization, indicating that most Fe is present as atomically dispersed Fe-N_x sites. This trend is also suitable for other Fe precursors, such as $Fe(NO_3)_3$ and FePc. By combining the best precursor ($Fe(NO_3)_3$) and high M content (R/M=2/2), the best catalyst was obtained with a $MA_{0.8}$=3.58 A g^{-1} (at 0.8 V vs. RHE and in 0.05 M H_2SO_4) in RDE setup which is close to the commercial Pajarito powder (PMF D14401). In H_2/O_2 PEMFC, $Fe(NO_3)_3$-R/M=2/2 also shows the highest current density of 113 mA cm^{-2} at 0.8 V, and the current density of 44 mA cm^{-2} is reached at 0.85 V, which is only 0.05 V lower than the DOE 2025 target for platinum group metal-free catalyst[156]. Besides, the polarization curve does not collapse at high current density, indicating its good mass transport properties, which is promising to be widely used in the future.

This study highlights is the successful preparation of Fe-N-C catalysts with adjustable and high-purity Fe-N_4 active sites embedded in a carbon aerogel substrate. We show that Fe-N-C aerogel can lead to a highly efficient ORR catalyst by controlling the synthesis conditions: (i) a soluble Fe(III) precursor should be selected, such as $FeCl_3$ and $Fe(NO_3)_3$, to ensure that the Fe and N precursors are atomically mixed; (ii) high melamine (nitrogen source) content is necessary for RMF aerogel to facilitate the formation of active sites. The major Fe-N_4 active site was determined to be D1 configuration by mutual confirmation of the XPS spectrum of nitrogen (N 1s) and ^{57}Fe Mössbauer spectrum. Compared to the traditional preparation method of Fe-N-C catalysts, *i.e.*, mixing a microporous support (carbon black, such as BP2000 or metal-organic framework, such as ZIF-8), a pore filler (nitrogen precursor, such as phenanthroline), and Fe precursor by ball-milling method, followed by pyrolysis, our one-pot synthesis method can atomically mix Fe and N precursors in the solution, thus reducing the yield of Fe-rich nanoparticles. Comparing to the ordered mesopore carbon-based Fe-N-C catalysts prepared from the sacrificial support method (*i.e.*, Pajarito powders), the synthesis of aerogel-based catalysts is more environmentally friendly since there is no need to remove silica support by hydrofluoric acid, suggesting this method is more suitable for scaling up production in future.

However, the durability of Fe-N-C aerogel catalysts still needs to be improved before their application in the practical PEMFC. All aerogel-based catalysts lost more than 90% of their initial activity after a strong AST process (conducted by LEPMI, between 0.6 and 1 V for 10,000 cycles at 80 ℃ in O_2 saturated 0.1 M H_2SO_4), which is far from reaching the DOE 2025 target. Two aspects should be considered:

The first is to further clarify the mechanism of the ammonia treatment process on the activation of catalysts because although this treatment can significantly increase the initial ORR activity of Fe-N-C catalyst, their long-term stability is usually decreased. In this manuscript, we made a primary investigation to elucidate the effect of NH_3 treatment on increasing the mass activity of Fe-N-C catalyst. Two main functions of NH_3 treatment can be inferred from their different XPS spectra and polarization curves: (i) As NH_3 corrodes the carbon layers, more active sites are exposed. Meanwhile, some released free Fe atoms react with pyrrolic N and are anchored on the carbon surface. The reaction between NH_3 and Fe is excluded because pyridinic N is not involved in the formation of Fe-N_4 active sites. (ii) The pyridinic N introduced by NH_3 treatment increases the basicity on the surface of catalyst, which can significantly enhance the TOF of active sites. The variation of Fe center before and after treatment should be further characterized by the Mössbauer spectrum to confirm the results of XPS. The NH_3 treated catalyst exhibits a decreased durability during AST in O_2-saturated electrolyte, possibly due to the highly basic nitrogen groups introduced by NH_3 that increase the demetallation rate of Fe-

N-C catalysts in acid medium. The nitrite adsorption/reduction method should be performed before and after the different AST to observe the evolution of the SD and the TOF value of catalysts.

The second is to introduce a scavenger of H_2O_2 to improve the durability of Fe-N-C catalysts. Primary research on CeO_2 scavenger was conducted in this manuscript. The CeO_2 doping in Fe-N-C aerogel catalyst does not affect its durability regardless of Ce precursor and Ce content. The final Ce contents of all samples are lower than the theoretical Fe/Ce values due to the loss of Ce precursor during the solvent exchange step. The catalyst with the best activity is the one with 0.11 at.% Ce loading. When the content of CeO_2 is further increased, excessive CeO_2 may hinder the formation and exposure of Fe-N_4 active sites, resulting in a decline in the micropore volume and ORR performance. Although the special ability of CeO_2 to scavenge peroxides has been reported in previous publications, the CeO_2 doped Fe-N-C catalysts do not exhibit better durability than the pristine catalyst in our durability test. The possible reason is CeO_2 nanoparticles are only deposited on the carbon surface, resulting in a weak interaction with Fe-N_4 active sites. Therefore, the CeO_2 doping method should be further modified to obtain a better synergy between CeO_2 and Fe-N_4 active sites, such as preparing few-layer carbon encapsulated CeO_2 to closely combine two types of sites. Besides, CeO_2 can also be replaced by some Pt-based nanoparticles as a highly efficient peroxide scavenger. As reported in the literature, an ultra-low introduced Pt content (1 wt.%) is expected to lead to Pt nanoparticles that can exhibit a synergetic effect with Fe-N_4 sites and scavenge H_2O_2 intermediate to protect the carbon layer. This method is promising to get low-cost Fe-N-C catalysts with high ORR performance and durability to reach DOE 2025 target. Studies are in progress on our best catalyst by ICGM.

Annexes

A.1 The preparation of Piranha Solution

H_2O_2 (35%) solution was purchased from ACROS Organics™, and H_2SO_4 (96%) was purchased from Fisher Scientific. All chemicals were used directly without any treatment.

1. 500 mL of 35% H_2O_2 solution was poured into a flask which was placed in an ice bath. The solution was under vigorous magnetic stirring.
2. 500 mL of 96% H_2SO_4 was introduced by successive addition of 15 mL. During this step, ice should be supplied regularly to ensure the temperature at 0 ℃.
3. When H_2SO_4 was totally added, the mixture is kept stirring at room temperature for 24 h.

A.2 Characterization techniques and operating conditions

A.2.1 Dynamic light scattering analysis

Particle size measurements were performed using a dynamic light scattering analyser (HPPS, Malvern Instruments Inc, Worcestershire, UK) incorporating Non-Invasive Back-Scattered optics. Catalyst suspensions were prepared using 1 mg of catalyst in 20 mL of absolute ethanol. After 60 minutes of sonication at 20 ℃, the catalyst suspensions were placed in a disposable PMMA cuvette and loaded in the instrument sample holder. The temperature was allowed to equilibrate for 10 minutes at 25 ℃. Samples were then analyzed using a collection time of 20 minutes.

A.2.2 Nitrogen sorption analysis at -196 ℃

Nitrogen sorption isotherms were measured with a Micromeritics ASAP 2020 instrument. The weight of empty sample tube was recorded at the beginning of the preparation. A mass of *ca.*150 mg of catalyst was then weighed and sealed in the sample tube. Prior to the measurement, the sample was degassed under 10 mmHg pressure at 200 ℃ for 8.3 hours with a ramp rate of 10 ℃ min^{-1}. The mass of catalyst was calculated by mass of degassed tube minus empty tube. The N_2 adsorption/desorption measurement was carried out at -196 ℃ in a liquid nitrogen Dewar bottle. BET area was determined via the Brunauer–Emmett–Teller equation while the total pore volume (V_t) was estimated from the adsorption isotherm at the relative pressure of 0.995. The pore size distribution (PSD) of micropore volume (V_{micro}) and mesopore volume (V_{meso}) was calculated with Solution of the Adsorption Integral Equation Using Splines (SAIEUS) program based on the adsorption isotherms. 2D-NLDFT-Heterogeneous Surface model was used which incorporates energy heterogeneity and geometric corrugation on the surface of carbon pores.

A.2.3 X-ray diffraction

X-ray diffraction (XRD) analysis was performed using an X"pert Pro Philips diffractometer using filtered Cu Kα radiation (λ=0.15418 nm) generated at 40 kV and 30 mA. The signal was recorded from 2θ=10-60 ºwith a 0.05 ºstep and 5 sec hold per step in order to obtain high quality

XRD signals. The diffraction angles of the peaks were determined with High score software. The interlayer spacing of carbon layer (d_{002}) was calculated by Bragg's law:

$$d_{002} = \frac{2sin\theta}{\lambda} \quad \text{(A-1)}$$

The average values of perpendicular graphene layers (L_c) were calculated from the Debye-Scherrer equation:

$$L_c = \frac{0.88\lambda}{\beta cos\theta} \quad \text{(A-2)}$$

where β is the line broadening at half the maximum intensity in radians after subtracting the background.

A.2.4 Raman spectroscopy

Raman spectroscopy was used to differentiate the carbon structure of the different electrocatalysts. A Renishaw InVia instrument in a backscattering configuration (with 532 nm as excitation) was used for each measurement. An objective focus of X50 was used to collect the scattered radiation. In order to prevent the excess heating or probable degradation of the samples under the laser beam, the spectrometer was used in a 'line mode' with low incident power densities (~50 μW μm^{-2}). LabSpec 5.0 software was used for fitting the Raman spectra and five bands were considered, as our previous work.[244] The average values of in-plane graphite crystallite size (L_a) was calculated from the Knight and White equation:[257]

$$L_a(nm) = 4.4\ (\frac{I_{D1}}{I_G})^{-1} \quad \text{(A-3)}$$

A.2.5 X-ray photoelectron spectroscopy

X-ray photoelectron spectroscopy (XPS) was used to identify the elemental composition on the surface of catalysts. To prepare the sample for analysis, appropriate amount of powder was taken by a straw and poured on the support. The powder was then pressed by a spoon with the protection of aluminum foil to get a plat and dense surface. The support was put in an ultra-high vacuum chamber and then close the entrance to start the vacuum pump until the pressure is lower than 5×10^{-8} mbar.

The measurements were performed using Thermo ScientificTM K-AlphaTM spectrometer equipped with a RESOLVE 120MCD5 hemispherical electron analyzer and an Al Kα1,2 monochromatic source (1486.6 eV). The constant pass energy mode was used to record both survey and high-resolution spectra, with pass energies 100 and 20 eV respectively. All samples were analyzed with a spot size of 200 μm and repetitive tests were conducted on four different spots of all samples to ensure the accuracy of the measurements. A survey spectrum and higher resolution multiplex scan spectra (C 1s, O 1s, N 1s, and Fe 2p core levels) were obtained and analyzed by Avantage. The intensity of the Fe 2p peak in the high-resolution scan is very low due to low Fe content in the catalysts, we increase the scan number to 64 to increase the signal/noise ratio of final spectrum.

Quantitative calculations were performed using the XPS peak areas. The surface ratio of all elements of the samples was calculated by using the area of the core level peaks, normalized to the photoemission cross section by assuming a homogeneous distribution arrangement model. The calculation was conducted on five spots and the final element content was determined by the average of five values. Further deconvolution of N1s spectra was conducted based on the method of Atanassov *et al.*, containing six components: nitrile, pyridinic, Fe-N_x or amine, pyrrolic, quaternary, and graphitic. The binding energy of pyridinic N was fixed at 398.8 eV as the benchmark, and the position of other peak was determined by their binding energy difference with pyrinidic N. For the major components (pyrrolic, Fe-N_x, and nitrile), the uncertainty of binding energy position was limited in ±0.2 eV. The value is enlarged to ±0.4 eV for the minor components (quaternary and graphitic) due to low intensity of signal at high binding energy. For the consistency among all other spectra from electrocatalysts, the peaks during spectral curve fitting were constrained to have a full width at half maximum (fwhm) between 1.2 and 1.3 eV.

A.2.6 ^{57}Fe Mössbauer spectroscopy

The ^{57}Fe Mössbauer spectra (Wissel, Germany) were acquired in transmission mode. The source was ^{57}Co: Rh. The velocity driver was operated in constant acceleration mode with a triangular velocity waveform, and the velocity scale was calibrated with the magnetically split sextet of a high-purity α-Fe foil at room temperature. A mass of *ca.* 200 mg of catalyst was mounted in a 2 cm^2 holder. Mössbauer measurements were performed at -268 ℃ with a helium flow cryostat (SHI-850 Series from Janis, USA). The spectra were analyzed by fitting the experimental spectrum with an appropriate combination of quadrupole doublets and sextets with Lorentzian profiles.

A.2.7 X-ray absorption spectroscopy

Fe K-edge XAS were collected at room temperature at SAMBA beamline (Synchrotron SOLEIL, Saint-Aubin, France). The beamline is equipped with a sagittally focusing Si 220 monochromator, and X-ray harmonics are removed by two Pd-coated mirrors. The catalyst powders were pelletized as disks of 10 mm diameter with 1 mm thickness, using Teflon powder (1 μm particle size) as a binder. Measurements were carried out in transmission or fluorescence mode, depending on the iron content.

A.2.8 Nitrite stripping

The nitrite adsorption method was used to determine the active SD and TOF of catalysts. The measurement was realized through the method first introduced by Malko *et al* using 0.125 M $NaNO_2$ in acetate buffer 0.5 M pH 5.2 and a loading of 0.3 mg cm^{-2} of catalysts prepared from different R/M ratio[231]. ORR polarization curves were carried out at 5 mV s^{-1} and 1600 rpm of rotation for unpoisoned, poisoned and recovered catalysts surface. The nitrite stripping was recorded in a potential range of 0.2 to -0.2 V *vs.* RHE. The SD and TOF were determined using the following equations:

$$SD(g^{-1}) = \frac{Q_{strip}(C\ g^{-1})\ \ N_A(mol^{-1})}{n_{strip}\ \ F\ (C\ mol^{-1})} \quad (6\text{-}1)$$

$$TOF(s^{-1}) = \frac{MA_{0.8}\ (A\ g^{-1})}{MSD\ (mol\ g^{-1})\ \times F\ (C\ mol^{-1})} \quad (6\text{-}2)$$

Where Q_{strip} is the excess coulometric charge associated with the reduction of one adsorbed nitrite ligand per site and and n_{strip} is the number of electrons associated with this stripping. F and NA are the Faraday and Avogadro constants, respectively. $MA_{0.8}$ is the mass activity measured at 0.8 V *vs.* RHE at pH = 1 and MSD is the SD expressed in mol g^{-1}. In this work, the SD values were calculated considering a 3 electrons process for the reduction reaction with the formation of NH_3OH^+ [258].

A.2.9 Inductively coupled plasma mass spectrometry (ICP-MS)

A PerkinElmer NexION 2000c instrument was used. Daily prepared iron (^{56}Fe) solutions were used for the calibration curves. Five solutions were prepared from commercial standard mono-element ICP-MS solution (Carl Roth GmbH & co. KG, 1000 mg L^{-1}) in order to obtain five-point calibration curves at 0, 2, 5, 10, and 20 µg L^{-1}. Rhodium (^{103}Rh) was used as the internal standard. To avoid any polyatomic interferences, the helium collision mode was used.

Reference

1. Hua, Y., Oliphant, M. & Hu, E. J. Development of renewable energy in Australia and China: A comparison of policies and status. *Renewable Energy* **85**, 1044–1051 (2016).
2. Global Energy Review: CO2 Emissions in 2021. *International Energy Agency* (2021).
3. The Future of Hydrogen. *International Energy Agency* 203 (2019).
4. Witt, T., Dumeier, M. & Geldermann, J. Combining scenario planning, energy system analysis, and multi-criteria analysis to develop and evaluate energy scenarios. *Journal of Cleaner Production* **242**, 118414 (2020).
5. Chu, S. & Majumdar, A. Opportunities and challenges for a sustainable energy future. *Nature* **488**, 294–303 (2012).
6. Seh, Z. W. *et al.* Combining theory and experiment in electrocatalysis: Insights into materials design. *Science* **355**, eaad4998 (2017).
7. Nazir, H. *et al.* Is the H2 economy realizable in the foreseeable future? Part I: H2 production methods. *International Journal of Hydrogen Energy* **45**, 13777–13788 (2020).
8. Sharaf, O. Z. & Orhan, M. F. An overview of fuel cell technology: Fundamentals and applications. *Renewable and Sustainable Energy Reviews* **32**, 810–853 (2014).
9. Nazir, H. *et al.* Is the H2 economy realizable in the foreseeable future? Part III: H2 usage technologies, applications, and challenges and opportunities. *International Journal of Hydrogen Energy* **45**, 28217–28239 (2020).
10. Thompson, S. T. *et al.* Direct hydrogen fuel cell electric vehicle cost analysis: System and high-volume manufacturing description, validation, and outlook. *Journal of Power Sources* **399**, 304–313 (2018).
11. Barbir, F. & Gómez, T. Efficiency and economics of proton exchange membrane (PEM) fuel cells. *International Journal of Hydrogen Energy* **22**, 1027–1037 (1997).
12. Akula, S. *et al.* Mesoporous textured Fe-N-C electrocatalysts as highly efficient cathodes for proton exchange membrane fuel cells. *Journal of Power Sources* **520**, 230819 (2022).
13. Akula, S. *et al.* Mesoporous textured Fe-N-C electrocatalysts as highly efficient cathodes for proton exchange membrane fuel cells. *Journal of Power Sources* **520**, 230819 (2022).
14. Pletcher, D. *A First Course in Electrode Processes*. (Royal Society of Chemistry, 2019).
15. Bard, A. J., Faulkner, L. R., Leddy, J. & Zoski, C. G. *Electrochemical Methods: Fundamentals and Applications*. *New York: wiley* vol. 2 (1980).
16. Reshetenko, T. *et al.* Design of PGM-free cathodic catalyst layers for advanced PEM fuel cells. *Applied Catalysis B: Environmental* **312**, 121424 (2022).
17. Reshetenko, T., Serov, A., Kulikovsky, A. & Atanassov, P. Impedance Spectroscopy Characterization of PEM Fuel Cells with Fe-N-C-Based Cathodes. *J. Electrochem. Soc.* **166**, F653 (2019).
18. Reshetenko, T. V., Bender, G., Bethune, K. & Rocheleau, R. Systematic study of back pressure and anode stoichiometry effects on spatial PEMFC performance distribution. *Electrochimica Acta* **56**, 8700–8710 (2011).
19. Jiao, K. *et al.* Designing the next generation of proton-exchange membrane fuel cells. *Nature* **595**, 361–369 (2021).
20. Gittleman, C., Lai, Y.-H. & Miller, D. Durability of Perfluorosulfonic Acid Membranes for PEM Fuel Cells. *Proceedings of the AIChE 2005 Annual Meeting* (2005).
21. Kraytsberg, A. & Ein-Eli, Y. Review of Advanced Materials for Proton Exchange Membrane Fuel Cells. *Energy Fuels* **28**, 7303–7330 (2014).
22. Wang, Y., Ruiz Diaz, D. F., Chen, K. S., Wang, Z. & Adroher, X. C. Materials, technological status, and fundamentals of PEM fuel cells – A review. *Materials Today* **32**, 178–203 (2020).

23. Aminudin, M. A. *et al.* An overview: Current progress on hydrogen fuel cell vehicles. *International Journal of Hydrogen Energy* **48**, 4371–4388 (2023).
24. Mekhilef, S., Saidur, R. & Safari, A. Comparative study of different fuel cell technologies. *Renewable and Sustainable Energy Reviews* **16**, 981–989 (2012).
25. Pan, Z. F. Advances and challenges in alkaline anion exchange membrane fuel cells. *Progress in Energy and Combustion Science* (2018).
26. Rosli, R. E. *et al.* A review of high-temperature proton exchange membrane fuel cell (HT-PEMFC) system. *International Journal of Hydrogen Energy* **42**, 9293–9314 (2017).
27. Gröger, O., Gasteiger, H. A. & Suchsland, J.-P. Review—Electromobility: Batteries or Fuel Cells? *J. Electrochem. Soc.* **162**, A2605 (2015).
28. Duclos, L. *et al.* Closing the loop: life cycle assessment and optimization of a PEMFC platinum-based catalyst recycling process. *Green Chem.* **22**, 1919–1933 (2020).
29. Xu, F., Mu, S. & Pan, M. Recycling of membrane electrode assembly of PEMFC by acid processing. *International Journal of Hydrogen Energy* **35**, 2976–2979 (2010).
30. Zhao, J., He, X., Tian, J., Wan, C. & Jiang, C. Reclaim/recycle of Pt/C catalysts for PEMFC. *Energy Conversion and Management* **48**, 450–453 (2007).
31. Duclos, L., Svecova, L., Laforest, V., Mandil, G. & Thivel, P.-X. Process development and optimization for platinum recovery from PEM fuel cell catalyst. *Hydrometallurgy* **160**, 79–89 (2016).
32. Sharma, R., Andreasen, S. J., Chamier, J. & Andersen, S. M. Pt/C Electrocatalyst Synthesis from Recycling of the Spent PEMFC Membrane Electrode Assembly: A Closed Loop Circular Economy. *J. Electrochem. Soc.* **166**, F963 (2019).
33. Chong, L. *et al.* Ultralow-loading platinum-cobalt fuel cell catalysts derived from imidazolate frameworks. *Science* **362**, 1276–1281 (2018).
34. Chen, H., Zhao, X., Zhang, T. & Pei, P. The reactant starvation of the proton exchange membrane fuel cells for vehicular applications: A review. *Energy Conversion and Management* **182**, 282–298 (2019).
35. Zheng, Y., Jiao, Y., Jaroniec, M., Jin, Y. & Qiao, S. Z. Nanostructured Metal-Free Electrochemical Catalysts for Highly Efficient Oxygen Reduction. *Small* **8**, 3550–3566 (2012).
36. Banham, D. & Ye, S. Current Status and Future Development of Catalyst Materials and Catalyst Layers for Proton Exchange Membrane Fuel Cells: An Industrial Perspective. *ACS Energy Lett.* **2**, 629–638 (2017).
37. Wu, G. & Zelenay, P. Nanostructured Nonprecious Metal Catalysts for Oxygen Reduction Reaction. *Acc. Chem. Res.* **46**, 1878–1889 (2013).
38. Shao, M., Chang, Q., Dodelet, J. P. & Chenitz, R. Recent Advances in Electrocatalysts for Oxygen Reduction Reaction. *Chemical Reviews* **116**, 3594–3657 (2016).
39. Zhang, X., Truong-Phuoc, L., Asset, T., Pronkin, S. & Pham-Huu, C. Are Fe–N–C Electrocatalysts an Alternative to Pt-Based Electrocatalysts for the Next Generation of Proton Exchange Membrane Fuel Cells? *ACS Catal.* **12**, 13853–13875 (2022).
40. Wang, H.-F., Tang, C. & Zhang, Q. A Review of Precious-Metal-Free Bifunctional Oxygen Electrocatalysts: Rational Design and Applications in Zn−Air Batteries. *Advanced Functional Materials* **28**, 1803329 (2018).
41. Kulkarni, A., Siahrostami, S., Patel, A. & Nørskov, J. K. Understanding Catalytic Activity Trends in the Oxygen Reduction Reaction. *Chem. Rev.* **118**, 2302–2312 (2018).
42. Shao, M., Chang, Q., Dodelet, J.-P. & Chenitz, R. Recent Advances in Electrocatalysts for Oxygen Reduction Reaction. *Chem. Rev.* **116**, 3594–3657 (2016).
43. Marković, N. M., Schmidt, T. J., Stamenković, V. & Ross, P. N. Oxygen Reduction Reaction on Pt and Pt Bimetallic Surfaces: A Selective Review. *Fuel Cells* **1**, 105–116 (2001).

44. Nie, Y., Li, L. & Wei, Z. Recent advancements in Pt and Pt-free catalysts for oxygen reduction reaction. *Chem. Soc. Rev.* **44**, 2168–2201 (2015).
45. Vojislav, R. S. *et al.* Improved Oxygen Reduction Activity on Pt3Ni(111) via Increased Surface Site Availability. *Science* **315**, 493–497 (2007).
46. Perez-Alonso, F. J. *et al.* The Effect of Size on the Oxygen Electroreduction Activity of Mass-Selected Platinum Nanoparticles. *Angewandte Chemie International Edition* **51**, 4641–4643 (2012).
47. Shao, M., Peles, A. & Shoemaker, K. Electrocatalysis on Platinum Nanoparticles: Particle Size Effect on Oxygen Reduction Reaction Activity. *Nano Lett.* **11**, 3714–3719 (2011).
48. Nie, Y., Li, L. & Wei, Z. Recent advancements in Pt and Pt-free catalysts for oxygen reduction reaction. *Chemical Society Reviews* **44**, 2168–2201 (2015).
49. Stamenkovic, V. *et al.* Changing the Activity of Electrocatalysts for Oxygen Reduction by Tuning the Surface Electronic Structure. *Angewandte Chemie* **118**, 2963–2967 (2006).
50. Stamenkovic, V. R. *et al.* Trends in electrocatalysis on extended and nanoscale Pt-bimetallic alloy surfaces. *Nature Materials* **6**, 241–247 (2007).
51. Liang, Y. *et al.* Co3O4 nanocrystals on graphene as a synergistic catalyst for oxygen reduction reaction. *Nature Mater* **10**, 780–786 (2011).
52. Kumar, K. *et al.* Effect of the Oxide–Carbon Heterointerface on the Activity of Co_3O_4/NRGO Nanocomposites toward ORR and OER. *J. Phys. Chem. C* **120**, 7949–7958 (2016).
53. Shao, M., Chang, Q., Dodelet, J.-P. & Chenitz, R. Recent Advances in Electrocatalysts for Oxygen Reduction Reaction. *Chem. Rev.* **116**, 3594–3657 (2016).
54. Zhao, D. *et al.* Effect of Se in Co-based selenides towards oxygen reduction electrocatalytic activity. *Journal of Power Sources* **206**, 103–107 (2012).
55. Gao, M.-R., Xu, Y.-F., Jiang, J. & Yu, S.-H. Nanostructured metal chalcogenides: synthesis, modification, and applications in energy conversion and storage devices. *Chem. Soc. Rev.* **42**, 2986 (2013).
56. Zhao, D. *et al.* Tungsten doped Co–Se nanocomposites as an efficient non precious metal catalyst for oxygen reduction. *Electrochimica Acta* **91**, 179–184 (2013).
57. Flyagina, I. S., Hughes, K. J., Mielczarek, D. C., Ingham, D. B. & Pourkashanian, M. Identifying the Catalytic Active Sites in Heteroatom-Doped Graphene for the Oxygen Reduction Reaction. *Fuel Cells* **16**, 568–576 (2016).
58. Nagy, B., Villar-Rodil, S., Tascón, J. M. D., Bakos, I. & László, K. Nitrogen doped mesoporous carbon aerogels and implications for electrocatalytic oxygen reduction reactions. *Microporous and Mesoporous Materials* **230**, 135–144 (2016).
59. Jaouen, F., Marcotte, S., Dodelet, J.-P. & Lindbergh, G. Oxygen Reduction Catalysts for Polymer Electrolyte Fuel Cells from the Pyrolysis of Iron Acetate Adsorbed on Various Carbon Supports. *J. Phys. Chem. B* **107**, 1376–1386 (2003).
60. Lefèvre, M., Proietti, E., Jaouen, F. & Dodelet, J.-P. Iron-Based Catalysts with Improved Oxygen Reduction Activity in Polymer Electrolyte Fuel Cells. *Science* **324**, 71–74 (2009).
61. Yang, Z. *et al.* Boosting Oxygen Reduction Catalysis with $Fe–N_4$ Sites Decorated Porous Carbons toward Fuel Cells. *ACS Catal.* **9**, 2158–2163 (2019).
62. Santori, P. G. *et al.* Effect of Pyrolysis Atmosphere and Electrolyte pH on the Oxygen Reduction Activity, Stability and Spectroscopic Signature of FeN_x Moieties in Fe-N-C Catalysts. *J. Electrochem. Soc.* **166**, F3311–F3320 (2019).
63. Tan, H. *et al.* Rational design and construction of nanoporous iron- and nitrogen-doped carbon electrocatalysts for oxygen reduction reaction. *J. Mater. Chem. A* **7**, 1380–1393 (2019).

64. Xiao, M. *et al.* Microporous Framework Induced Synthesis of Single-Atom Dispersed Fe-N-C Acidic ORR Catalyst and Its in Situ Reduced Fe-N $_4$ Active Site Identification Revealed by X-ray Absorption Spectroscopy. *ACS Catal.* **8**, 2824–2832 (2018).
65. Proietti, E. *et al.* Iron-based cathode catalyst with enhanced power density in polymer electrolyte membrane fuel cells. *Nat Commun* **2**, 416 (2011).
66. Jasinski, R. A New Fuel Cell Cathode Catalyst. *Nature* **201**, 1963–1964 (1964).
67. Wiesener, K. N4-chelates as electrocatalyst for cathodic oxygen reduction. *Electrochimica Acta* **31**, 1073–1078 (1986).
68. Liu, S. *et al.* Atomically dispersed iron sites with a nitrogen–carbon coating as highly active and durable oxygen reduction catalysts for fuel cells. *Nat Energy* **7**, 652–663 (2022).
69. Mehmood, A. *et al.* High loading of single atomic iron sites in Fe–NC oxygen reduction catalysts for proton exchange membrane fuel cells. *Nat Catal* **5**, 311–323 (2022).
70. Jiao, L. *et al.* Chemical vapour deposition of Fe–N–C oxygen reduction catalysts with full utilization of dense Fe–N4 sites. *Nat. Mater.* **20**, 1385–1391 (2021).
71. Kisand, K. *et al.* Templated Nitrogen-, Iron-, and Cobalt-Doped Mesoporous Nanocarbon Derived from an Alkylresorcinol Mixture for Anion-Exchange Membrane Fuel Cell Application. *ACS Catal.* **12**, 14050–14061 (2022).
72. Sun, Y. *et al.* Activity–Selectivity Trends in the Electrochemical Production of Hydrogen Peroxide over Single-Site Metal–Nitrogen–Carbon Catalysts. *J. Am. Chem. Soc.* **141**, 12372–12381 (2019).
73. Tse, E. C. M., Varnell, J. A., Hoang, T. T. H. & Gewirth, A. A. Elucidating Proton Involvement in the Rate-Determining Step for Pt/Pd-Based and Non-Precious-Metal Oxygen Reduction Reaction Catalysts Using the Kinetic Isotope Effect. *J. Phys. Chem. Lett.* **7**, 3542–3547 (2016).
74. Chen, Y., Asset, T., Lee, R., Artyushkova, K. & Atanassov, P. Kinetic Isotopic Effect Studies of Iron–Nitrogen–Carbon Electrocatalysts for Oxygen Reduction Reaction. *J. Phys. Chem. C* **123**, 11476–11483 (2019).
75. Kramm, U. I. *et al.* Structure of the catalytic sites in Fe/N/C-catalysts for O2-reduction in PEM fuel cells. *Phys. Chem. Chem. Phys.* **14**, 11673–11688 (2012).
76. Bouwkamp-Wijnoltz, A. L. *et al.* On Active-Site Heterogeneity in Pyrolyzed Carbon-Supported Iron Porphyrin Catalysts for the Electrochemical Reduction of Oxygen: An In Situ Mössbauer Study. *J. Phys. Chem. B* **106**, 12993–13001 (2002).
77. Ramaswamy, N., Tylus, U., Jia, Q. & Mukerjee, S. Activity Descriptor Identification for Oxygen Reduction on Nonprecious Electrocatalysts: Linking Surface Science to Coordination Chemistry. *J. Am. Chem. Soc.* **135**, 15443–15449 (2013).
78. Lefèvre, M., Proietti, E., Jaouen, F. & Dodelet, J.-P. Iron-Based Catalysts with Improved Oxygen Reduction Activity in Polymer Electrolyte Fuel Cells. *Science* **324**, 71–74 (2009).
79. Koslowski, U. I., Abs-Wurmbach, I., Fiechter, S. & Bogdanoff, P. Nature of the Catalytic Centers of Porphyrin-Based Electrocatalysts for the ORR: A Correlation of Kinetic Current Density with the Site Density of Fe−N4 Centers. *J. Phys. Chem. C* **112**, 15356–15366 (2008).
80. Jia, Q. *et al.* Experimental Observation of Redox-Induced Fe–N Switching Behavior as a Determinant Role for Oxygen Reduction Activity. *ACS Nano* **9**, 12496–12505 (2015).
81. Liu, J. *et al.* Metal-Free Nitrogen-Doped Carbon Foam Electrocatalysts for the Oxygen Reduction Reaction in Acid Solution. *J. Electrochem. Soc.* **163**, F1049 (2016).
82. Guo, D. *et al.* Active sites of nitrogen-doped carbon materials for oxygen reduction reaction clarified using model catalysts. *Science* **351**, 361–365 (2016).

83. Olson, T. S., Pylypenko, S., Fulghum, J. E. & Atanassov, P. Bifunctional Oxygen Reduction Reaction Mechanism on Non-Platinum Catalysts Derived from Pyrolyzed Porphyrins. *J. Electrochem. Soc.* **157**, B54 (2009).
84. Strickland, K. *et al.* Highly active oxygen reduction non-platinum group metal electrocatalyst without direct metal–nitrogen coordination. *Nat Commun* **6**, 7343 (2015).
85. Wiggins-Camacho, J. D. & Stevenson, K. J. Mechanistic Discussion of the Oxygen Reduction Reaction at Nitrogen-Doped Carbon Nanotubes. *J. Phys. Chem. C* **115**, 20002–20010 (2011).
86. Deng, D. *et al.* Iron Encapsulated within Pod-like Carbon Nanotubes for Oxygen Reduction Reaction. *Angewandte Chemie* **125**, 389–393 (2013).
87. Hu, Y. *et al.* Hollow Spheres of Iron Carbide Nanoparticles Encased in Graphitic Layers as Oxygen Reduction Catalysts. *Angewandte Chemie* **126**, 3749–3753 (2014).
88. Kramm, U. I. *et al.* Structure of the catalytic sites in Fe/N/C-catalysts for O2-reduction in PEM fuel cells. *Phys. Chem. Chem. Phys.* **14**, 11673 (2012).
89. Wu, G. *et al.* Synthesis–structure–performance correlation for polyaniline–Me–C non-precious metal cathode catalysts for oxygen reduction in fuel cells. *J. Mater. Chem.* **21**, 11392 (2011).
90. Jiang, W.-J. *et al.* Understanding the High Activity of Fe–N–C Electrocatalysts in Oxygen Reduction: Fe/Fe3C Nanoparticles Boost the Activity of Fe–Nx. *J. Am. Chem. Soc.* **138**, 3570–3578 (2016).
91. Sun, X. *et al.* Atomic-Level Fe-N-C Coupled with Fe3C-Fe Nanocomposites in Carbon Matrixes as High-Efficiency Bifunctional Oxygen Catalysts. *Small* **16**, 1906057 (2020).
92. Ao, X. *et al.* Unraveling the high-activity nature of Fe–N–C electrocatalysts for the oxygen reduction reaction: the extraordinary synergy between Fe–N4 and Fe4N. *J. Mater. Chem. A* **7**, 11792–11801 (2019).
93. Ao, X. *et al.* Markedly Enhanced Oxygen Reduction Activity of Single-Atom Fe Catalysts via Integration with Fe Nanoclusters. *ACS Nano* **13**, 11853–11862 (2019).
94. Choi, C. H. *et al.* Unraveling the Nature of Sites Active toward Hydrogen Peroxide Reduction in Fe-N-C Catalysts. *Angewandte Chemie International Edition* **56**, 8809–8812 (2017).
95. Li, L. *et al.* Fe3O4-Encapsulating N-doped porous carbon materials as efficient oxygen reduction reaction electrocatalysts for Zn–air batteries. *Chem. Commun.* **55**, 7538–7541 (2019).
96. Varnell, J. A. *et al.* Identification of carbon-encapsulated iron nanoparticles as active species in non-precious metal oxygen reduction catalysts. *Nat Commun* **7**, 12582 (2016).
97. Wu, G., More, K. L., Johnston, C. M. & Zelenay, P. High-Performance Electrocatalysts for Oxygen Reduction Derived from Polyaniline, Iron, and Cobalt. *Science* **332**, 443–447 (2011).
98. Zitolo, A. *et al.* Identification of catalytic sites for oxygen reduction in iron- and nitrogen-doped graphene materials. *Nature Mater* **14**, 937–942 (2015).
99. Artyushkova, K., Serov, A., Rojas-Carbonell, S. & Atanassov, P. Chemistry of Multitudinous Active Sites for Oxygen Reduction Reaction in Transition Metal–Nitrogen–Carbon Electrocatalysts. *J. Phys. Chem. C* **119**, 25917–25928 (2015).
100. Li, Y. *et al.* Preparation of Fe–N–C catalysts with FeNx (x = 1, 3, 4) active sites and comparison of their activities for the oxygen reduction reaction and performances in proton exchange membrane fuel cells. *J. Mater. Chem. A* **7**, 26147–26153 (2019).
101. Asset, T. & Atanassov, P. Iron-Nitrogen-Carbon Catalysts for Proton Exchange Membrane Fuel Cells. *Joule* **4**, 33–44 (2020).

102. Kabir, S., Artyushkova, K., Kiefer, B. & Atanassov, P. Computational and experimental evidence for a new TM–N3/C moiety family in non-PGM electrocatalysts. *Phys. Chem. Chem. Phys.* **17**, 17785–17789 (2015).
103. Liu, Q., Li, Q. & Chen, S. Metal–nitrogen coordination moieties in carbon for effective electrocatalytic reduction of oxygen. *Current Opinion in Electrochemistry* **21**, 46–54 (2020).
104. Lai, Q. *et al.* Metal–Organic-Framework-Derived Fe-N/C Electrocatalyst with Five-Coordinated Fe-Nx Sites for Advanced Oxygen Reduction in Acid Media. *ACS Catal.* **7**, 1655–1663 (2017).
105. Li, J. *et al.* Identification of durable and non-durable FeNx sites in Fe–N–C materials for proton exchange membrane fuel cells. *Nat Catal* **4**, 10–19 (2021).
106. Singh, K., Razmjooei, F. & Yu, J.-S. Active sites and factors influencing them for efficient oxygen reduction reaction in metal-N coordinated pyrolyzed and non-pyrolyzed catalysts: a review. *J. Mater. Chem. A* **5**, 20095–20119 (2017).
107. Herranz, J. *et al.* Unveiling N-Protonation and Anion-Binding Effects on Fe/N/C Catalysts for O $_2$ Reduction in Proton-Exchange-Membrane Fuel Cells. *J. Phys. Chem. C* **115**, 16087–16097 (2011).
108. Li, J. *et al.* Structural and mechanistic basis for the high activity of Fe–N–C catalysts toward oxygen reduction. *Energy Environ. Sci.* **9**, 2418–2432 (2016).
109. Jia, Q. *et al.* Experimental Observation of Redox-Induced Fe–N Switching Behavior as a Determinant Role for Oxygen Reduction Activity. *ACS Nano* **9**, 12496–12505 (2015).
110. Jia, Q. *et al.* Spectroscopic insights into the nature of active sites in iron–nitrogen–carbon electrocatalysts for oxygen reduction in acid. *Nano Energy* **29**, 65–82 (2016).
111. Li, J., Alsudairi, A., Ma, Z.-F., Mukerjee, S. & Jia, Q. Asymmetric Volcano Trend in Oxygen Reduction Activity of Pt and Non-Pt Catalysts: In Situ Identification of the Site-Blocking Effect. *J. Am. Chem. Soc.* **139**, 1384–1387 (2017).
112. D'Angelo, P., Zitolo, A., Migliorati, V. & Persson, I. Analysis of the detailed configuration of hydrated lanthanoid(III) ions in aqueous solution and crystalline salts by using K- And L3-edge XANES spectroscopy. *Chemistry - A European Journal* **16**, 684–692 (2010).
113. Lefèvre, M., Dodelet, J. P. & Bertrand, P. Molecular oxygen reduction in PEM fuel cells: Evidence for the simultaneous presence of two active sites in Fe-based catalysts. *Journal of Physical Chemistry B* **106**, 8705–8713 (2002).
114. Herranz, J., Lefèvre, M., Larouche, N., Stansfield, B. & Dodelet, J. P. Step-by-step synthesis of non-noble metal electrocatalysts for O 2 reduction under proton exchange membrane fuel cell conditions. *Journal of Physical Chemistry C* **111**, 19033–19042 (2007).
115. Ohms, D. *et al.* Influence of metal ions on the electrocatalytic oxygen reduction of carbon materials prepared from pyrolyzed polyacrylonitrile. *Journal of Power Sources* **38**, 327–334 (1992).
116. Li, J. *et al.* The challenge of achieving a high density of Fe-based active sites in a highly graphitic carbon matrix. *Catalysts* **9**, (2019).
117. Jaouen, F. & Dodelet, J. P. Average turn-over frequency of O2 electro-reduction for Fe/N/C and Co/N/C catalysts in PEFCs. *Electrochimica Acta* **52**, 5975–5984 (2007).
118. Osmieri, L. *et al.* Fe-N/C catalysts for oxygen reduction reaction supported on different carbonaceous materials. Performance in acidic and alkaline direct alcohol fuel cells. *Applied Catalysis B: Environmental* **205**, 637–653 (2017).
119. Jaouen, F., Lefèvre, M., Dodelet, J. P. & Cai, M. Heat-treated Fe/N/C catalysts for O2 electroreduction: Are active sites hosted in micropores? *Journal of Physical Chemistry B* **110**, 5553–5558 (2006).

120. Bouwkamp-Wijnoltz, A. L., Visscher, W. & Van Veen, J. A. R. The selectivity of oxygen reduction by pyrolysed iron porphyrin supported on carbon. *Electrochimica Acta* **43**, 3141–3152 (1998).
121. Wei, W. *et al.* Well-elaborated, mechanochemically synthesized Fe-TPP⊂ZIF precursors (Fe-TPP = tetraphenylporphine iron) to atomically dispersed iron–nitrogen species for oxygen reduction reaction and Zn-air batteries. *Nano Energy* **52**, 29–37 (2018).
122. Faubert, G. *et al.* Iron catalysts prepared by high-temperature pyrolysis of tetraphenylporphyrins adsorbed on carbon black for oxygen reduction in polymer electrolyte fuel cells. *Electrochimica Acta* **43**, 341–353 (1998).
123. Kalvelage, H., Mecklenburg, A., Kunz, U. & Hoffmann, U. Electrochemical reduction of oxygen at pyrolyzed iron and cobalt N4-chelates on carbon black supports. *Chemical Engineering and Technology* **23**, 803–807 (2000).
124. Faubert, G., Cote, R., Dodelet, J. P., Lefevre, M. & Bertrand, P. Oxygen reduction catalysts for polymer electrolyte fuel cells from the pyrolysis of Fe " acetate adsorbed on dianhydride. *Electrochimica Acta* **44**, 2589–2603 (1999).
125. Gupta, S., Tryk, D., Bae, I., Aldred, W. & Yeager, E. Heat-treated polyacrylonitrile-based catalysts for oxygen electroreduction. *Journal of Applied Electrochemistry* **19**, 19–27 (1989).
126. Yan, X. *et al.* Atomic interpretation of high activity on transition metal and nitrogen-doped carbon nanofibers for catalyzing oxygen reduction. *Journal of Materials Chemistry A* **5**, 3336–3345 (2017).
127. Jaouen, F. *et al.* Oxygen reduction activities compared in rotating-disk electrode and proton exchange membrane fuel cells for highly active FeNC catalysts. *Electrochimica Acta* **87**, 619–628 (2013).
128. Fu, X. *et al.* In Situ Polymer Graphenization Ingrained with Nanoporosity in a Nitrogenous Electrocatalyst Boosting the Performance of Polymer-Electrolyte-Membrane Fuel Cells. *Advanced Materials* **29**, (2017).
129. Shi, W. *et al.* A mesoporous Fe/N/C ORR catalyst for polymer electrolyte membrane fuel cells. *Cuihua Xuebao/Chinese Journal of Catalysis* **37**, 1103–1108 (2016).
130. Serov, A., Robson, M. H., Artyushkova, K. & Atanassov, P. Templated non-PGM cathode catalysts derived from iron and poly(ethyleneimine) precursors. *Applied Catalysis B: Environmental* **127**, 300–306 (2012).
131. Niu, K. *et al.* Graphene-based non-noble-metal Co/N/C catalyst for oxygen reduction reaction in alkaline solution. *Journal of Power Sources* **243**, 65–71 (2013).
132. Jiang, R. & Chu, D. Remarkably Active Catalysts for the Electroreduction of O[sub 2] to H[sub 2]O for Use in an Acidic Electrolyte Containing Concentrated Methanol. *Journal of The Electrochemical Society* **147**, 4605 (2000).
133. Antolini, E. Carbon supports for low-temperature fuel cell catalysts. *Applied Catalysis B: Environmental* **88**, 1–24 (2009).
134. Kramm, U. I. *et al.* Structure of the catalytic sites in Fe/N/C-catalysts for O 2-reduction in PEM fuel cells. *Physical Chemistry Chemical Physics* **14**, 11673–11688 (2012).
135. Wu, G. *et al.* Nitrogen-doped graphene-rich catalysts derived from heteroatom polymers for oxygen reduction in nonaqueous lithium-O2 battery cathodes. *ACS Nano* **6**, 9764–9776 (2012).
136. Li, J. *et al.* The Challenge of Achieving a High Density of Fe-Based Active Sites in a Highly Graphitic Carbon Matrix. *Catalysts* **9**, 144 (2019).
137. Wang, H., Côté, R., Faubert, G., Guay, D. & Dodelet, J. P. Effect of the pre-treatment of carbon black supports on the activity of Fe-based electrocatalysts for the reduction of oxygen. *Journal of Physical Chemistry B* **103**, 2042–2049 (1999).

138. Lefevre, M., Dodelet, J. P. & Bertrand, P. O2 reduction in PEM fuel cells: Activity and active site structural information for catalysts obtained by the pyrolysis at high temperature of Fe precursors. *Journal of Physical Chemistry B* **104**, 11238–11247 (2000).
139. Wang, M. Q. *et al.* Pyrolyzed Fe-N-C composite as an efficient non-precious metal catalyst for oxygen reduction reaction in acidic medium. *ACS Catalysis* **4**, 3928–3936 (2014).
140. Zhang, Q. *et al.* Porous carbon electrocatalyst with exclusive metal-coordinate active sites for acidic oxygen reduction reaction. *Carbon* **132**, 85–94 (2018).
141. Lef èvre, M., Dodelet, J. P. & Bertrand, P. Molecular oxygen reduction in PEM fuel cell conditions: ToF-SIMS analysis of Co-based electrocatalysts. *Journal of Physical Chemistry B* **109**, 16718–16724 (2005).
142. Xiao, M. *et al.* Microporous Framework Induced Synthesis of Single-Atom Dispersed Fe-N-C Acidic ORR Catalyst and Its in Situ Reduced Fe-N4 Active Site Identification Revealed by X-ray Absorption Spectroscopy. *ACS Catalysis* **8**, 2824–2832 (2018).
143. Nallathambi, V., Lee, J. W., Kumaraguru, S. P., Wu, G. & Popov, B. N. Development of high performance carbon composite catalyst for oxygen reduction reaction in PEM Proton Exchange Membrane fuel cells. *Journal of Power Sources* **183**, 34–42 (2008).
144. Jaouen, F., Lef èvre, M., Dodelet, J. P. & Cai, M. Heat-treated Fe/N/C catalysts for O2 electroreduction: Are active sites hosted in micropores? *Journal of Physical Chemistry B* **110**, 5553–5558 (2006).
145. Jaouen, F., Marcotte, S., Dodelet, J. P. & Lindbergh, G. Oxygen reduction catalysts for polymer electrolyte fuel cells from the pyrolysis of iron acetate adsorbed on various carbon supports. *Journal of Physical Chemistry B* **107**, 1376–1386 (2003).
146. Sa, Y. J. *et al.* A General Approach to Preferential Formation of Active Fe-Nx Sites in Fe-N/C Electrocatalysts for Efficient Oxygen Reduction Reaction. *Journal of the American Chemical Society* **138**, 15046–15056 (2016).
147. Moreno-Castilla, C. & Maldonado-H ódar, F. J. Carbon aerogels for catalysis applications: An overview. *Carbon* **43**, 455–465 (2005).
148. Job, N., Marie, J., Lambert, S., Berthon-Fabry, S. & Achard, P. Carbon xerogels as catalyst supports for PEM fuel cell cathode. *Energy Conversion and Management* **49**, 2461–2470 (2008).
149. Pekala, R. W. Organic aerogels from the polycondensation of resorcinol with formaldehyde. *Journal of Materials Science* **24**, 3221–3227 (1989).
150. Zanto, E. J., Al-Muhtaseb, S. A. & Ritter, J. A. Sol-gel-derived carbon aerogels and xerogels: Design of experiments approach to materials synthesis. *Industrial and Engineering Chemistry Research* **41**, 3151–3162 (2002).
151. Tamon, H., Ishizaka, H., Yamamoto, T. & Suzuki, T. Preparation of mesoporous carbon by freeze drying. *Carbon* **37**, 2049–2055 (1999).
152. Wang, Y. & Berthon-Fabry, S. One-Pot Synthesis of Fe-N-Containing Carbon Aerogel for Oxygen Reduction Reaction. *Electrocatalysis* **12**, 78–90 (2021).
153. Wang, Y. *et al.* Influence of the synthesis parameters on the proton exchange membrane fuel cells performance of Fe–N–C aerogel catalysts. *Journal of Power Sources* **514**, 230561 (2021).
154. Morozan, A. & Jaouen, F. Metal organic frameworks for electrochemical applications. *Energy and Environmental Science* **5**, 9269–9290 (2012).
155. Furukawa, H. *et al.* Ultrahigh porosity in metal-organic frameworks. *Science* **329**, 424–428 (2010).
156. Thompson, S. T. *et al.* ElectroCat: DOE's approach to PGM-free catalyst and electrode R&D. *Solid State Ionics* **319**, 68–76 (2018).

157. Pekala, R. W., Alviso, C. T., Kong, F. M. & Hulsey, S. S. Aerogels derived from multifunctional organic monomers. *Journal of Non-Crystalline Solids* **145**, 90–98 (1992).
158. Kramm, U. I., Herrmann-Geppert, I., Bogdanoff, P. & Fiechter, S. Effect of an ammonia treatment on structure, composition, and oxygen reduction reaction activity of Fe-N-C catalysts. *Journal of Physical Chemistry C* **115**, 23417–23427 (2011).
159. Koslowski, U. *et al.* Evaluation and Analysis of PEM-FC Performance using Non-Platinum Cathode Catalysts based on Pyrolysed Fe- and Co-Porphyrins - Influence of a Secondary Heat-treatment. *ECS Transactions* **13**, 125–141 (2019).
160. Chen, Z., Higgins, D., Yu, A., Zhang, L. & Zhang, J. A review on non-precious metal electrocatalysts for PEM fuel cells. *Energy and Environmental Science* **4**, 3167–3192 (2011).
161. Al-Muhtaseb, S. A. & Ritter, J. A. Preparation and properties of resorcinol-formaldehyde organic and carbon gels. *Advanced Materials* **15**, 101–114 (2003).
162. Mayer, S. T. The Aerocapacitor: An Electrochemical Double-Layer Energy-Storage Device. *Journal of The Electrochemical Society* **140**, 446 (1993).
163. Yamamoto, T., Nishimura, T., Suzuki, T. & Tamon, H. Control of mesoporosity of carbon gels prepared by sol-gel polycondensation and freeze drying. *Journal of Non-Crystalline Solids* **288**, 46–55 (2001).
164. Hanzawa, Y., Hatori, H., Yoshizawa, N. & Yamada, Y. Structural changes in carbon aerogels with high temperature treatment. *Carbon* **40**, 575–581 (2002).
165. Zhou, H. *et al.* Facile preparation and ultra-microporous structure of melamine-resorcinol-formaldehyde polymeric microspheres. *Chemical Communications* **49**, 3763–3765 (2013).
166. Vesel á, P. & Slov ák, V. Monitoring of N-doped organic xerogels pyrolysis by TG-MS. *Journal of Thermal Analysis and Calorimetry* **113**, 209–217 (2013).
167. Barbosa, M. B. *et al.* Electrochemical properties of carbon xerogel containing nitrogen in a carbon matrix. *Microporous and Mesoporous Materials* **162**, 24–30 (2012).
168. Mac ás, C. *et al.* Mn-Containing N-Doped Monolithic Carbon Aerogels with Enhanced Macroporosity as Electrodes for Capacitive Deionization. *ACS Sustainable Chemistry and Engineering* **4**, 2487–2494 (2016).
169. Flyagina, I. S., Hughes, K. J., Mielczarek, D. C., Ingham, D. B. & Pourkashanian, M. Identifying the Catalytic Active Sites in Heteroatom-Doped Graphene for the Oxygen Reduction Reaction. *Fuel Cells* **16**, 568–576 (2016).
170. Nagy, B. *et al.* Synergism of nitrogen and reduced graphene in the electrocatalytic behavior of resorcinol - Formaldehyde based carbon aerogels. *Carbon* **139**, 872–879 (2018).
171. Yang, Y. *et al.* Flexible counter electrodes based on nitrogen-doped carbon aerogels with tunable pore structure for high-performance dye-sensitized solar cells. *Carbon* **77**, 113–121 (2014).
172. Rasines, G. *et al.* N-doped monolithic carbon aerogel electrodes with optimized features for the electrosorption of ions. *Carbon* **83**, 262–274 (2015).
173. Rasines, G. *et al.* On the use of carbon black loaded nitrogen-doped carbon aerogel for the electrosorption of sodium chloride from saline water. *Electrochimica Acta* **170**, 154–163 (2015).
174. Horikawa, T. *et al.* Preparation of nitrogen-doped porous carbon by ammonia gas treatment and the effects of N-doping on water adsorption. *Carbon* **50**, 1833–1842 (2012).
175. Bert óti, I., Mohai, M. & L ászl ó, K. Surface modification of graphene and graphite by nitrogen plasma: Determination of chemical state alterations and assignments by quantitative X-ray photoelectron spectroscopy. *Carbon* **84**, 185–196 (2015).

176. Lin, Y. C., Lin, C. Y. & Chiu, P. W. Controllable graphene N-doping with ammonia plasma. *Applied Physics Letters* **96**, (2010).
177. Yu, J. *et al.* Simple fabrication of an ordered nitrogen-doped mesoporous carbon with resorcinol-melamine-formaldehyde resin. *Microporous and Mesoporous Materials* **190**, 117–127 (2014).
178. Zidar, J. *et al.* Stability and reactivity of progressively methylolated melamine derivatives. *Computational and Theoretical Chemistry* **1006**, 85–91 (2013).
179. Nagy, B., Villar-Rodil, S., Tascón, J. M. D., Bakos, I. & László, K. Nitrogen doped mesoporous carbon aerogels and implications for electrocatalytic oxygen reduction reactions. *Microporous and Mesoporous Materials* **230**, 135–144 (2016).
180. Wang, Q. *et al.* N-Doped 3D Carbon Aerogel with Trace Fe as an Efficient Catalyst for the Oxygen Reduction Reaction. *ChemElectroChem* **4**, 514–520 (2017).
181. Chen, H., Zhao, X., Zhang, T. & Pei, P. The reactant starvation of the proton exchange membrane fuel cells for vehicular applications: A review. *Energy Conversion and Management* **182**, 282–298 (2019).
182. Thompson, S. T. *et al.* Direct hydrogen fuel cell electric vehicle cost analysis: System and high-volume manufacturing description, validation, and outlook. *Journal of Power Sources* **399**, 304–313 (2018).
183. Lefèvre, M. & Dodelet, J. P. Fe-based catalysts for the reduction of oxygen in polymer electrolyte membrane fuel cell conditions: Determination of the amount of peroxide released during electroreduction and its influence on the stability of the catalysts. *Electrochimica Acta* **48**, 2749–2760 (2003).
184. Goellner, V. *et al.* Degradation of Fe/N/C catalysts upon high polarization in acid medium. *Phys. Chem. Chem. Phys.* **16**, 18454–18462 (2014).
185. ElKhatat et Al-Muhtaseb - 2011 - Advances in Tailoring Resorcinol-Formaldehyde Orga.pdf.
186. Wang, Y. & Berthon-Fabry, S. One-Pot Synthesis of Fe-N-Containing Carbon Aerogel for Oxygen Reduction Reaction. *Electrocatalysis* **12**, 78–90 (2021).
187. Wang, Y. *et al.* Influence of the synthesis parameters on the proton exchange membrane fuel cells performance of Fe–N–C aerogel catalysts. *Journal of Power Sources* **514**, 230561 (2021).
188. Jaouen, F., Lefèvre, M., Dodelet, J.-P. & Cai, M. Heat-Treated Fe/N/C Catalysts for O2 Electroreduction: Are Active Sites Hosted in Micropores? *J. Phys. Chem. B* **110**, 5553–5558 (2006).
189. Marr, C. & Li, X. Composition and performance modelling of catalyst layer in a proton exchange membrane fuel cell. *Journal of Power Sources* **77**, 17–27 (1999).
190. Gasteiger, H. A., Kocha, S. S., Sompalli, B. & Wagner, F. T. Activity benchmarks and requirements for Pt, Pt-alloy, and non-Pt oxygen reduction catalysts for PEMFCs. *Applied Catalysis B: Environmental* **56**, 9–35 (2005).
191. Li, J. *et al.* Designing the 3D Architecture of PGM-Free Cathodes for H2/Air Proton Exchange Membrane Fuel Cells. *ACS Appl. Energy Mater.* **2**, 7211–7222 (2019).
192. Jhong, H.-R. "Molly", Brushett, F. R. & Kenis, P. J. A. The Effects of Catalyst Layer Deposition Methodology on Electrode Performance. *Advanced Energy Materials* **3**, 589–599 (2013).
193. Ratso, S. *et al.* Effect of Ball-Milling on the Oxygen Reduction Reaction Activity of Iron and Nitrogen Co-doped Carbide-Derived Carbon Catalysts in Acid Media. *ACS Appl. Energy Mater.* **2**, 7952–7962 (2019).
194. Jaouen, F., Lefèvre, M., Dodelet, J.-P. & Cai, M. Heat-Treated Fe/N/C Catalysts for O2 Electroreduction: Are Active Sites Hosted in Micropores? *J. Phys. Chem. B* **110**, 5553–5558 (2006).

195. Jaouen, F. *et al.* Oxygen reduction activities compared in rotating-disk electrode and proton exchange membrane fuel cells for highly active FeNC catalysts. *Electrochimica Acta* **87**, 619–628 (2013).
196. Lo Vecchio, C., Aricò, A. S., Monforte, G. & Baglio, V. EDTA-derived Co N C and Fe N C electro-catalysts for the oxygen reduction reaction in acid environment. *Renewable Energy* **120**, 342–349 (2018).
197. Roiron, C., Celle, C., Jacques, P.-A., Heitzmann, M. & Simonato, J.-P. Structure–Property Relationship of Cryogel-Based Fe–N–C Catalysts for the Oxygen Reduction Reaction. *Energy Fuels* **35**, 16814–16821 (2021).
198. R. Lide, D. *Handbook of Chemistry and Physics*. (CRC Press, 2003).
199. Guilbaud, R., Butler, I. B., Ellam, R. M. & Rickard, D. Fe isotope exchange between Fe(II)aq and nanoparticulate mackinawite (FeSm) during nanoparticle growth. *Earth and Planetary Science Letters* **300**, 174–183 (2010).
200. ElKhatat, A. M. & Al-Muhtaseb, S. A. Advances in Tailoring Resorcinol-Formaldehyde Organic and Carbon Gels. *Adv. Mater.* **23**, 2887–2903 (2011).
201. Al-Muhtaseb, S. A. & Ritter, J. A. Preparation and Properties of Resorcinol-Formaldehyde Organic and Carbon Gels. *Adv. Mater.* **15**, 101–114 (2003).
202. Zion, N., Cullen, D. A., Zelenay, P. & Elbaz, L. Heat-Treated Aerogel as a Catalyst for the Oxygen Reduction Reaction. *Angew. Chem. Int. Ed.* **59**, 2483–2489 (2020).
203. Wang, D. H. *et al.* A pure organic heterostructure of μ-oxo dimeric iron(III) porphyrin and graphitic-C $_3$ N $_4$ for solar H $_2$ roduction from water. *J. Mater. Chem. A* **4**, 290–296 (2016).
204. Artyushkova, K. & Atanassov, P. X-Ray Photoelectron Spectroscopy for Characterization of Bionanocomposite Functional Materials for Energy-Harvesting Technologies. *ChemPhysChem* **14**, 2071–2080 (2013).
205. Artyushkova, K. Misconceptions in interpretation of nitrogen chemistry from x-ray photoelectron spectra. *Journal of Vacuum Science & Technology A* **38**, 031002 (2020).
206. Artyushkova, K., Serov, A., Rojas-Carbonell, S. & Atanassov, P. Chemistry of Multitudinous Active Sites for Oxygen Reduction Reaction in Transition Metal–Nitrogen–Carbon Electrocatalysts. *J. Phys. Chem. C* **119**, 25917–25928 (2015).
207. Unni, S. M., Devulapally, S., Karjule, N. & Kurungot, S. Graphene enriched with pyrrolic coordination of the doped nitrogen as an efficient metal-free electrocatalyst for oxygen reduction. *J. Mater. Chem.* **22**, 23506 (2012).
208. Matter, P. H., Wang, E., Arias, M., Biddinger, E. J. & Ozkan, U. S. Oxygen reduction reaction activity and surface properties of nanostructured nitrogen-containing carbon. *Journal of Molecular Catalysis A: Chemical* **264**, 73–81 (2007).
209. Jaouen, F. *et al.* Recent advances in non-precious metal catalysis for oxygen-reduction reaction in polymer electrolyte fuelcells. *Energy Environ. Sci.* **4**, 114–130 (2011).
210. Shinagawa, T., Garcia-Esparza, A. T. & Takanabe, K. Insight on Tafel slopes from a microkinetic analysis of aqueous electrocatalysis for energy conversion. *Sci Rep* **5**, 13801 (2015).
211. Sgarbi, R. *et al.* Oxygen reduction reaction mechanism and kinetics on M-NxCy and M@N-C active sites present in model M-N-C catalysts under alkaline and acidic conditions. *J Solid State Electrochem* **25**, 45–56 (2021).
212. Rasines, G. *et al.* N-doped monolithic carbon aerogel electrodes with optimized features for the electrosorption of ions. *Carbon* **83**, 262–274 (2015).
213. Li, J. *et al.* The evolution pathway from iron compounds to Fe1(II)-N4 sites through gas-phase iron during pyrolysis. *Journal of the American Chemical Society* **142**, 1412–1423 (2020).

214. Li, J. *et al.* The Challenge of Achieving a High Density of Fe-Based Active Sites in a Highly Graphitic Carbon Matrix. *Catalysts* **9**, 144 (2019).
215. Martell, A. E., Motekaitis, R. J., Chen, D., Hancock, R. D. & McManus, D. Selection of new Fe(III)/Fe(II) chelating agents as catalysts for the oxidation of hydrogen sulfide to sulfur by air. *Can. J. Chem.* **74**, 1872–1879 (1996).
216. Jamal, M. M. E. & Hammud, H. H. ABOUT THE INSTABILITY OF [Fe(III)(phen)3]3+. 8 (2008).
217. Zitolo, A. *et al.* Identification of catalytic sites in cobalt-nitrogen-carbon materials for the oxygen reduction reaction. *Nat Commun* **8**, 957 (2017).
218. Rasines, G. *et al.* On the use of carbon black loaded nitrogen-doped carbon aerogel for the electrosorption of sodium chloride from saline water. *Electrochimica Acta* **170**, 154–163 (2015).
219. Kumar, K. *et al.* Physical and Chemical Considerations for Improving Catalytic Activity and Stability of Non-Precious-Metal Oxygen Reduction Reaction Catalysts. *ACS Catal.* **8**, 11264–11276 (2018).
220. Hao, R. *et al.* Microporous Fe–N4 cataysts derived from biomass aerogel for a high-performance Zn–air battery. *Materials Today Energy* **21**, 100826 (2021).
221. Li, X. *et al.* Rechargeable Zn–Air Batteries with Outstanding Cycling Stability Enabled by Ultrafine FeNi Nanoparticles-Encapsulated N-Doped Carbon Nanosheets as a Bifunctional Electrocatalyst. *Nano Lett.* **21**, 3098–3105 (2021).
222. Sarapuu, A. *et al.* Electrocatalysis of oxygen reduction by iron-containing nitrogen-doped carbon aerogels in alkaline solution. *Electrochimica Acta* **230**, 81–88 (2017).
223. Liang, C., Sha, G. & Guo, S. Resorcinol–formaldehyde aerogels prepared by supercritical acetone drying. *Journal of Non-Crystalline Solids* **271**, 167–170 (2000).
224. Liu, L. *et al.* Ordered mesoporous carbons: citric acid-catalyzed synthesis, nitrogen doping and CO2 capture. *J. Mater. Chem.* **21**, 16001 (2011).
225. Weiss, S., Urdl, K., Mayer, H. A., Zikulnig-Rusch, E. M. & Kandelbauer, A. IR spectroscopy: Suitable method for determination of curing degree and crosslinking type in melamine–formaldehyde resins. *J Appl Polym Sci* **136**, 47691 (2019).
226. Berthon-Fabry, S., Hildenbrand, C. & Ilbizian, P. Lightweight superinsulating Resorcinol-Formaldehyde-APTES benzoxazine aerogel blankets for space applications. *European Polymer Journal* **78**, 25–37 (2016).
227. Higashimoto, S. *et al.* Synthesis, characterization and photocatalytic properties of robust resorcinol-formaldehyde polymer fine particles. *Applied Catalysis A: General* **623**, 118240 (2021).
228. Rasines, G. *et al.* N-doped monolithic carbon aerogel electrodes with optimized features for the electrosorption of ions. *Carbon* **83**, 262–274 (2015).
229. Rasines, G. *et al.* Mesoporous carbon black-aerogel composites with optimized properties for the electro-assisted removal of sodium chloride from brackish water. *Journal of Electroanalytical Chemistry* **741**, 42–50 (2015).
230. Rasines, G. *et al.* On the use of carbon black loaded nitrogen-doped carbon aerogel for the electrosorption of sodium chloride from saline water. *Electrochimica Acta* **170**, 154–163 (2015).
231. Kumar, K. *et al.* Fe–N–C Electrocatalysts' Durability: Effects of Single Atoms' Mobility and Clustering. *ACS Catal.* **11**, 484–494 (2021).
232. Can çado, L. G. *et al.* General equation for the determination of the crystallite size La of nanographite by Raman spectroscopy. *Appl. Phys. Lett.* **88**, 163106 (2006).
233. Sgarbi, R. *et al.* Oxygen reduction reaction mechanism and kinetics on M-NxCy and M@N-C active sites present in model M-N-C catalysts under alkaline and acidic conditions. *J Solid State Electrochem* **25**, 45–56 (2021).

234. Jia, Q. *et al.* Spectroscopic insights into the nature of active sites in iron–nitrogen–carbon electrocatalysts for oxygen reduction in acid. *Nano Energy* **29**, 65–82 (2016).
235. Mineva, T. *et al.* Understanding Active Sites in Pyrolyzed Fe–N–C Catalysts for Fuel Cell Cathodes by Bridging Density Functional Theory Calculations and 57Fe Mössbauer Spectroscopy. *ACS Catal.* **9**, 9359–9371 (2019).
236. Goenaga, G. A., Roy, A. L., Cantillo, N. M., Foister, S. & Zawodzinski, T. A. A family of platinum group metal-free catalysts for oxygen reduction in alkaline media. *Journal of Power Sources* **395**, 148–157 (2018).
237. Primbs, M. *et al.* Establishing reactivity descriptors for platinum group metal (PGM)-free Fe–N–C catalysts for PEM fuel cells. *Energy & Environmental Science* **13**, 2480–2500 (2020).
238. Kumar, K. *et al.* On the Influence of Oxygen on the Degradation of Fe-N-C Catalysts. *Angewandte Chemie* **132**, 3261–3269 (2020).
239. Li, J. *et al.* Identification of durable and non-durable FeNx sites in Fe–N–C materials for proton exchange membrane fuel cells. *Nat Catal* **4**, 10–19 (2021).
240. Koslowski, U. *et al.* Evaluation and Analysis of PEM-FC Performance using Non-Platinum Cathode Catalysts based on Pyrolysed Fe- and Co-Porphyrins - Influence of a Secondary Heat-treatment. *ECS Trans.* **13**, 125–141 (2008).
241. Bauer, L. & Anderson, H. J. Comments on the Treatment of Aromaticity and Acid-Base Character of Pyridine and Pyrrole in Contemporary Organic Chemistry Textbooks. *J. Chem. Educ.* **76**, 1151 (1999).
242. Wang, Y. *et al.* Fundamentals, materials, and machine learning of polymer electrolyte membrane fuel cell technology. *Energy and AI* **1**, 100014 (2020).
243. Garc á, Á. *et al.* Study of the evolution of FeN C and Fe3C species in Fe/N/C catalysts during the oxygen reduction reaction in acid and alkaline electrolyte. *Journal of Power Sources* **490**, 229487 (2021).
244. Castanheira, L. *et al.* Carbon Corrosion in Proton-Exchange Membrane Fuel Cells: Effect of the Carbon Structure, the Degradation Protocol, and the Gas Atmosphere. *ACS Catal.* **5**, 2184–2194 (2015).
245. Matsumoto, M., Manako, T. & Imai, H. Electrochemical STM Investigation of Oxidative Corrosion of the Surface of Highly Oriented Pyrolytic Graphite. *J. Electrochem. Soc.* **156**, B1208 (2009).
246. Goellner, V., Armel, V., Zitolo, A., Fonda, E. & Jaouen, F. Degradation by Hydrogen Peroxide of Metal-Nitrogen-Carbon Catalysts for Oxygen Reduction. *J. Electrochem. Soc.* **162**, H403–H414 (2015).
247. Katsounaros, I. *et al.* Hydrogen peroxide electrochemistry on platinum: towards understanding the oxygen reduction reaction mechanism. *Phys. Chem. Chem. Phys.* **14**, 7384–7391 (2012).
248. Choi, C. H. *et al.* The Achilles' heel of iron-based catalysts during oxygen reduction in an acidic medium. *Energy Environ. Sci.* **11**, 3176–3182 (2018).
249. Li, X. *et al.* First-principles study of the initial oxygen reduction reaction on stoichiometric and reduced CeO2 (111) surfaces as a cathode catalyst for lithium–oxygen batteries. *J. Mater. Chem. A* **5**, 3320–3329 (2017).
250. Yu, Y. *et al.* Trivalent cerium-preponderant CeO2/graphene sandwich-structured nanocomposite with greatly enhanced catalytic activity for the oxygen reduction reaction. *J. Mater. Chem. A* **5**, 6656–6663 (2017).
251. Wei, H. *et al.* A CeO2 modified phenylenediamine-based Fe/N/C with enhanced durability/stability as non-precious metal catalyst for oxygen reduction reaction. *Electrochemistry Communications* **88**, 19–23 (2018).

252. Lv, L. *et al.* A Universal Method to Engineer Metal Oxide–Metal–Carbon Interface for Highly Efficient Oxygen Reduction. *ACS Nano* **12**, 3042–3051 (2018).
253. Bai, S. *et al.* Fabricating Nitrogen-Rich Fe−N/C Electrocatalysts through CeO_2 -Assisted Pyrolysis for Enhanced Oxygen Reduction Reaction. *ChemElectroChem* **6**, 4040–4048 (2019).
254. Zhang, G., Chenitz, R., Lefèvre, M., Sun, S. & Dodelet, J.-P. Is iron involved in the lack of stability of Fe/N/C electrocatalysts used to reduce oxygen at the cathode of PEM fuel cells? *Nano Energy* **29**, 111–125 (2016).
255. Choi, J.-Y. *et al.* Is the rapid initial performance loss of Fe/N/C non precious metal catalysts due to micropore flooding? *Energy & Environmental Science* **10**, 296–305 (2017).
256. Banham, D. *et al.* Critical advancements in achieving high power and stable nonprecious metal catalyst–based MEAs for real-world proton exchange membrane fuel cell applications. *Science Advances* **4**, eaar7180 (2018).
257. Knight, D. S. & White, W. B. Characterization of diamond films by Raman spectroscopy. *Journal of Materials Research* **4**, 385–393 (1989).
258. Kim, D. H. *et al.* Selective electrochemical reduction of nitric oxide to hydroxylamine by atomically dispersed iron catalyst. *Nat Commun* **12**, 1856 (2021).

RÉSUMÉ

La pile à combustible à membrane échangeuse de protons (PEMFC) est un dispositif crucial pour le développement de l'économie basée sur l'hydrogène comme vecteur énergétique. Une grande quantité de catalyseur à base de platine est nécessaire à la cathode pour accélérer la réaction de réduction de l'oxygène, ce qui limite la commercialisation de la pile à combustible à grande échelle. Aujourd'hui, le matériau Fe-N-C est considéré comme un catalyseur prometteur à base de métal non noble pour remplacer le platine, mais son activité plus faible et le transport de matière avec ce type de catalyseur restent problématiques. Dans ce manuscrit, une série de catalyseurs à base d'aérogels de Fe-N-C a été synthétisée par pyrolyse d'aérogels de résorcinol-mélamine-formaldéhyde (RMF) contenant un précurseur de Fe. La structure très poreuse de l'aérogel facilite le transport de matière et sa méthode de synthèse permet de contrôler sa composition. Les impacts de la nature du précurseur de Fe et de la teneur en mélamine sur les propriétés des centres actifs et l'activité ORR des catalyseurs ont été étudiés et des liens entre paramètres de synthèse et performances électrochimiques ont été établi, en RDE comme en monocellule. Concernant la durabilité, une étude de l'ajout de CeO_2 comme piégeur de peroxyde a également été menée.

MOTS CLÉS

Catalyseur Fe-N-C, aérogel de carbone, réaction de réduction de l'oxygène, pile à combustible à membrane échangeuse de protons

ABSTRACT

The proton exchange membrane fuel cell (PEMFC) is a crucial device for the development of the hydrogen energy economy. A large amount of platinum-based catalyst is required at the cathode to accelerate the oxygen reduction reaction, which limits the commercialization of the fuel cell on a large scale. Today, Fe-N-C material is regarded as a promising non-noble metal catalyst to replace platinum, but its lower activity and material transport with this type of catalyst remain problematic. In this manuscript, a series of Fe-N-C aerogel catalysts were synthesized by pyrolysis of resorcinol-melamine-formaldehyde (RMF) aerogels containing an Fe precursor. The highly porous structure of the aerogel facilitates the transport of material and its synthesis method allows to control its composition. The impacts of the nature of the Fe precursor and the melamine content on the properties of the active centers and the ORR activity of the catalysts have been studied and links between synthesis parameters and electrochemical performances have been established, in RDE as well as in single cell. Concerning the durability, a study of the addition of CeO_2 as a peroxide scavenger has also been carried out.

KEYWORDS

Fe-N-C catalyst, carbon aerogel, oxygen reduction reaction, proton exchange membrane fuel cell